(NASA-CR-160051) DESIGN STUDIES FOR A FAR INFRARED ABSOLUTE SPECTROMETER FOR THE COSMIC BACKGROUND EXPLORER Final Technical Report (Block Engineering, Inc.) 266 p HC A12/MF A01 CSCL 14B G3/35

N81-12385

Unclas 29355

BE-79-808

INSTRUMENT DEFINITION REPORT

DESIGN STUDIES FOR A FAR INFRARED ABSOLUTE SPECTROMETER FOR THE COSMIC BACKGROUND EXPLORER

23 January 1980

Contract No. NAS 5-25535

For

National Aeronautics and Space Administration
Goddard Space Flight Center
Greenbelt, Maryland 20771

By

Block Research and Engineering Division
Bio-Rad Laboratories, Inc.
19 Blackstone Street
Cambridge, Massachusetts 02139

Prepared by:

Norman J.E. Johnson
Chief Scientist

Approved by:

E.R. Schildkraut
Division Manager

BLOCK
ENGINEERING

TABLE OF CONTENTS

TABLE OF CONTENTS (Continued)

TABLE OF CONTENTS (Continued)

LIST OF FIGURES

LIST OF FIGURES (Continued)

LIST OF FIGURE (Continued)

LIST OF TABLES

1.0 INTRODUCTION

The work described in this final technical report was performed under Contract No. NAS 5-25535 for the National Aeronautics and Space Administration/Goddard Space Flight Center at Greenbelt, Maryland. Design studies were carried out to describe the Far Infrared Absolute Spectrometer (FIRAS) for the Cosmic Background Explorer (COBE) in sufficient detail to define its performance and permit evaluation against the desired science. This work supports efforts under way at Goddard and at the Massachusetts Institute of Technology under the auspices of the COBE Science Team, appointed by NASA Headquarters and given the overall responsibility to define the COBE instrument complement. The results of this work are encouraging and clear recommendations for future effort in specific areas is given in Section 12.0.

1.1 FIRAS DESIGN APPROACH

The FIRAS instrument design presented here represents the end result of a sustained evolution from the instruments used in recent years for cosmic background measurement, particularly that developed by Mather et al (1974). The interferometer design recommended for FIRAS is an improvement of a design suggested by Johnson (1977), based on the conception of Martin and Puplett (1970). The improved version was described by the Science Team in the statement of work for the subject contract, and this interferometer configuration was fabricated and tested at MIT prior to the present effort.

The most difficult requirement for FIRAS is that of thermal balance to an unprecedented degree, and the fundamental design principle responsive to this requirement is that of unrelenting symmetry of design. The difficult requirement for increased spectral range is met by greatly increased instrumental throughput to achieve the problematic long wavelength limit and by internal refinement to achieve the short wavelength limit.

The design approach taken by Block is directed toward the refinement and realization of a FIRAS instrument utilizing the best technology available, as developed by the Science Team and as provided by Block's extensive experience in interferometer spectrometer systems. A critical factor in the design approach was the initial briefing at GSFC and the careful evaluation of pertinent earlier work. The design effort proceeded from this base, beginning with the optical configuration and extending through the mechanical, thermal, cryogenic, and electronic areas to the related subjects of calibration and testing.

The specific tasks accomplished under this contract were defined in the statement of work. These were:

1. Design of the FIRAS instrument according to given specifications and Science Team inputs within general interface limits.
2. Evaluation of an optical design meeting the system requirements, including error analysis with mechanical and thermal stresses.
3. Development of a thermal/mechanical instrument design meeting requirements of the system.
4. Design of bolometer signal de-glitching circuits compatible with the chosen bolometers and system data requirements.
5. Identification of necessary commands and telemetry to meet the requirements of the system.
6. Consideration of the testing requirements for the FIRAS instrument.
7. Preparation of Instrument Definition Report fully characterizing the FIRAS in sufficient detail to generate inputs for cost modeling purposes and to guide subsequent work.

In the course of the contracted effort, Block received verbal direction to de-emphasize de-glitching circuit design (item 4) based on reduced particle count predictions for most of the orbit.

Primary program efforts went into the optical design and analysis, the mechanical/thermal design and analysis, and the electronic/data system definition. During the six month period covered by these efforts, Block maintained contact with the Science Team, incorporating their inputs into the design where appropriate, but maintaining an independent viewpoint. At the design review meeting in June, Block presented two instrument concepts which satisfied or exceeded the instrumental requirements, and eliminated certain problems present in earlier designs. After discussions with GSFC/MIT personnel, a third instrumental concept has been developed which is presented here, representing the concensus of those discussions.

1.2 FIRAS SUMMARIZED SPECIFICATIONS

The FIRAS instrument is a cryogenically cooled, rapid scan interferometer spectrometer of the fully symmetrized Martin-Puplett configuration conceived specifically for this application. Inputs are obtained from Winston cone optical flux collectors, one open to space and a second coupled to a blackbody reference source. The spectrometer is a differential instrument, producing outputs corresponding to the Fourier transform of the spectral radiance difference between the two inputs. (One output is the inverse of the other.) The two outputs are sensed by four detectors, two optimized for shorter wavelength response, and two optimized for longer wavelengths. The FIRAS instrument configuration is shown in Figure 1.2-1 and the summarized specifications for the recommended instrument (Block Concept C) are given in Table 1.2-I.

The most important accomplishment of this study has been the increase in the instrument throughput to 1.5 cm^2-sr, with a corresponding increase in the effective aperture of the instrument and improvement in sensitivity, at especially longer wavelengths. This has been accompanied by increase in the size of critical apertures internally, with a reduction in diffraction losses. A powerful, highly linear drive motor and bearing have been devised to provide virtually error-free drive at velocities from zero to the maximum desired, corresponding to 10 cm/sec optical path change, with very reliable performance and minimal power dissipation.

1.3 COBE/FIRAS OPERATIONAL CONSTRAINTS

The FIRAS instrument is mounted in vacuum within the COBE liquid helium dewar, and shares this chamber with the DIRBE instrument. Both instruments fit onto a framework bolted to the bottom of the dewar, with special thermal conductance paths to the helium reservoir surrounding the cavity as necessary. The FIRAS and DIRBE instruments are covered with a liquid helium cooled cover until operational orbit is attained, when the cover is cast away and the instruments operate continually, always facing away from the earth in a sun-synchronous polar orbit, shielded from sun (and earth) by a sunshield. The entire sky is mapped by the FIRAS instrument over a period of at least one year, and the heat introduced by the cold instrumentation is therefore sharply limited.

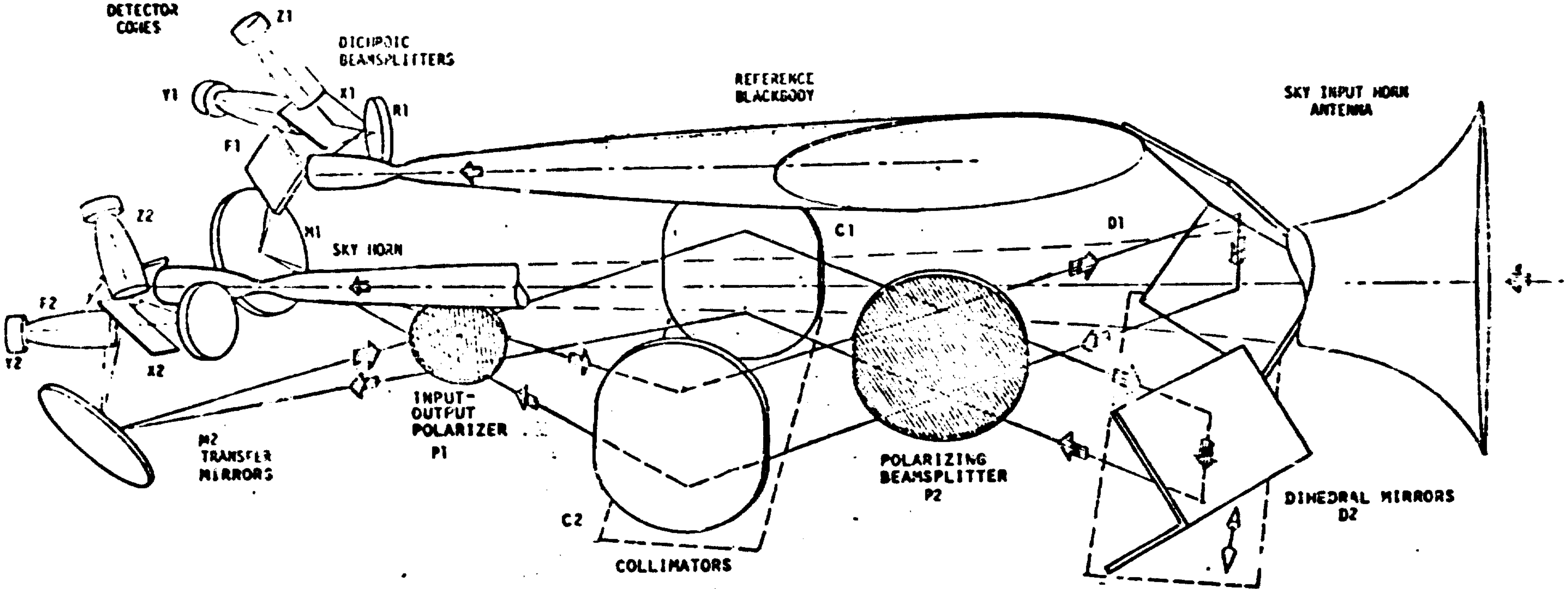

Figure 1.2-1. Fully Symmetrized FIRAS Interferometer

TABLE 1.2-I

FIRAS TECHNICAL SPECIFICATIONS

Field of View	7° full angle
Throughput	1.5 cm^2-sr nominal
Spectral Resolution	0.05 cm^{-1} (best unapodized)
Spectral Range	100μm to 1.0 cm
Retardation	±10 cm maximum, two sided interferogram
Retardation Rate	0 to 10 cm/sec
Spectral Precision	0.05 cm^{-1}
Instrumental Temperature	1.8 K nominal
Detectors	Silicon bolometers (4)
Size	0.4 cm square
NEP (1.8 K)	$<1 \times 10^{-14}$ watts/$Hz^{1/2}$
Power (Total)	<10 watts
Power Cryogenics	<1 milliwatt average <10 milliwatt peak
Operational Lifetime	>1 year
Optical Efficiency	0.07
System Sensitivity (NESR)	5×10^{-16} watts/cm^2-sr-cm^{-1}
Integration Time	3×10^4 seconds
Resolution	1.0 cm^{-1}
Total Mass	<40 kg including horns
Data Rate	200 bps without buffer
Commands	130 bits, issued by sequencer

The COBE satellite rotates about the centroid axis parallel to the FIRAS projected optical axis at one revolution per minute. During the launch and initial orbital maneuvering the FIRAS instrument is protected from vibration and acceleration by magnetically locking its scanning mechanism. In operation, the dihedral mirror assembly is scanned over a selected path at a selected rate, with the calibrator source stowed and the sky input horn open. The instrument is calibrated at intervals by the insertion of the calibrator source into the sky input horn, and the measurement of the calibrator radiation input over an appropriate range of temperatures. In the event of chance exposure to excess radiation, the calibrator also serves as a thermal radiation shield for the FIRAS instrument.

The FIRAS interface with the COBE system is mechanical, thermal, and electrical in nature. Mechanically, the FIRAS must fit into the COBE dewar and its electronics into the COBE electronics package. The FIRAS must contribute no significant uncompensated dynamic forces to the COBE operation. The thermal requirements in the COBE dewar are stringent, and directly affect mission life through cryogen loss. Electrical requirements involve wiring required to penetrate the dewar, with associated thermal aspects, power requirements from the spacecraft supply, and signal and housekeeping data outputs.

2.0 OPTICAL DESIGN

The optical configuration used in this study is based on the symmetrized Martin-Puplett interferometer and on the experimental model designed and evaluated at MIT. The use of specialized coupling optics allows efficient collection and transfer of radiation at millimeter wavelengths, while providing almost optical quality operation for the shorter wavelengths. The high throughput (area-solid angle product) utilized in Block's approach to the optical design assures that system response at the longest wavelengths will be acceptable.

The optical design has proceeded from in-line ray diagrams to folded configurational drawings fitted to the dewar constraints. The folded configurations are computerized and optimized using Block's generalized BOOST code. Finally, computer ray tracing is used to evaluate geometric aberrations at critical points, using spot diagrams.

2.1 BOOST OPTIMIZATION PROGRAM

This program was developed by Connors (1978) based on the LASL routine of Brixner (1973) and required some modifications for use in the FIRAS optical design. These modifications were necessary to permit optimization of very aberrated optical configurations with large angle tilting out of a plane. Some difficulties were encountered in implementing these modifications, but the modified program became fully operational during the contract period.

Surfaces can be any rotationally symmetric conic section, on or off axis, with arbitrary tilts, refractive or reflective. A total of 25 surfaces, excluding object and image planes, is possible. Up to 25 simultaneous variables can be selected from the assemblage of surface parameters, which are the coordinates, tilt, vertex curvature, and eccentricity of each surface.

The relative evaluation of a surface parameter set is derived from multiple ray r.m.s. spot size/position data. Several bundles, each bundle containing from two to seventeen rays in either of two colors, are traced through an optical system to form spots on a given or derived focal plane. A figure of merit equal to the mean square sum of the following "aberrations" is determined:

1. Focal error
2. Chromatic focal error
3. Sum of the r.m.s. spot sizes
4. R.m.s. sum of the spot centroid deviations
5. R.m.s. sum of the spot centroid chromatic deviations
6. Sum of the r.m.s. deviations in the optical path length
7. Penalty factor from violations of various constraints

Focal errors are determined by comparison of the focus for each spot to the average focus for all rays or from a desired focal plane. Spot centroid deviations are determined relative to a desired image or pupil configuration.

Optimization utilizes the damped least squares technique to minimize the sum of squares of the residual "aberrations". This balances the aberrations according to a preselected weighting scheme, permitting the emphasis and tighter control of certain variables. The damping is automatically adjusted based on the observed reduction in r.m.s. error relative to that predicted for linear convergence. In each iteration, all parameters are adjusted until reduction in the r.m.s. error is observed, subject to weighting and damping limitations. Each iteration takes approximately one-half hour with the NOVA computer used in this work.

For the FIRAS design, the angles off axis and the separations of certain curved mirrors were fixed. Distances from these mirrors to the input focal plane and to the dihedral mirrors were permitted to vary slowly, while the curvatures of the mirrors and their eccentricities provide the primary variables. In the early stages of the program, some difficulties were encountered in varying the eccentricities for elements far off axis, but this has been satisfactorily worked out. The input and output cones were not included in the optimization, as they are not conics and are well defined in non-imaging optical terms, but do not lend themselves to imaging analyses.

2.2 GSFC/MIT FIRAS DESIGN

The optical configuration represented in Figure 2.2-1 was implemented at MIT using available metal paraboloid mirrors, dihedral mirror assembly and drive made at MIT, and various beamsplitter techniques. The optical parameters indicated in Table 2.2-I, were particularly compact, and could fit into the COBE dewar envelope without modification. The design used a single input horn and coupling cone optic in tests performed, and the results were generally satisfactory with a single output detector and cone optic. Some optical analysis was performed at GSFC and MIT on this configuration, and that analysis served as a good test for the BOOST optimization program.

Examination of this optical design revealed that with an afocal entrance cone the alignment of radiation into the diagonal mirror (D1 and D2) became skew away from the primary system axis leading to excessive apodization at shorter wavelengths and higher throughput. This was corrected by increasing the spacing between the transfer mirrors (M1 and M2) and the collimator mirrors (C1 and C2) in the Block Concept A and B configurations, and by use of a quasi-focusing entrance optic in the Concept C configuration. Figure 2.2-2 shows the in-line optical schematic for the GSFC/MIT configuration with the afocal entrance optic. Figure 2.2-3 gives the spot diagram for this system as optimized at an output focal plane corresponding to the input cone aperture position. The desired output spot configuration here is identical to the input configuration but inverted downwards. The effect of the dihedral mirrors effectively cancels out aberrations normal to the primary interferometer plane, but does little to reduce aberrations parallel to that plane, as can be seen in the spot diagram.

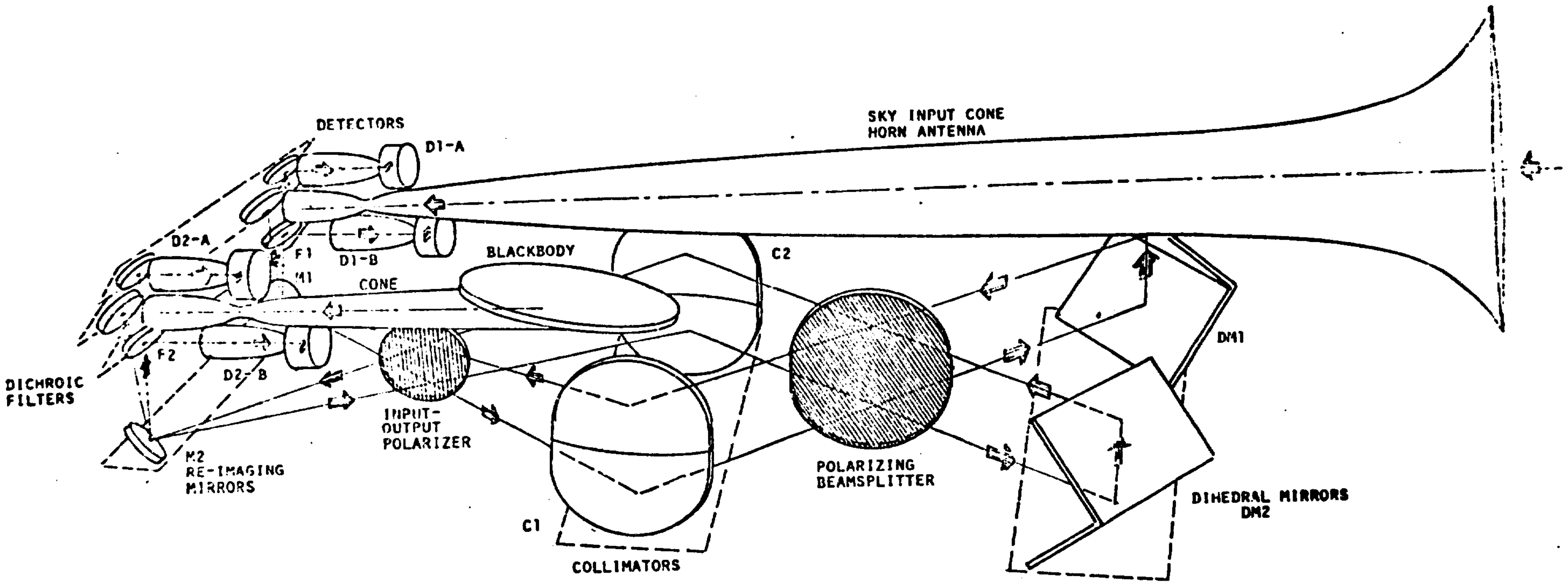

Figure 2.2-1. GSFC/MIT Design Concept

TABLE 2.2-I

GSFC/MIT OPTICAL PARAMETERS

Item	Description	Clear Aperture	Focal Length	Separation
SB, BB,	Input Horns	8.0/0.45 cm	80 cm	-
W1, W2,	Input Winston Cones	0.45/1.57	3.36	0.0 cm
M1, M2,	Parabolic Mirrors	13.0	1.40*	14.0*
P1	Input/Output Polarizer	18 × 20	Inf	20.0*
C1, C2,	Parabolic Mirrors	20 × 23	40.0*	20.0*
P2	Polarizing Beamsplitter	16 × 20	Inf	20.0*
1, D2,	Dihedral Mirrors	10 × 18	Inf	20.0*
Y1, Y2,	Output Winstorn Cones	4.0 (3.75)	14.39 (12.7)	3.4
B1, B2,	Bolometers	0.4 × 0.4	Inf	-
E1, E2,	Cavities	0.45	-	-

---

* Nominal

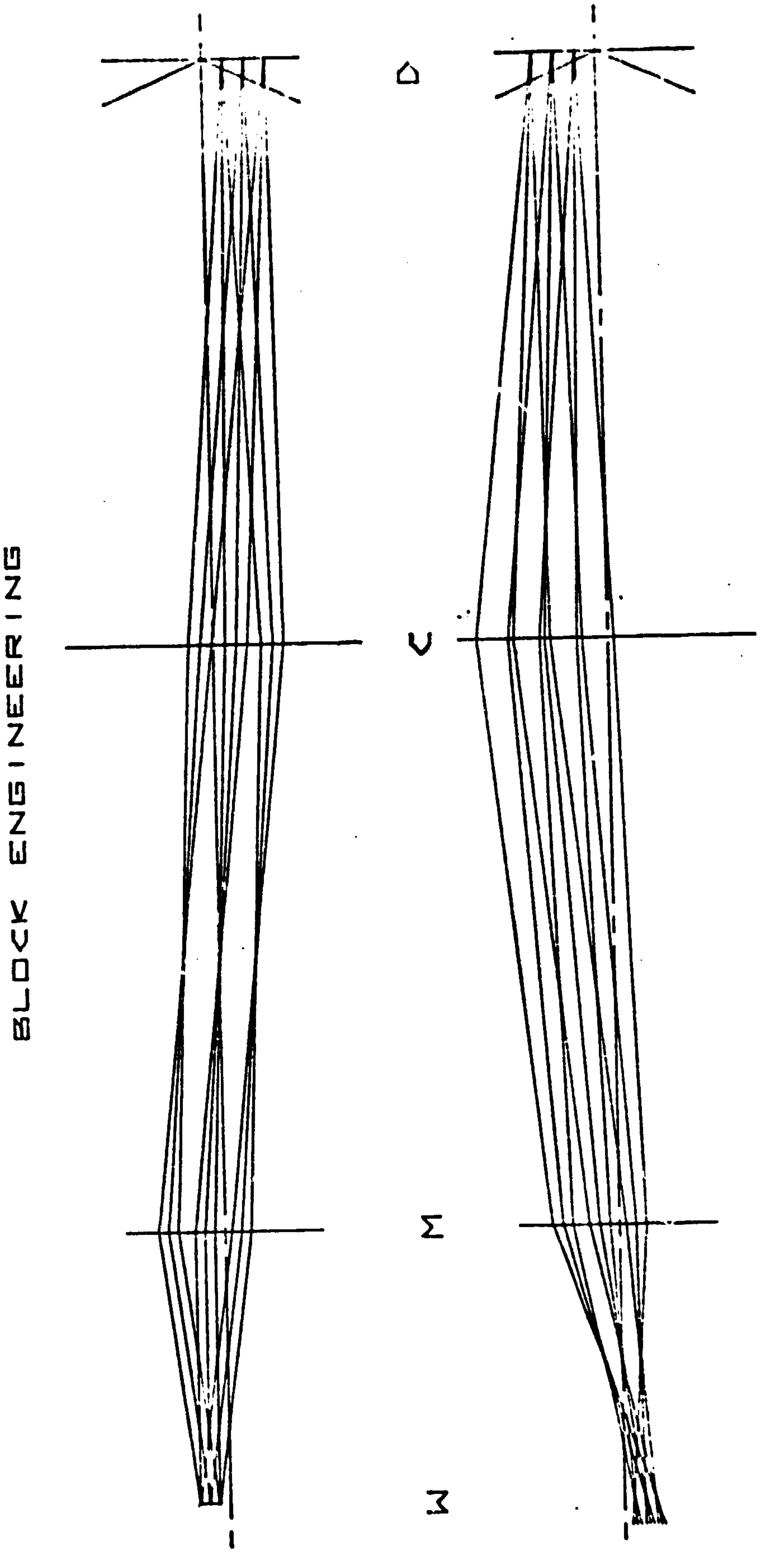

Figure 2.2-2. GSFC/MIT Optical Schematic

Figure 2.2-3. GSFC/MIT Spot Diagram Optimized

The aberrations at the dihedral mirror are more severe normal to the system plane, however, and these rapidly become excessive with increasing throughput. Reduction of dihedral aberrations is accomplished in Block designs through decrease in the angle off axis at the transfer mirror.

2.3 BLOCK CONCEPT A DESIGN

This design concept is shown in Figure 2.3-1 and 2.3-2, with nominal optical parameters indicated in Table 2.3-I. Two flat mirrors (F1 and F2) are used at the collimator focal planes to direct the radiation from the vertical input horns and transfer mirrors (M1 and M2) into the horizontal interferometer plane. As indicated earlier, this design shifts the transfer mirrors farther away from the collimators (C1 and C2), creating a distinct pupil at the flats that is later reimaged onto the detector cone apertures (Y1, Z1, Y2, and Z2). The schematic in-line ray trace in Figure 2.3-3 shows this, and it is clear that the afocal entrance cone is consistent with paraxial ray bundles entering the dihedrals. The detectors receive radiation picked off by the flat mirrors (F2 and F4), and this radiation is refocused by the output mirrors (M3 and M4). The detector cone apertures are located at pupil planes, thus avoiding focus shifts that arise at the output image plane due to scanning of the dihedral mirrors at the intermediate image plane.

The throughput of the sky input horn was increased to 1.0 cm^2-sr in this design to improve the response of the system at the longest wavelengths. Since the throughput of the GSFC/MIT interferometer configuration internally exceeds 1.5 cm^2-sr, no increase in these component sizes was necessary.

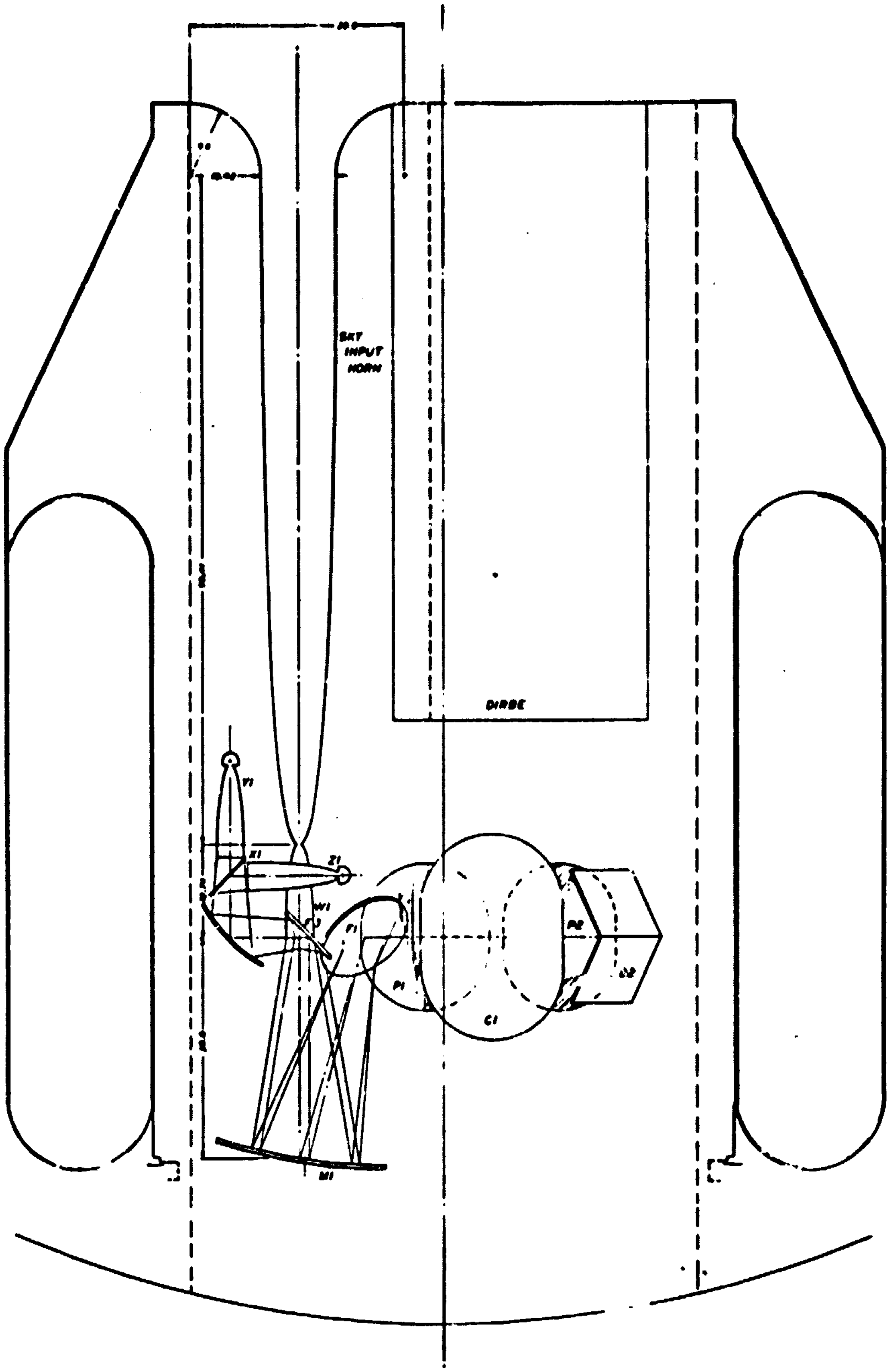

Figure 2.3-1. Firas Design Concept A, Side View

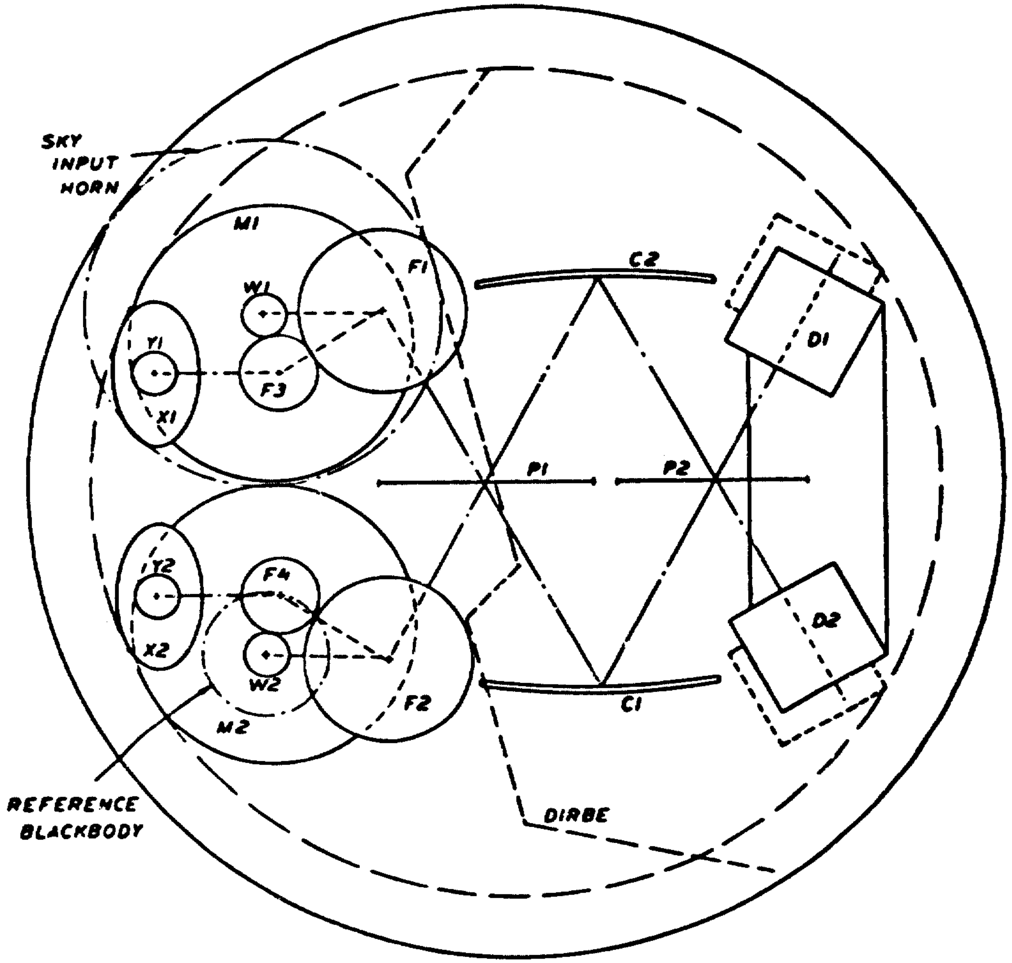

Figure 2.3-2. Firas Design Concept A, Top View

TABLE 2.3-I

FIRAS A OPTICAL PARAMETERS

Item	Description	Clear Aperture	Focal Length	Separation
SB, BB,	Input Horns	10.42/0.64 cm	90.41 cm	-
W1, W2,	Input Winston Cones	0.64/3.75	12.74	0.0 cm
M1, M2,	Parabolic Mirrors	24.0	30.0*	30.0*
F1, F2,	Flat Mirrors	14.0	Inf	30.0*
P1	Input/Output Polarizer	18 × 20	Inf	20.0*
C1, C2,	Parabolic Mirrors	20 × 28	40.0*	20.0*
P2	Polarizing Beamsplitter	16 × 20	Inf	20.0*
D1, D2,	Dihedral Mirrors	10 × 18	Inf	20.0*
F3, F4,	Flat Mirrors	6.5	Inf	At W1, W2
T1, T2,	Parabolic Mirrors	12.0	11.0*	12.0*
X1, X2,	Dichroic Beamsplitters	5 × 7	Inf	8.6
Y1, Y2, Z1, Z2,	Output Winston Cones	4.0 (3.75)	14.39 (12.7)	3.4
B1, B2, B3, B4,	Bolometers	0.4 × 0.4	Inf	0.4
E1, E2, E3, E4,	Ellipsoidal Cavities	0.64	0.4	0.4

---

* Nominal

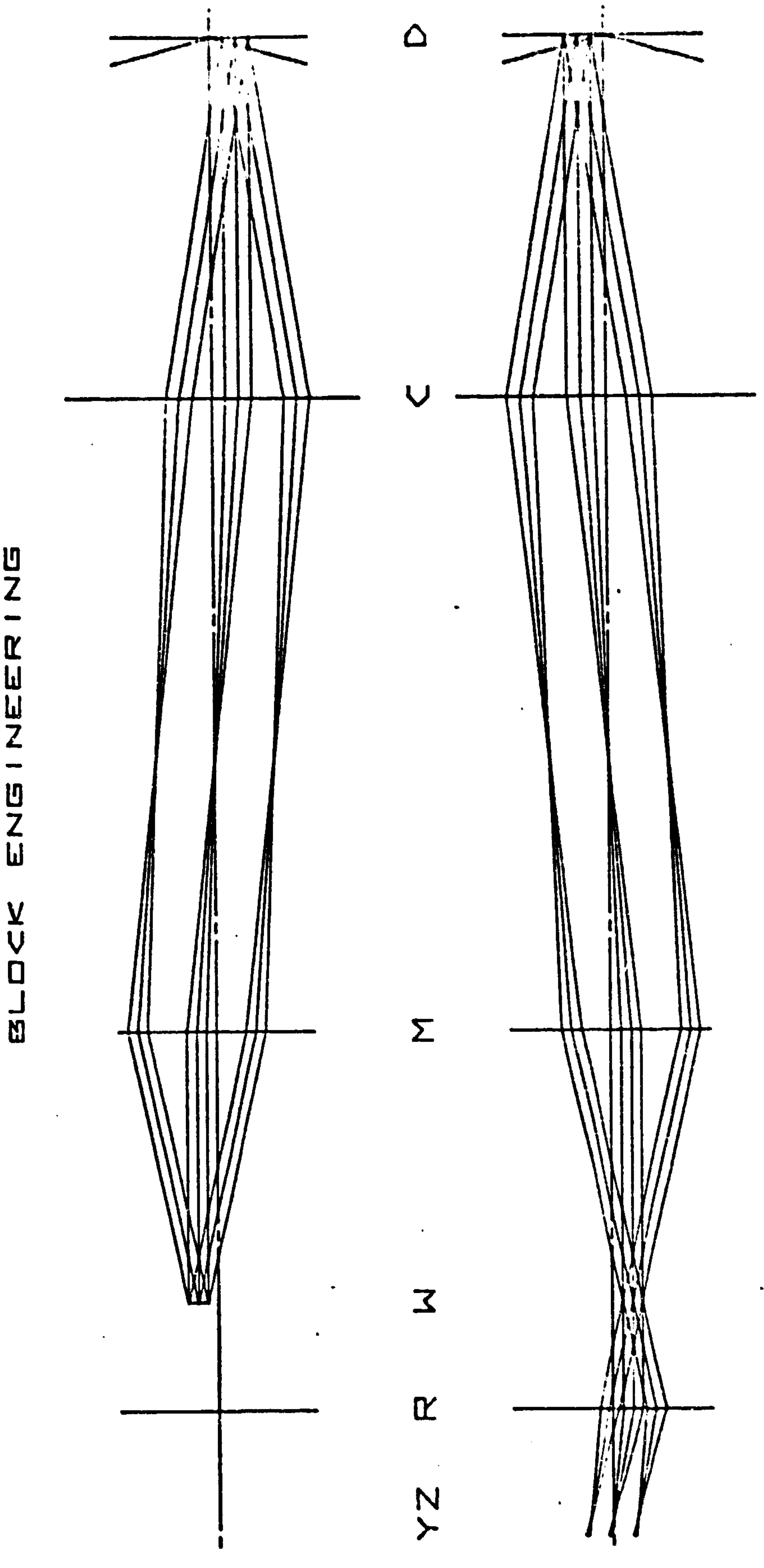

Figure 2.3-3. Firas A Optical Schematic

The Winston cones at the input and output were increased in throughput correspondingly, and their aperture diameters were increased even more to reduce internal diffraction losses. The optical system just fit within the COBE dewar constraints, although the outer lip of the sky input horn extended to the maximum limit of the instrument package. (This is true of all Block designs, and is considered marginally acceptable on the basis that it extends at the top of the structure, and will not interfere with insertion or connection of the instrument package to the dewar. Another way of treating this is to simply cut off the part of the outer lip that overextends.)

Optimization of the Concept A design was carried out earlier in the contracted effort, before the programming was able to vary eccentricities of the components. The spot diagrams shown in Figures 2.3-4 and 2.3-5 were obtained, and the input rays are also shown above the output rays at the image plane containing the entrance cone apertures and the flat mirrors leading to the detector cones. The improvement obtained from this limited optimization can be seen by comparison of these figures. Further optimization was not performed since the increase in throughput to 1.5 cm^2-sr was planned, and modification of the optics would follow.

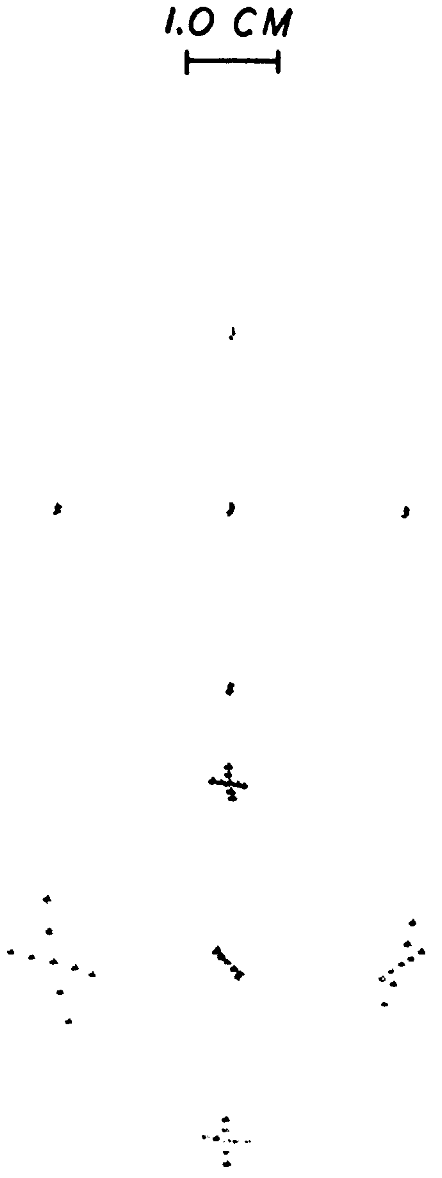

Figure 2.3-4. FIRAS A Spot Diagram Nominal

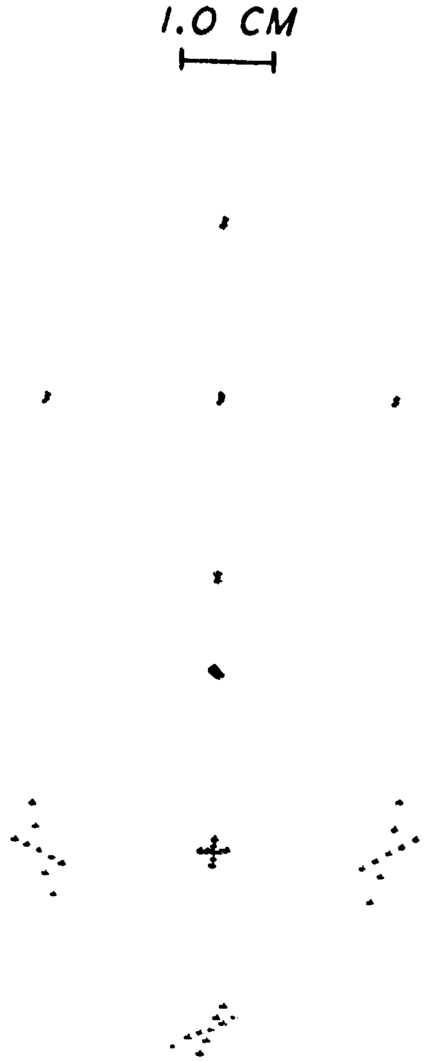

Figure 2.3-5. Firas A Spot Diagram Optimized

2.4 BLOCK CONCEPT B DESIGN

An important possibility was carefully investigated, which resulted in the development of the Concept B design shown in Figures 2.4-1 and 2.4-2. Table 2.4-I gives the optical parameters for this configuration. This design permitted the switching of the two radiative inputs prior to modulation in the interferometer, so that all instrumental imbalance following the switching could be cancelled out, leaving only the variations in the input optics to affect the measurement. A great many configurations were considered, and the system presented is the best of these. Even this design has certain problems, however, arising from the difficulty of separating the input and output beams while still permitting switching.

Separation of the beams must occur at a plane imaging the dihedral mirrors, and since it is impractical to interchange the input horns, the switching plane is optically separated from the horn apertures through the transfer mirrors (M1 and M2). The switching could, of course, be done farther into the instrument (e.g. by rotating the entire interferometer - P1, C1, C2, P2, D1, and D2 - about an axis through P1 and P2 in the Concept A design), but this is still affected by thermal imbalances in the earlier optics and by the more massive mechanism involved.

The switching is done by inserting and removing a two-sided flat mirror (S1) that reflects the two input beams to the same side reimaging mirrors (T1 and T2) or permits them to pass to the opposite side mirrors (T2 and T1).

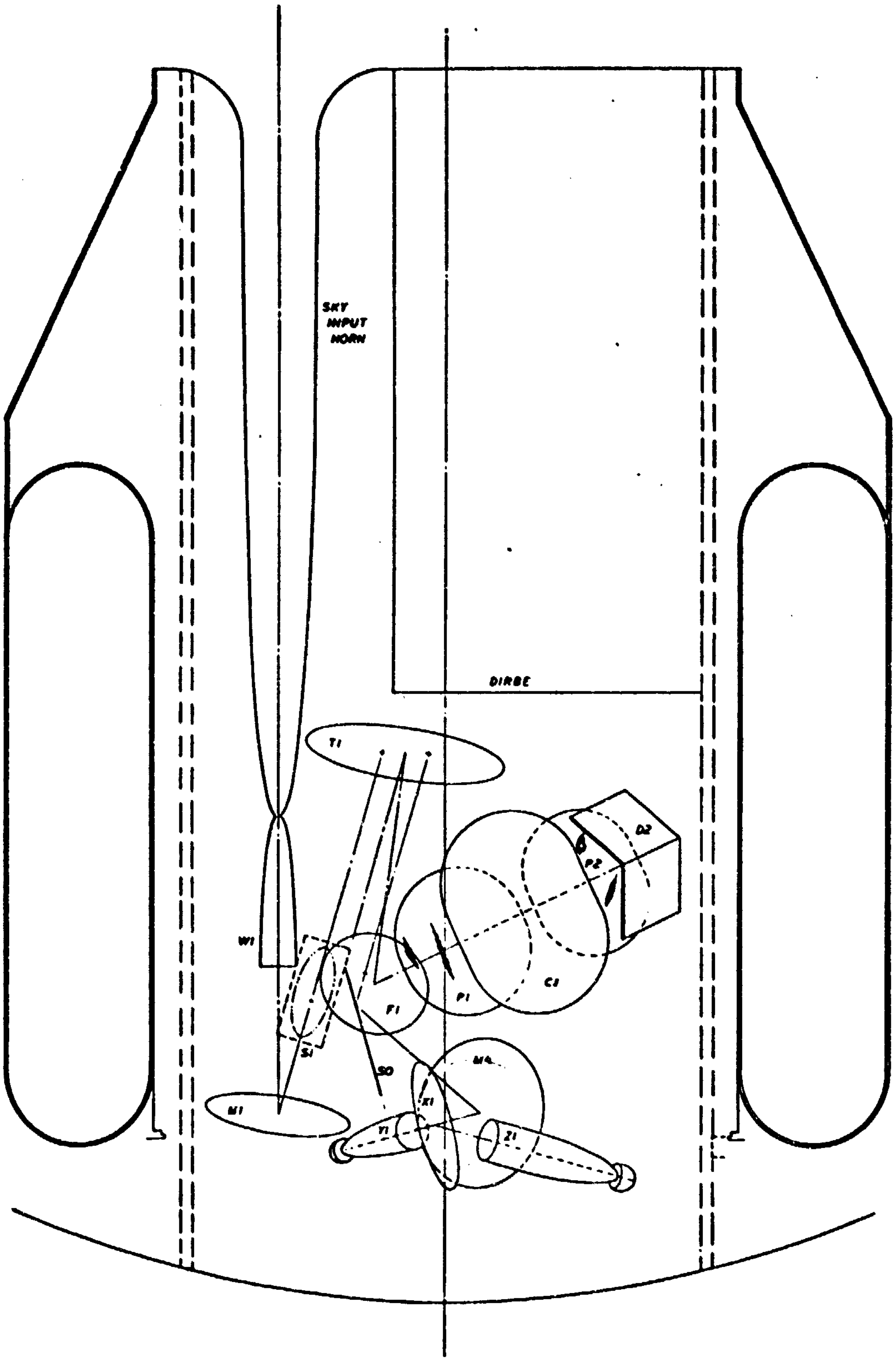

Figure 2.4-1. Firas Design Concept B, Side View

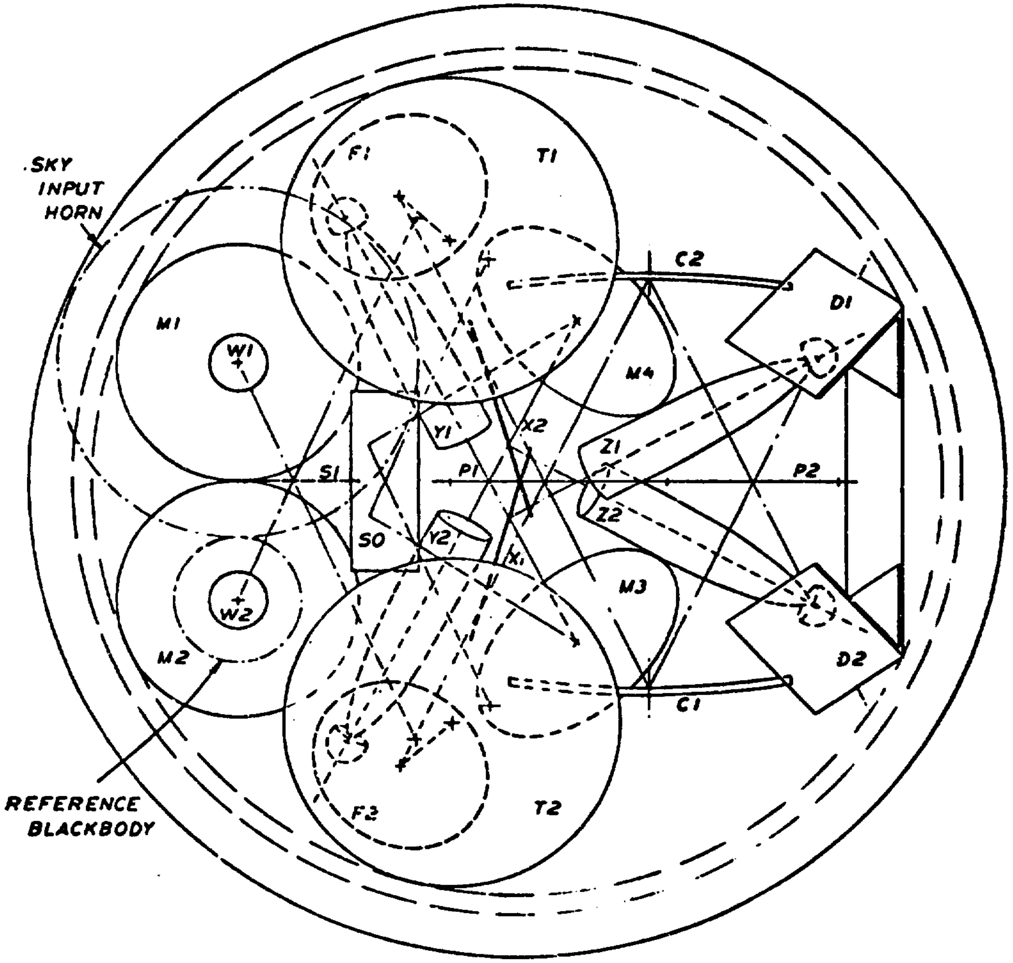

Figure 2.4-2. Firas Design Concept B, Top View

TABLE 2.4-I
FIRAS B OPTICAL PARAMETERS

Item	Description	Clear Aperture	Focal Length	Separation
SB, BB	Input Horns	10.42/0.64 cm	90.41 cm	-
W1, W2,	Input Winston Cones	0.64/3,75	12.74	0.0 cm
M1, M2,	Parabolic Mirrors	18.0	20.0*	20.0*
S1	Beam Switching Mirror	7 × 14	Inf	20.0
T1, T2,	Parabolic Mirrors	22.0	40.0*	40.0*
F1, F2	Flat Mirrors	12.0	Inf	40.0
P1	Input/Output Polarizer	18 × 20	Inf	20.0
C1, C2,	Parabolic Mirrors	20 × 28	40.0*	20.0
P2	Polarizing Beamsplitter	16 × 20	Inf	20.0
D1, D2,	Dihedral Mirrors	10 × 18	Inf	20.0
SO	Flat Mirror	10 × 18	Inf	40.0 (T1,T2)
M3, M4,	Parabolic Mirrors	18.0	8.1	25.0
X1, X2,	Dichroic Beamsplitters	5 × 7	Inf	8.6
Y1, Y2, Z1, Z2,	Output Winston Cones	4.0 (3.75)	14.39 (12.7)	3.4
B1, B2, B3, B4,	Bolometers	0.4 × 0.4	Inf	0.4
E1, E2,	Bolometer Cavities	0.64	0.4	0.4

---

* Nominal values given

On the return pass, the output beams are picked off by the fixed flat mirror (SO), crossing over to the opposite side detector mirrors (M3 and M4). The location of the detector cones with their dichroic beamsplitters is complicated by the complex configuration, and it was necessary to arrange these assymetrically to fit the dewar envelope.

In order to obtain the minimum image at the separation plane (S1), with maximum possible separation of the input and output beams, it was necessary to tilt the entire interferometer up at 30° from the Concept A interferometer plane. The separation is not entirely adequate, since although it separates the geometric beams perfectly, diffracted radiation overlaps the upper edge of the output mirror pickoff (SO) significantly. The angle that SO makes with the beams is such that the intersection extends well out of the focal plane, reducing the benefits of increased separation.

The input cone is located at a pupil plane, reimaged to the flat mirrors (F1 and F2), as can be seen in the schematic in-line ray trace in Figure 2.4-3, and finally reimaged onto the detector cone. This is an ideal sequence, since the primary diffraction appears in the conjugate planes (at S1, D1/D2, and SO), and losses due to diffraction can be minimized everywhere except at S1 and SO. The throughput of this design is 1.0 cm^2-sr at the input horn and over 1.5 cm^2-sr elsewhere, as before. The same Winston cones are used in this design as in the Concept A design.

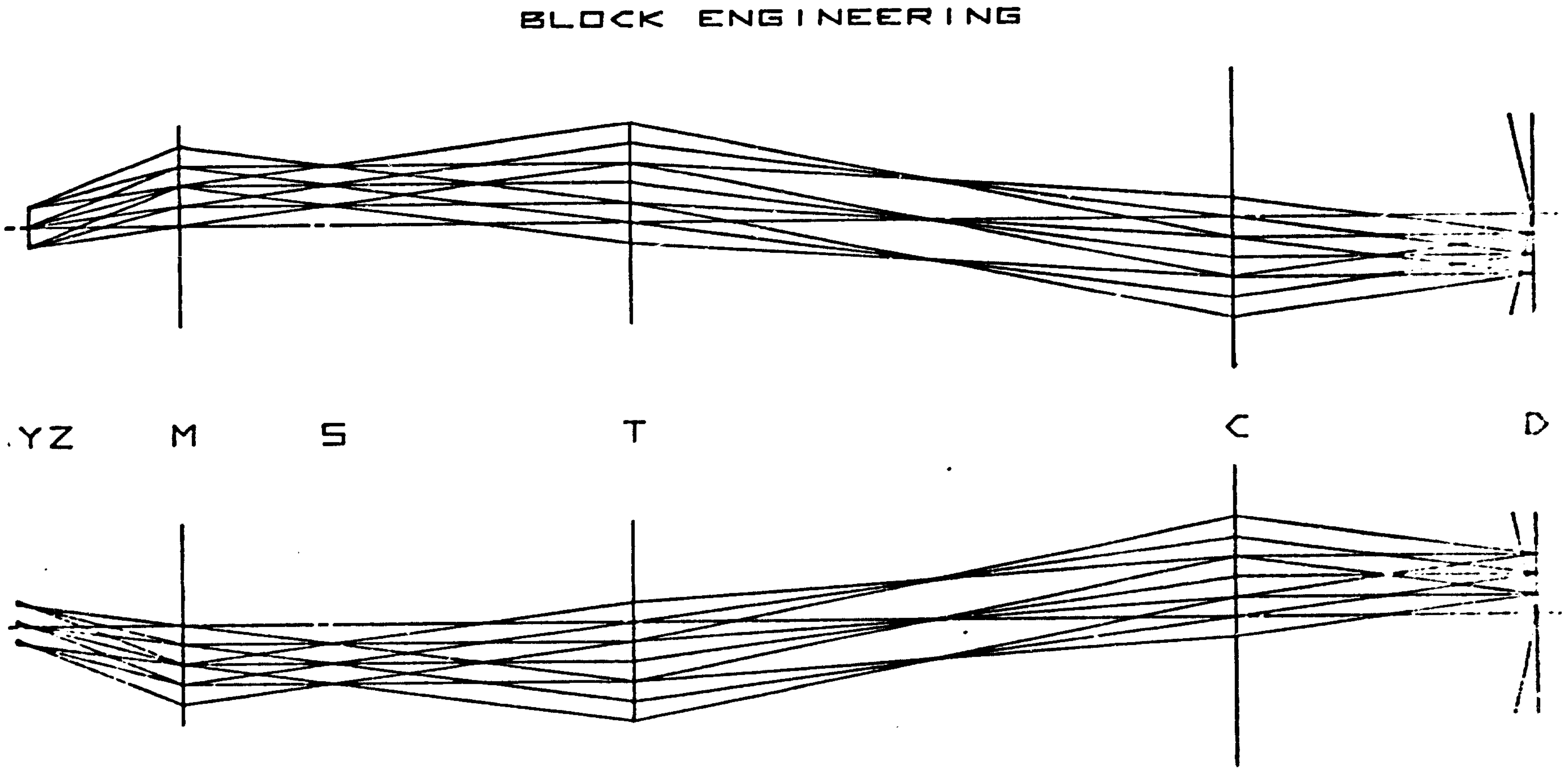

Figure 2.4-3. Firas B Optical Schematic

Optimization was not performed on this design because Block does not recommend this approach. This is based on several factors; the increased number of optical components the difficult problems with the separation mirrors (S1 and SO), the assymetry of the output optics, and the generally tight configuration, which makes baffling much more difficult. At the same time, Block strongly recommends the technique of beam switching to eliminate instrumental error, if an approach could be found without compromise of design simplicity and symmetry.

2.5 BLOCK CONCEPT C DESIGN

After discussions with GSFC/MIT members of the Science Team, it appeared desirable to investigate increase in the instrument throughput to 1.5 cm^2-sr. This is nearly equal to the throughput of an 0.4 cm round detector fully illuminated on both sides but sufficiently below that for the selected 0.4 cm square detector, similarly illuminated, to make this throughput useful. An additional recommendation of the science team was the use of an elliptical cone concentrator as the input coupling optic, since this device provides an effective focal plane at a selected position in front of it, allowing a more compact configuration than with the parabolic cone concentrator.

The design developed with these desired capabilities is shown in Figure 2.5-1 and 2.5-2. The figures show the use of the elliptical input cones, but since an additional flat mirror was necessary on each side to fold the beams appropriately, the number of components is the same as for the Concept A design and the afocal input cones might have been used. Table 2.5-I shows the optical parameters for this configuration.

The schematic in-line ray trace is given in Figure 2.5-3, and we can see that placing the elliptical cone "focal planes" at the transfer mirrors (M1 and M2) gives paraxial ray bundles at all points entering the dihedral mirrors.

Full optimization has been carried out for this design and the spot diagrams are given in Figures 2.5-4 and 2.5-5 at the output coupling cones for zero and 10.0 cm retardations, with a sharp pupil at the transfer mirror. Figure 2.5-6 shows the image of the input coupling cone at the dihedral mirrors at zero retardation. Table 2.5-II and Table 2.5-III give the optimized parameters obtained after nine iterations of the BOOST program, using the nominal inputs indicated in Table 2.5-I. The coordinate system for the optimization is described in Figure 2.5-7. The quantities K(KSURF) and C(CSURF) are obtained for the general surface of revolution as described in Appendix B. Input and output cosines are given for the primary axis following the radiation bundle through the system. The optical diagram showing all component positions and orientations is given in the drawing BE650486. This includes the offset position of the exit cone apertures and the optimized locations and orientations for all components.

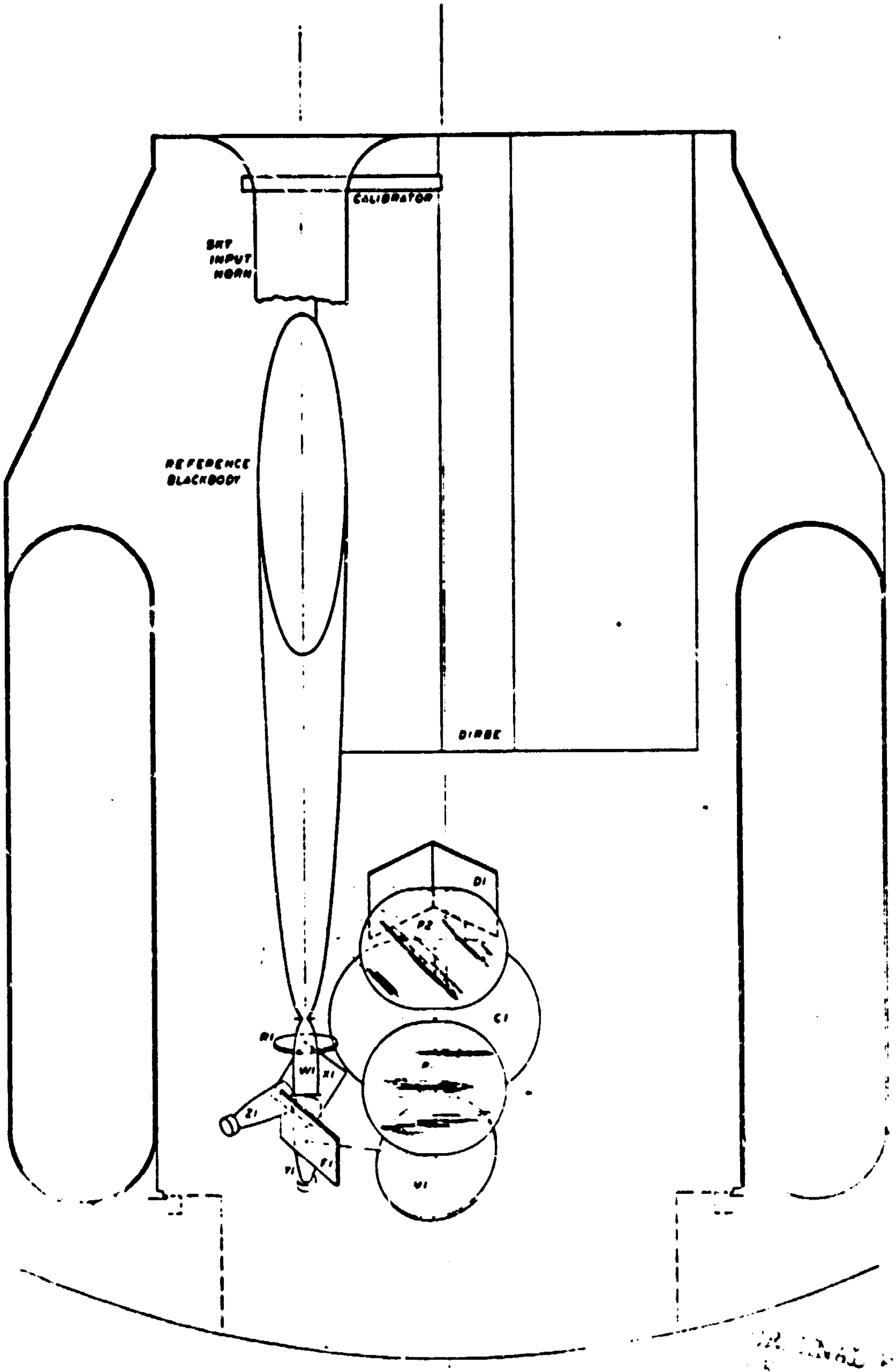

Figure 2.5-1 FIRAS Design Concept C, Side View

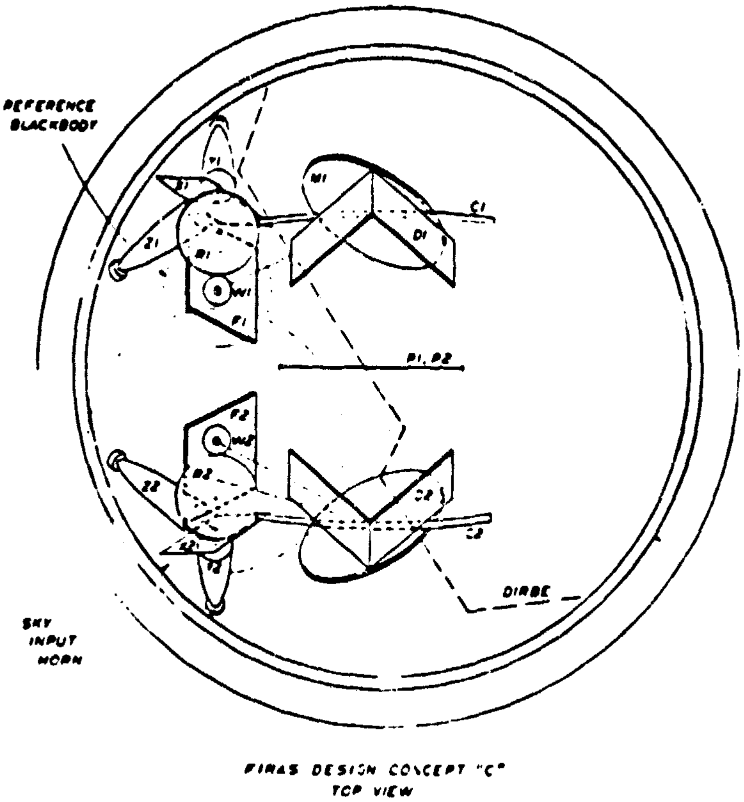

Figure 2.5-2 FIRAS Design Concept C, Top View

TABLE 2.5-I
FIRAS C OPTICAL PARAMETERS

Item	Description	Clear Aperture	Focal Length	Separation
SB, BB,	Input Horns	12.77/0.78 cm	110.73 cm	-
W1, W2,	Input Elliptical Cones	0.78/3.17	10.37	0.0 cm
F1, F2,	Flat Mirrors	10 × 12	Inf	4.0*
M1, M2,	Parabolic Mirrors	15 × 18	25.0	21.0
P1	Input/Output Polarizer	19 × 21	Inf	20.0*
C1, C2,	Parabolic Mirrors	20 × 28	40.0*	20.0*
P2	Polarizing Beamsplitter	15 × 20	Inf	20.0*
D1, D2,	Dihedral Mirrors	10 × 18	Inf	20.0*
R1, R2,	Elliptical Mirrors	10.0	-	7.5 From W1, W2
X1, X2,	Dichroic Beamsplitters	8 × 10	Inf	7.0
Y1, Y2, Z1, Z2.	Output Winston Cones	3.89	11.47	2.8
B1, B2, B3, B4,	Bolometers	0.4 × 0.4	Inf	0.4
E1, E2,	Cylindrical Cavities	0.78	0.8 deep	0.4
E3, E4,	Semisoidal Cavities	0.78	0.59 radius	0.0

---

* Nominal

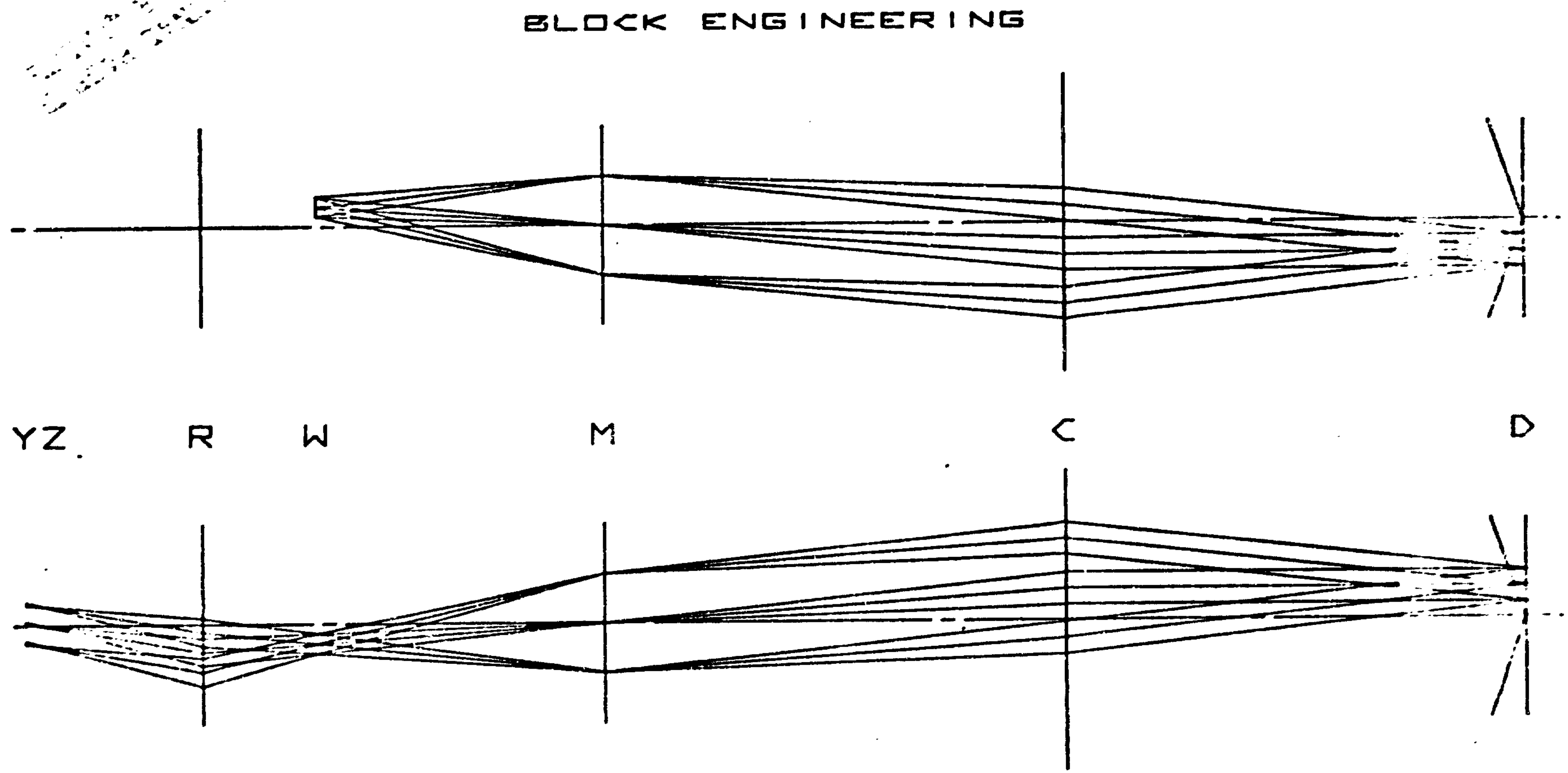

Figure 2.5-3. Firas C Optical Schematic

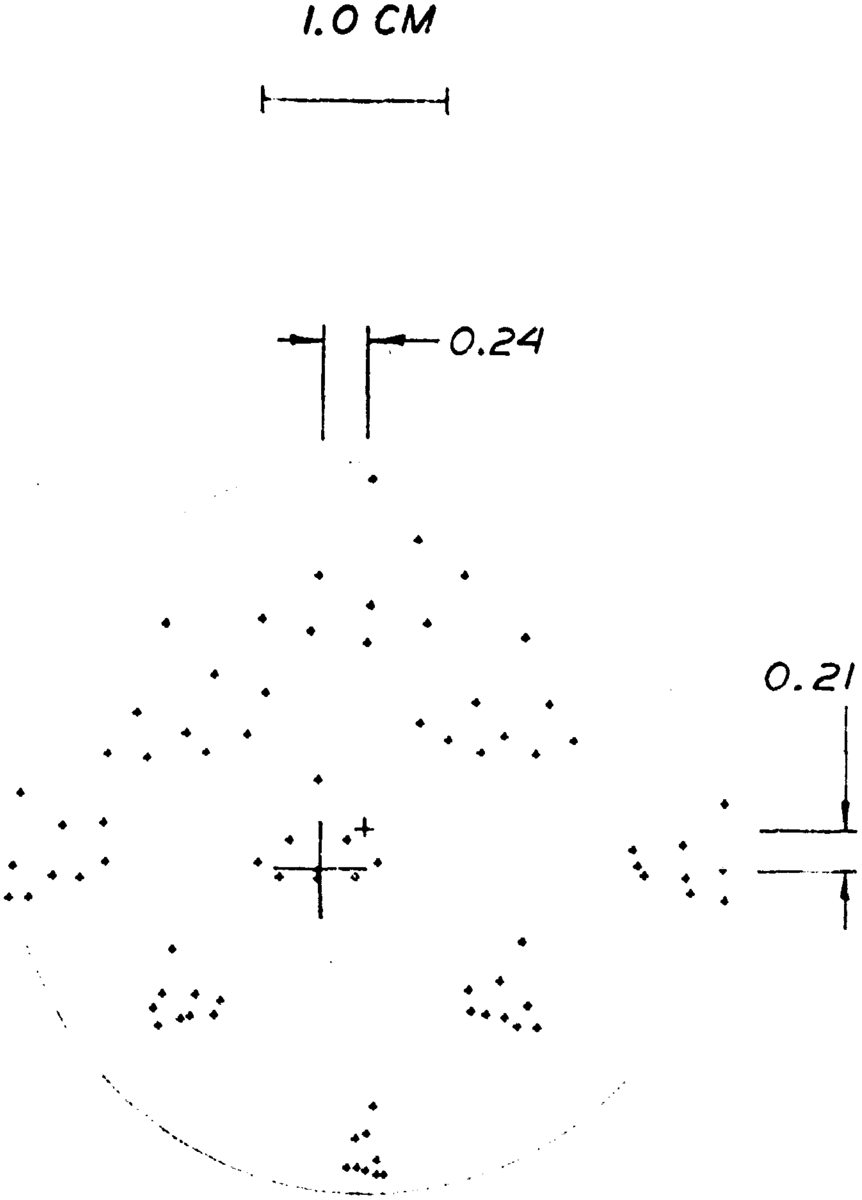

Figure 2.5-4. Output Spot Diagram Zero Retardation

Figure 2.5-5. Output Spot Diagram at 10.0 cm Retardation

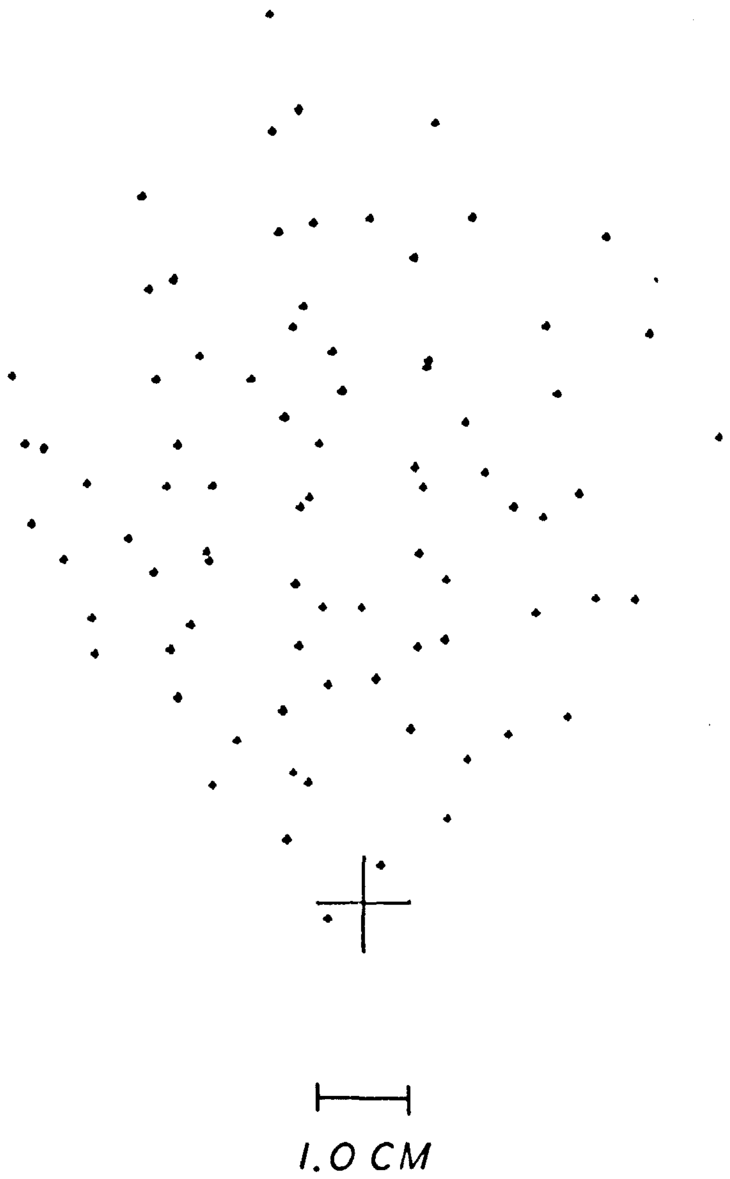

Figure 2.5-6. Dihedral Spot Diagram
Zero Retardation

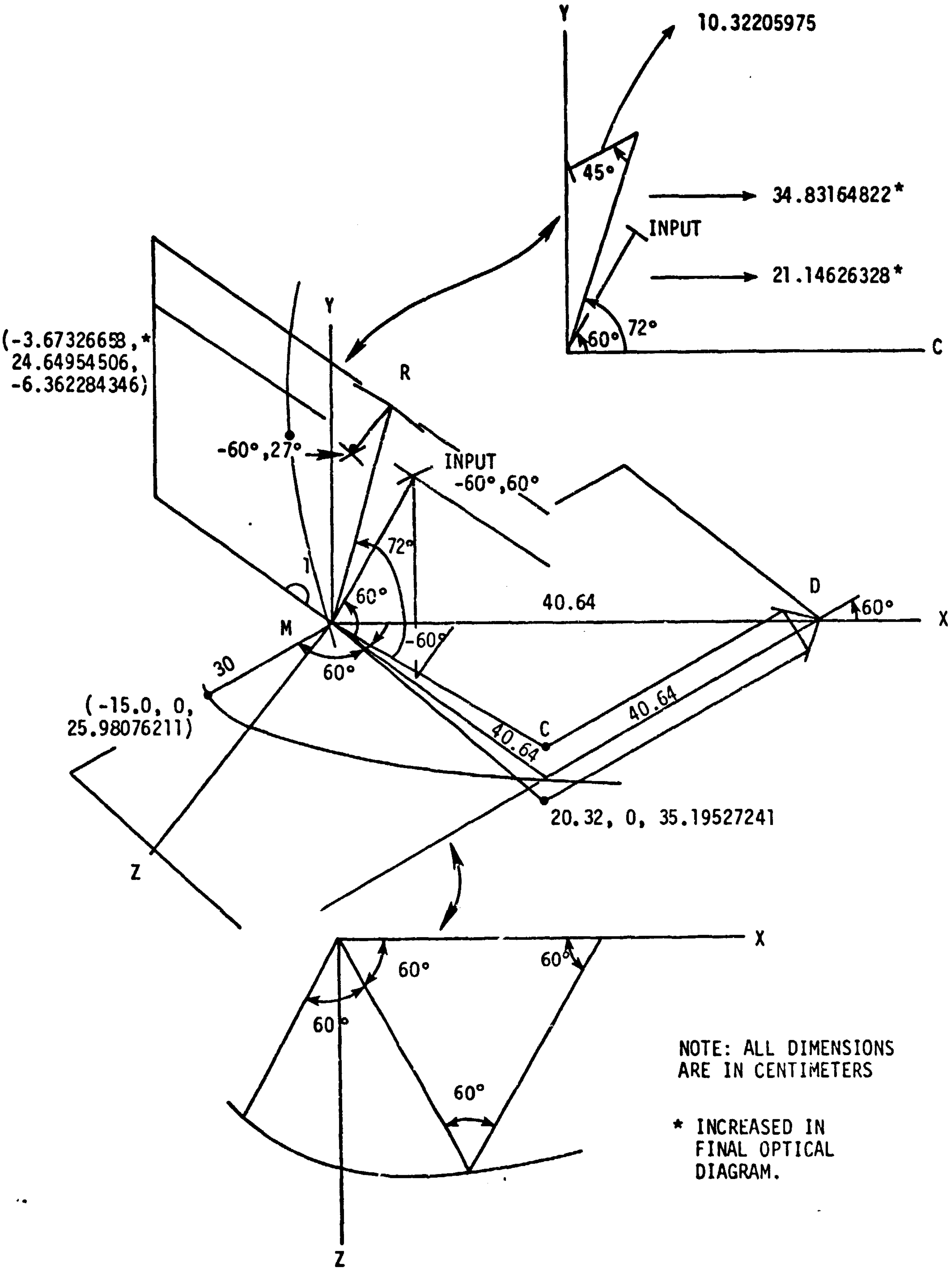

NOTE: ALL DIMENSIONS ARE IN CENTIMETERS

* INCREASED IN FINAL OPTICAL DIAGRAM.

Figure 2.5-7. Coordinate System for BOOST

TABLE 2.5-II

BOOST OPTIMIZATION PARAMETERS

```
W:  SURFACE =        0
    TRANSLATE THE RAYS INTO THE LOCAL SYSTEM
    REFRACTIVE
     INDICIES=    0.100000E  1    0.100000E  1
     PLANE
    EXPLICIT YZX
    THETA=         -0.6000000000000000E  2
     PHI=           0.6000000000000000E  2
     PSI=           0.0000000000000000E  0

     XOFF=           0.5266565788532674E  1
     YOFF=           0.1931320121202355E  2
     ZOFF=           0.9156600581611779E  1

M:  SURFACE =        1
    REFLECTIVE

    OFF AXIS PY          -0.6800418962136414E  1

     CONIC
     VERTEX RADIUS =            0.3360704803746600E  2
     KSURF         =            0.9539327260496742E -1
    EXPLICIT YZX
    THETA=         -0.6000000000000000E  2
     PHI=         -0.3411714999823680E  1
     PSI=           0.0000000000000000E  0

     XOFF=         -0.3673266579855832E  1
     YOFF=           0.2464954505890925E  2
     ZOFF=         -0.6362284346000255E  1

C:  SURFACE =        2
    REFLECTIVE

    OFF AXIS PY           0.0000000000000000E  0

     CONIC
     VERTEX RADIUS =            0.6000000000000000E  2
     KSURF         =            0.0000000000000000E  0
    EXPLICIT ZX
     ANGLE=           0.6000000000000000E  2

     XOFF=         -0.1500000000000000E  2
     YOFF=           0.0000000000000000E  0
     ZOFF=           0.2598076211000000E  2

D:  SURFACE =        3
    REFRACTIVE
     INDICIES=    0.100000E  1    0.100000E  1
     PLANE
    EXPLICIT YZX
    THETA=          0.6000000000000000E  2
     PHI=          0.0000000000000000E  0
     PSI=          0.0000000000000000E  0

     XOFF=          0.4064000000000000E  2
     YOFF=          0.0000000000000000E  0
     ZOFF=          0.0000000000000000E  0
```

ORIGINAL PAGE IS
OF POOR QUALITY

TABLE 2.5-II (continued)

```
C:  SURFACE =        4
    PICK UP FROM         2
    CURVATURE
    OFFSET
    ORIENTATION

    REFLECTIVE

    OFF AXIS BY          0.0000000000000000E  0

     CONIC
     VERTEX RADIUS =            0.6000000000000000E  2
     KSURF         =            0.0000000000000000E  0
    EXPLICIT ZX
     ANGLE=         0.6000000000000000E  2

     XOFF=         -0.1500000000000000E  2
     YOFF=          0.0000000000000000E  0
     ZOFF=          0.2598070211000000E  2
```

```
Y/Z: SURFACE =        7
     REFRACTIVE
      INDICIES=     0.1000000E  1    0.1000000E  1
      PLANE
     EXPLICIT YZX
     THETA=          -0.6000000000000000E  2
      PHI=           0.2700000000000000E  2
      PSI=           0.0000000000000000E  0

      XOFF=           0.7637743372483454E  0
      YOFF=           0.2844074891714250E  2
      ZOFF=           0.1358671005959300E  1
```

```
M:  SURFACE =        5
    PICK UP FROM         1
    CURVATURE
    OFFSET
    ORIENTATION

    REFLECTIVE

    OFF AXIS BY         -0.8000418962138414E  1

     CONIC
     VERTEX RADIUS =            0.3360704803746000E  2
     KSURF         =            0.9539327200496742E -1
    EXPLICIT YZX
    THETA=         -0.6000000000000000E  2
     PHI=         -0.3411714999823680E  1
     PSI=          0.0000000000000000E  0

     XOFF=         -0.3673266579858832E  1
     YOFF=          0.2464954505890925E  2
     ZOFF=         -0.6302284346060255E  1

R:  SURFACE =        6
    REFLECTIVE

    OFF AXIS BY          0.0000000000000000E  0

     CONIC
     VERTEX RADIUS =            0.1621609387220980E  2
     KSURF         =            0.2484100118474490E  1
    EXPLICIT YZX
    THETA=         -0.6000000000000000E  2
     PHI=         -0.1385000000000000E  3
     PSI=          0.0000000000000000E  0

     XOFF=          0.5381785626932832E  1
     YOFF=          0.3312696598090604E  2
     ZOFF=          0.9321526198772140E  1
```

TABLE 2.5-III

OPTICAL AXIS PARAMETERS

```
W:     THETA=           0.15000000000000000E  3
       PHI  =           0.00000000000000000E  0

                0.00700000000000000E  0
                0.00000000000000000E  0
                0.00000000000000000E  0

                0.5286565786532074E  1
                0.1631320121202355E  2
                0.9156600591911779E  1

       INPUT COSINES=
               -0.25000000000000002E  0
               -0.8660254037844386E  0
               -0.4330127018922191E  0
       OUTPUT COSINES
                0.4972009484905056E  0
                0.1045284620040626E  0
                0.8612812257023445E  0
M:     SURFACE=        1
       CSURF=           0.2975566312415636E -1
       KSURF=           0.9539327260496742E -1
       REFLECTIVE
       INDEX BEFORE SURFACE=           0.10000000000000000E  1
       INDEX AFTER SURFACE=           0.10000000000000000E  1

       VERTEX CO-ORDS=
               -0.3673266579855832E  1
                0.2464954505590925E  2
               -0.6362284346060255E  1

       AXIS INTERSECTS AT=
               -0.2701802026550126E -7
                0.3184236163633614E -7
               -0.8278812068032010E -8
       RAY LENGTH=            0.2114626326220276E  2
       LOCAL X AXIS=
                0.4991138404805150E  0
               -0.5951047775950546E -1
                0.8644905304730795E  0




       OUTPUT COSINES
                0.5000000004973361E  0
               -0.8029554917559971E -9
               -0.8660254034973013E  0
C:     SURFACE=        2
       CSURF=           0.1066666666666667E -1
       KSURF=           0.0000000000000000E  0
       REFLECTIVE
       INDEX BEFORE SURFACE=           0.1000000000000000E  1
       INDEX AFTER SURFACE=           0.1000000000000000E  1

       VERTEX CO-ORDS=
               -0.1500000000000000E  2
                0.0000000000000000E  0
                0.2598076211000000E  2

       AXIS INTERSECTS AT=
                0.1992068250000993E  2
```

TABLE 2.5-III (continued)

```
              0.4108787305094034E  1
              0.3451427330468030E  2
    RAY LENGTH=         0.4007317503618173E  2
    LOCAL Y AXIS=
              0.5000000000000001E  0
              0.0000000000000000E  0
             -0.8660254037844386E  0



    OUTPUT COSINES
             -0.4999999995026640E  0
              0.8029585481759971E -9
              0.8660254042715755E  0
D:  SURFACE=        3
    CSURF=          0.0000000000000000E  0
    KSURF=          0.1000000000000000E  1
    REFRACTIVE
    INDEX BEFORE SURFACE=        0.1000000000000000E  1
    INDEX AFTER SURFACE=        0.1000000000000000E  1

    VERTEX CO-ORDS=
              0.4064000000000000E  2
              0.0000000000000000E  0
              0.0000000000000000E  0

    AXIS INTERSECTS AT=
              0.4005023750759143E  2
              0.4108787353677502E  1
             -0.3404957337500357E  0
    RAY LENGTH=         0.4024682497495240E  2
    LOCAL Y AXIS=
              0.5000000000000001E  0
              0.0000000000000000E  0
             -0.8660254037844396E  0



    OUTPUT COSINES
             -0.4999999995026640E  0
              0.8029585481759971E -9
              0.8660254042715755E  0
D:  SURFACE=        4
    CSURF=          0.0000000000000000E  0
    KSURF=          0.1000000000000000E  1
    REFRACTIVE
    INDEX BEFORE SURFACE=        0.1000000000000000E  1
    INDEX AFTER SURFACE=        0.1000000000000000E  1

    VERTEX CO-ORDS=
              0.4064000000000000E  2
              0.0000000000000000E  0
              0.0000000000000000E  0

    AXIS INTERSECTS AT=
              0.4005023750759143E  2
             -0.4108787353677502E  1
             -0.3404957337500357E  0
    RAY LENGTH=         0.1094130311302909E 45
    LOCAL Y AXIS=
              0.5000000000000001E  0
              0.0000000000000000E  0
             -0.8660254037844386E  0
```

TABLE 2.5-III (continued)

```
   OUTPUT COSINES
             -0.4972609484840227E  0
              0.1045784019906552E  0
             -0.8612812257007270E  0
C: SURFACE=        5
   CSURF=           0.1666666666666667E -1
   KSURF=           0.0000000000000000E  0
   REFLECTIVE
   INDEX BEFORE SURFACE=          0.1000000000000000E  1
   INDEX AFTER SURFACE=          0.1000000000000000E  1

   VERTEX CO-ORDS=
             -0.1500000000000000E  2
              0.0000000000000000E  0
              0.2598076211000000E  2

   AXIS INTERSECTS AT=
              0.1992882585117861E  2
             -0.4108787321360970E  1
              0.3451427330866066E  2
   RAY LENGTH=          0.4024682495287482E  2
   LOCAL X AXIS=
              0.5000000000000001E  0
              0.0000000000000000E  0
             -0.8660254037844386E  0




   OUTPUT COSINES
              0.1545064969873178E  0
              0.9510565154866584E  0
              0.2676165704191158E  0
M: SURFACE=        6
   CSURF=           0.2075566312415636E -1
   KSURF=           0.9539327260496742E -1
   REFLECTIVE
   INDEX BEFORE SURFACE=          0.1000000000000000E  1
   INDEX AFTER SURFACE=          0.1000000000000000E  1

   VERTEX CO-ORDS=
             -0.3673266579855832E  1
              0.2464054505890925E  2
             -0.6762284346060255E  1

   AXIS INTERSECTS AT=
              0.8106476334511598E -5
              0.3581731178314680E -7
             -0.3153068299153147E -7
   RAY LENGTH=          0.4007317506789969E  2
   LOCAL X AXIS=
              0.4991136406605158E  0
             -0.5951047775950546E -1
              0.8644905304730795E  0
```

TABLE 2.5-III (continued)

```
    OUTPUT COSINES
              -0.4455032019259883E  0
              -0.4539905030268885E  0
              -0.7716342830478028E  0
R:  SURFACE=        7
    CSURF=           0.6166405030057072E -1
    TSURF=           0.2464100116424400E  1
    REFLECTIVE
    INDEX BEFORE SURFACE=           0.1000000000000000E  1
    INDEX AFTER SURFACE=           0.1000000000000000E  1

    VERTEX CO-ORDS=
               0.5301785620932632E  1
               0.3312066596090604E  2
               0.9321526198772140E  1

    AXIS INTERSECTS AT=
               0.5301765016723096E  1
               0.3312006596607992E  2
               0.9321526197671232E  1
    RAY LENGTH=          0.3463104616474197E  2
    LOCAL Y AXIS=
              -0.3247240241658019E  0
              -0.7604059656000309E  0
              -0.5624385068921630E  0




    OUTPUT COSINES
              -0.4455032019259887E  0
              -0.4539905030266885E  0
              -0.7716342830478027E  0
Y/Z: SURFACE=        8
    CSURF=           0.0000000000000000E  0
    TSURF=           0.1000000000000000E  1
    REFRACTIVE
    INDEX BEFORE SURFACE=           0.1000000000000000E  1
    INDEX AFTER SURFACE=           0.1000000000000000E  1

    VERTEX CO-ORDS=
               0.7632743372462464E  0
               0.2644074891714250E  2
               0.1350071005659360E  1

    AXIS INTERSECTS AT=
               0.7632743301337357E  0
               0.2644074666970636E  2
               0.1356671026077515E  1
    RAY LENGTH=          0.1032205974569296E  2
    LOCAL Y AXIS=
               0.4455032620941640E  0
               0.4539904997395466E  0
               0.7716342646646004E  0
```

2.6 OPTICAL COMPONENTS

Each component of the FIRAS optical system has been examined, and detailed information has been developed. All components have been defined in terms of Concept C configuration, but application to other concept configurations is relatively straightforward. Metal optics have been selected for all components. This results from the need to achieve good cooling of all components, the easier fabrication of certain structures in metal, and the general ruggedness and reliability of metal optics.

2.6.1 Sky Input Horn

As described in the statement of work, this horn is a Winston (1970, 1979) cone collector, used with a circular flare section for the attenuation of sidelobes in the diffraction field. The Winston cone is a parabolic section rotated about an axis shifted to the throat centerline, with the focus at the opposite edge of the throat opening. The horn extends to the point where the throat subtends the desired field of view with the entrance aperture, and the parabola of rotation is tangent to the enclosing cylinder at that point.

If the throat diameter is d, the throughput G, the entrance aperture D, the length L, and the half-angle of the field of view ϕ, the following relationships can be demonstrated:

$$d \cong \frac{2\sqrt{G}}{\pi} \qquad (2.6.1\text{-}1)$$

$$D = \frac{d}{\text{Sin } \phi} \qquad (2.6.1\text{-}2)$$

$$L = \frac{(d + D)}{2 \text{ Tan } \phi} \qquad (2.6.1\text{-}3)$$

For the desired throughput of 1.5 cm^2-sr, the throat diameter is 0.78 cm, the entrance aperture is 12.77 cm, and the length is 110.78 cm. Figure 2.6-1 shows the sky input horn configuration.

The circular flare section was assumed to be 30 cm maximum diameter, and since the flare leaves the horn without any junction discontinuity, the radius of the flare is 8.62 cm. The effect of the flare in suppressing sidelobe diffraction was worked out for an 11 cm radius by Mather (1979) on the basis of Keller diffraction theory. His expression for the intensity of radiation passing around a cylinder curve of radius A at wavelength λ coming from angles greater than Θ away from the junction between the cylindrical section and the cone wall, where the cone width is D, is

$$R = K(\lambda/D)\ (A/\lambda)^{1/3} \exp(-B\Theta) \qquad (2.6.1\text{-}4)$$

where

$B \geqq 2.5\ (A/\lambda)^{1/3}$ for E perpendicular to the surface

$B \geqq 5.0\ (A/\lambda)^{1/3}$ for E parallel to the surface

We may consider the effect of decreasing the radius A by taking the ratio relative to the design radius A_o (note that 30-2A=D)

$$R/R_o = (D_o/D)\ (A/A_o)^{1/3} \exp(B_o - B)\Theta. \qquad (2.6.1\text{-}5)$$

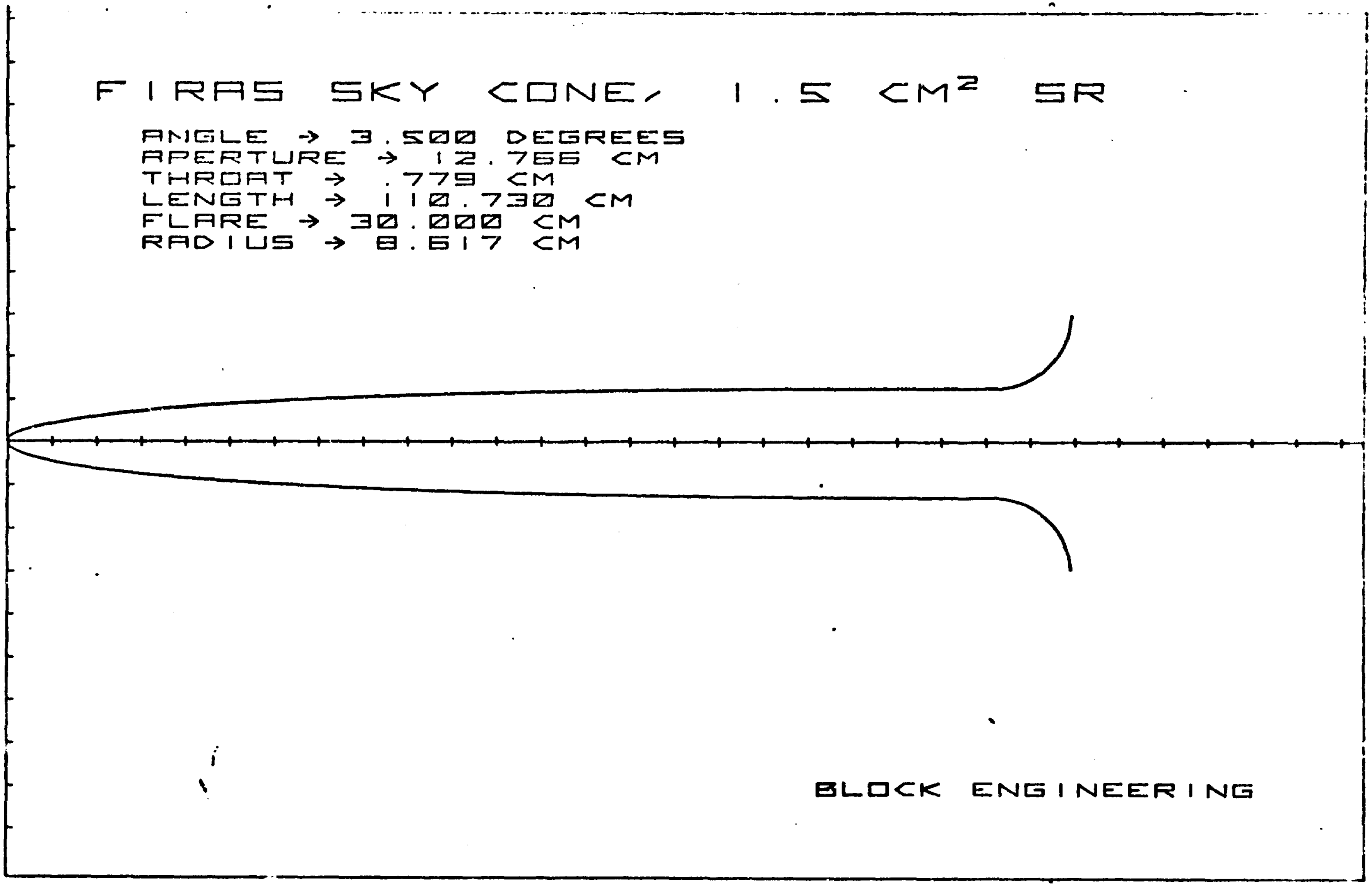

Figure 2.6-1. Sky Input Horn

The resulting variation is plotted at 1.0 cm wavelength in Figure 2.6-2 for the field polarized perpendicular to the surface and in Figure 2.6-3 for the field parallel to the surface. The relative insensitivity of the horn diffraction to small changes in the radius means that we may proceed to the larger throughput horn without any pronounced change in the sidelobe rejection. (A factor of two change is essentially trivial here, since the exponential decrease extends over many orders of magnitude.)

The above discussion assumes that a dielectric absorber, such as Eccosorb,*is used to fabricate the flare surface of the horn. It has also been suggested that a superconducting metal surface be used for this purpose, but this technology represents greater cost and risk at present, and should be considered developmental. Block is not aware of the actual implementation of exposed superconducting metal surfaces in such extended life space applications, but there does not appear to be any fundamental reason why such a technique would not work.

The dielectric absorber does, however, permit a more compact and thermally satisfactory calibrator technique. In this approach, which is discussed in more detail in the section on the calibrator, the calibrator is inserted into the horn aperture through the flare wall. The calibrator is mounted in a flat plate which also contains a ring-shaped section of the horn. When the calibrator is rotated out of position, the ring-shaped section is rotated in, to complete the flare wall structure. Only very small gaps are required to permit easy motion of the calibrator, and these gaps open into the cold inner structure.

---

* Emerson-Cummings,

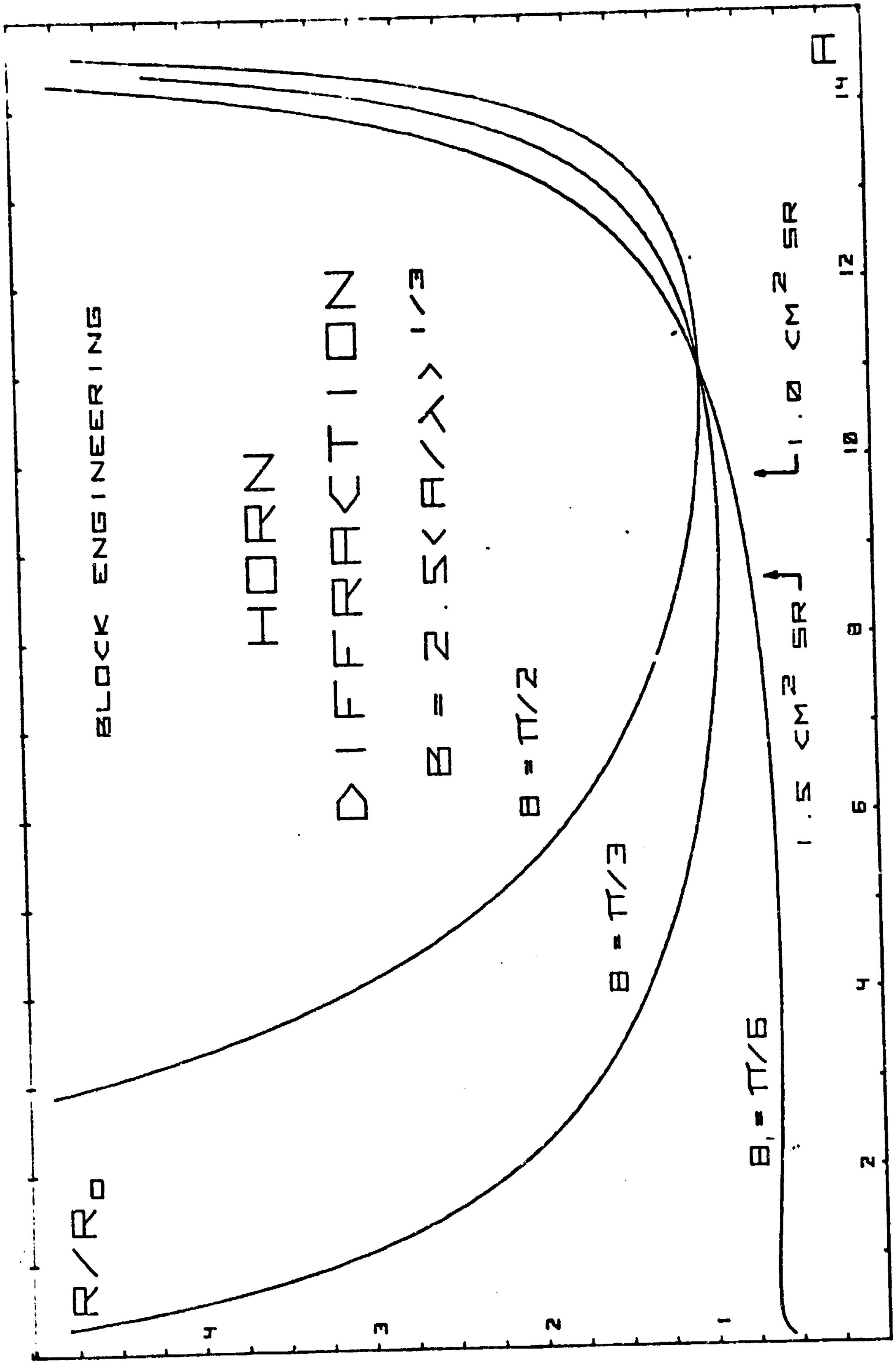

Figure 2.6-2. Horn Diffraction, E_1

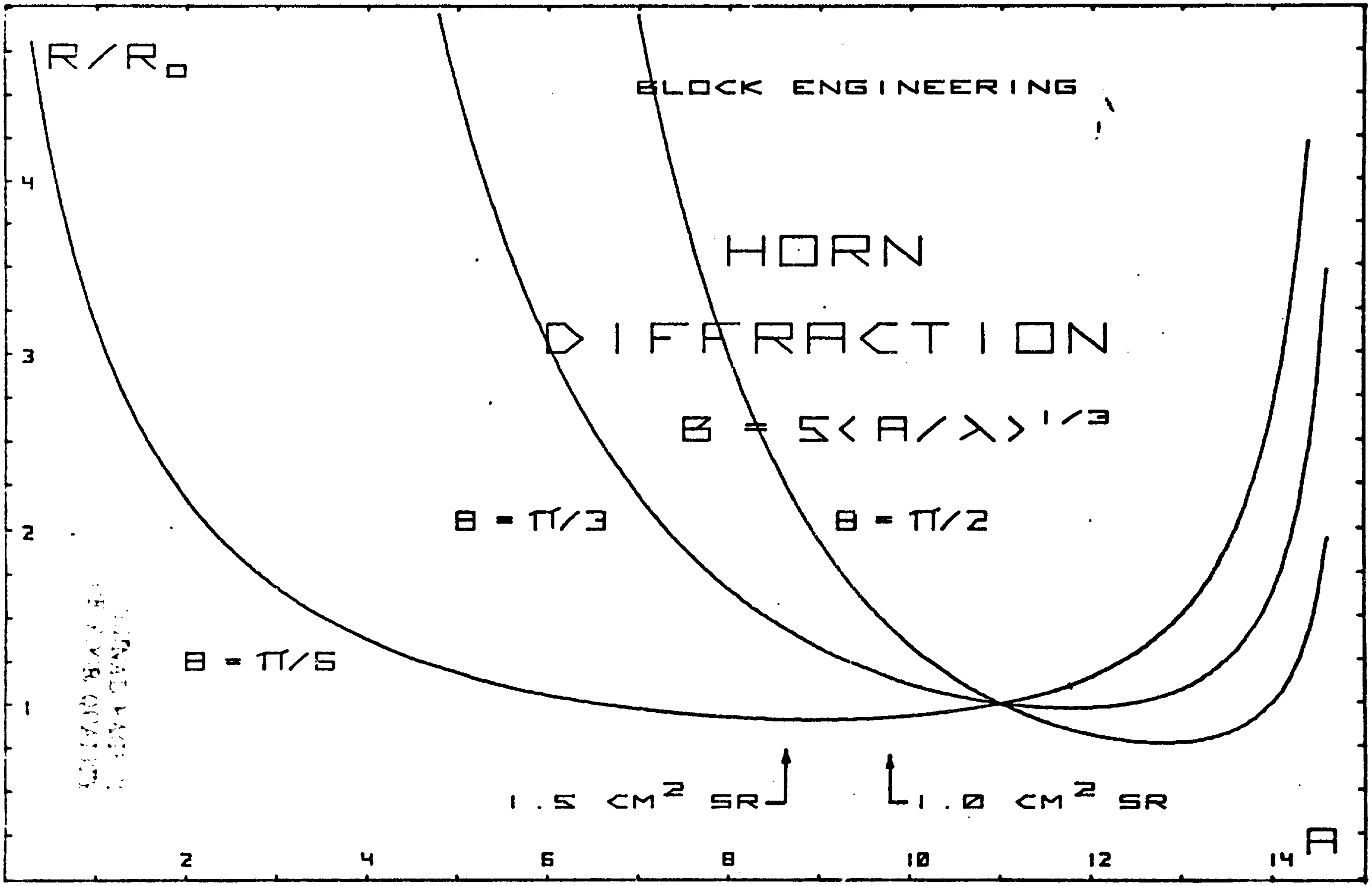

Figure 2.6-3. Horn Diffraction, E_{11}

The gaps are smaller than the more diffracted longer wavelengths, and are located beyond the curve for the geometric beam. The flare ring section is slightly larger in inner diameter than the normal flare surface so that a slight misalignment is permitted without protruding past that surface. The difference in diameters is comparable to the gaps, and is thus smaller than the longer wavelengths of interest.

A continuing concern has been expressed about the coupling of long wavelength radiation through the throat of the Winston cone, especially when the throat diameter is smaller than the wavelengths of radiation considered. Even with a 1.5 cm^2-sr horn, the throat diameter is 0.78 cm, and many rays reach this opening at an oblique angle, making its apparent size much smaller in one dimension. It is difficult to analyze this wave interaction, since the horn is non-imaging, and Block recommends the use of ripple tank simulation to provide some insight into this difficult problem. Although Block does not have such an apparatus, it may be possible to utilize equipment available at MIT or GSFC.

Block concurs with the Science Team suggestion that the sky input horn and the reference blackbody horn be fabricated by electroforming the optic over a precision polished mandril. It may be possible to use the same mandril for the two elements, which are identical, but the large size of these optics makes this uncertain. A superconducting surface might be feasible by first electroplating the prepared mandril with appropriate material, followed by an interface layer of copper to provide satisfactory bonding, and then a supporting shell of nickle. The most desirable materials would be indium (3.407 K) or niobium, (9.17 K) which retain their surface properties to cryogenic temperatures (tin undergoes a phase change) and which are relatively inert (lead and lanthanam tarnish in air). Indium is commonly electroplated, and the technology is developed in terms of small scale structures. Niobium may be difficult to handle in this way, as it is one of the refractory metals (as are tantalum and vanadium). Both indium and niobium are rare metals, and a superconducting surface using these materials would be expensive. It is probably not possible to electroplate any of the superconducting alloys or compounds.

The optical quality required for the horn reflecting surface (which must be present on the mandril) should be equivalent to a high quality machine polish. The area near the throat aperture is most critical, since the angle of incidence becomes smaller there. Since the horn is a non-imaging device, the accuracy for the figure is less critical than for optical imagers, and a reasonable tolerance for first order errors is 1% of the dimension involved. (First order errors have a wavelength comparable to the dimension.)

Higher order errors in the surface must be suppressed more strictly because the slope errors along the horn are inversely proportional to the wavelength of the error perturbation. This is accomplished by specifying the local deviations from the desired curve for the mandril surface, and by using a large diameter polishing device and polishing along the cone rather than circumferentially. The use of a computer controlled milling machine would be desirable for fabrication of the mandril, but optical comparison with the desired curve under magnification will reveal if undulations occur along its length. Typical periodicities in machine polishing have wavelengths on the order of a centimeter, and the corresponding maximum surface error is then ±0.003 cm to give a maximum deviation of about one milliradian, which is just tolerable.

2.6.2 Reference Blackbody Cone

The second input to the interferometer is provided by the reference blackbody cone, which is identical to the sky input cone except that it is terminated by a flat plate blackbody source cutting it at 15°. This flat plate is temperature controlled and monitored at four points. The emitting surface of the blackbody is made of Eccosorb MF-110*, cut with V-grooves running parallel to its longest dimension. They are cut at a V-angle of 45°, but should be structurally large enough to allow several wavelengths interaction within the V-groove at the longest wavelength, and a peak height of at least one centimeter is recommended. The emitting surface is arranged so that it extends into the horn, and a radiative interlock is arranged at the junction.

The effective emissivity of the reference blackbody source can be estimated in several ways. We will use the method developed in Appendix A.I, in which the contributions from the flat plate and the reflective optic are determined separately. In this formulation, the reflection functions F(r) and G(r) are approximated by normalized series ratios which provide for summations of multiple reflection components, including a direct transfer term. The series is not derived from the actual configuration but represents a reasonable fit to an exceedingly complex situation.

---

* Emerson-Cumings

The function F(r) is determined for the reference blackbody cone by computation for k and estimation of geometric contributions at differing numbers of reflections for m. The function G(r) is similar to F(r) except that the non-reflective term is based on the orientation of the flat plate relative to the reflective walls. In F(r) it is based on the orientation of one side of the V-grooves to the other. The solution for P in G(r) is done simultaneously with the solution for k in F(r).

The normal surface emissivities for the Eccosorb material are obtained from commercial literature and from the work of Grammer et al (1978). The long wavelength emissivity of this material is computed from the relation

$$e = 1 - \left[\frac{1-Z}{1+Z}\right]^2 \qquad (2.6.2\text{-}1)$$

where Z is given as 0.5 at longer wavelengths, resulting in an emissivity of 0.89. The emissivity at 100 μm is given by Grammer et al as approximately 0.92, and their longer wavelength measured values are consistent with the computation above, when corrected for a greater thickness of material.

Figures 2.6.2-1 and 2.6.2-2 show the emissivity of the reference blackbody horn obtained for metallic reflectivity varying from 0.985 to 1.000 (superconducting), with surface emissivities of 0.89 (1 cm) and 0.92 (100 μm). The use of superconducting surfaces within the cones has the advantage of entirely decoupling the emissivity from the temperature of the reflecting surface, although the error resulting is very small even for the minimum emissivity value. The sensitivity to temperature differences between the emitting (ε_a) and reflecting (ε_b) surfaces is quite significant, however.

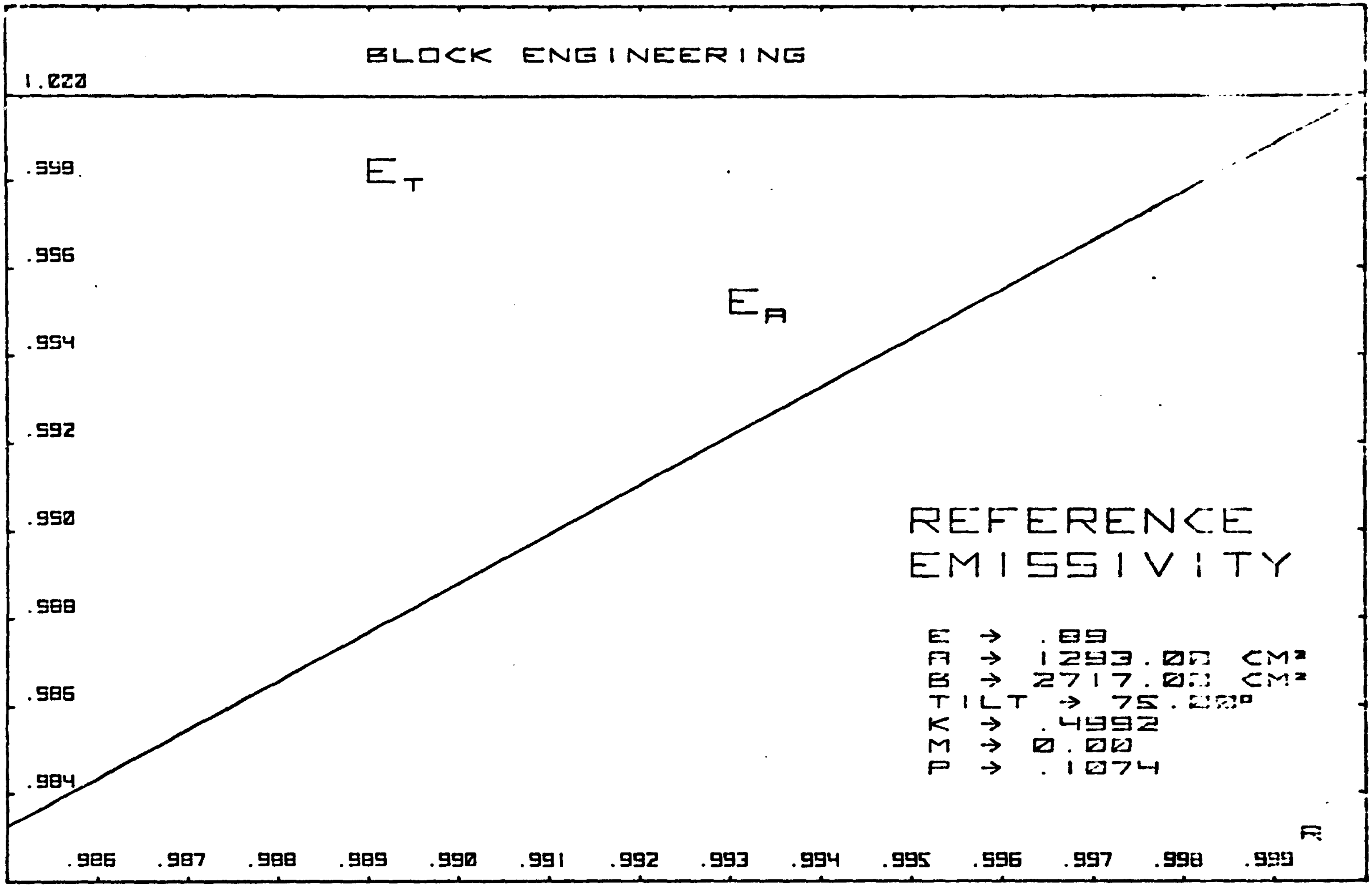

Figure 2.6.2-1. Reference Blackbody Emissivity at 1.0 cm

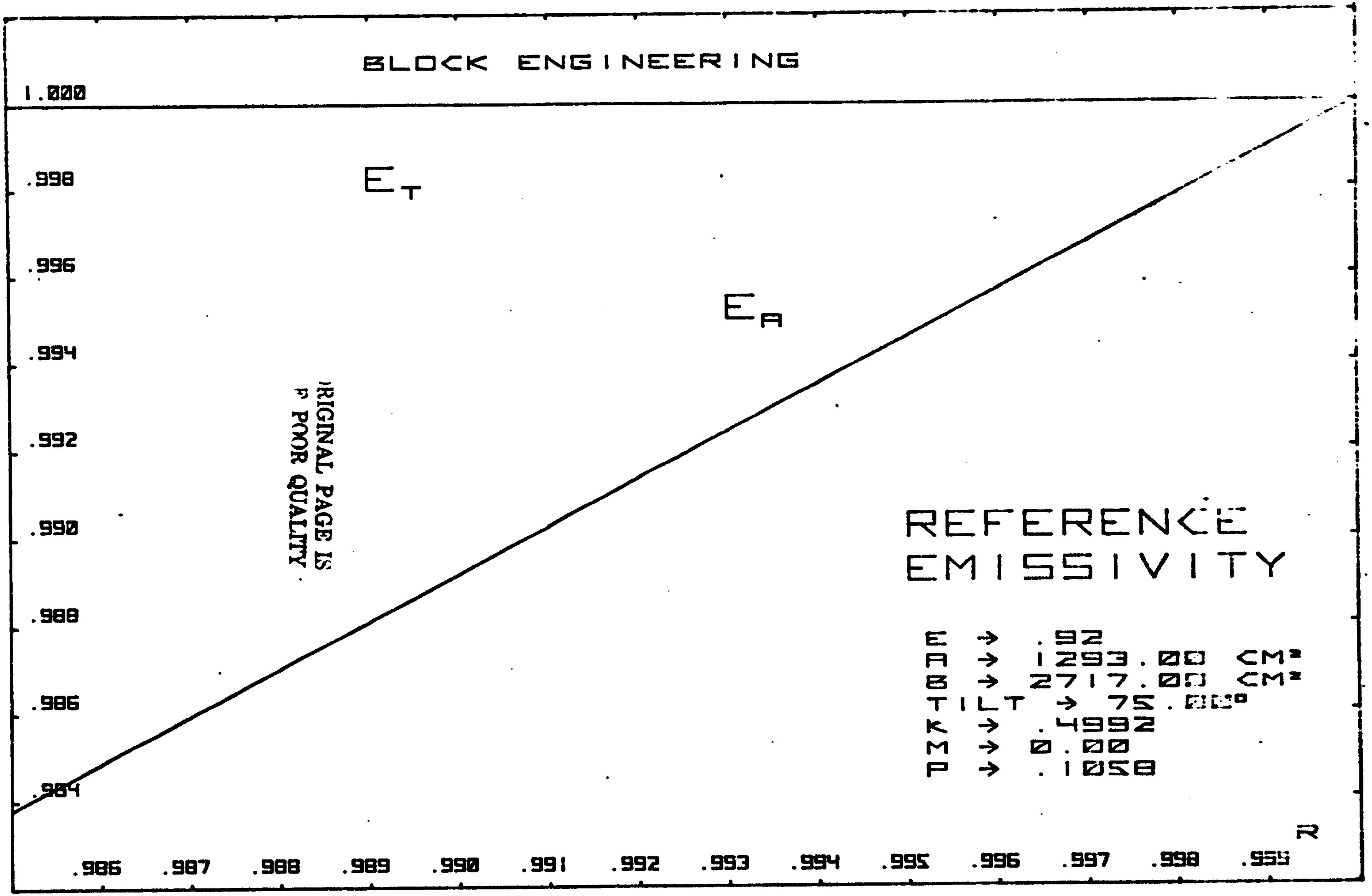

Figure 2.6.2-2. Reference Blackbody Emissivity at 100μm

This is shown in the figures, where the contribution of the emissive surface alone is indicated (ε_a).

2.6.3 Calibrator Blackbody Source

The insertion of the calibrator blackbody source in the sky input horn provides a similar emission situation to that in the reference blackbody cone, except that the temperature of the calibrator is varied intentionally to determine the operational performance of the FIRAS system. The calibrator is a flat plate standing in front of the full sky horn at 90° to the horn axis, and is temperature controlled separately from the sky horn. The emitting surface of the blackbody is made of Eccosorb MF-110, either cut in V-grooves or in pyramidal cones. The V-angles are assumed to be 45° the but the depth of the structures is limited by the calibrator insertion mechanism to about one centimeter peak height. The surface extends past the projected diameter of the sky cone aperture, and is blocked radiatively at the edges to prevent leakage from the blackbody cavity.

To evaluate the emissivity, we again use the method developed in Appendix A.I, however the parameters are somewhat different. The reflection function F(r) of the calibrator for radiation leaving and returning to the emitting surface contains no terms for one or two reflections, as can be seen by study of the normally truncated Winston cone. (The reference blackbody cone provides substantial one and two reflection components from the region adjacent to the 15°cut.) This is not the case for the function G(r) dealing with emission from the reflecting surface, which is similar to the same term for the reference blackbody cone.

The emissivity curves are given in Figures 2.6.3-1 and 2.6.3-2, which also indicate the parameters used. Emissivity is obtained for the wavelength limits of the FIRAS system, which are also the best and worst case emissivity values. As a result, the use of a superconducting layer on the reflective surface is strongly recommended, but represents a developmental aspect with an attendant risk. The effect of the temperature difference between the calibrator plate and the sky horn can be seen in the emissive surface component (ε_a) alone. In normal conducting material, the temperature difference between the calibrator and the sky horn gives an emissivity error which is greatest at wavelengths somewhat shorter than the peak of the blackbody curve. In general, the variation is small, and can be almost entirely eliminated by use of superconducting material in the horn reflecting surface. It is also possible to compensate for the error in the data processing of the interferometer output, since the emissivity of the FIRAS optics, reference blackbody, calibrator, and horns will be accurately determined before the mission.

Degradation of calibrator emissivity or horn reflectivity with time can arise if micrometeorite impact or calibrator operation produce debris in the horn. It is essential that the calibrator operation be mechanically protected from abrading the emissive surface of the calibrator or the flare of the sky horn. Permitting helium vapor to escape through the horn throat will help to ensure that debris does not enter the instrument, and may prevent it from staying in the horn.

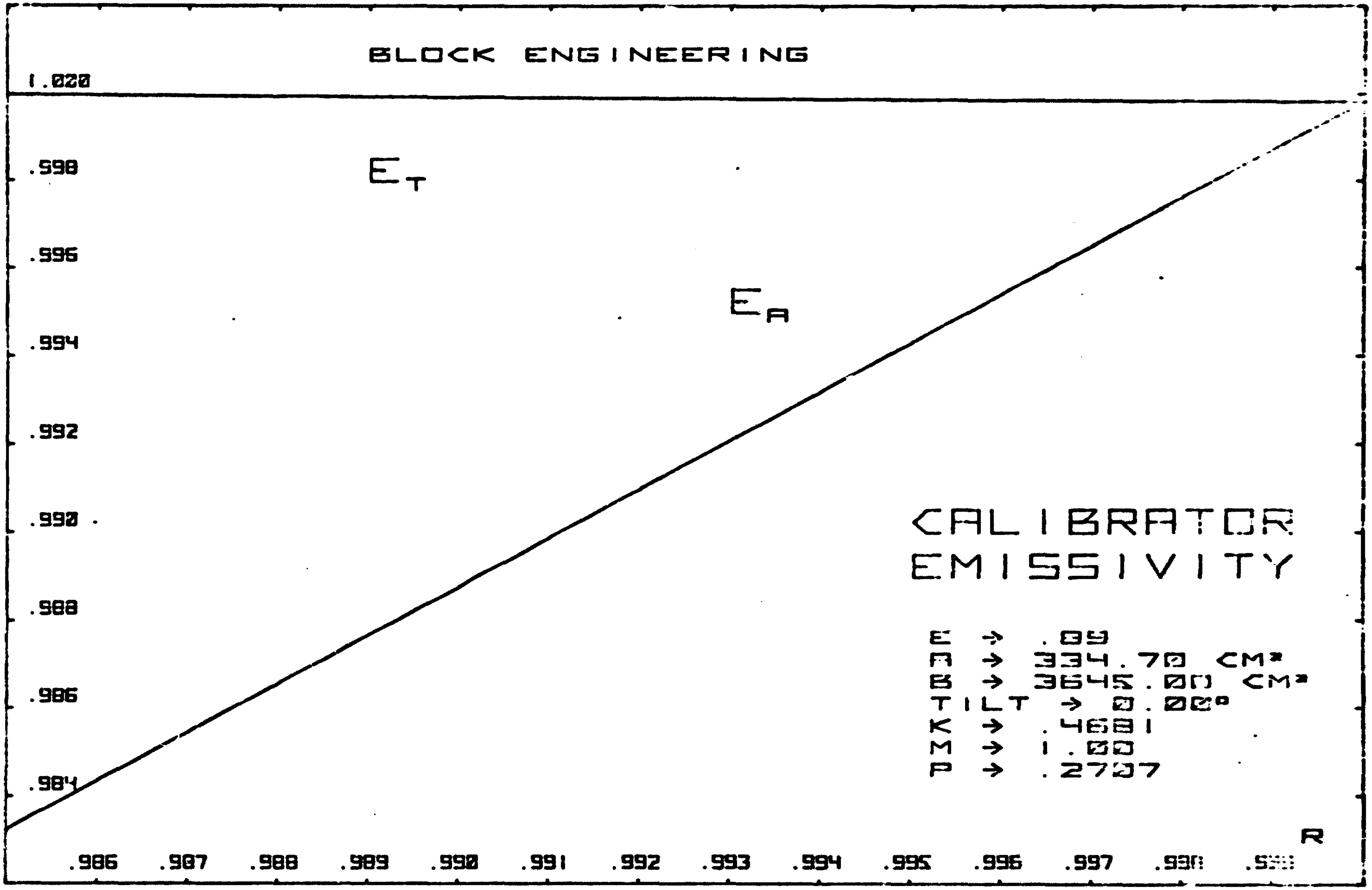

Figure 2.6.3-1. Calibrator Blackbody Emissivity at 1.0 cm

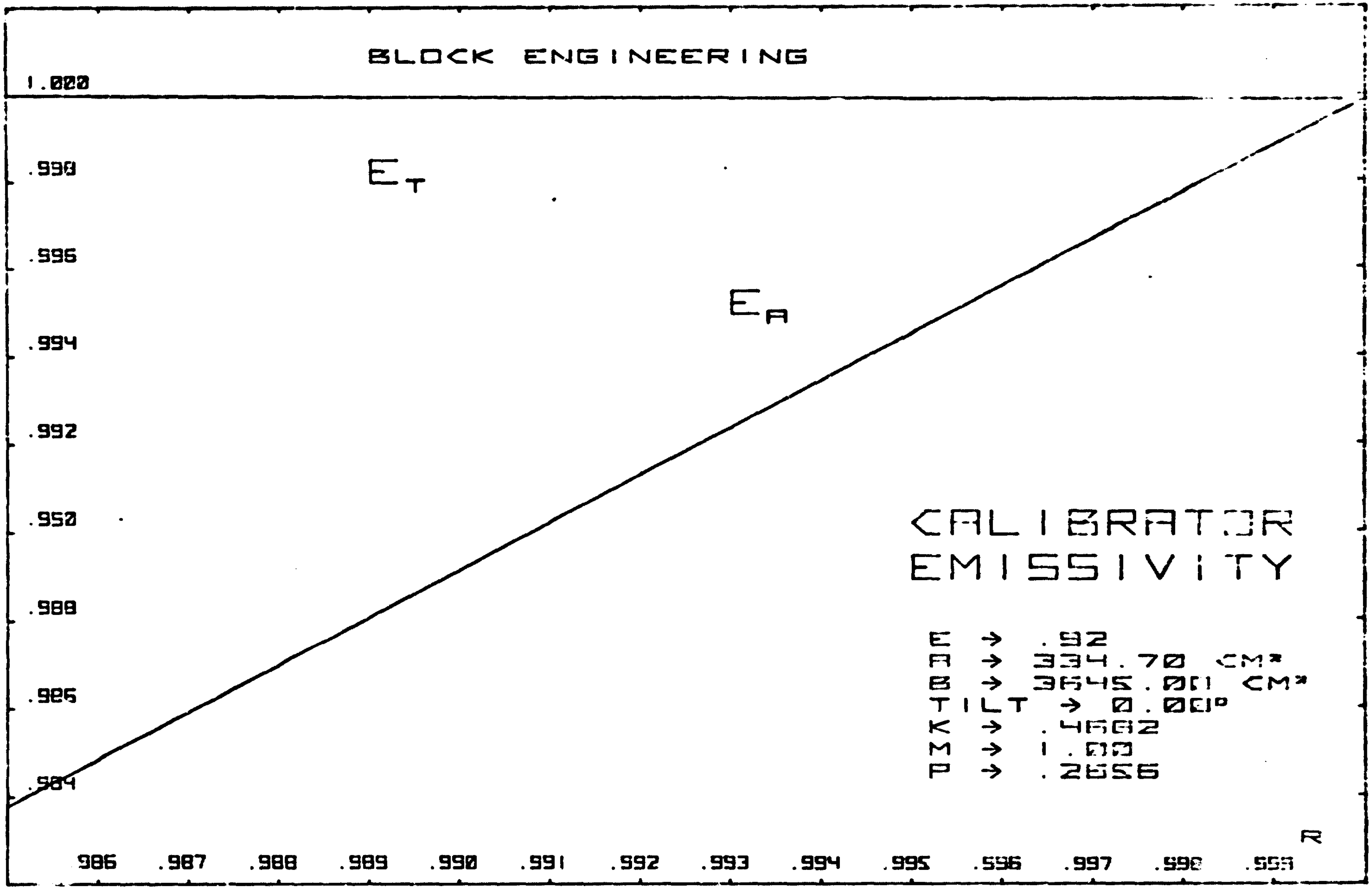

Figure 2.6.3-2. Calibrator Blackbody Emissivity at 100µm

2.6.4 Input Coupling Cone (W1 and W2)

The earlier designs used the parabolic Winston cone as the input coupling optic, taking the output of the sky input horn and providing an afocal beam into the interferometer optics. Mather (GSFC) suggested the use of the concentric elliptical cone to provide a quasi-focusing optic, allowing a somewhat shorter input optical train. This device, conceived by Welford and Winston (1978), has been incorporated into the Concept C design with the surfaces indicated in Figure 2.6.4-1.

If the throat diameter is d, the throughput G, the entrance aperture D, the length L, the separation from exit aperture to the "focal plane" S, and the remote "pupil" diameter P, the following relationships are obtained:

$$d \cong \frac{2\sqrt{G}}{\pi} \qquad (2.6.4\text{-}1)$$

$$D^2 = \frac{P^2 + 4\,S^2 - G^2/\pi^2}{P^2\pi^2/4G - 1} \qquad (2.6.4\text{-}2)$$

$$L = \frac{S\,(D + d)}{P - D} \qquad (2.6.4\text{-}3)$$

With a throughput of 1.5 cm^2-sr, the exit aperture of the cone is 3.17 cm and the length is 10.37 cm. These parameters were obtained for a separation distance of 25 cm and a pupil diameter of 12.7 cm, which were chosen to conform to interferometer system requirements.

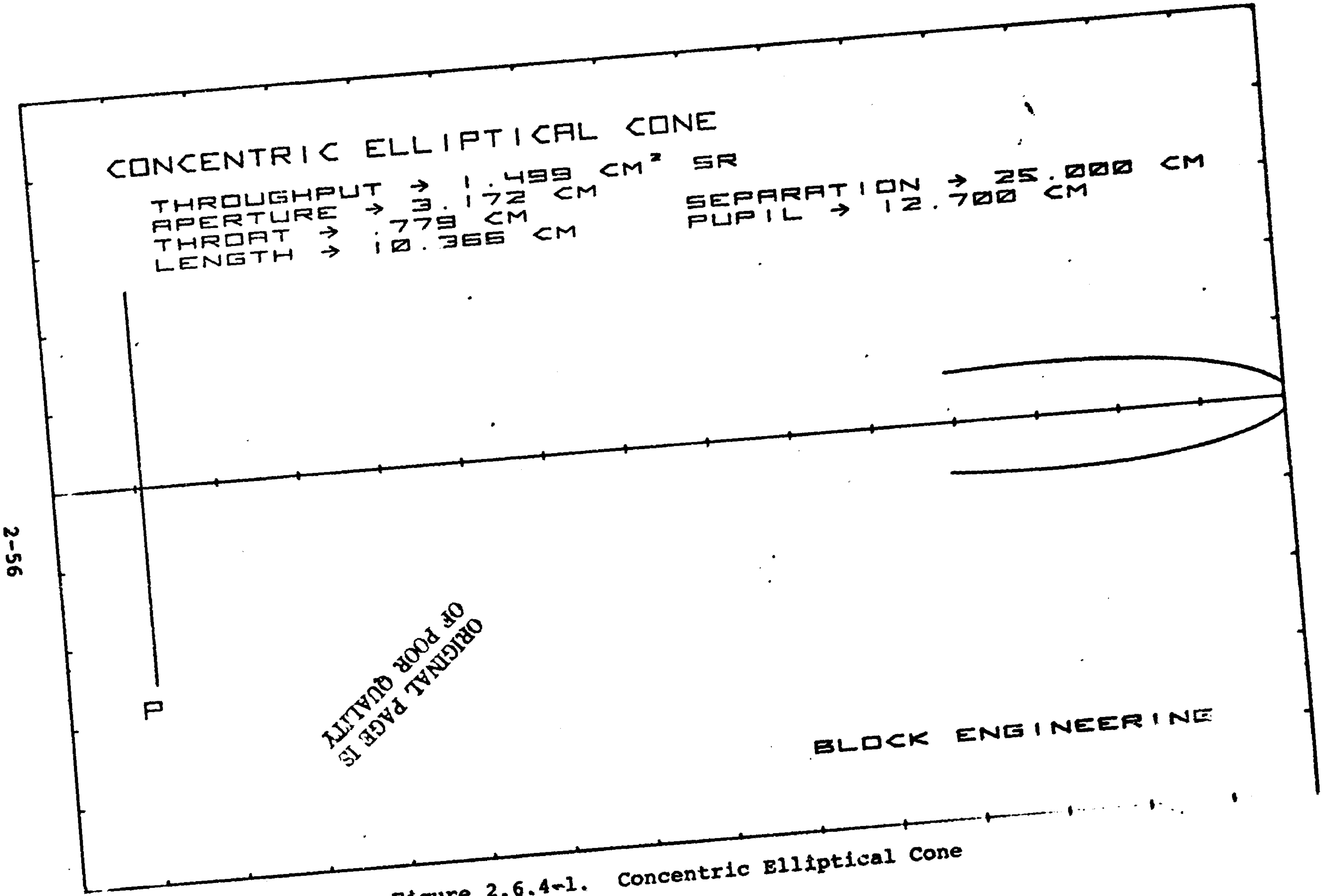

Figure 2.6.4-1. Concentric Elliptical Cone

This cone can be thermally connected to the reference blackbody cone structure, and stabilized with it with minimal complication. The cone would be electroformed over a polished, expendable mandril, and a second cylindrical shell attached for support, much as for the sky input horn. A superconducting reflective surface would minimize losses in this element, but is considered developmental.

2.6.5 Folding Mirror (F1 and F2)

These flat mirrors are used to turn the radiation from the input coupling cones to the transfer mirrors, and to direct the output radiation from the transfer mirrors to the detector optics. The flatness of these mirrors is relatively uncritical, although the surface roughness should be equivalent to a good machine polish. A small overlap of input and output beams does occur at the folding mirror, and scattering due to roughness should be avoided, since it can throw radiation from the output back into the input, producing second harmonic ghost spectra. The mirror figure should be accurate to one wave at the shortest wavelength of interest over the entire surface to minimize overall angular distortions.

2.6.6 Transfer Mirror (M1 and M2)

The curved transfer mirror acts with the collimator mirror to provide collimated radiation to the interferometer through the two beamsplitters and to refocus the outputs back onto the exit image and pupil planes. The mirror acting as a system pupil, operates off axis to deflect radiation in and out of the interferometer plane from the plane of the dihedral mirror shift. The dihedral mirrors introduce correction for this off-axis operation, as viewed at the exit image and pupil planes, but off-axis distortions appear at the dihedral due to the transfer mirror. The angle off axis for the transfer mirrors has been reduced to 60° in this design to reduce the distortions at the dihedrals.

The quality of this optical element, like the other entrance/exit optics, need only be accurate to nominal tolerances. Figure should be accurate to at worst about one wave (100 micrometers) over the surface to produce acceptable imaging in conjunction with the other optics. Since this mirror is a pupil common to input and output, surface roughness should be as low as is consistent with the finest machine polish, with the avoidance of short period undulations as in the sky horn, especially those scattering normal to the interferometer plane. Scratches and digs should be correspondingly minimized.

2.6.7 Collimator Mirror (C1 and C2)

The collimator mirrors provide the radiation to the interferometer dihedral mirrors, where the input and output images are again separated. At the collimator mirrors, there is a considerable overlap due to the spreading away from the image, and the mirrors are elongated normal to the interferometer plane to collect the entire energy.

The quality of the collimator mirrors is similar in general to that of the transfer mirror, although less of the surface is common to input and output, and scattering is important in the central region for that reason, and less important away from the interferometer central plane. Surface roughness and quality specifications can actually be written to emphasize the central third of the element.

2.6.8 Beamsplitter (B1 and B2)

The two beamsplitters in the FIRAS design act to polarize the radiation and then to split each polarized beam into two parts for the interference process. The general approach to polarizing beamsplitters has been to use wire grids of appropriate spacings, the input/output beamsplitter (P1) oriented with the wires at 0° or 90° to the interferometer plane, and the polarizing beamsplitter (P2) at 45° to that plane. The original interferometer modeled at MIT used a deposited wire grid on a plastic substrate, and relatively satisfactory performance was noted. An improved beamsplitter fabricated and now being tested at MIT uses a free-standing wire grid held in tension by a rigid frame, and detailed analysis of the behavior of this beamsplitter is being made there.

Measurements were made by Ade et al (1979) on a free standing wire grid using 5 μm wire with 12.5 μm spacings which shows excellent performance from 25 to 100 cm^{-1} at normal incidence, as shown in Figure 2.6.8-1. Further measurements with 25, 50, and 100 μm spacings by Mok et al (1979) show the increasing scattering effects at shorter wavelengths, which have been studied analytically by Chambers et al (1979). In these measurements, excessive scattering possibly resulting from uneven spacings is noted, although this does not seem to be present in the 12.5 μm spacing data, where one might expect it most. These beamsplitters will eventually be commercially available from Analytical Accessories Limited, but our experience suggests that there may be considerable delays before such commercial units can be obtained.

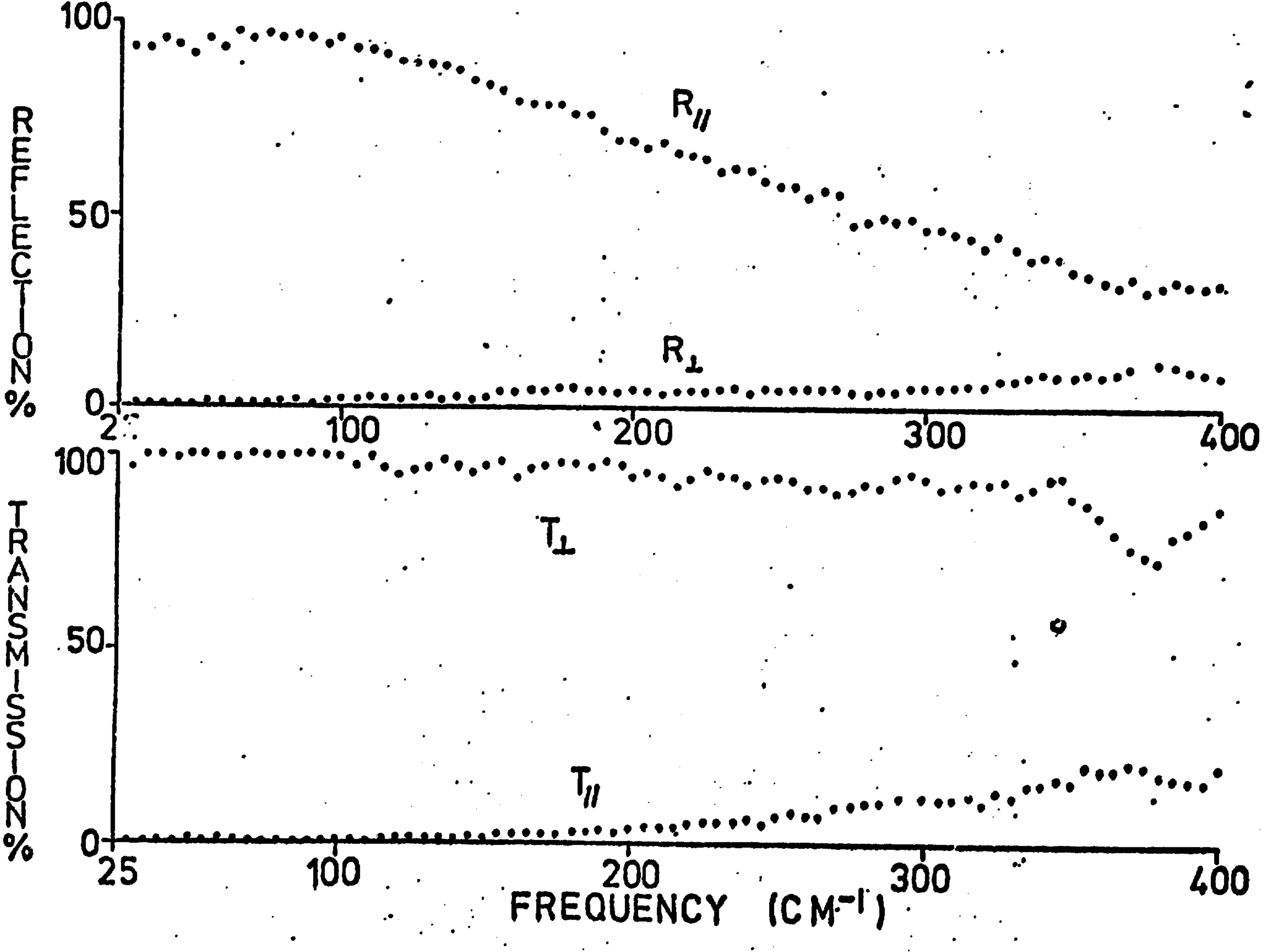

Figure 2.6.8-1. Wire Grid Beamsplitter Efficiency
(Ade et al)

The free standing wire grid beamsplitters are made with tungsten wire coated with gold, for which the penetration depth is less than 0.43 μm at wavelengths less than 1.0 cm. The use of a superconducting coating for the wires does not appear to be necessary, based on the good performance of the gold coated tungsten, which will improve at low temperatures in any case.

Wire spacing can be controlled by having the wire frame cut with notches, using a precision ruling engine, as is used in making diffraction gratings. If the spacing of the wires becomes a problem, a technique was suggested in Block's original proposal (TP-921) of using an etched grill with support bars running perpendicular to the wires. The performance of this beamsplitter was described by Soglasnova et al (1978), and although the fabrication of a large beamsplitter using this technique would be developmental, it has certain advantages. These include greater uniformity of coating possible prior to etching, the possible interferometric quality of the lines, and the greater strength of the supported wires.

The fabrication using a photomaster requires a very considerable effort in the artwork, but a technique like the holographic grating fabrication might be used. The photosensitive coating on the metal sheet is irradiated through a special line mask which produces a diffraction pattern over an area of the surface. Support wires are masked by simply laying thin wires over the area to be illuminated orthogonal to the desired grid wires. Jobin-Yyvon has perfected the technique of exposing gratings for later etching in this way, but the special diffracting mask used to give a space-to-line ratio of 2-4:1 requires development. Handling of this grill would be difficult unless the metal sheet were very carefully mounted before etching, using uniform low tension. A thickness of no more than 10 μm would be necessary in obtaining 5 μm wires, and the use of tungsten sheet would provide sufficient strength.

Block recommends that the primary emphasis should be given to free-standing wire grid using the thinnest gold coated tungsten wires possible, with spacings of 15-20μm. The uniformity of spacing is very important, and the wire surface of the polarizing beamsplitter (B2) must be flat to one-twentieth of a wavelength (5μm). This means that the beamsplitter frame must be lapped to this figure prior to wire attachment and that a careful look must be given to frame distortion after soldering. The flatness of the input/output beamsplitter (B1) is much less critical, and should be better than one wave (100μm) over the area.

2.6.9 Dihedral Mirrors (D1 and D2)

Each path in the interferometer proper leads to a dihedral mirror which reflects the radiation back to the polarizing beamsplitter rotated by 90° in polarization. The beam entering the dihedral mirror is shifted from above the interferometer plane to below it, providing the output image shift necessary for separation of input and output. Each dihedral mirror set consists of two flat mirrors at 90° to each other, and at 45° to the interferometer plane, providing retroreflection in one plane (normal to the interferometer plane) along that axis. Change in the optical path of the interferometer is made by shifting these mirror sets in and out along their optical axes in opposition, and it is convenient to connect them together, moving them at an angle of 30° to the desired scan direction so that the beams shift half the scan distance back and forth along the mirrors during each scan. The mirrors must move 1.155 times the scan distance, and at 1.155 times the desired scan velocity in their physical motion at 30° to the axes.

Since these mirrors are critical to the interference of radiation, their optical quality must be the highest of any component in the interferometer. The double reflection means that error tolerances in each plane mirror component of a set must be half that of a mirror in an ordinary plane mirror Michelson interferometer. Block commonly uses a tolerance on flat mirror figure of one fortieth of a wave in a plane mirror instrument, and so we recommend one-eightieth of a wave (1.3μm) for each surface of the dihedral mirror set. The actual tolerance on the included 90° angle between mirror components is not critical in itself, but the two dihedral mirror sets must be matched to better than thirty arc seconds. The alignment of the dihedral sets to the optical axis within the plane of the interferometer must also be maintained to better than thirty arc seconds, but the tilting of the dihedral sets normal to that plane is uncritical.

Surface quality, on the other hand, is actually not as critical, since the beams are relatively isolated at this point in the system. It is difficult to measure figure if the surface is grossly imperfect, of course, but scratch/dig tolerances at ordinary commercial levels are more than adequate, and a value of 100/80 could be accepted.

An optical quality surface technique must be used to provide the figure for the dihedrals, and this will allow the necessary suppression of short period errors, particularly if the manufacturer is familiar with metal imaging optics. It is desirable, although not essential, that each mirror set be made as a single piece, with both surfaces ground and polished in place, using strain relieved metal. This will minimize thermal cycling deformations, as will be described in a later section. Mechanical distortions of the dihedral mirror sets must never approach the elastic limits for the material so that the above tolerances are maintained, and this will also be considered in the thermal/mechanical section.

2.6.10 Detector Mirror (R1 and R2)

These curved mirrors take the output radiation from the image planes at the input coupling cone apertures and refocus this energy onto a pupil (corresponding to the transfer mirrors) at the detector output coupling cones. They operate 45° off axis to permit isolation of the detector optics from the input/output plane images without vignetting. The figure quality here is equivalent to that of the transfer mirrors, but the surface roughness can be significantly poorer. The relatively short focal lengths also mean that surface undulations are less effective, and some beam spreading can be tolerated, up to perhaps 15 arc minutes.

2.6.11 Dichroic Beamsplitter (X1 and X2)

This flat surfaced component is designed to reflect radiation shorter than 500 micrometers to one detector cone, while transmitting radiation longer than this to the second detector cone. A wide variety of possible beamsplitting filters can be considered, but only the metal capacitive grids appear to have entirely satisfactory characteristics. These include high transmission at longer wavelengths, sharp cutoff at the desired spectral point, good reflection of shorter wavelengths, and a minimum of undulations in the spectral function.

These grids have been described in detail by Ulrich (1967a) who also gives details of their preparation (Ulrich, 1976b). Pradhan (1970), Holah and Auton (1974), and Grag and Pradhan (1978) have described these filters. Holah and Auton have, in fact, designed a low pass filter for use in cosmic background measurements, operated at liquid helium temperatures with some deterioration of performance. Their measurements at 1.8 K relative to 77 K or room temperature, reported in the above paper show increased transmission at shorter wavelengths which they ascribe to observed wrinkling of the mylar substrates. Figure 2.6.11-1 shows a recent three grid low pass filter designed by Holah to have a cutoff at about 30 cm^{-1}, available through Edinburgh Instruments Ltd. This filter was designed for normal incidence, but filters for FIRAS will be required to operate at 45° incidence. Holah et al (1979) have achieved some success with a Fabry-Perot filter at temperatures to 1.1 K.

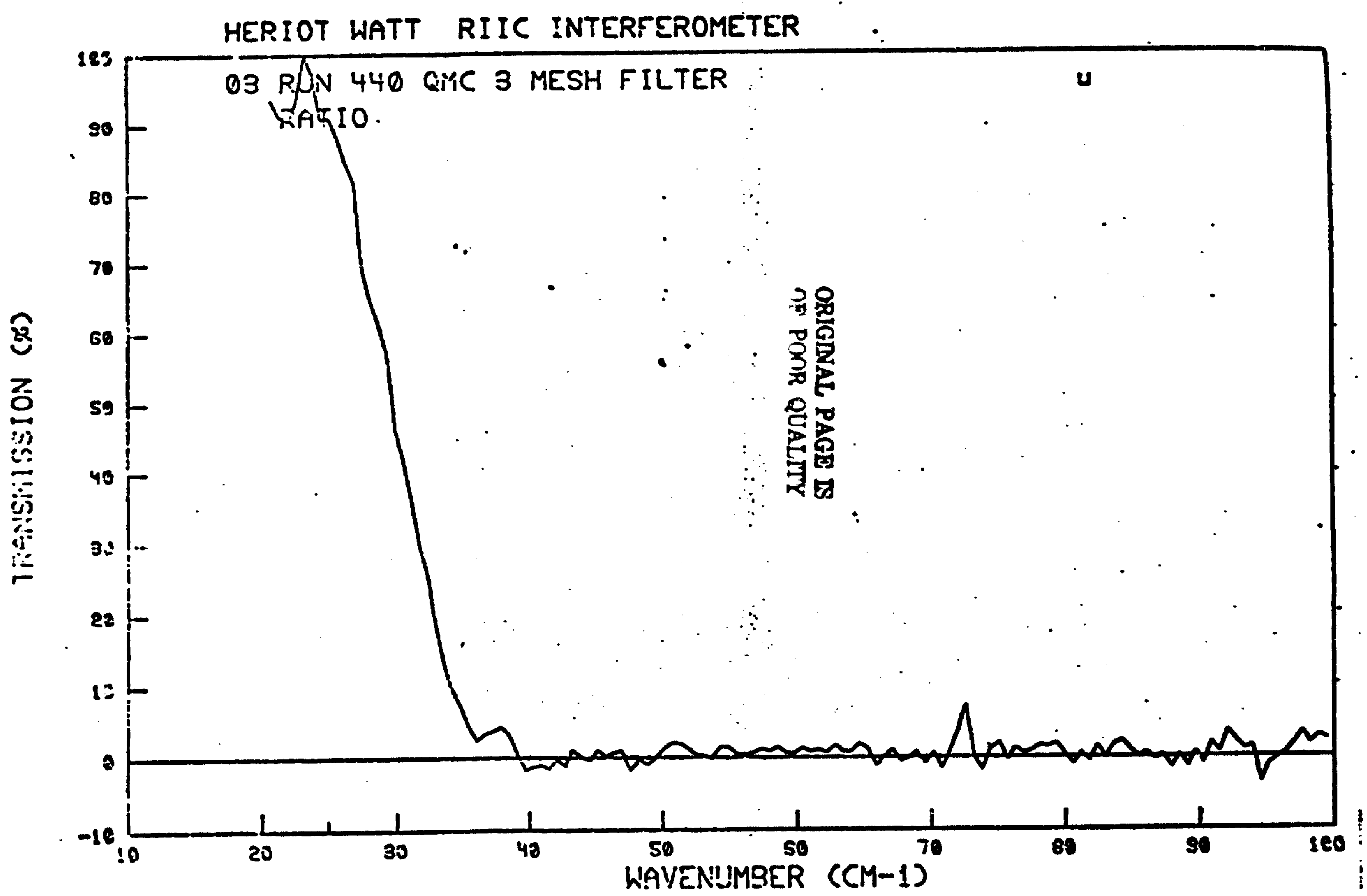

Figure 2.6.11-1. Three Grid Low Pass Filter (Holah)

The surface quality of the dichroic beamsplitters is not critical as far as the detector optics are concerned, but it is very significant in the terms of the desired spectral performance. These are interference filters, and the spacings must be held accurately, generally to a twentieth of a wave or better, to provide optimum spectral response. In the FIRAS instrument, the size of the beamsplitter is fairly large, and consequently the problems with surface distortion are greater. The mounting frames from the substrates must also fit into a relatively difficult optical configuration. With little room available Block recommends the preparation of detailed configuration drawings of the beamsplitter frame to avoid interference with the detector cones and the mounting structure, the interaction with the manufacturer to achieve a mutually satisfactory design, and the testing of the design at liquid helium temperature.

2.6.12 Output Coupling Cone (Y1, Y2, Z1, Z2)

The FIRAS C design uses parabolic Winston cones at the output of the detector mirrors to couple the radiation into the detector cavities. The optical distortions of the system are such that the concentric elliptical concentrator (see Section 2.6.4) could possibly be used, but the rays reaching this optic favor the parabolic cone. At this point there does not seem to be a strong cost benefit in making all coupling cones identical, but we have done so.

A diffraction loss occurs at this optical component, but this is now a fixed loss, and does not change with the retardation. At 1.0 cm wavelength it is becoming significant, but we tolerate it since we exceed the already limiting throughput capability of the detector by expanding the optic.

The expressions for the critical parameters of the cones are given in Section 2.6.1, and the variation of the aperture D and length L with the cone angle ϕ are shown in Figures 2.6.12-1 and 2.6.12-2. (The cone relation for a given aperture deviates very slightly from the throughput obtained from the aperture-solid angle product. The throughput is not actually sharply defined due to the spreading of skew rays.) The nominal FIRAS C design produces the surfaces shown in Figure 2.6.12-3, but the optimized design could incorporate a slightly larger aperture with slightly reduced cone angle. Slight increase in the output cone throughput could be considered to pick up diffracted rays to a greater extent, and it has also been suggested that the output cone throughput to the detector be reduced to define the system throughput at this point. Block recommends maintaining the 1.5 cm^2-sr throughput here, on the basis that the increased throughput itself is the best technique for minimizing the diffraction loss. Definition of throughput at the detector horn does not actually limit the instrumental throughput, since the mixing of the radiation by the input horn loses the geometric definition of the internal optics, resulting instead in nonuniformity in the field response. We note that the inability to couple perfectly into the detector element will produce some throughput loss in any case.

This cone will be electroformed similarly to the input coupling cone, and similar tolerances apply. Since the long wavelength detectors could utilize cones with poor quality surfaces, these can be specified separately from the short wavelength detector coupling cones, however the possibility exists of making a reusable mandril for all output cones. This would require the mandril surface to be sufficiently good for the entire spectral range.

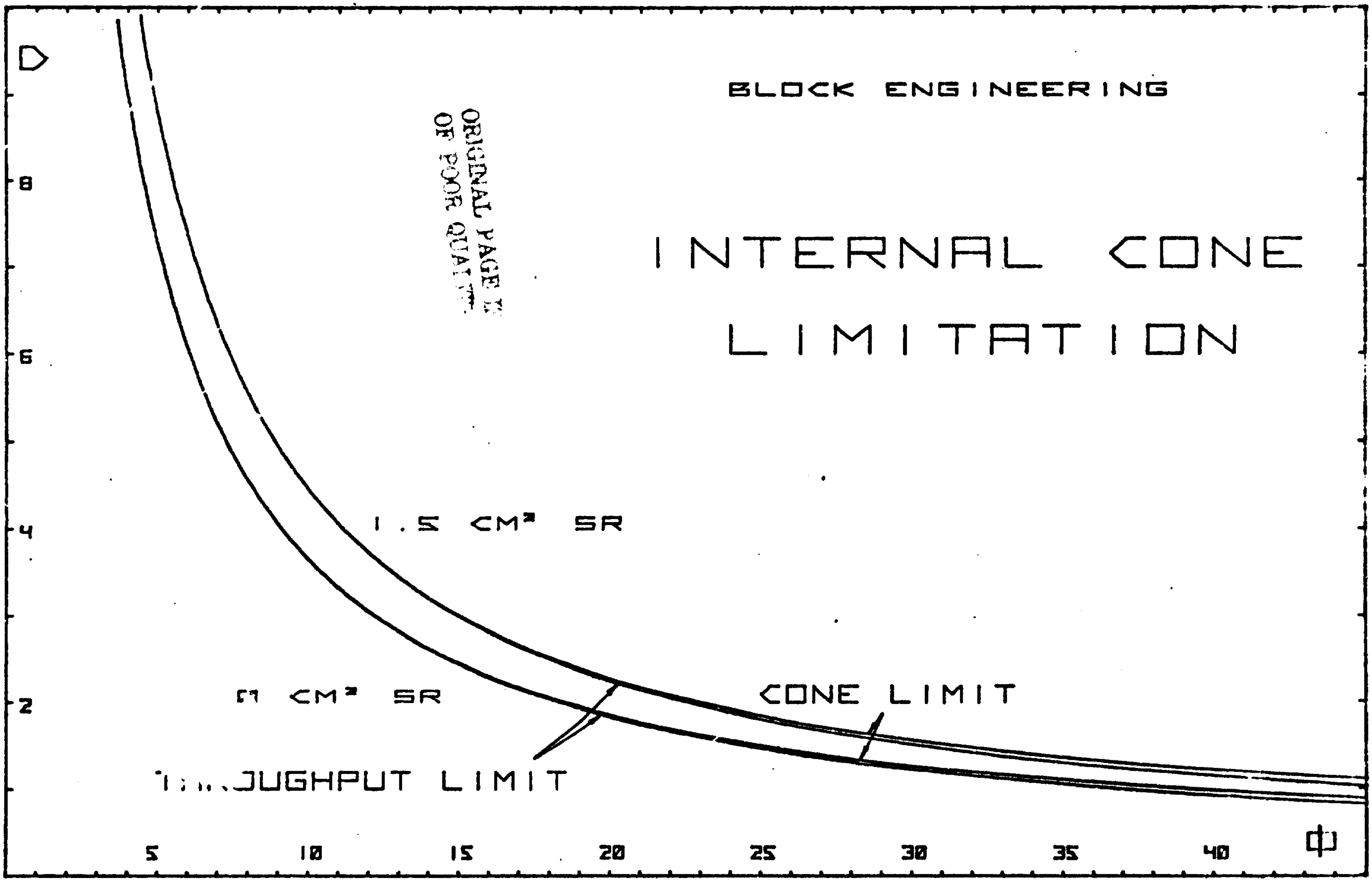

Figure 2.6.12-1. Winston Cone, D vs. ϕ

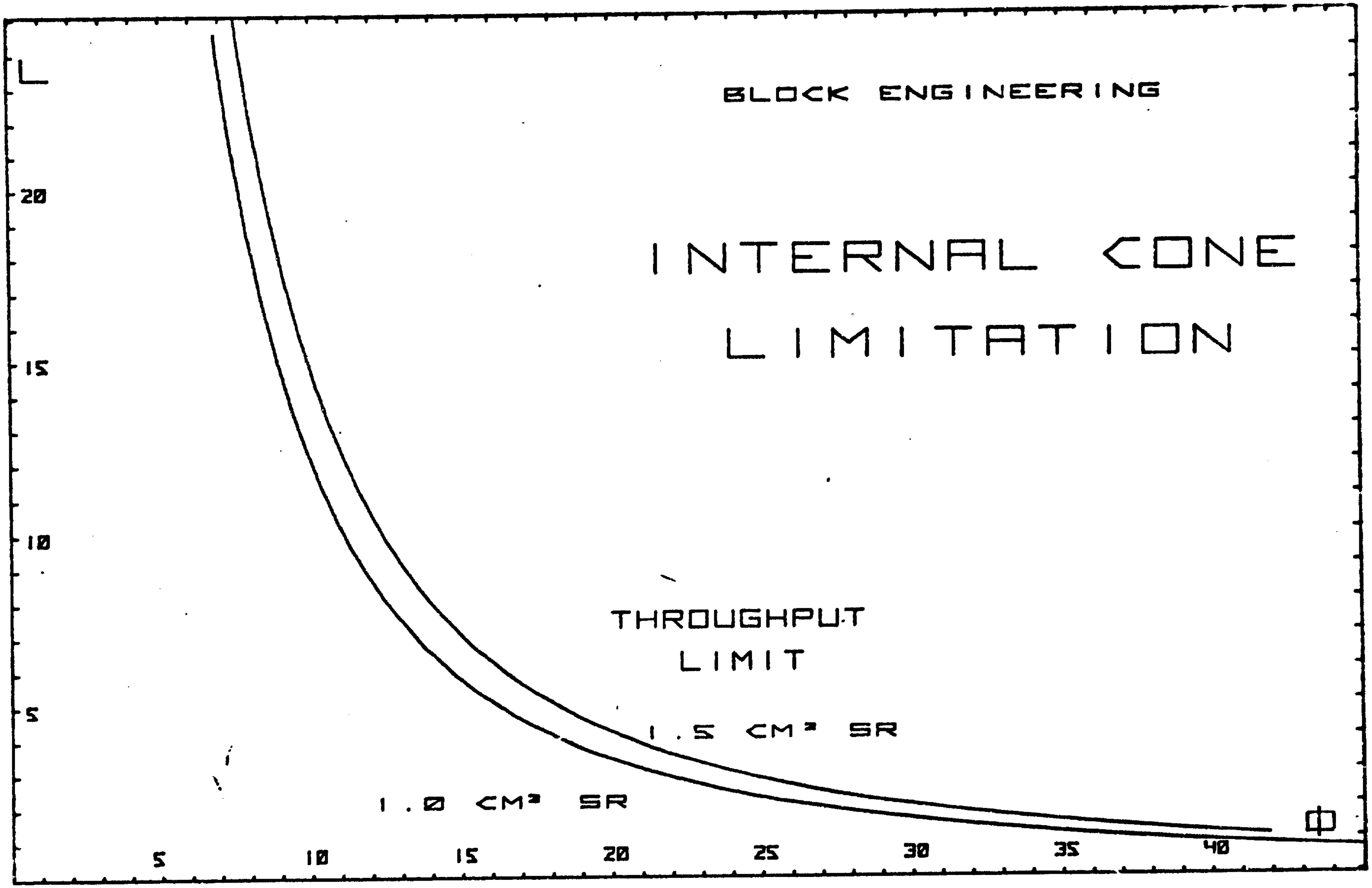

Figure 2.6.12-2. Winston Cone, L vs. ϕ

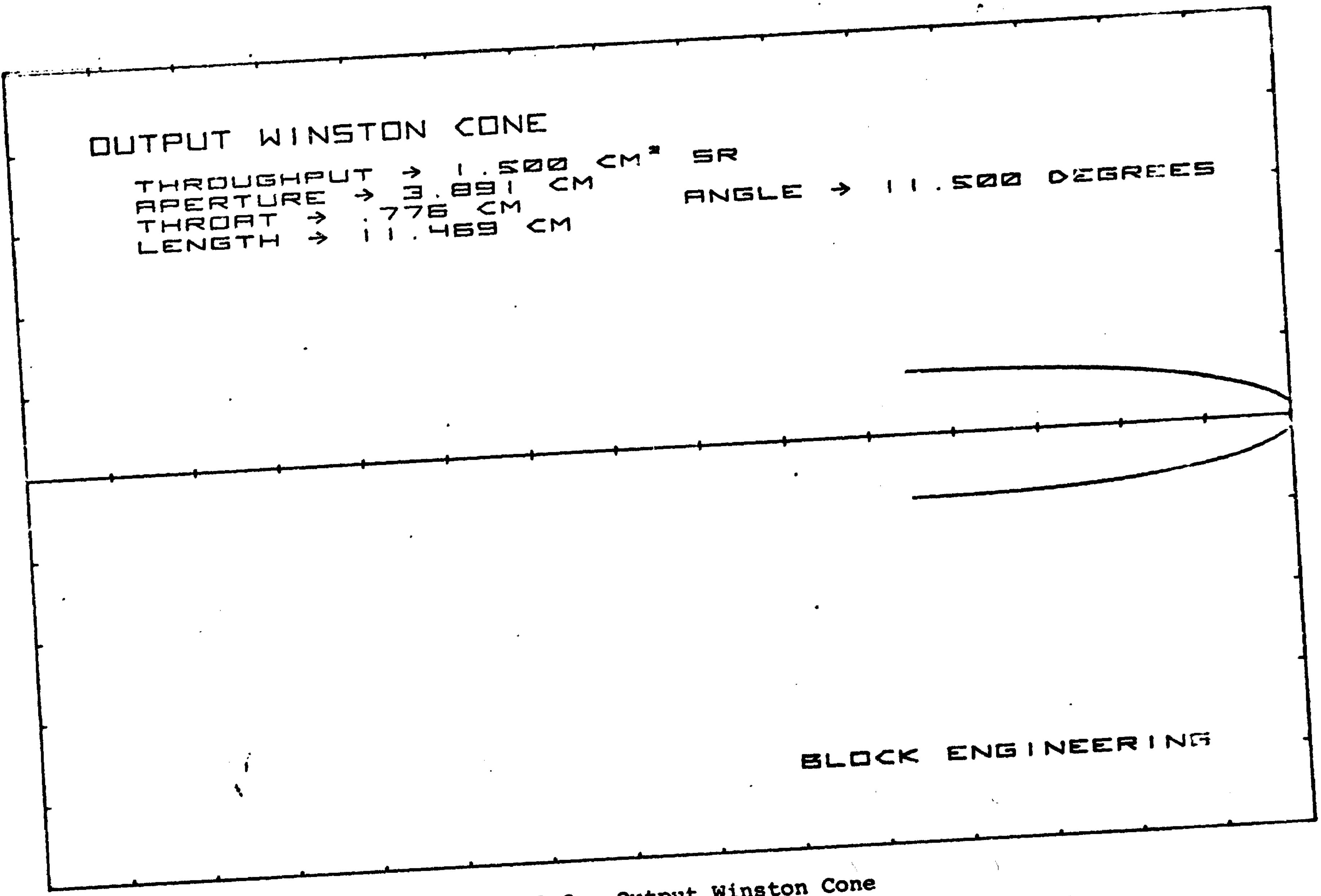

Figure 2.6.12-3. Output Winston Cone

2.6.13 Detector Cavity

The coupling of radiation into the detector element becomes much more significant as we proceed to throughputs which exceed that possible from one side of the element alone. In the past, millimeter wave detector cavities have been based on the conception that diffraction mixes the radiation more or less completely, and that resonant cavity techniques should be used. The present design extends to wavelengths which behave optically, at least for the short wavelength detectors, and these cavities should optimize geometrical coupling.

A wide variety of cavities have been examined, using a simple ray tracing program which determines cavity efficiency for a set of rays at angles in the radial plane, proceeding from the center point to the edge of the throat. Each ray is weighted to include the area effective (πRdR Cos θ, R the radius and θ the angle in the radial plane), and efficiency is computed based on the weighted number of rays that hit the detector, assumed round. It is true that this analysis neglects skew rays, which can be quite significant, but it provides a useful indication of performance.

The hemispherical cavity suggested by Harper et al (1976) was examined with several values of A, the offset of the center of curvature from the throat aperture plane, as shown in Figure 2.6.13-1. Best results here were observed with the radius and detector at that plane, and with the radius of the circle equal to the throat radius. The efficiency for these rays was so poor that investigation of other configurations was clearly necessary.

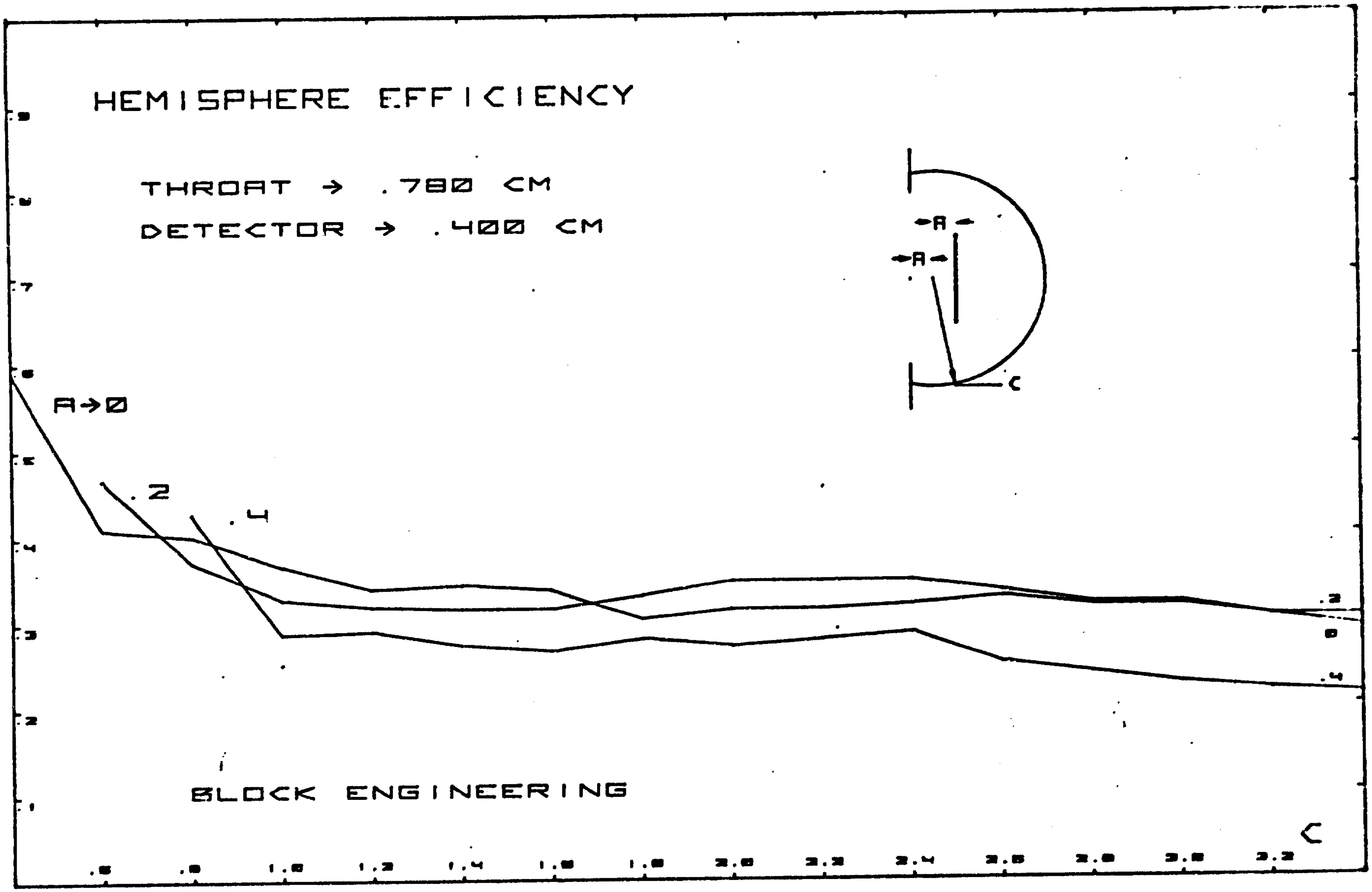

Figure 2.6.13-1. Hemispheric Cavity Efficiency

General optical considerations suggest that an ellipsoid would provide some improvement, with the detector at one focus and the aperture at the other. This cavity is shown in Figure 2.6.13-2, and although the behavior was relatively invariant with increasing separation P, the efficiency was still poor.

A consideration of the flux collectors led to a related optical device, which is termed a positive semisphere. This curve is obtained by rotating a semicircle about an optical axis which is offset from the semicircle center. The optimum position for the center is at the edge of the detector, since this will permit rays which miss the element to be directed back toward it. The configuration shown in Figure 2.6.13-3 produces the highest apparent efficiency of any cavity, but the effects of skew rays are obviously more significant than in other designs, because the important tip which extends back toward the detector is too small and actually diverges the rays. A significant bundle of rays can pass behind the detector and exit without touching the element.

A more useful cavity is indicated in Figure 2.6.13-4, which is termed a negative semisphere. The semicircular section center is offset to the opposite side of the detector, and two reflections are generally necessary to hit the element. The efficiency is highest with the detector in the throat aperture plane, dropping off significantly as it is moved inwards. The effects of skew rays are not excessively lossy in this design, and Block suggests that this approach may be suitable for the short wavelength detectors.

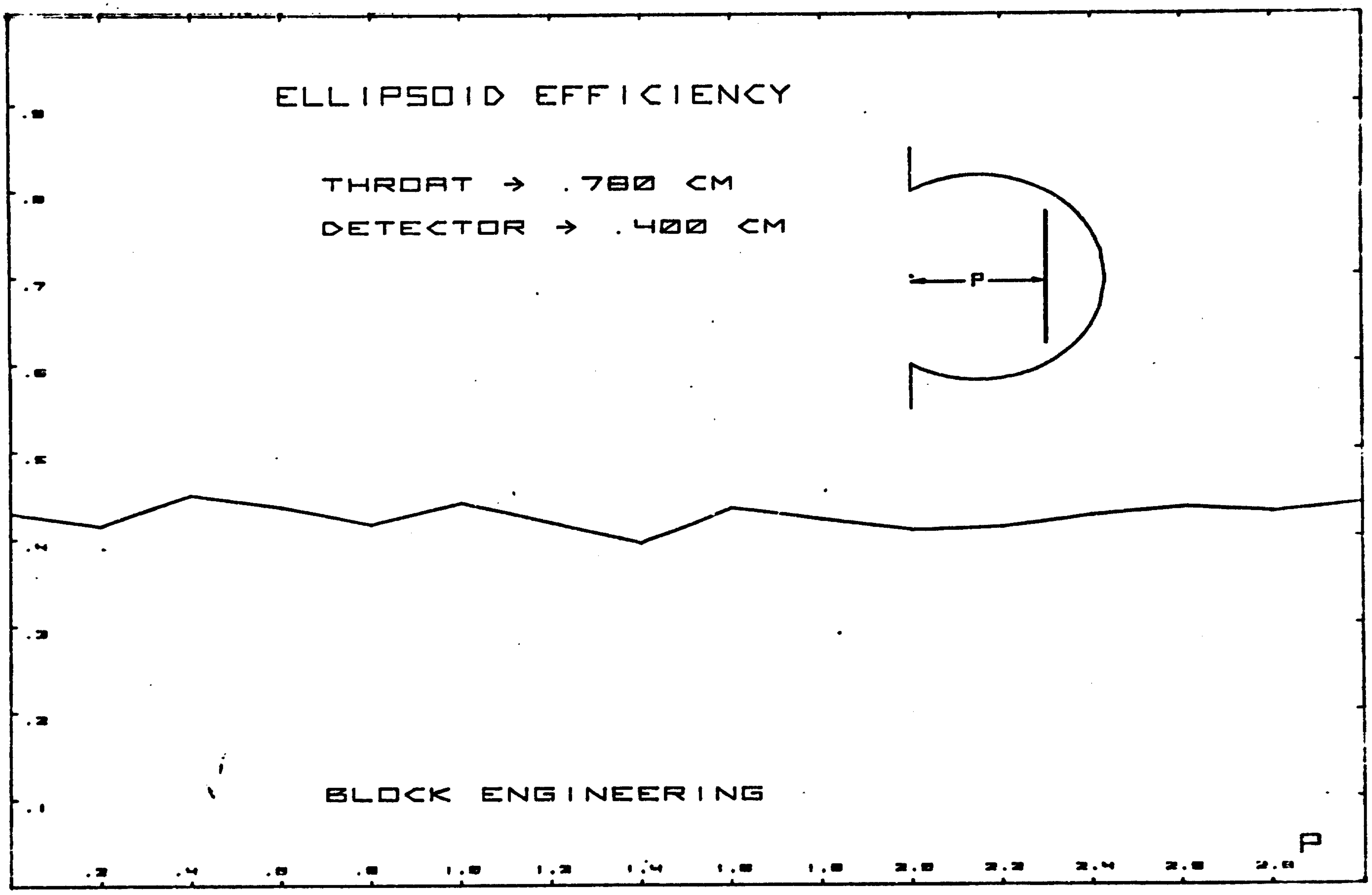

Figure 2.6.13-2. Ellipsoidal Cavity Efficiency

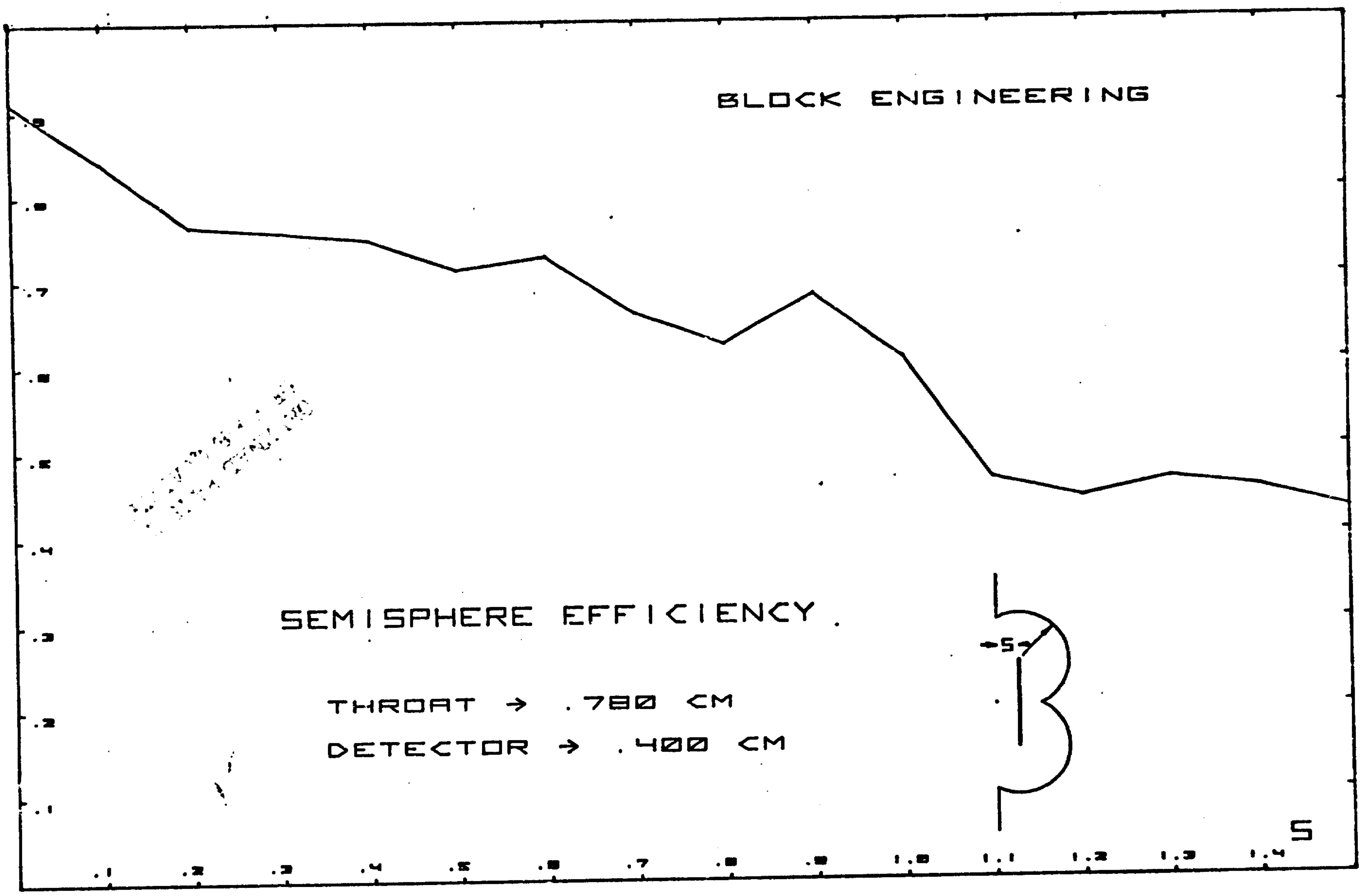

Figure 2.6.13-3. Positive Semispherical Cavity Efficiency

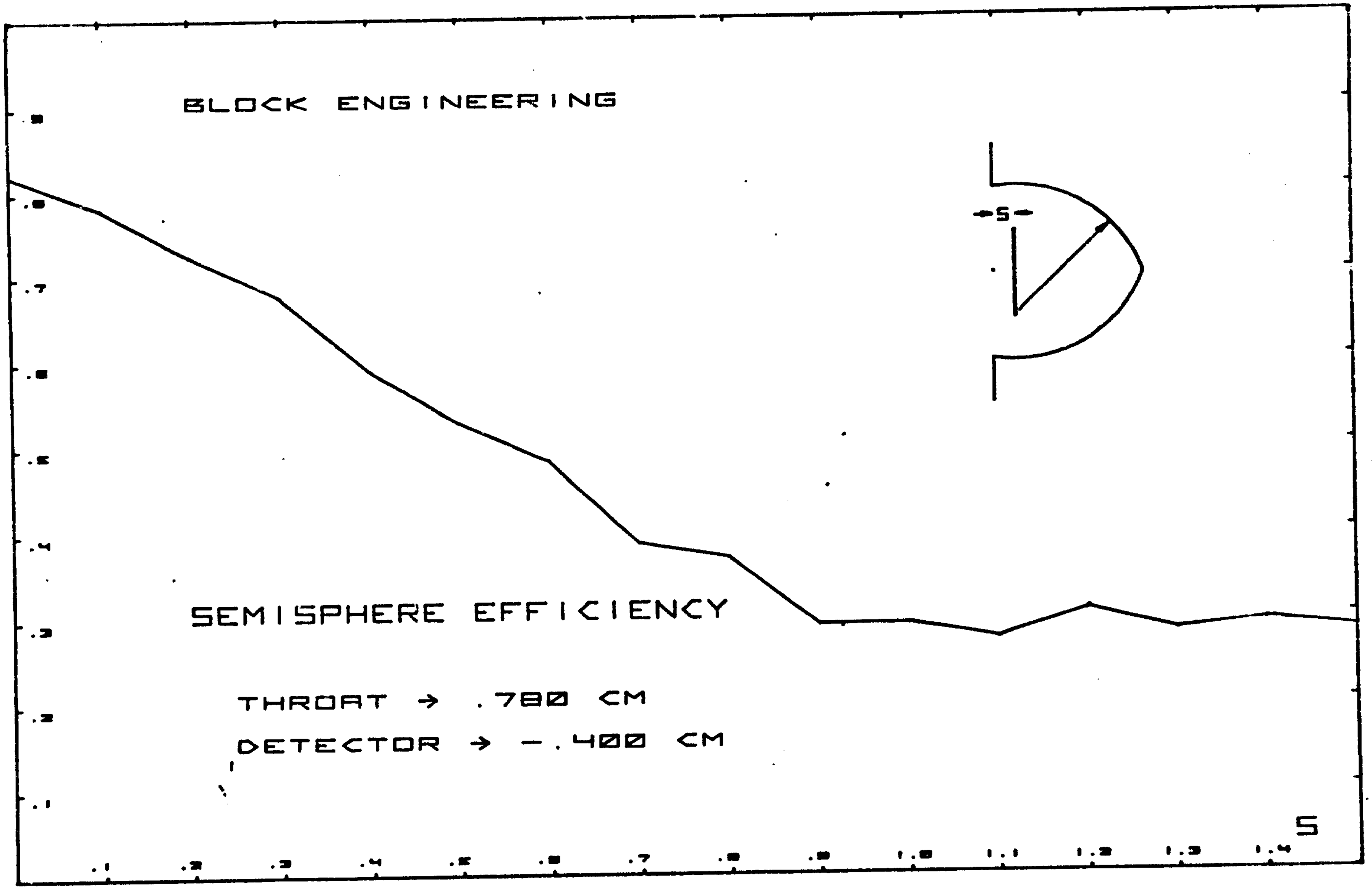

Figure 2.6.13-4. Negative Semispherical Cavity Efficiency

Finally, the cylindrical cavity (Figure 2.6.12-5) was included because it is widely used and understood, subject to the limitations of the present analysis. As might be expected, the cylinder produces best efficiency with the detector behind the throat aperture plane, but this cavity is not as efficient as the semispheres. The loss in efficiency with skew rays is somewhat more pronounced with this configuration, however, since there is no internal curvature that tends to bring these rays closer to the center. The formation of an enclosed cavity by extending the inner cylindrical wall while keeping the throat aperture fixed may be desirable to form a resonant cavity for the long wavelengths, but it does not improve the optical imaging. This is easily seen by considering the detector as a series of images reflected in the mirror wall sections. Looking into the throat, the detector images form an array of "elements" regularly spaced in the mirrored reflections, and extending the side walls only moves these "elements" farther apart along with the aperture images, providing no net gain.

The cavity is an important part of the increased throughput system, and we believe that an efficiency of 0.8 is possible for the square detector, including skew rays and internal diffraction. The analysis of this is simply too complex for the limited program undertaken by Block, and we can only point in certain probable directions. The throughput of the horn is 1.5 cm^2-sr, which gives an effective solid angle of π sterradians at the throat, equivalent to a Lambertian source. We expect that an effective throughput of 1.2 cm^2-sr will be realized at the detector, but diffraction and optical mixing by the non-imaging optics will spread this out to the 1.5 cm^2-sr limit. The ultimate uniformity of the FIRAS field of view is affected in this way, but adjustment of the cavity size and

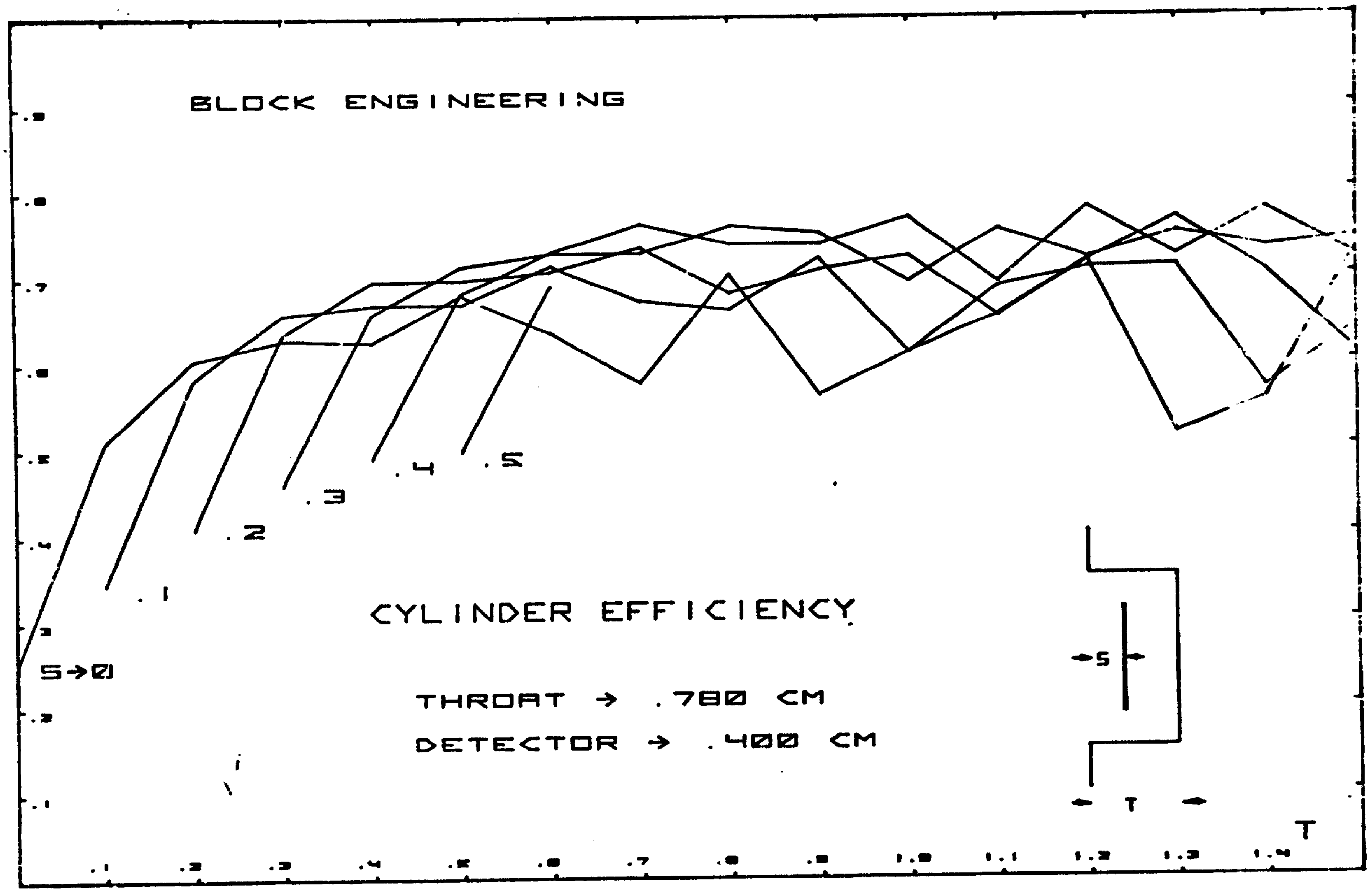

Figure 2.6.12-5. Cylindrical Cavity Efficiency

shape may permit achieving a more uniform distribution. Unfortunately, the full optical analysis of this system, including diffraction, is beyond the scope of the present program.

The optical surfaces of the cavity are dependent on the spectral range desired. The short wavelength detector cavity should have a good machine polish, but figure is quite uncritical, and undulations have very minor effect. The scratch/dig tolerances should be good, perhaps 100/80, because the small scale of the optic increases the proportional loss. The long wavelength detector cavity barely requires polishing at all, and optical characteristics are almost unimportant.

2.7 OPTICAL FABRICATION

Since the entire optical system utilizes metal optics, the techniques involved are generally fairly recent, especially regarding the production of nearly optical quality surfaces. A large number of firms now produce metal optical components by many diverse technologies, and this section is devoted to some remarks and reccmmendations in this area.

2.7.1 Machine Finishing

In the fabrication of metal optical surfaces, an early and successful technique has been the machining, fine grinding, and polishing of copper, aluminum, beryllium, and other metals. Such machine techniques can provide a good reflecting surface directly, but more often a nickel "Kanigen" surface has been chemically deposited on the machine polished surface to permit optical polishing and aluminizing, with greatly improved figures.

Mirrors of this sort are made by companies such as Special Optics, which can provide paraboloids, ellipses and spherical sections. Off-axis paraboloid sections can also be provided, within the approximate limits indicated in Figure 2.7.1-1. The distance from the center of an off axis section to the focus of the paraboloid is given as FL (cm) and the angle of the centerline to the optical axis of the paraboloid is A in the figure. These curves are limited at the maximum angle A shown due to the size of the tooling available with the nominal focal length indicated, but special tooling can be obtained for other nominal focal lengths and maximum sizes. The optimized FIRAS C system does not conform exactly with available tooling for every element, but this has been attempted for the large collimator mirrors, although the maximum size capability is exceeded in providing increased throughput.

2.7.2 Diamond Turned Optical Components

A more recent innovation is the computer controlled milling machine, which can easily provide accurate surfaces to fairly arbitrary functions, and is available at greater expense. The use of a prepared diamond edge in a laser/computer controlled milling machine permits the cutting of optical quality surfaces directly, without polishing. This technique is rapidly coming into favor for metal optics, avoiding many intermediate steps in obtaining the final surface, and circumventing the difficult thermal control problems that afflict metal optical finishing. The technique has been expensive in the past, but the costs should be considerably reduced through the competitive process when the FIRAS fabrication begins.

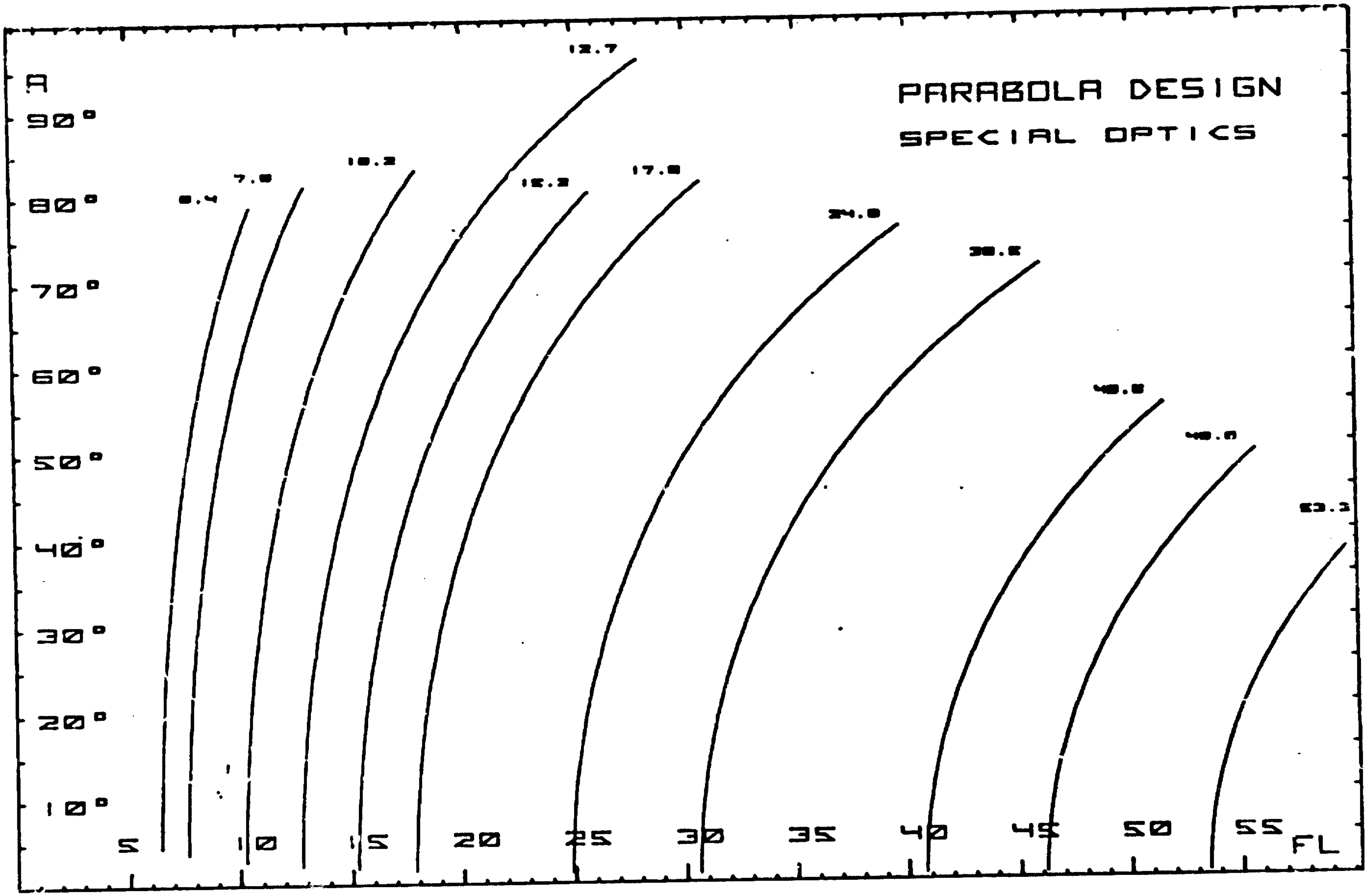

Figure 2.7.1-1. Parabola Design
(Special Optics)

The dihedral mirror sets are ideally suited to this type of process, which avoids the necessity of separating the precision mirror surfaces from the mounting providing the 90° angle setting, and allows an ideally configured mirror assembly from the thermal viewpoint. The technique could also be used for the detector cavities.

2.7.3 Electroformed Optical Components

In structures as complex as the Winston cones, parabolic or elliptical, the depth of the structures makes any normal machining process very awkward, and it is difficult to achieve good near-optical polish in deep, narrow structures. A molding process could be used to advantage over a precisely finished mandril, and the electroforming process allows this to be done to near-optical precision.

The fabrication of a cone is accomplished by the chemical deposition of the desired metal on a mandril which can later be melted or dissolved. This process is capable of reproducing optical surface quality present on the mandril, and also allows the deposition of supporting flanges, ribs, and other convenient aids to mounting the optic. The large size of the sky and reference horns may present difficulties to some manufacturers, and we were unable to find a company able to fabricate these horns as a single structure. Science Team members indicated that companies did exist that could fabricate these horns entire but it is not unreasonable to make them in sections or to support the vendor development of the capability for making them whole, if it does not exist. The fabrication of the mandrils can be done by the above mentioned processes, and it is probably desirable to obtain the mandrils from optical

C-2

fabrication firms, interacting with the electroforming company to insure that the mandril design is appropriate to their technique.

A related fabrication process for the manufacture of far infrared components which do not require optical quality surface is the casting of the component using the lost wax (or equivalent) process. The advantage here is that the master form can be made in an easily workable medium, and the entire process can be carried out in any reasonably equipped workshop. The use of indium metal (m.p. 156°C) will result in a superconducting component that can be satisfactorily supported in a machined copper mount (which can form part of the mold). This might be a suitable process to use with the long wave detector cavity, for example.

2.7.4 Surface Coatings

In general, the highest reflectivity is obtained with evaporated coatings, even on polished metal substrates. Of course, if diamond turned aluminum is used, no reflective coating is required unless superconducting surfaces are needed. Machine polished metal optics are generally provided with aluminized surfaces, often protected with a thin SiO_2 overcoat to prevent oxidation. It is also possible to evaporate indium onto the surface, producing a superconducting coating that also has good warm visible reflectivity. The characteristics of indium coatings in the near infrared are described by Motulevich and Shubin (1963), and in the visible by Bor and Bartholomew (1966). It is likely that no protective overcoat would be needed. The thickness of the indium coating could not exceed about 0.1 micron without the possibility of increasing surface irregularities due to electrostatic concentration of material, although this would be trivial at far infrared wavelengths. The utility of having good visible reflectivity is the ability to perform alignments with visible light aids, and this is considered a most desirable capability.

The normal metal surface cone optics, however, operate at various angles approaching grazing incidence, and metallic absorption becomes high for one polarization of the incoming rays. A technique to avoid this (Mather, 1974) is the coating of a polished copper surface with a dielectric layer of polyethylene 500 microns thick, but this is considerably too thick and possibly not uniform enough for the present application. We would recommend that the layer be less than 100 microns if used in the FIRAS instrument. A technique which might be used to apply a uniform coating of this thickness is to make a preformed balloon of the material, inflate it slightly in the cleaned electroformed cone, and heat the cone until a complete bond is obtained, decreasing pressure as this occurs to avoid pulling at the ends. Of course, this is unnecessary if a superconducting layer is utilized in these cones. An expendable electroforming mandril can be used to form several balloons prior to the fabrication of the cones, if used with an appropriate release agent. Rotation of the horizontal mandril while coating will avoid uneveness in the resulting balloons.

We note that a strong absorption line occurs at 73 cm^{-1} (Prettl and Frank, 1979) which increases markedly at low temperatures to give an absorption coefficient of about 5 cm^{-1} below 30K. This will produce a noticable loss in system transmission, but is not considered excessive. Most rays experience only one reflection in each Winston cone optic, giving a loss of only 0.7 overall at the line center.

2.8 OPTOMECHANICAL CONSTRAINTS

Tolerances for the alignment of the FIRAS optical train as well as sensitivity of the design to thermal and mechanical variations can be seen by variational analysis. Effects of alignment and scan motion errors in the interferometer proper require consideration of the interference phenomena, except for gross vignetting effects.

2.8.1 Variational Analysis

Using the FIRAS C optical design as optimized by the BOOST program, ray tracing was performed to provide output plane spot diagrams with selected individual optical components offset from their preferred positions. Nearly all data were obtained at the optimized exit pupil corresponding to the position of the output coupling cone aperture. The approximate appearance of the exit ray caustic can be seen from Figure 2.8-1, 2.8-2, and 2.8-3, which are at -1 cm, zero, and +1 cm along the optical axis from this position. (Figure 2.8-2 is a duplication of Figure 2.5-4, at the zero retardation position without any variations. A normal retardation of 10 cm or 2.5 cm actual shift of one dihedral mirror is shown in Figure 2.5-5.) We note that in these spot diagrams at the output coupling cone aperture there is a consistent offset of the centroid of the ray pattern to the right and slightly upward. As indicated earlier, we offset the cone aperture to correspond to the ray pattern, and the nominal aperture circle is shown offset by a fixed amount in each figure.

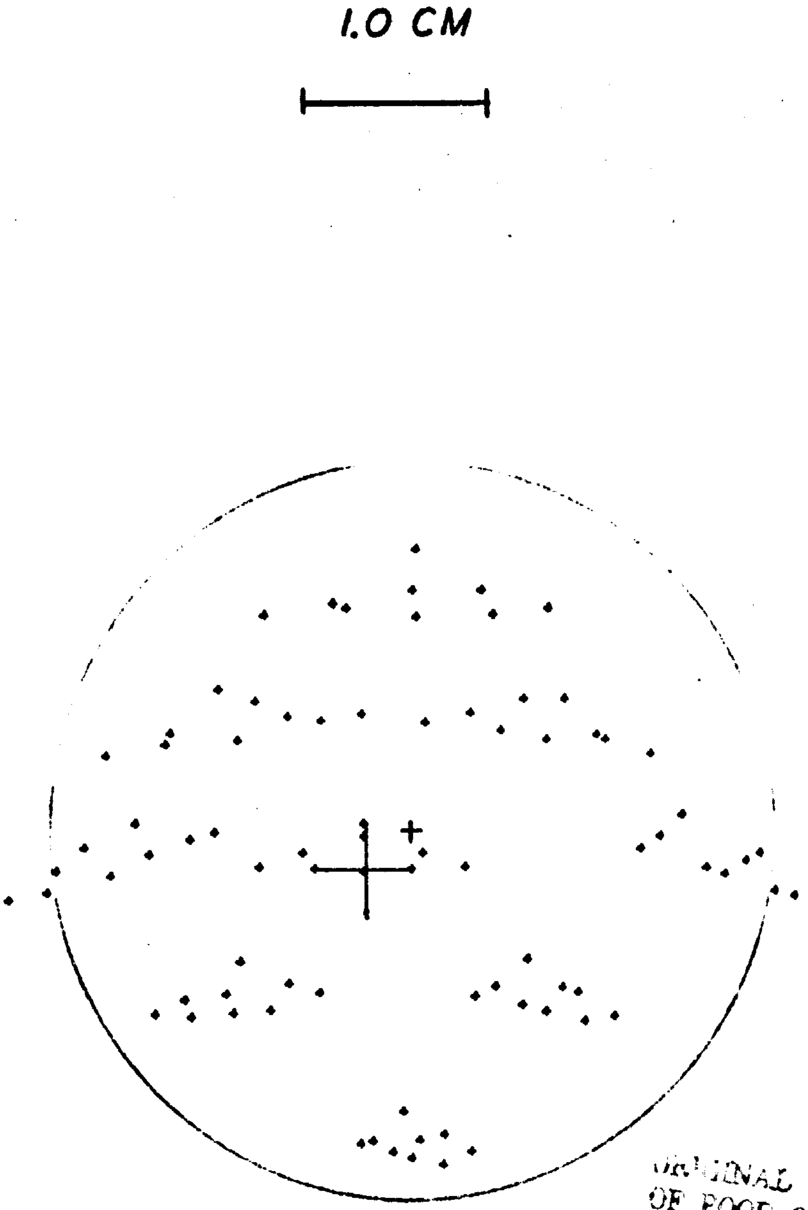

Figure 2.8-1. Output Spot Diagram at -1.0 cm From Focal Plane

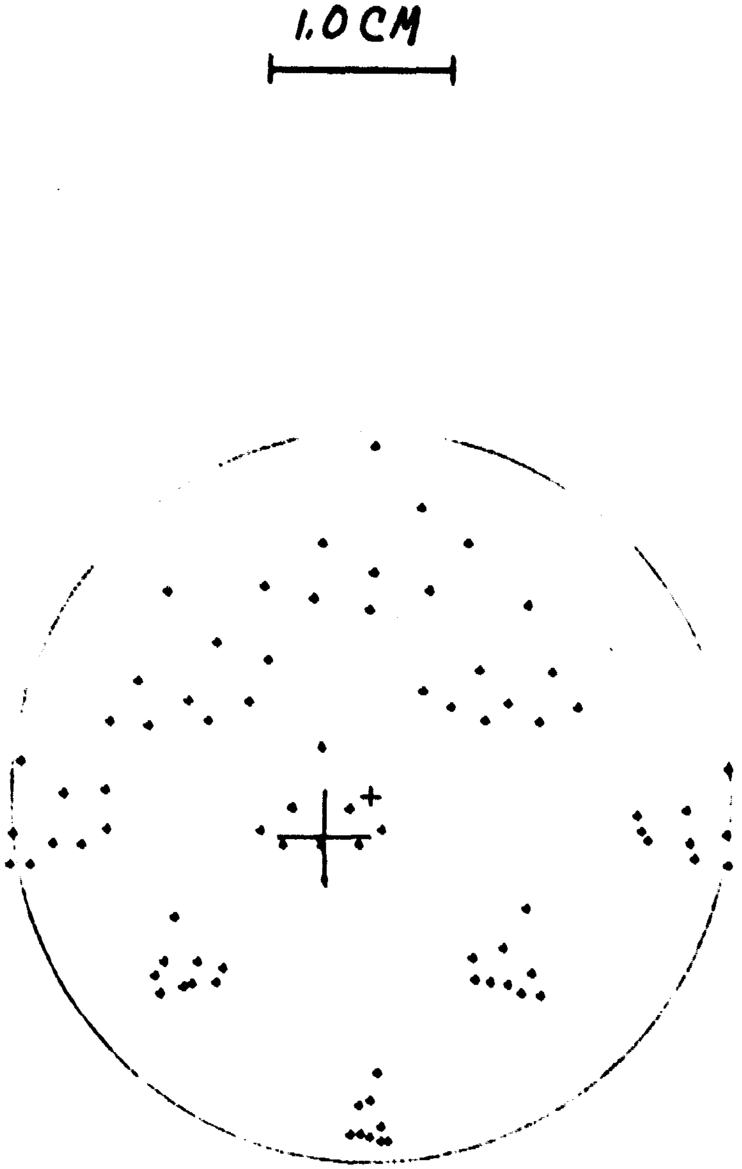

Figure 2.8-2. Output Spot Diagram at Focal Plane

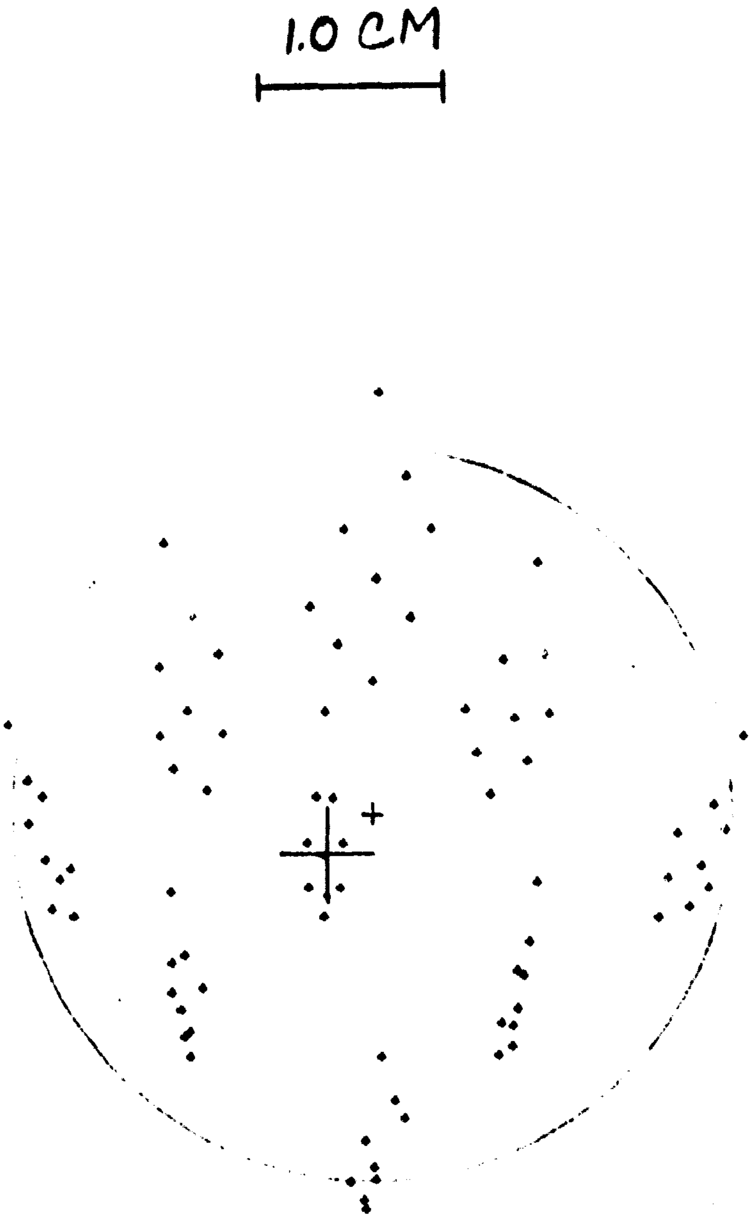

Figure 2.8-3. Output Spot Diagram at +1.0 cm from Focal Plane

Variation in the entrance coupling cone aperture position along the optical axis shown in Figure 2.8-4 (-1 cm) and 2.8-5 (+1 cm). This represents a variation of special interest since the cone and the larger input cone to which it is attached are made of nickel, while the instrument frame is made of aluminum. The effect of this variation is relatively insignificant, resulting in a centroid shift up and down of about ±0.05 cm and a slight narrowing of the beam in the other axis. The expected variation with temperature is a downward shift of the aperture by -0.05 cm with cooldown, which conceivably could be compensated for in assembly.

Variation in the collimator mirrors was considered of special significance and Figures 2.8-6 and 2.8-7 show the effect of shifting one collimator mirror in and out by 1.0 cm along the normal to the mirror center. This results in the lateral centroid shift of approximately ±0.35 cm, which is the largest variation noted. Figures 2.8-3 and 2.8-9 show the effects of shifting one collimator mirror in and out by 1.0 cm along the optical axis joining it with the transfer mirror, resulting in a trivial centroid shift up and down by approximately ±0.05 cm. Shifting the collimator mirror normal to its central surface is representative of the most probable alignment error for this component. The collimators are subject to one of the longest mechanical/thermal connections in the instrument, going from one side of the dewar to the other around the sides of a square structure. If even moderate thermal stability is attained, the error in a warm alignment taken to low temperatures should be considerably less than ±0.1 cm for this component, giving less than ±0.04 cm centroid shift.

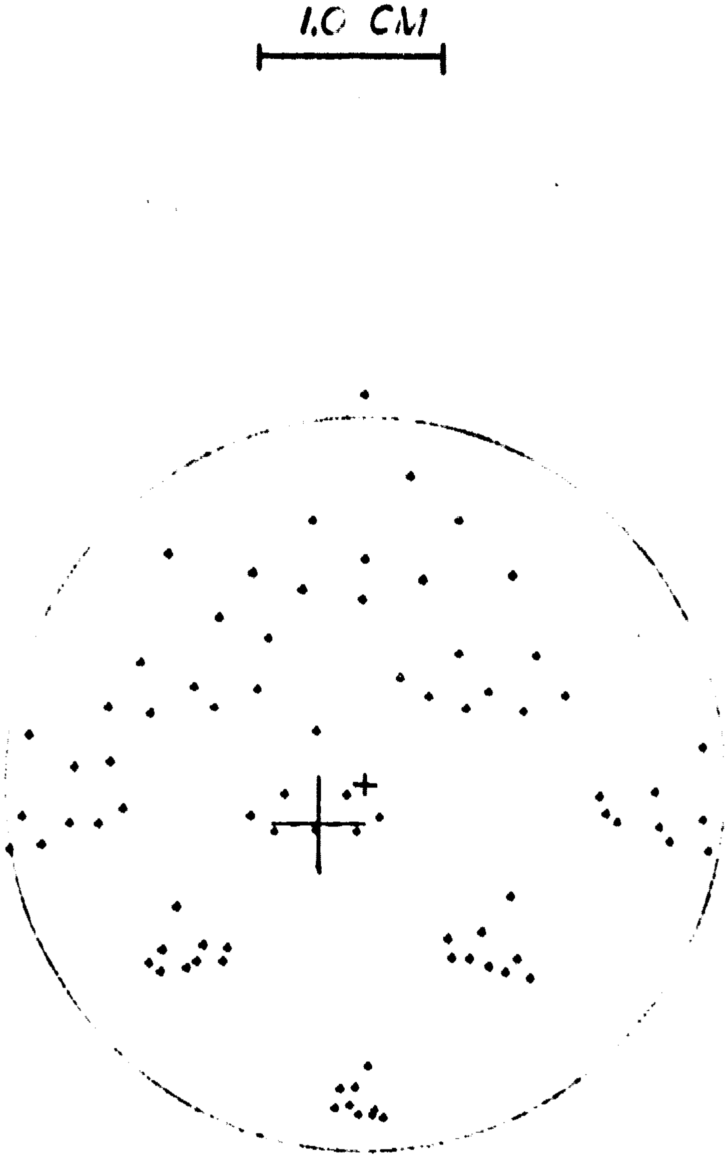

Figure 2.8-4. Output Spot Diagram with Entrance Shifted - 1.0 cm

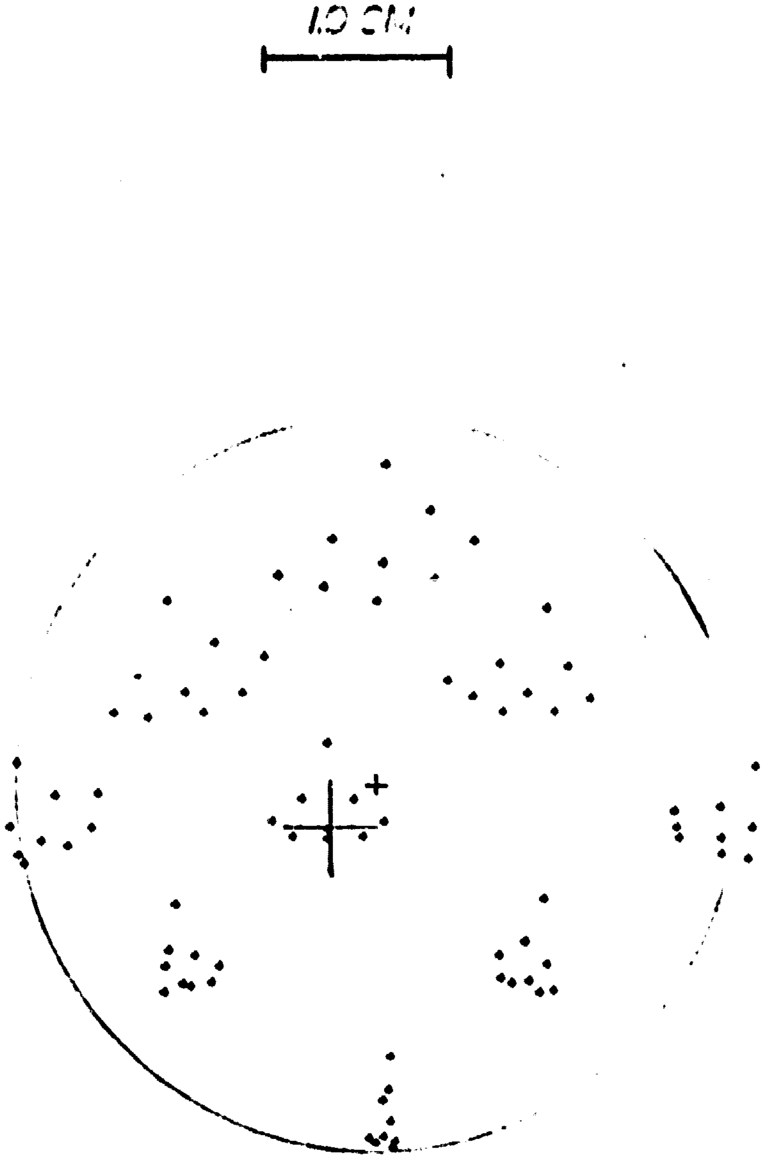

Figure 2.8-5. Output Spot Diagram with Entrance shifted +1.0 cm

Figure 2.8-6. Output Spot Diagram with Collimator shifted normal -1.0 cm

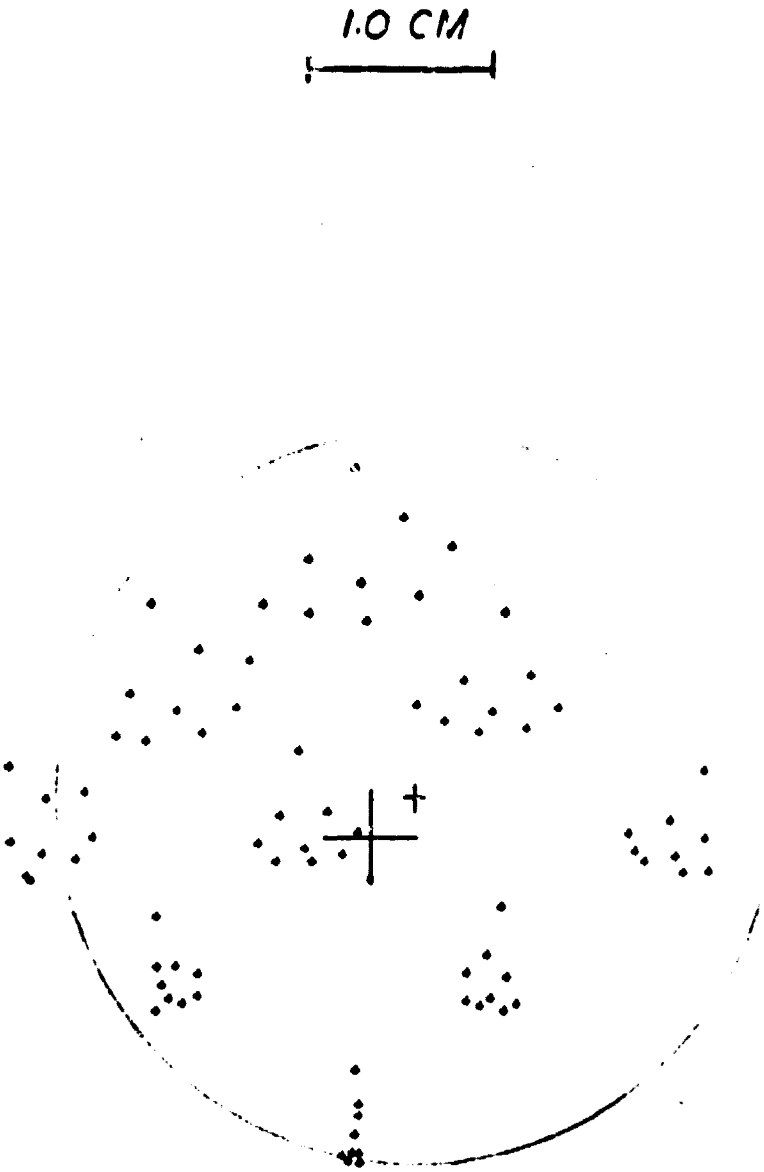

Figure 2.8-7. Output Spot Diagram with Collimator shifted normal +1.0 cm

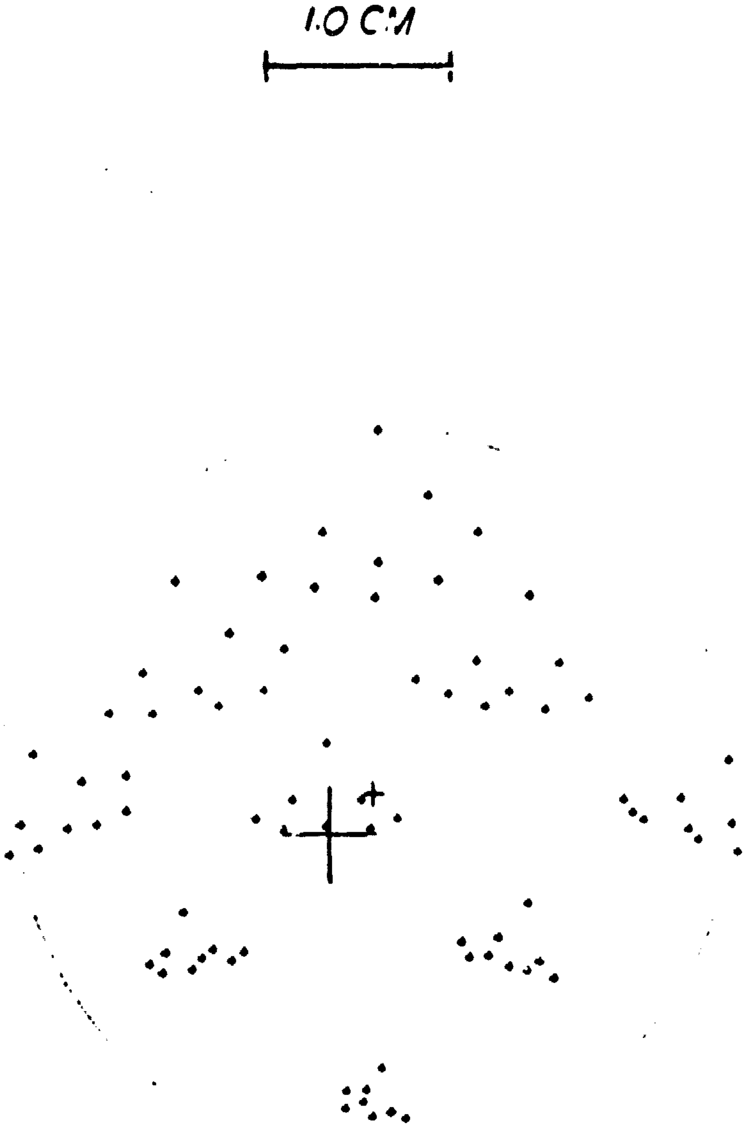

Figure 2.8-8. Ouput Spot Diagram with Collimator shifted -1.0 m on axis

Figure 2.8-9. Output Spot Diagram with Collimator shifted +1.0 cm on axis

ORIGINAL PAGE IS
OF POOR QUALITY

The combination of detectors, output coupling cones, dichroic beamsplitter, and detector mirror are made as a close knit structure, and it is unlikely that relative variation will occur between these components. The shift of this assembly, however, is considered relative to the rest of the optical system in Figures 2.8-10 and 2.8-11, taken ±1.0 cm along the optical axis leading to the transfer mirror. The result in this case is a change in the size of the pupil at the output cone aperture of ±0.05 cm in radius, with size decreasing as the separation is increased.

The effect of tilts in the optical train can be significant, but it was not possible to analyze tilting during this program. The design of the instrument has been made with the goal of being able to align the instrument at room temperature and maintain that alignment adequately at low temperature. The effect of temperature and expansion coefficient differentials in the system is to change dimensions in the first order and angles in the second order. The major vertical dimension change in the FIRAS instrument (apart from the nickel cone structures) amounts to 0.24 cm over the 65 cm height in going from ambient temperature to below 10K. If an error of 10% of this amount existed between the two sides of the instrument, the tilting of the upper bulkhead would amount to 1.4 arc minutes. This would shift the entrance cone apertures by 0.02 cm and the projected pupil by 0.03 cm, with a consequent shift at the output cone aperture of less and 0.01 cm. Other thermal tilting effects are expected to be proportion to the sizes and separations involved, and should be trivial.

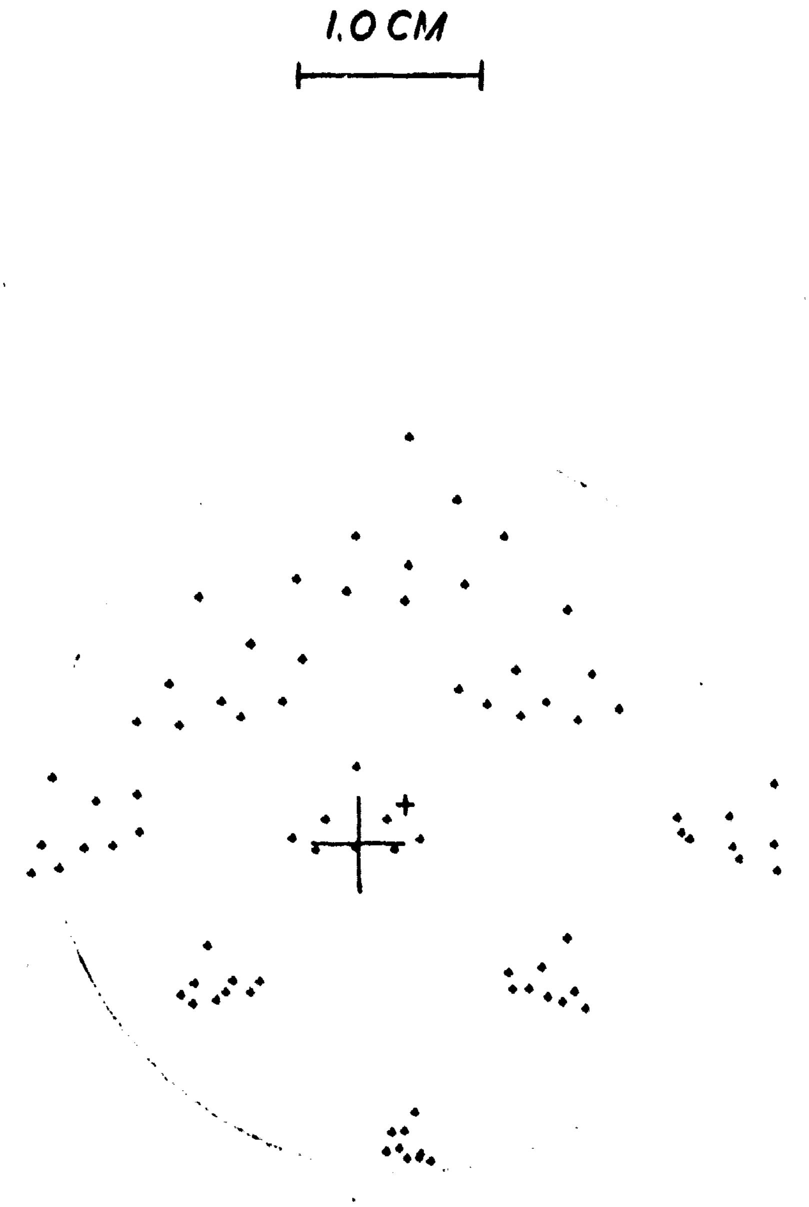

Figure 2.8-10. Output Spot Diagram with exit assembly shifted -1.0 cm.

Figure 2.8-11. Output Spot Diagram with exit assembly shifted +1.0 cm

If the alignment of the mirrors in the system is jarred loose by the acceleration or vibration during launch, any conceivable tilt error could be produced, and it is not reasonable to analyze component tilting with this kind of error in mind.

The conclusions which may be made from this analysis in general terms are that the design is relatively uncritical in terms of any specific dimensions or orientations, and the expected thermal effects will not significantly alter the alignment. The effects of mechanical forces or actions on the instrument are important only if they alter the alignment afterwards, and the components must be able to take the anticipated mechanical forces without plastic deformation. If the alignment is altered by such forces, it will generally be in error by unpredictable and presumably large offsets indicative of mechanical failure. Unless the mechanical strength of the component mounts and support structure is greatly reduced by incorrect weight reduction in detailing, the addition of special "fail-safe" alignment aids does not seem to be warranted.

This does not mean, however, that the optical alignment of the instrument should be compromised. Careful and accurate alignment should be carried out on the instrument, and the alignment should be locked mechanically and reverified, preferably at low temperature. If satisfactory, the alignment should be rechecked prior to permanent fixing of the alignment, and again after final lockup. This degree of care will ensure that the system starts with the optimum possible configuration, and consequently has the best chance of success.

2.8.2 Interferometric Effects

A detailed study of this interferometer configuration including optical component tilts and shifts has been done by Weiss (1979) and the Martin-Puplett interferometer has been analyzed by Lambert and Richards (1979). Block began an effort to model the interferometer in the computer, producing interferogram outputs which could show the effects of tilting on large throughput beams of 3° radiation. Accurate artificial interferograms were obtained, as shown in Figures 2.8.2-1 which included both a blackbody emission and a narrow feature (a gaussian line at 4 cm^{-1}), and the effect of a small (5 mr) tilt of one mirror can be seen in the lower figure in terms of the apodization of the line component. The obliquity angle of the radiation was assumed to be 10°. This effort was not completed, due to difficulties encountered in obtaining output transformations showing effects at a level of better than a part in a thousand of the blackbody intensity. It is not clear at this time what the source of the difficulties was, but it may have been due to some imperfections in the input parameter digitization.

2.8.2.1 Spectral Errors Due to Imperfections in Sampling

This source of noise falls under the category of modulation noise since it translates signal from one spectral region to another, in this case by a phase modulation process. Its manifestation depends on the nature of the spectrum and characteristics of the modulation. In case of emission spectral or absorption spectra with isolated lines and for deterministic modulation

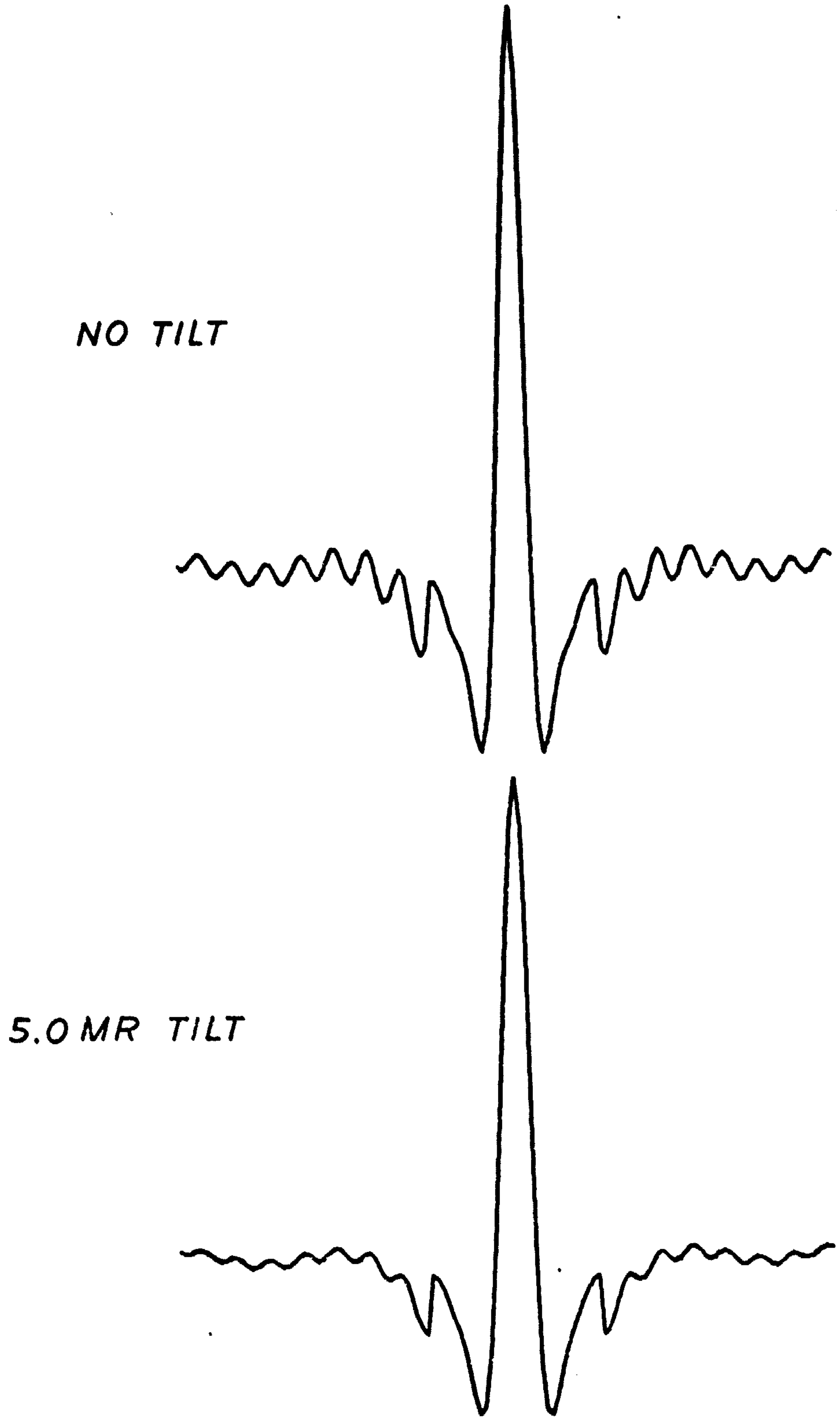

Figure 2.8.2-1. Artificial Interferogram, 3°K Blackbody with 4.0 cm^{-1} Gaussian line

(e.g., sinusoidal) additional lines or ghosts are introduced. For random errors, saddles are created at either side of the lines and line intensities reduced. For an absorption spectrum, lines are filled in and a shoulder usually at the short wavelength end of the spectrum can be present depending on the slope of the cut-off. The average intensity of the spectrum is little affected. The allowable magnitude for these errors can be expressed in terms of a desired spectral signal to noise ratio $(SNR)_s$ from the relationship developed in Appendix D for an absorption-like spectrum or

$$\varepsilon \leq \frac{\sqrt{2}}{\pi\nu_s} \frac{1}{(SNR)_s} \tag{2.8.2-1}$$

and

$$\varepsilon \leq \frac{1}{\pi\nu_s} \frac{1}{(SNR)_s} \tag{2.8.2-2}$$

where (2.8.2-1) is for a sinusoidal error and (2.8.2-2) for a random error and

ε = the magnitude of the error (cm)

ν_s = the wavenumber (cm^{-1})

For convenience all units are in spatial terms, frequency and distance, as pointed out in Appendix D; they are readily convertible into electrical frequency units by multiplying by scan velocity $V=\dot{B}$, where B is the optical retardation.

Using the above relationships we can compute some allowable sampling errors. Taking as a reference a desire to maintain a radiometric (SNR) $\geq$ 1000 and taking the shortest wavelength as a worst case or $\nu_s = 100 \text{ cm}^{-1}$ (100 µm)

$$\varepsilon \leq 5 \times 10^{-6} \text{cm } (0.05 \mu\text{m}) \text{ Sinusoidal error}$$

$$\varepsilon \leq 3 \times 10^{-6} \text{cm } (0.03 \mu\text{m}) \text{ Random error}$$

We can use these values to define limits on certain sources of error.

2.8.2.2 Non-Uniform Scan Velocity

Two cases can be distinguished, equi-time sampling and fringe reference sampling. In the first case, equispaced time pulses derived from an electrical clock are used to sample the interferograms at fixed time intervals. Clearly in this case the allowable scan velocity error $\Delta V \leq \frac{\varepsilon}{\Delta t}$ where Δt is the time in between samples, which points out the fact that in case of under-sampling (heterodyning) the allowable velocity error decreases.

The second case (and more usual practice) is to sample at positions derived from the zero crossings of a scan-derived reference waveform. An error still results from the fact that the reference channel and signal channels usually have different delays. Because of the typically high signal to noise available from the reference channel no filtering is used and a filter with a delay time constant $t_d = 1/2\pi f_c$ is used in the signal channel, where f_c is the 3dB cut off frequency of the low pass on the bandpass filter used. Since $f_c \leq f_s/2$, f_s = sampling frequency per the sampling criterion,

$$t_d = \frac{1}{\pi f_s} \qquad (2.8.2.2\text{-}1)$$

and the resulting sampling error

$$\varepsilon = \Delta V \, t_d = \frac{\Delta V}{\pi f_s} \quad \text{or} \quad \Delta V \leq \pi f_s \, \varepsilon \qquad (2.8.2.2\text{-}2)$$

For the same nominal sampling frequency $f_s = \frac{1}{\Delta t}$ in the comparison of equi-time sampling and fringe reference sampling, the latter is a factor π more tolerant to velocity errors.

Using a figure $\varepsilon \leq 3 \times 10^{-6}$ cm, a retardation velocity $\dot{B} = 10$ cm/sec and $f_s = \dot{B}\nu_r = 2000$ Hz for $\nu_r = 200$ cm^{-1} we obtain a r.m.s. velocity error limit for fringe reference sampling

$$\Delta V \leq 1.9 \times 10^{-2} \text{ cm/sec} \qquad (2.8.2.2\text{-}3)$$

allowing a percentage velocity error $\frac{\Delta V}{V}$ of 0.19%. This can then be used to define the requirements for the servo-controlled scan system in terms of stiffness to external and self-induced disturbances. Equi-time sampling requires an r.m.s. velocity error controlled to $\Delta V \leq 6 \times 10^{-3}$ cm/sec for random errors, which corresponds to a percentage velocity error $\frac{\Delta V}{V}$ of 0.06%.

3.0 DETECTOR AND SIGNAL CHANNEL

The increased throughput in the FIRAS C instrument requires that the detectors be at least 0.4 cm square, while the sensitivity requirement is such that a noise-equivalent power of about 1×10^{-14} watts/Hz$^{1/2}$ is desired. This appears to be possible with technology recently developed, using composite bolometers or implanted silicon bolometers, and further detector development appears to be a matter of optimization of parameters. Composite bolometers have been developed by several workers, and are commercially available*. Implanted silicon bolometers were developed by Hauser and Weiss of the COBE Science Team, and are currently being improved for this specific application. A most important result of this improvement has been the suppression of the 1/f noise onset to below 1.0 Hz, which permits operation of the interferometer at very low scan speeds, with the corresponding decrease in drive power dissipation. Drive power dissipation has been reduced to an acceptably low level, even at the highest retardation rate, making this factor less important in the present application.

The detector signal channel should be designed so that each detector is optimized in terms of its noise contribution. The signal frequency produced by a given wavelength is

$$f = \dot{B}/\lambda \quad \text{Hz} \qquad (3.0\text{-}1)$$

where $\dot{B}$ is the retardation rate (cm/sec) and λ is the wavelength (cm). At the highest rate, 10 cm/sec, the signal band extends from 10 to 1000 Hz, while at the lowest rate,

---

* Infrared Laboratories, Tucson, Arizona.

0.1 cm/sec it extends from 0.1 to 10 Hz. The dichroic beamsplitter provides a crossover point at 200 Hz to 2 Hz, depending on rate. Bolometer time constants are controllable within broad limits, but sensitivity decreases with faster response, and the desired N.E.P. is obtained with time constants that are probably not much faster than 10 milliseconds. The lower frequency limit is generally set by the onset of 1/f noise, and boosting the response at higher frequencies produces an effective increase in noise there, making the optimum band somewhere in between. The long wavelength detector should probably extend from the 1/f point at 1 cm^{-1} to beyond the upper frequency break at 20 cm^{-1}. The lowest scan rate should be used with the short wavelength detector, although some tradeoff in sensitivity for faster response would be desirable, so that a single retardation rate could be used for both spectral bands. The frequency roll-off produces phase error in the output interferogram and a time delay between signal variation and the electronic response. Too hard a roll-off requires a greater degree of correction in the data processing, with attendant errors, and it is probably better to accept a somewhat higher noise bandwidth, since this factor enters only as the square root. The harder roll-off also makes the correlation between the reference signal and the output interferogram more difficult to maintain under all conditions, leading to sampling errors.

For the FIRAS application, there should be additional elements in the electronic design to provide for diagnostics, calibration, and parameter control in addition to the signal channels and reference channel. Apart from the usual electronic test outputs, the use of light-emitting diodes to inject precisely controlled signals into the detector allows very complete evaluation of system performance, including the low noise preamplifier.

Block recommends that the first stage of the preamplifier be located near the detector, and consist of a pair of matched JFET devices operating at a temperature of approximately 60°K. This temperature can be maintained by self-heating, with the device in a thermally isolated package as close to the detector as possible. This first stage can be either a "source follower" mode or configured to have some gain. The choice depends on the relative noise level of the detector, first stage, and subsequent preamplifier stages. For the relatively low frequency operation contemplated for FIRAS, the predominant noise will be generation-recombination noise in the detector, 1/f noise in the first stage, and possibly some 1/f noise contribution from the detector if the frequency band extends low enough. The JFET devices should be selected for minimum noise in the desired frequency band. Adequate digitization of the detector and preamplifier noise for long periods of time with and without detector bias provides one technique for quantifying this noise. A spectral density measurement analysis can provide relative noise level for the different conditions of bias.

The JFET operating current and voltage should be adjusted to optimize noise performance and minimize heat load. As the input voltage noise for a JFET is inversely proportional to the operating current, the lowest operating current commensurate with an acceptable noise level should be selected. For a high quality matched pair of JFET devices, for example, an operating current of about 200 microamperes is consistent with a voltage noise of less than 5 nanovolts and control of the operating voltage at about 1 volt gives a heat load of about 200 microwatts.

A previous cryogenic interferometer built by Block Engineering used this type of detector preamplifier. A problem encountered with the preamplifier was the cutoff of the JFET devices due to a period at low temperature with power removed. A simple solution for this problem consisted of several forward biased diodes in thermal contact with the JFET devices, arranged to provide conduction if the JFET operating current becomes too low and hence heat the JFETs until normal operation was achieved.

The preamplifier circuit configuration is shown in Figure 3.0-1. This amplifier is of the current of transimpedance type, which has proven advantageous for voltage amplification. The sketch does not show the use of heater diodes, but this is easily developed for a given type of JFET. (They were added after the instrument and drawings were completed.) The figure does show the addition of a GaAs LED to provide for diagnostics and detector bias control. A typical diagnostic possible with this approach is the generation of an artificial signal especially designed to verify system behavior. An indication of frequency response could be produced based on the expected system characteristics, or various computed interferograms could be introduced to the full data system processing. Another application is the demonstration of detector and feedback resistor linearity. The typical Eltek feedback resistor used is distinctly nonlinear with voltage, and this must be measured and compensated to minimize distortion in the interferogram central fringes.

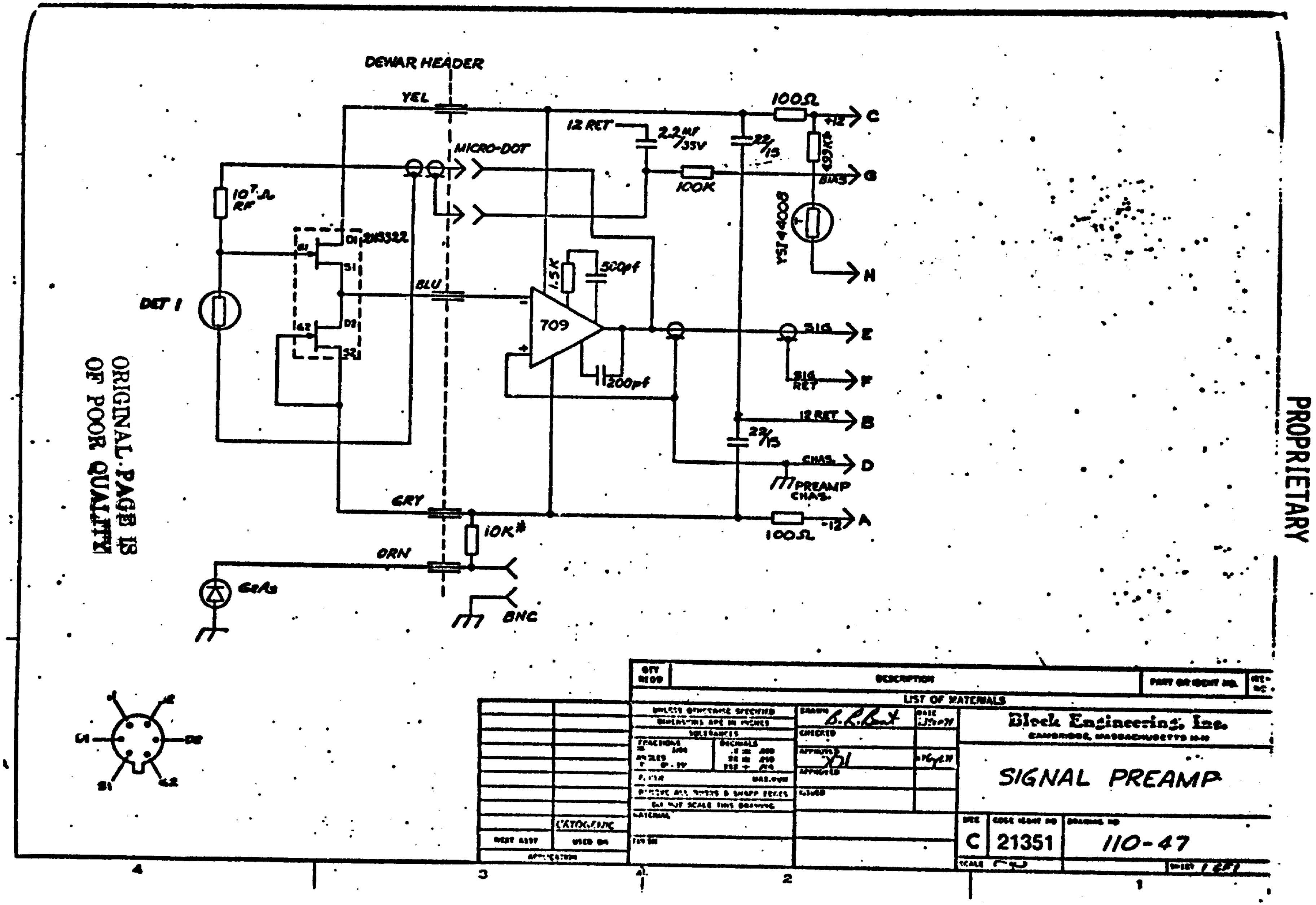

Figure 3.0-1. Preamplifier Circuit Configuration

ORIGINAL PAGE IS
OF POOR QUALITY

3.1 DEGLITCHING

While recent discussions with GSFC personnel indicate that less concern exists regarding the potential introduction of noise due to charged particles, it is still probably worth while to reiterate Block's strategy to minimize this effect. In general, this strategy requires that the signal processing have excess electrical bandwidth over that required for the interferogram, and that each interferogram be compared with the previous interferogram or a weighted average of previous interferograms. A criterium is established to detect the pulse produced by a charged particle(e.g. a pulse five times the rms noise level) and the interferogram data containing the pulse is replaced by "clean" data from the previous interferograms(s). This clearly requires onboard storage and delay capability, and a sampling rate higher than strictly required for the interferogram. The number of samples could be reduced after this process by averaging a number of adjacent samples to produce the desired interferogram sample rate.

4.0 SYSTEM SENSITIVITY

The sensitivity of the FIRAS instrument is fundamentally tied to the sensitivity of the detectors that will be available when the instrument is realized, and at present this can only be estimated. The radiometric stability of the instrument, its throughput and efficiency, its spectrometric capabilities, the accuracy of calibration and its performance as an interferometer all have an impact of the actual sensitivity of the device, and also affect the optimization of the detectors.

4.1 SCIENCE REQUIREMENTS

Although of the greatest intellectual interest and significance, the science requirements affect the instrument design only in determining limits. The need to measure a 3°K blackbody to a part in a thousand results from the possible deviations from the blackbody function that may be detectable at that level of sensitivity. The present state of measurements of the cosmic background is summarized in terms of observational limits in Figure 4.1-1, taken from the Interim Study Report for COBE (1977). Very rough indications have been obtained of the radiation flux using broad and narrow band radiometers (square areas, error bars), which included measurements of the cyanogen lines (CN). Spectral measurements have been made with ground-based and balloon-borne spectrometers (curved line limits), and blackbody curves at various temperatures are indicated (dashed lines). Clearly, the achievement of the FIRAS/COBE mission will go far toward resolving this unsatisfactory state of affairs.

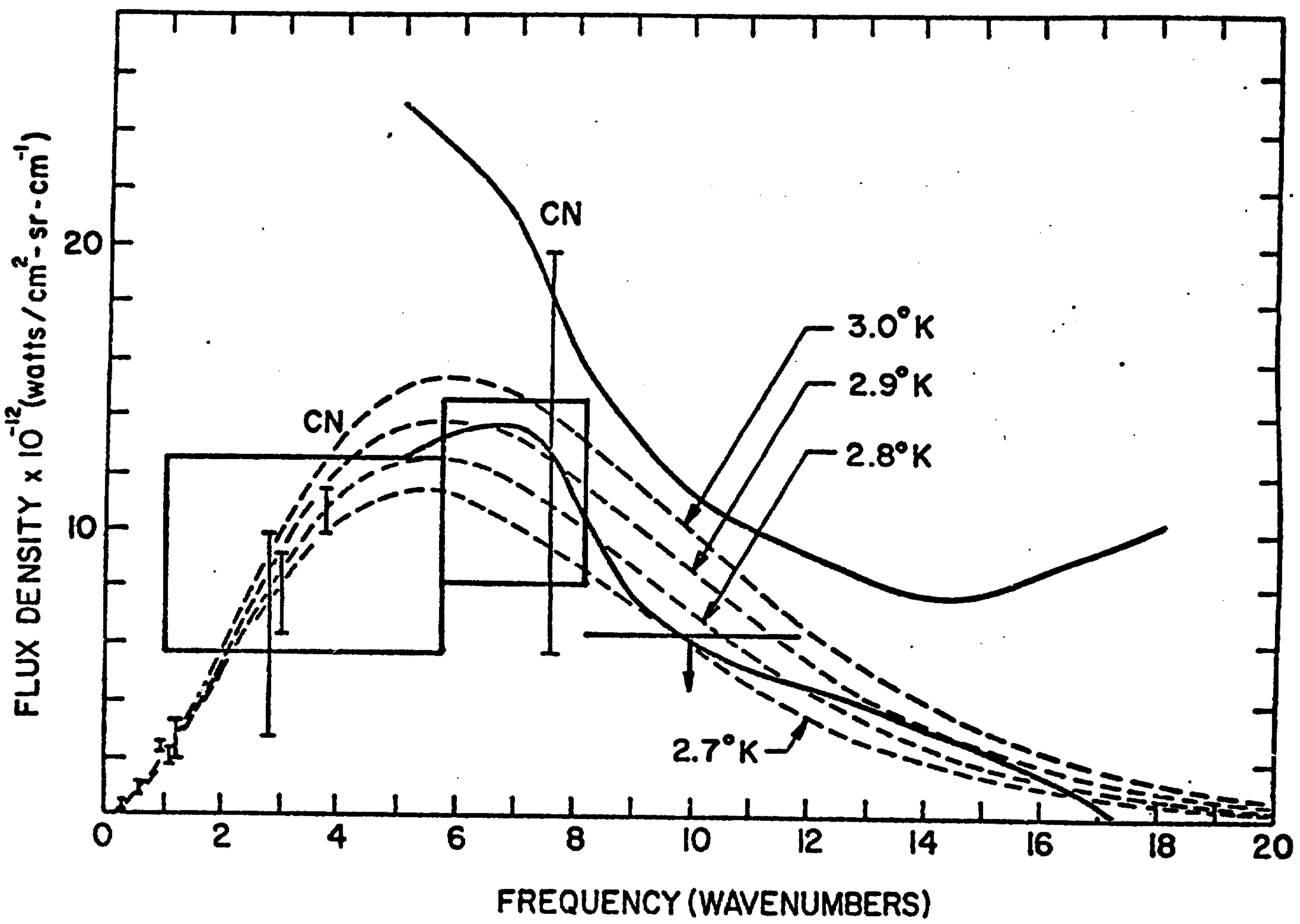

Figure 4.1-1. Observed Limitations to Cosmic Background Radiation

Extension of the spectral response of the FIRAS system to 100 cm^{-1} permits the measurement of interstellar dust, and this measurement is also important in relation to the cosmic background since the spectra overlap somewhat. This is shown in Figure 4.1-2, taken from the same report, where possible interstellar dust emission from the galactic pole is given for two temperatures, and the experimental measurements appear (limit bars, x symbols). The accuracy of measurement in the FIRAS is not quite adequate to relate to the isotropy determinations made by the microwave radiometers on COBE, but the spectral range will overlap the relate to the diffuse infrared background measurements made by the DIRBE instrument, after adjustment for the larger FIRAS field of view.

4.2 RADIOMETRIC PERFORMANCE

The sensitivity of the FIRAS instrument is given in terms of the noise equivalent spectral radiance, NESR, through the relation

$$\mathrm{NESR} = \frac{\mathrm{NEP}}{A\Omega\eta\Delta\nu t^{1/2}} \quad \mathrm{watts/cm^2\text{-}sr\text{-}cm^{-1}} \qquad (4.2\text{-}1)$$

where

NEP: Detector noise equivalent power, watts/$Hz^{1/2}$

$A\Omega$: Instrumental throughput, cm^2-sr

η: Instrumental efficiency

$\Delta\nu$: Spectral resolution, cm^{-1}

t: Integration time, seconds.

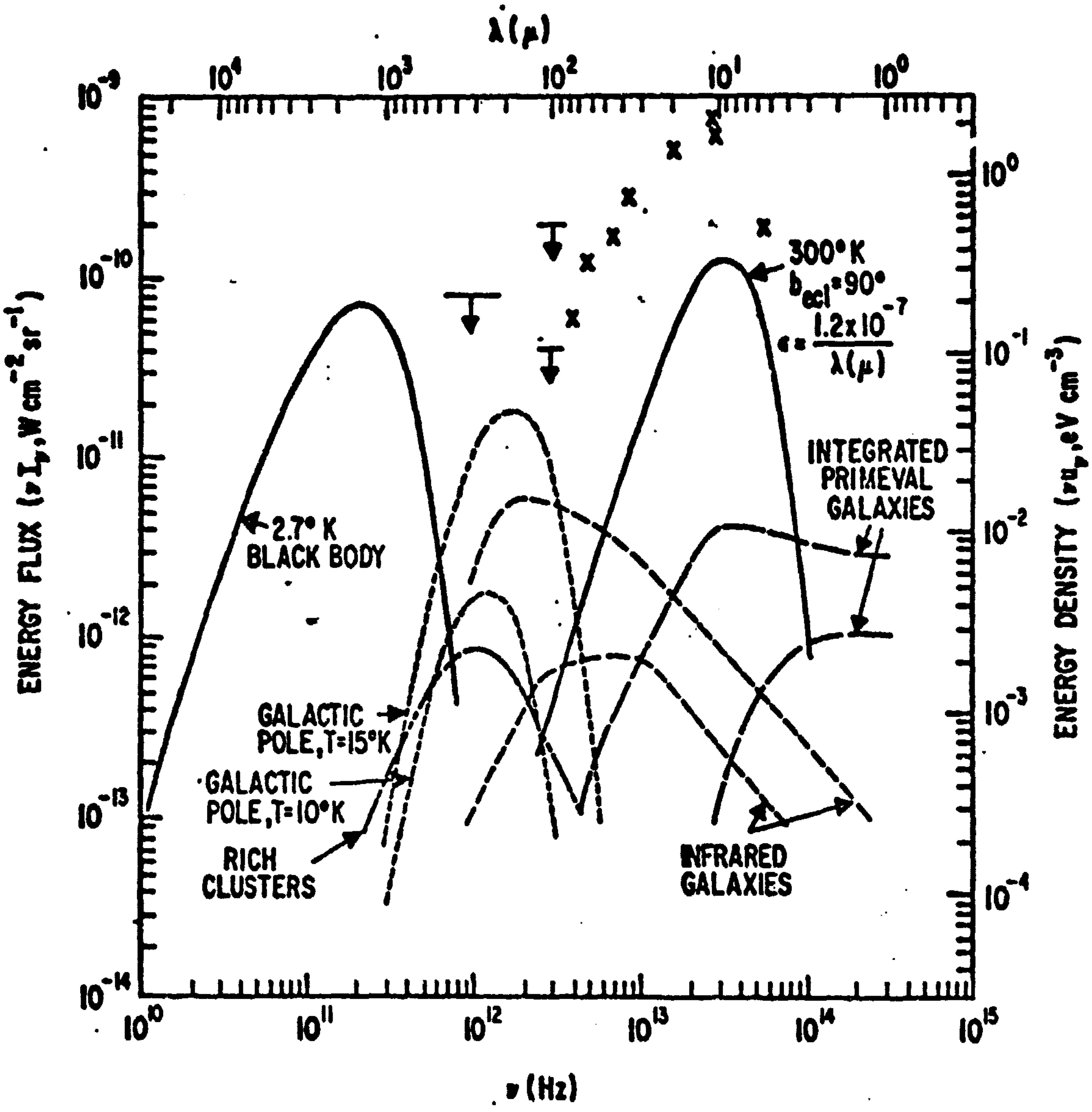

Figure 4.1-2. Estimated Diffuse Radiation Fluxes.

Detection of one-thousandth of the peak radiance expected from the cosmic background requires that the instrument should be capable of 1.5×10^{-15} watts/cm^2-sr-cm^{-1} over as much of the spectral range from 1 to 20 cm^{-1} as possible, and certainly over the range from 2 to 20 cm^{-1}.

Emission from the interstellar dust extending to 100 cm^{-1} (100μm) may be from one to two orders of magnitude higher, and the detection sensitivity could be correspondingly poorer, except that it is desirable to evaluate the transition region near 20 cm^{-1}, where roughly comparable sensitivities would be necessary .

4.2.1 Instrumental Throughput

As indicated, the basic instrumental throughput for FIRAS is 1.5 cm^2-sr, as defined by the sky input horn. Some distortions in the throughput occur internally but the mixing of the input optics tend to redistribute these distortions as referred to the input. Incomplete coupling at the detector and diffraction losses at the edges of the beam are effectively blurred and shifted so that the instrumental field of view is apparently attenuated, with only slight loss in beam uniformity. Consequently, these distortions are treated as losses in instrumental efficiency, and will be estimated in the next section. The losses are localized to the transfer mirror and output coupling cone (diffraction) and to the detector cavity (incomplete coupling).

4.2.2 Instrumental Efficiency

Inefficiencies in the optical train arise from absorption, scattering, diffraction, and vignetting. In addition, the interference of radiation is affected by geometric factors, so that significant optical distortion or misalignment of radiation fields can result in a modulation efficiency below that which can be predicted on the basis of optical efficiency along. Tables 4.2.2-I and 4.2.2-II show the complete breakdown of instrumental efficiency factors on a component level, considered for normal and superconducting reflective surfaces respectively. Some diffraction loss was assumed for the sky input horn, the transfer mirror, and the output coupling cone at 1.0 cm, as each of these has some aspect in which diffractive loss is possible. Some scattering loss is assumed for the beamsplitters at 100 microns, although it is hoped that the wire spacings will be close enough so that scattering is not significant in the desired spectral band. Some vignetting is also assumed at the output coupling cone due to blurring of the pupil at the imaged transfer mirror. An efficiency of 0.6 to 0.8 is assumed for the detector cavities, since the cavity is presumably different for the 100 cm^{-1} detector. It is probable that the efficiency of the cavity will depend strongly on the diffraction at 1.0 cm^{-1}, and so this estimate may be difficult to achieve without going to a resonant cavity that will probably be less efficient at 10 cm^{-1}. The dichroic beamsplitters are assumed to be optimized for transmission at the longer wavelengths.

TABLE 4.2.2-I

Normal Instrumental Efficiency

Component	Spectral Frequency		
	$1.0\ cm^{-1}$	$10\ cm^{-1}$	$100\ cm^{-1}$
Sky Input Horn	0.80 (d)	0.99	0.99
Input Coupling Cone	0.99	0.99	0.99
Folding Mirror (2)	0.98	0.98	0.97
Transfer Mirror (2)	0.80 (d)	0.98	0.97
Polarizing B/S (2)	0.95	0.93	0.90 (s)
Collimator (2)	0.98	0.98	0.97
Input/Output B/S (2)	0.95	0.93	0.90 (s)
Dihedral mirrors (2)	0.98	0.98	0.97
Detector Mirror	0.98	0.98	0.97
Dichroic B/S	0.95	0.80 (t)	0.90 (s)
Output Coupling Cone	0.85 (d,v)	0.95 (v)	0.95 (v)
Detector Cavity	0.70 (nv)	0.60 (nv)	0.80 (nv)
Detector	0.70	0.75	0.80
Modulation Efficiency	0.99	0.97	0.95
Michelson Efficiency	0.50	0.50	0.50
Conversion Efficiency	0.71	0.71	0.71
Overall Efficiency	0.05	0.07	0.09

s: Scattering significant
d: Diffraction significant
v: Vignetting significant; nv: Radiation lost around detector
t: Transition at $20\ cm^{-1}$

TABLE 4.2.2-II

Superconducting Instrumental Efficiency

Components	Spectral Frequency		
	$1.0\ cm^{-1}$	$10\ cm^{-1}$	$100\ cm^{-1}$
Sky Input Horn	0.82	1.00	1.00
Input Coupling Cone	1.00	1.00	1.00
Folding Mirror (2)	1.00	1.00	1.00
Transfer Mirror (2)	0.82 (d)	1.00	1.00
Polarizing B/S (2)	0.96	0.94	0.91 (s)
Collimator (2)	1.00	1.00	1.00
Input/Output B/S (2)	0.96	0.94	0.91 (s)
Dihedral Mirrors (2)	1.00	1.00	1.00
Detector Mirror	1.00	1.00	1.00
Dichroic B/S	0.96	0.81 (t)	0.91 (v)
Output Coupling Cone	0.87 (d,v)	0.96 (v)	0.96 (v)
Detector Cavity	0.72 (d,v)	0.62 (nv)	0.82 (nv)
Detector	0.70	0.75	0.80
Modulation Efficiency	0.99	0.97	0.95
Michelson Efficiency	0.50	0.50	0.50
Conversion Efficiency	0.71	0.71	0.71
Overall Efficiency	0.08	0.10	0.13

s: Scattering significant
d: Diffraction significant
v: Vignetting significant; nv: Radiation lost around detector
t: Transition at 20 cm^{-1}

The modulation efficiency is based on realistic efficiencies achieved with large throughput systems within the obliquity capabilities of the instrument. This is basically an estimate of how accurately the instrument operates relative to the wavelength of measurement, and the values are typical for a well designed instrument. The conversion efficiency is a term relating the constant radiance detected to the equivalent r.m.s. signal that is actually processed in the interferogram. This is a different factor than that implicit in the expression given in Section 4.2 for the NESR, which relates the deconvoluted noise bandwidth to the integration time. The factor is 0.71 rather than 0.35 because the polarizing interferometer does not produce the constant term in the output that is typical of the normal Michelson interferometer. The Michelson efficiency is simply the basic term describing the division of the output radiation between two detectors, and the improvement possible (1.41) in combining the detector outputs is not included.

The overall efficiency for the system averages 0.07 with normal reflecting surfaces and 0.10 with superconducting surfaces. This level of improvement is not really significant enough to warrent going to superconducting surfaces in most of the optics. As we have seen, however, the effective emissivity of the reference and calibrator blackbody sources is more significantly affected by using superconducting surfaces. If the development of superconducting coatings is undertaken and the resultant cost is within reasonable bounds, it could be utilized throughout the system.

4.2.3 Spectral Resolution

The output interferogram represents a truncated measurement function which is frequently modified by an artificial instrumental profile through the process termed apodization. The spectral resolution of the measurement is consequently determined by the nature of this apodization, which is used to avoid the artifacts (Gibbs phenomena) produced by the truncated function after transformation. If that function effectively becomes zero at both the beginning and the end of the scan, there is no need to apodize since the truncation error producing the artifacts is within the instrumental noise. If no narrow spectral features are present in the measured cosmic background, this will be the case, and the unapodized spectral resolution is given by

$$\Delta\nu = \frac{1}{2B} \quad \mathrm{cm}^{-1} \qquad (4.2.3\text{-}1)$$

where B is the retardation offset. The physical motion of each dihedral mirror set along the optical axis is one quarter of this motion, operating in opposition. A motion of 1.25 cm by each set produces a spectral resolution of 0.1 cm^{-1} in this way, but the system is capable of twice this motion. In the event that significant apodization is necessary, the additional motion will permit a spectral resolution of 0.1 cm^{-1} in this mode as well. With triangular apodization, the spectral resolution is

$$\Delta\nu = \frac{1}{B} \ \mathrm{cm}^{-1} \qquad (4.2.3\text{-}2)$$

and intermediate resolutions arise from other common apodizations.

In general, the spectral resolution required to resolve the expected cosmic background spectra is about 1.0 cm^{-1}. High resolution to 0.05 cm^{-1} (unapodized) is available for periodic measures of the stronger short wavelength interstellar dust emission.

4.2.4 Integration Time

The integration time adopted for these measurements is 3×10^4 seconds, or 8.33 hours, which is the average time devoted to each field of view. Since each orbit is 100 minutes in duration, and the instrument rotates once during each orbit, each 7° field of view passes in less than 2 minutes. The orbit itself precesses at about 1° per day, so that in about seven days the orbit has moved over by one field of view width. The orbit covers the entire spatial sphere twice in the year period, and the polar points are much more frequently observed. The minimum integration time is for the points in the plane of the earth's orbit, amounting to 2.4×10^4 seconds.

4.2.5 Sensitivity

Using the above indicated parameters, we can compute the FIRAS sensitivity. The average sensitivity is

$$\mathrm{NESR} = \frac{1 \times 10^{-14}}{1.5 \times 0.07 \times 1.0 \times (3 \times 10^4)^{1/2}} \tag{4.2.5-1}$$

$$= 5.5 \times 10^{-16} \text{ watts/cm}^2\text{-sr-cm}^{-1},$$

which is a factor of three better than that required. For the worst case field of view (earth orbit plane), the sensitivity is

$$\text{NESR} = 6.2 \times 10^{-16}\ \text{watts/cm}^2\text{-sr-cm}^{-1}, \qquad (4.2.5\text{-}2)$$

The peak signal-to-rms noise in a single interferogram taken at 1 cm/sec retardation rate can be computed for an unbalanced 3°K blackbody source. The single interferogram sensitivity is

$$\text{NESR} = 6.7 \times 10^{-14}\ \text{watts/cm}^2\text{-sr-cm}^{-1} \qquad (4.2.5\text{-}3)$$

where two seconds is required for the double-sided interferogram. The interferogram signal-to-noise is then

$$\begin{aligned} S/N &\cong \frac{1.5 \times 10^{-12}}{6.7 \times 10^{-14}} \quad (10)^{1/2} \qquad (4.2.5\text{-}4) \\ &\cong 71 \end{aligned}$$

for the long wavelength channel, where ten 1 cm^{-1} spectral increments are presumed to contain the energy. If the instrumental self-cancellation of radiation is effective in reducing the 3°K signal by 1/100, the resulting interferogram signal-to-noise is less than one, and digitization of the noisy signal must extend lower by a factor of at least ten.

5.0 MECHANICAL DESCRIPTION

The mechanical design is provided through the assembly drawing, BE 950272, a separate roll (J size) drawing. This drawing has been prepared consistent with the configurational and environmental constraints provided by the Science Team, and with good engineering design practice based on Block experience in aerospace equipment. The basic structure consists of two open bulkhead plates connected by cylindrical tube structures parallel to the primary instrument optical axis and the direction of launch acceleration. This approach is, we believe, minimal in mass while providing maximum structural strength and thermal equalization where it is needed. The principle of absolute design symmetry has been followed throughout.

5.1 INSTRUMENT CONFIGURATION

The FIRAS instrument mounts between two bulkhead plates which connect directly to the COBE instrument support frame, which in turn is bolted to the lower flange in the COBE dewar. The sky input horn, with the calibrator plate assembly, and the reference blackbody horn extend upward from the upper bulkhead as essentially free-standing structures. They can only be connected to the upper part of the instrument support frame in a manner that permits differential thermal expansion to take place between these structures. The entire lower structure is made of aluminum, with few exceptions, matching the thermal expansion coefficient of the support frame closely, and avoiding alignment and focusing errors in the aluminum optical components. This structure is shown in Figure 5.1-1 (side view) and Figure 5.1-2 (bottom view).

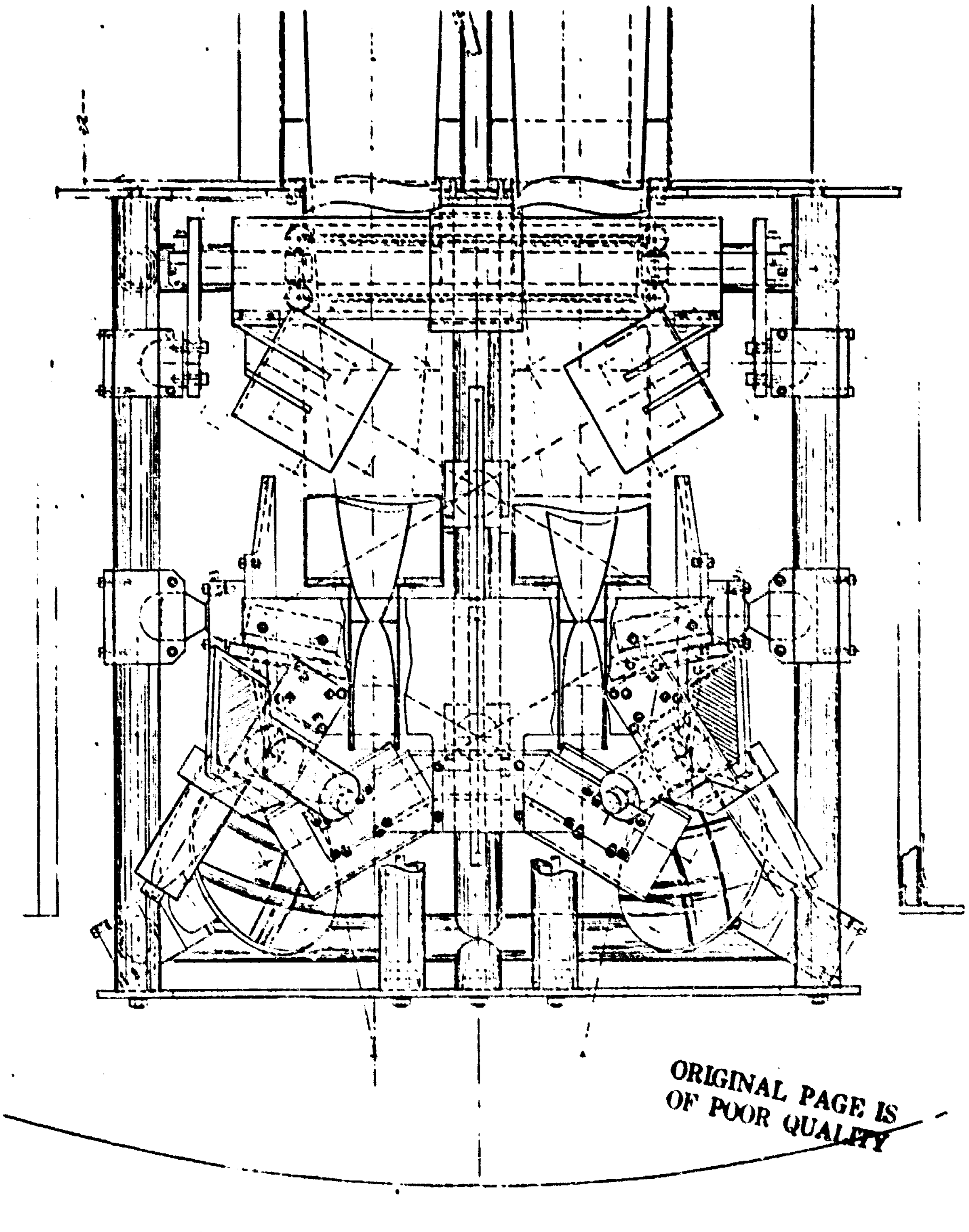

Figure 5.1-1. Instrument Mechanical Configuration, Side View

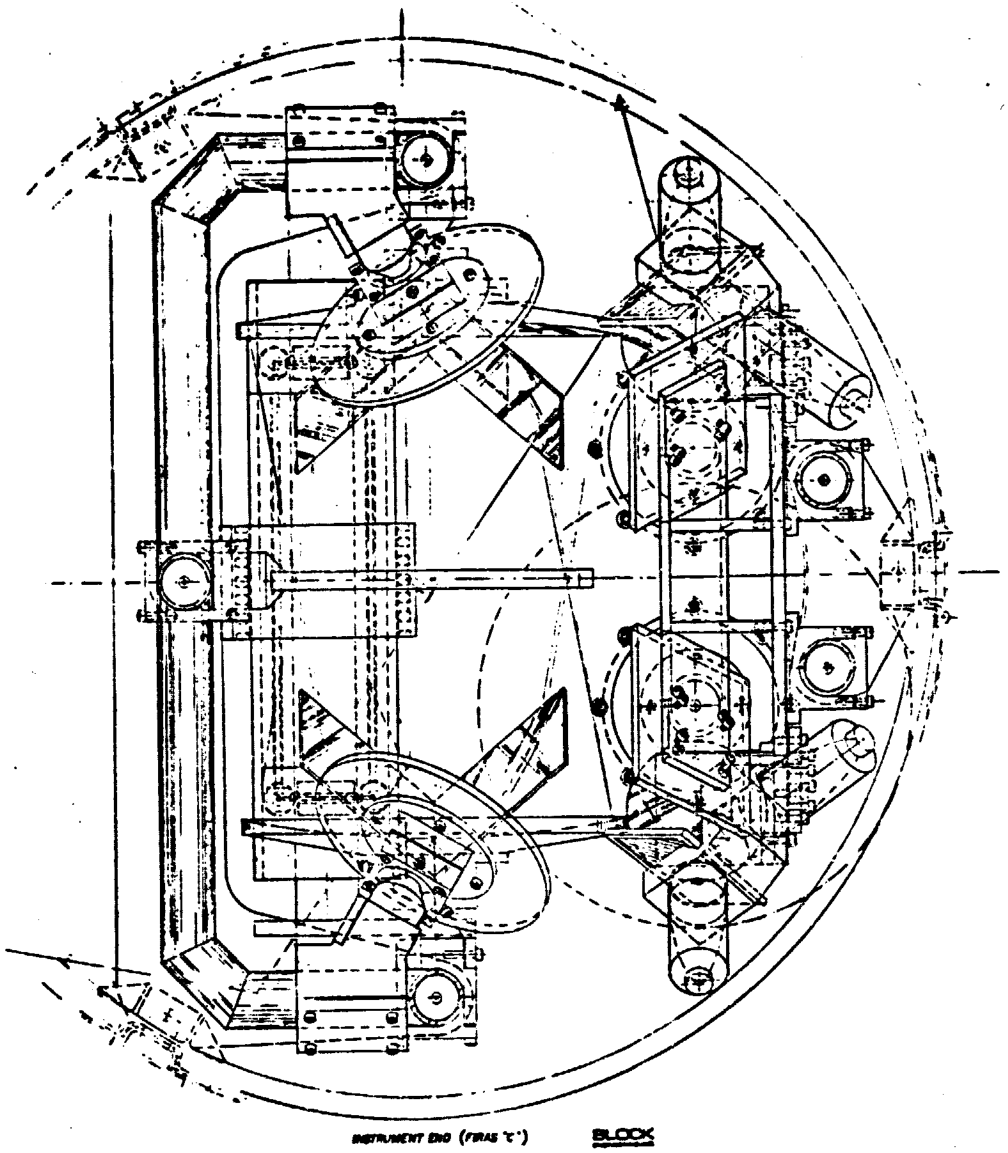

Figure 5.1-2. Instrument Mechanical Configuration, Bottom View

Virtually all optical components are attached to the FIRAS structure with adjustable thermally conductive mounts of extremely rugged character, permitting complete alignment and testing of the system at cryogenic temperatures before all mounts are injected with thermally conductive epoxy and locked into position. Optical components are generally coupled together in symmetrical sets through thermal conductance paths, and detectors are thermally tied to the COBE dewar flange using special straps (not shown in the drawing). The minute power dissipated by the interferometer drive motor passes mainly to the upper bulkhead and hence to the dewar, thus avoiding significant heating of the optics.

Two mechanisms are present in the FIRAS design, the calibrator insertion mechanism and the interferometer drive motor, An entirely new calibrator mechanism is presented which offers many advantages, and avoids all problems present in earlier designs. The interferometer drive motor utilizes the roller bearing and the linear magnetic motor technique to provide essentially frictionless operation with utter reliability.

Table 5.1-I lists all system components in the FIRAS C design, indicating material, quantity, volume, mass, and total heat at 293°K It is noted that the total mass of the system is 40 kg, which exceeds the limit given in the subject statement of work. The masses have been obtained for all structural components with only nominal lightening by opening and thinning uncritical structures. Significant decrease in mass is possible, but we believe that it is unlikely that the mass can be reduced to 20 kg and still maintain structural integrity under all conditions anticipated. Further reduction in weight will be possible in preparation of detailed component drawings, under engineering supervision.

TABLE 5.1-I

FIRAS C SYSTEM COMPONENTS

Item	Mat'l	Qty	Tot Vol	Tot Mass	Tot Heat (293°K)
Structure			(cm^3)	(kg)	(joules)
Bulkheads	Al	2	723	1.95	1.56×10^4
Tubes, vertical	Al	5	1023	2.76	2.20×10^4
Tubes, horizontal	Al	2	443	1.20	9.55×10^3
Tube rods, vertical	Al	5	104	.28	2.24×10^3
Input Optics					
Sky horn	Ni	1	182	1.62	6.32×10^3
Ref horn	Ni	1	146	1.30	5.07×10^3
Ref blackbody plate	Al	1	369	1.00	7.95×10^3
Sky horn cylinders	Ni	1	273	2.43	9.50×10^3
Ref horn cylinders	Ni	1	183	1.63	6.35×10^3
Calibrator	Al	1	201	.54	4.33×10^3
Calibrator Mtg plate	Envex	1	400	.61	7.20×10^3
Calibrator cavity	Envex	2	1488	2.27	2.68×10^4
Calibrator mtg top	Envex	1	447	.68	1.22×10^4
Calibrator mtg bot	Envex	1	422	.67	7.60×10^3
Calibrator side plt	Envex	2	643	.97	1.16×10^4
Horn flare support	Envex	1	170	.26	3.06×10^3
Eccosorb Flare	Ecco.	1	76	.35	1.00×10^3
Motor, bearing, shafts	Mixed	est	200	1.78	6.94×10^3

TABLE 5.1-I (continued)

Item	Mat'l	Qty	Tot Vol	Tot Mas	Tot Heat (293°K)
Internal Optics			(cm^3)	(kg)	(joules)
Collimator mirrors	Al	2	646	1.75	1.39×10^4
Transfer mirrors	Al	2	472	1.27	1.02×10^4
Flat mirrors	Al	2	130	.35	2.80×10^3
Detector mirrors	Al	2	158	.43	3.40×10^3
Dichroic beamsplitters	Al	2	72	.19	1.55×10^3
Beamsplitters	Al	2	177	.48	3.81×10^3
Output cones/cavity	Mixed	2	35	.31	1.16×10^3
Mirror mtg block, sm	Al	6	416	1.12	8.95×10^3
Mirror mtg block, lg	Al	4	390	1.06	8.40×10^3
Mirror mtg rods/balls	Al	4	214	.58	4.61×10^3
Mirror ball bkt	Al	4	316	.86	6.80×10^3
Output optic mtg bkt	Al	1	450	1.22	9.69×10^3
Flat mirror mtg bkt	Al	1	112	.30	2.41×10^3
Detector cone mtg bkt	Al	2	360	.97	7.78×10^3
Mount support	Al	2	96	.26	2.07×10^3
Detector Mirror mtg	Al	2	200	.54	4.31×10^3
Dihedral Mirrors/Drive					
Dihedral mirrors /mtg	Al	2	356	.96	7.67×10^3
Mirror support tube	Al	1	470	1.27	1.01×10^4
Rollers	Envex	8	76	.12	1.37×10^3
Retainer tubes	Al	4	27	.07	5.3×10^2
Retainer blocks	Al	8	33	.09	7.1×10^2
Motor drive shaft	Al	1	332	.90	7.10×10^3
Drive supprt bkg	Al	2	116	.31	2.50×10^3
Drive plates	Fe	4	72	.64	2.52×10^3
Magnet plates	Fe+	2	100	.89	3.50×10^3
Pole Pieces	Fe	2	100	.89	3.50×10^3
				40.13	2.966×10^5

5.1.1 Input Optics

The sky and reference horns are electroformed structures, fitted with ribs and encased in cylindrical support structures. The horns are primarily nickel, as are the support cylinders, and with differential contraction, the exposed end of the horn extends by 0.15 cm in cooling down relative to the aluminum instrument frame. The support cylinders may also be electroformed or they can be made of sheet stock, with open areas included to lighten them, and they can be soldered or welded to the horns along the ribs. The horns extend through the bulkhead, leading to the input coupling cones that are included in this assembly. The input coupling cone aperture extends by about 0.05 cm in cooldown relative to the rest of the optical system, but this can be determined and offset in alignment. Figure 5.1.1-1 and 5.1.1-2 show the mechanical configuration for these components.

5.1.2 Reference Blackbody Source

The reference blackbody cuts the cylinder at 15°, consisting of a metal support ring/plate, with source area heater sandwiched between it and the blackbody mounting plate. If the superconducting horn is used, the metal support ring contains an insulating space under a thin metal cover sheet, as shown. If a normally conducting horn is used, the metal support plate is a continuous structure across the back of the horn, and the horn is heated with the source by area heaters. The blackbody area heaters are commercially available nichrome wires imbedded in silicone rubber sheets with adhesive on one (or both) sides. The blackbody mounting plate is a metal plate machined with ribs to allow a good attachment surface for the Eccosorb MF-110 material, which is cast onto the plate and machined with V-grooves running

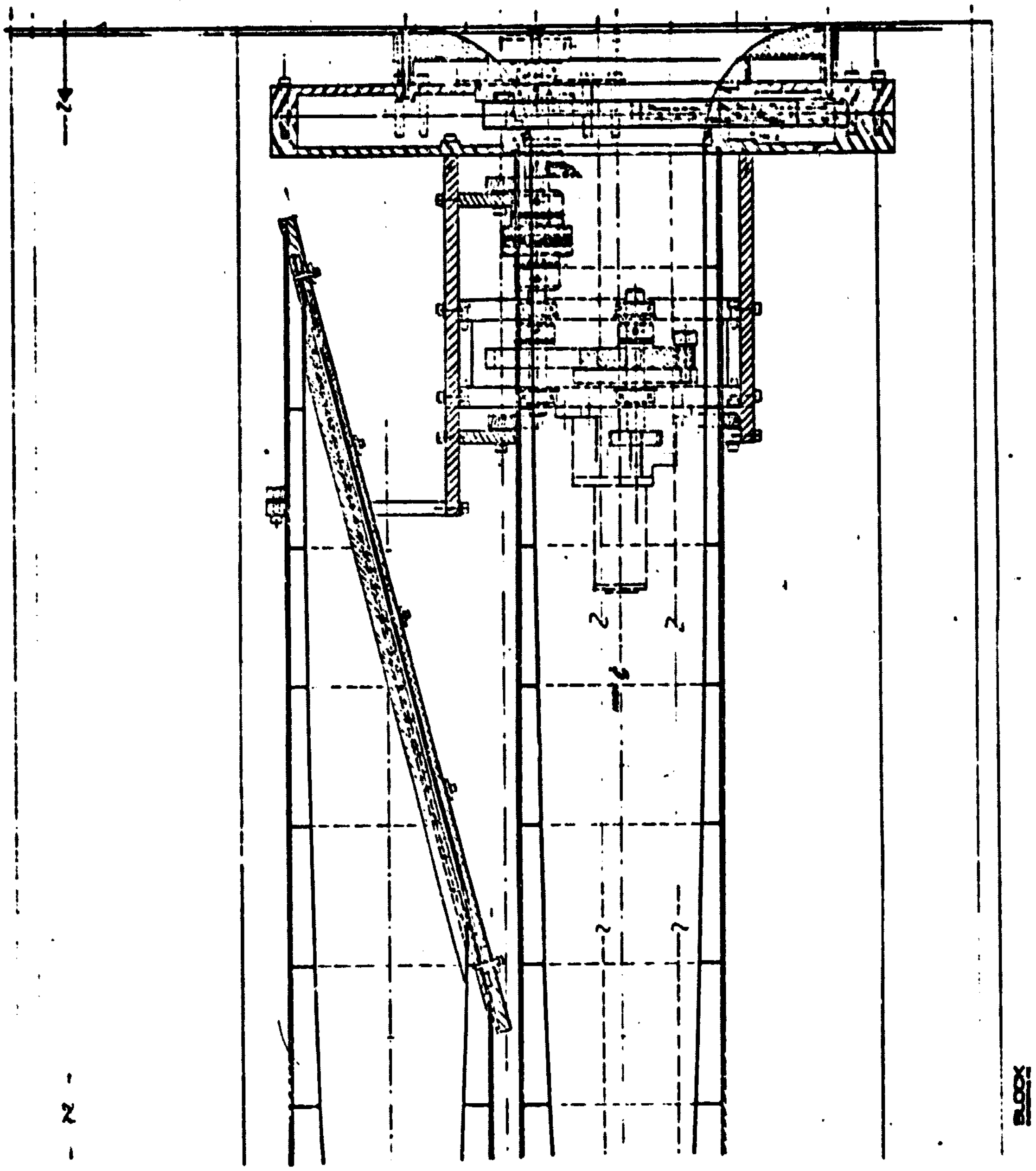

Figure 5.1.1-1. Input Optics Mechanical Configuration, Side View

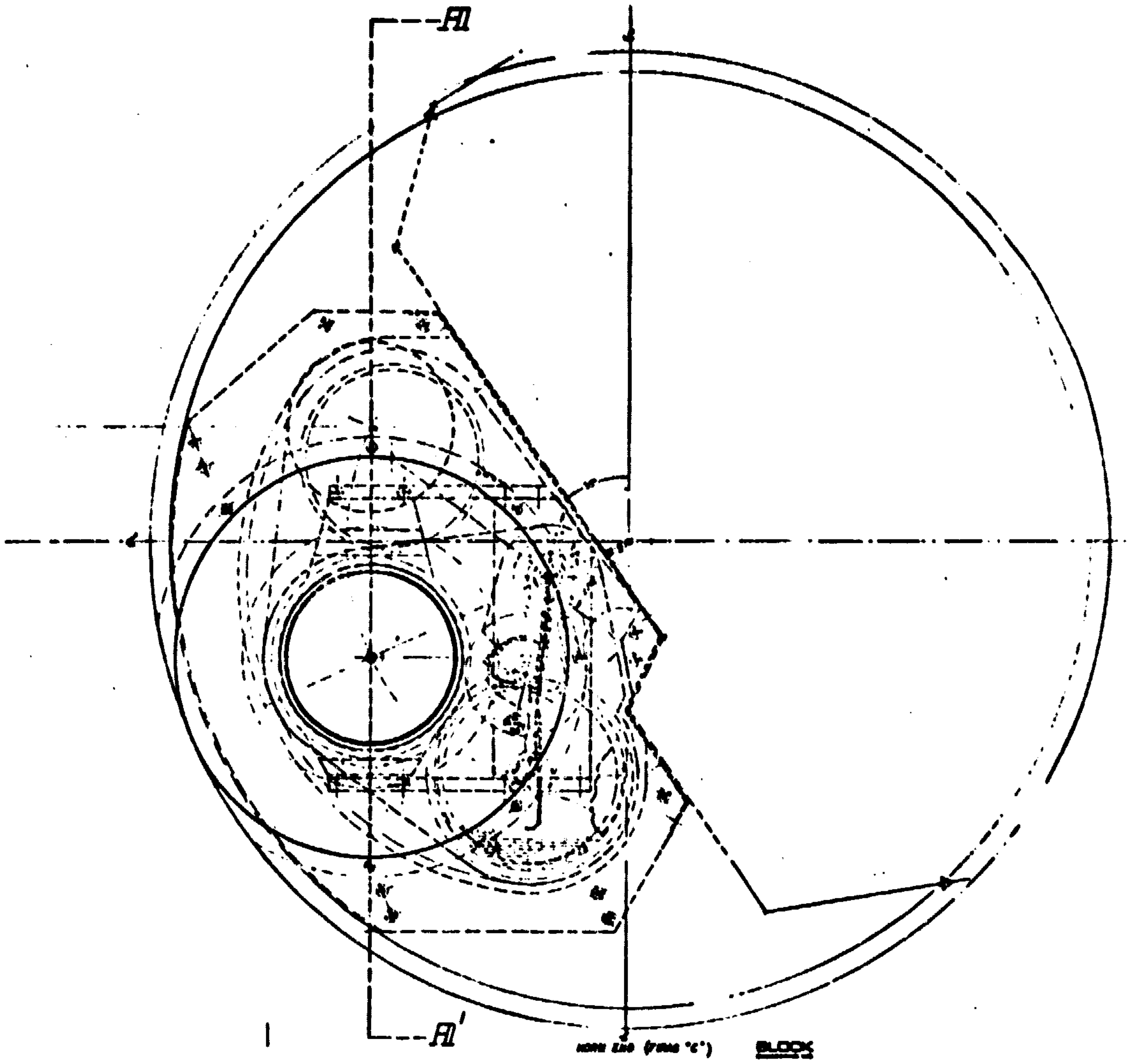

Figure 5.1.1-2. Input Optics Mechanical Configuration, Top View

parallel to the long dimension of the plate. Four temperature sensors are set into this plate to provide an accurate average temperature for the source. The mounting of the horns to the bulkhead is done so that differential thermal expansion can take place (0.007 cm relative to the horn centerline), probably using a thin teflon interface strip to permit the motion and to provide centering. If the entire horn is heated, this strip is thickened to give greater thermal isolation.

5.1.3 Calibrator Mechanism

The sky input horn entrance aperture must merge smoothly into the Eccosorb flare cast and machined in a metal plate structure extending beyond the calibrator mechanism. The calibrator, shown in Figures 5.1.1-1 and 5.1.1-2, consists of a plate with two apertures in it, one containing the calibrator blackbody source and the other an opening edged with Eccosorb, arranged so that a single rotation brings either aperture into position.

This approach does not enter the space above the instrument at all, and permits calibration to be checked with the FIRAS instrument detached from the instrument support frame exactly as when mounted. The calibrator is held within a thermally isolated cavity when it is not being viewed, and only its reflective back surface is ever exposed to space. Its insertion involves only a single rotary motion over an angle less than 180°. Although the integrity of the flare is interrupted, the actual gaps can be kept to 0.01 cm, and these gaps extend into a cold chamber. The opening edged with Eccosorb is slightly undersized to allow for the positioning tolerance, which should also be on the order of 0.01 cm.

At longer wavelengths, the flare is virtually unaffected, since this understep in the surface is only a fraction of a wavelength. At shorter wavelengths, the remaining part of the flare is more than sufficient for suppression of the sidelobe, and the understep is out of view of geometric beam. The temperature of the understepped ring can be controlled by use of a metal ring insert behind the Eccosorb, which is thermally strapped using a flexible cable through the insulating calibrator plate to the flare structure or equivalent temperature point.

Most important, however, is that the calibrator source must be located next to the metal end of the sky horn to avoid serious compromise of its blackbody emission character through reflection of the uncontrolled flare thermal emission by the calibrator surface. This is sufficient reason to reject any approach that places the calibrator at any high position on the Eccosorb, flare, which is inevitable with the external calibrator techniques. It is desirable to make the small section of the flare below the calibrator of reflective metal to avoid introducing diffracted energy at short wavelengths, but we believe that the position selected is a reasonable compromise between suppression of long wavelength diffraction sidelobes and rejection of short wavelength diffraction from the calibrator gaps.

The calibrator source is similar to the reference blackbody source, consisting of a metal backing, area heaters, a mounting plate ribbed to hold Eccosorb material reliably, and finally the Eccosorb surface itself, cut with V-grooves or pyramid structures. A high temperature center spot source has been included, separating a central 2-3 cm diameter area from the rest, and using a thin teflon layer to isolate it from the main calibrator body.

The area heater must have a corresponding hole in it, and a small area heater is used for the spot. The hot spot has a single temperature sensor mounted on it, while the rest of the calibrator source uses four temperature sensors to give an accurate average temperature. All wires are returned through the central calibrator mounting pivot, and constitute the most significant part of the thermal conduction from the calibrator sources.

There are many mechanisms which can rotate a plate at low angular velocity through an appropriate angle. Positioning of the plate after the rotation is another matter. A geared down motor turning to fixed mechanical stops, with a continual low torque left in the motor at all times will guarantee that the rotated device stays at the stop position without bouncing or drifting away. A worm gear drive will achieve this in a similar way, but even in this case power must be kept on slightly to prevent drifing from the end stop. Another method used is that of positional feedback to a servo amplifier, measuring from a potentiometer or a shaft encoder. This is also an active system, leaving low power on when accurate position must be maintained.

Several absolutely quiescent techniques are possible. In general, these require the use of a spring lock, which requires additional power in resetting for renewed operation. The technique suggested here does not, but obtains locking with a broad mechanical tolerance for the rotation "stop" positions. This device is the Geneva mechanism, often used by Block in accurate positioning of aperture stops. Although at first examination it is not clear that this is very reliable and trouble-free mechanism, Block has found it so in many years of field experience. It must be correctly configured, of course, but this is straightforward and uncomplicated. In the present design, only two positions are needed with 60° rotation angle, as shown in the drawing. The near-sliding fit between the crescent and the Geneva plate requires use of a rigid teflon-loaded plastic such as Vespel SP-211* for one of the two pieces, at least for the contracting surface. Since the plastic has a relatively large expansion coefficient#, it is desirable that its dimensions be limited, and this is best achieved by using it in the smaller crescent and in the associated cam runner. The Geneva plate and shafts can be made of steel, and a steel frame holds these components in alignment. The error produced in the positioning of the open aperture is less than ±0.02 cm with a crescent made of plastic secured to a steel structure.

The calibrator plate and its support structure must be made of the same material and since the calibrator slides within its cavity, the adjoining surfaces must be arranged with a sliding plastic layer to maintain separation, or the entire structure can be made of plastic. The drawing shows a calibrator cavity structure made of the Vespel or similar plastic, which provides excellent thermal isolation for the calibrator although it is somewhat bulky. The use of metal in this structure allows better dimensional control, and nickel is preferred to match the horn material, but appropriate plastic isolators must be used to give

---

* Dupont Company, Wilmington, Delaware

\# 54×10^{-6}/°C at 20°C

the calibrator a reliable time constant through the strap thermal conductors. No attempt is made to control the temperature of the calibrator support plate, but the cavity walls are thermally strapped to the support structure (strapping is not shown in the drawing).

5.1.4 Internal Optics

Block recommends that the entire internal structure except for the output coupling cones and the drive motor be made of aluminum, probably 6061T-6 or an equivalent. This has the effect of making the design free from thermal dimensional variations as long as the structure is essentially isothermal. The optical train is mounted on the five vertical tubes connecting the bulkheads and two C-shaped tubes connecting horizontally. These tubes are welded to the vertical tubes, which in turn are secured by bolts to the bulkheads, although it would be desirable to weld these connections once the structure is assembled to insure good thermal continuity. The bulkheads, which are shown only in the side view of the drawing, are largely open structures, but the instrument is shielded from the upper horns, calibrator, and DIRBE emissions by covering the open areas with thin metal foil. It would be most desirable if the COBE instrument support frame had mounting lugs at the two bulkheads, but if this is not possible, auxilliary mounting plates can be used as shown in the drawing (instrument end). The lower bulkhead actually lies slightly below the COBE dewar mounting flanges as indicated in the side view, and connection to these is made through sturdy brackets welded to the tubes.

5.1.5 Interferometer Drive

The interferometer dihedral mirror assembly is moved linearly back and forth about the central symmetrical position by a linear magnetic motor. Figure 5.1.5-1 shows the original assembly configuration provided with the FIRAS A conception. Discussions with Science Team members brought out the concern that the dihedral mirror sets were cantilevered too much, and they have been pulled in closer to the support tube in the FIRAS C design.

The motor is built around a linear bearing utilizing straight rollers on four sides of a square drive shaft. This bearing has been selected after consideration of a wide variety of alternative designs, including sliding bearings, ball bearings, flex pivots, hinge pivots, and magnetic bearings. The nature of the linear motor proposed is such that power dissipation only arises from friction in the bearing and from hysteresis losses in the magnetic material, which are very small. Thermal emission from the dihedral is also less significant than from certain other optical elements. Consequently, although thermal transfer through the bearing is desirable, it is not the dominant consideration. Uniformity of motion at all scan velocities is of great importance in achieving the instrument goals, but the overriding factor in our considerations has been long term reliability.

Block originally developed the tubular sliding bearing for interferometric applications, and extended this type of design to cryogenic vacuum applications with success. In our original proposal for FIRAS, Block recommended loosely fitting sliding bearings, based on new plastic materials available. Sliding bearings operate well at moderate to high velocities, but even PTFE-loaded materials show chattering at very low velocities, despite the fact that the static and dynamic friction coefficient are near identical.

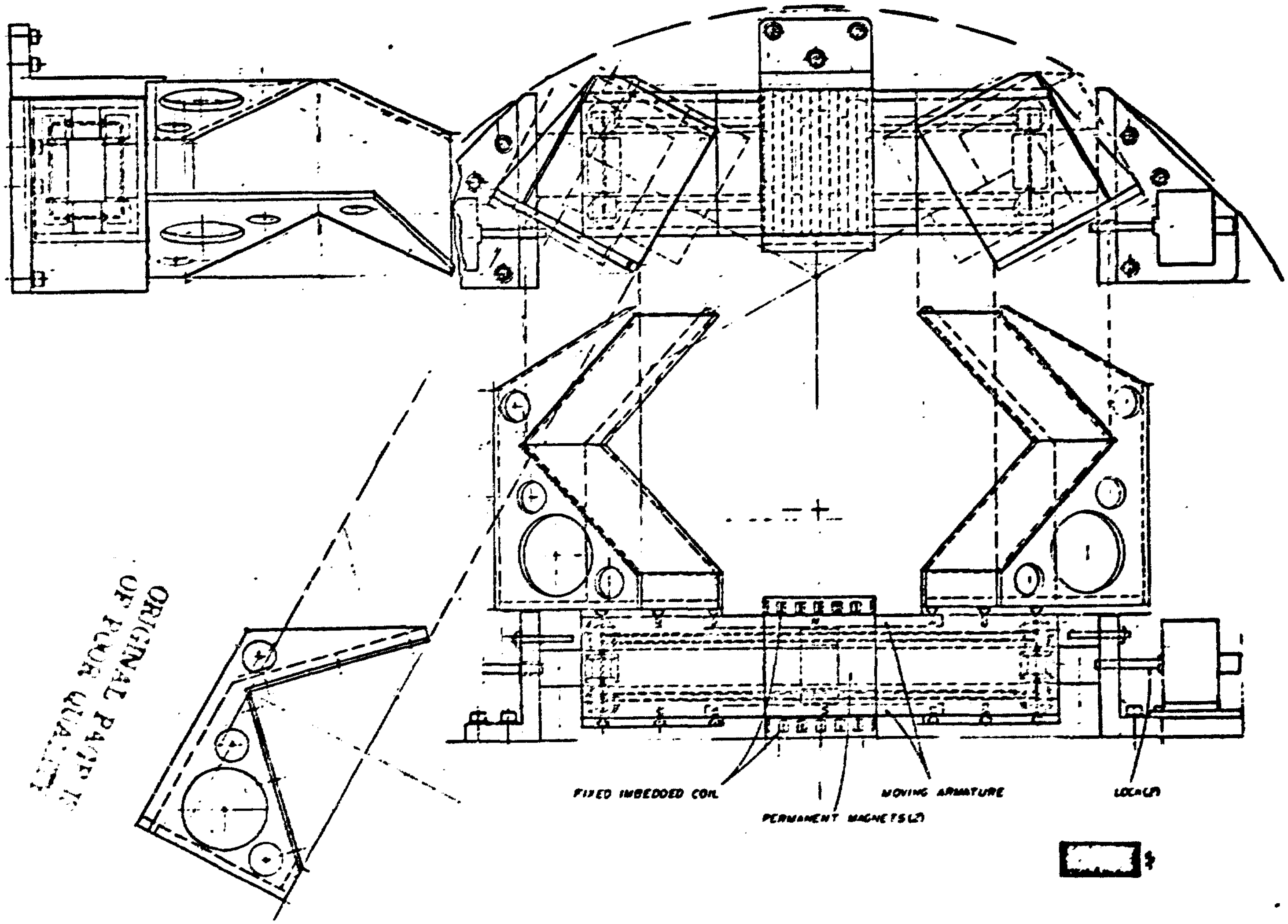

Figure 5.1.5-1. Firas Linear Motor

This is especially true in virtually unloaded situations, since the gentle microscopic contact cannot invoke the shear-like sliding mechanism which produces smooth motion at higher speeds or loads. This process is also applicable to CdS and graphite lubrication, and all of these processes involve the abrading of material at contacts. The result of this over long periods of time is the accumulation of microscopic flakes of material at the ends of travel, and only a loosely fitting bearing of this type can continue operation under such conditions. Block believes that a sliding bearing can operate in FIRAS successfully if the physical velocity does not have to drop much below about 0.5 cm/second and if a loose fit is tolerable. It is relatively easy to show that the power dissipation can be kept well below the required limits up to the maximum velocities indicated in the statement of work.

Once it became clear that even lower velocities were desirable for operation with the detectors, that the looseness of fit of the bearing was considered a marginal aspect of the design, that the absolute minimum of power dissipated was sought, and that utter reliability was critically important, Block sought other bearing designs.

The use of ball bearings was considered, and although no sliding occurs at the primary contacts, the necessity of a retainer which contacted the balls at their surfaces meant that sliding contacts still occured there, at the highest differential velocity point, with correspondingly increased frictional losses and abrading. The recirculation of balls in a linear bearing is also a problem, and Block has tested this type of bearing in other applications, finding that chattering is an overwhelming problem, especially following a reversal of direction, as the balls hit the retainers.

The flex pivot approach has been studied by NASA during this period, and is very attractive on the surface. Block has considered this approach less satisfactory on the basis of motion uniformity and reliability. Since the flex pivot is a kind of spring, the force required to move the attached assembly must vary correspondingly, as well as correcting for errors in the motion due to other effects. The small delay between the sensing of a motion error and the application of torque to correct it is normally a linear function, but when a spring is acting in the system, a second order term appears in the correction that is dependent on the direction of motion and the direction and magnitude of the correcting torque relative to the varying spring force. This means that to achieve the same correction as in a linear system, these parameters should be sensed and corrected, or the servo loop must be correspondingly tighter and the position monitor correspondingly more accurate. It is a fundamental error to complicate a design unnecessarily. The reliability factor arises from the specified and limited lifetime of flex pivots. It is true that this is computed to be much longer than the projected lifetime under the minimal loading present, but a device where plastic deformation is an inherent factor makes the operation subject to microscopic failures to a much greater extent, which is undesirable.

Hinge pivots have been used in short term cryogenic interferometer systems with some success. Pivoting "porch swing" carriages must be quite free, and the looseness of each pivot results in greater looseness of the entire carriage mechanism. Very low power is used in this approach, but the reliability of an assemblage of pivots is poor in terms of increasing looseness if designed without constraints or binding or seizing if constrained.

Magnetic bearings offer fully frictionless motion, but are subject to instabilities and complication. It is well known that three axis constraint is statically unstable, and that two axis stability increases with increasing velocity. The interferometer must stop at each end of the scan, and the slower motions desired are really much slower than are usually realized in magnetic bearing designs. The complication arises from the many poles and position sensors required to achieve satisfactory control in a linear motion carriage rigidly constrained in the other two axes. A further complication is the abrupt scan reversal at each end of the scan. It may be that ingenious design will permit the use of the magnetic bearing, but efforts in this program could not pursue this design given the very uncertain probability of success.

The roller bearing provides sliding contacts only at the thin retainer shafts, which can be quite loose without affecting the bearing accuracy. The lightly loaded rollers move only half of the full stroke, and are kept centered within the structure by rods at both ends that reset the bearings at the extreme ends of the travel. The rollers provide limited thermal conduction from the structure into the drive shaft, and improved thermal contact is provided at the extreme end of the stroke by contact of the dihedral support tube with the end plate (special contact pads are used) or possibly by the use of a flexible thermal strap. The retainer shafts are kept in alignment by use of a loose frame structure which can be stiffened at the center with a small open metal frame indicated in the figure. It may be sufficient to allow the retainer shafts to maintain the frame structure alignment simply by allowing less tolerance in their fit at the corner blocks. Four rollers at each end of the tube hold the mirror assembly in excellent alignment, and allow very small gaps at the linear motor pole/armature interface. The use of a thermally conductive plastic material with good metal interface characteristics is best, and the contact at the retainer shafts should use a PTFE-loaded plastic insert. A graphite-loaded plastic such as Vespel SP-22* provides five times the conductivity of the unloaded material, but the PTFE-loaded Vespel SP-211* provides minimal adhesion to the moving surfaces, with correspondingly reduced surface attrition.

In comparison with other techniques, the roller bearing is attractive because it is a very low power technique, does not require looseness in the mirror assembly, is inherently linear, and is fundamentally reliable. It is true that it is not technologically flashy, and even could be termed quaint in this application, but this neglects the reality of roller bearing usage. Rolling wheels on shafts have proven reliability in endless applications, as have rollers operated between moving plates or belts. In proposing a roller bearing for FIRAS, the certainty of successful operation for at least a year in vacuum and at low temperature makes this technqiue the best candidate.

Failure in roller bearings can occur due to surface attrition, from compressive stress failures due to loading or tension failures due to adhesion with the surface. Failure can occur due to retainer failure, resulting in misalignment of the roller and subsequent jamming. The spring loading of the bearing is light, so that the maximum stress experienced will occur due to vehicle acceleration and vibration.

---

* Dupont Company, Wilmington, Delaware

The dynamic aspects of the motor drive are obtained from consideration of the configuration and preferred response. The maximum velocity for the dihedral mirror assembly corresponding to a 10 cm/sec retardation rate is 2.5/Cos 30° = 2.89 cm/s. The mass of the dihedral mirror assembly is 3.18 kg, while the mass of the roller retainer assembly is 0.28 kg. The energy required to reverse this motion, achieving the same velocity in the opposite direction, is 2.71×10^{-3} joules, noting that the roller retainer assembly moves at half of the dihedral assembly velocity. A full two-sided interferogram providing 0.1 (1.0) cm^{-1} unapodized spectral resolution requires a retardation of ± 5 (0.5) cm, which takes 1.0 seconds at a 10 (1.0) cm/sec retardation rate. If we require that the duty cycle under these conditions should be about 95%, this gives 50 milliseconds for the turnaround. Assuming linear deceleration/acceleration, we obtain 1.16 $\mathrm{m/s}^2$ for the dihedral assembly and 0.58 $\mathrm{m/s}^2$ for the bearing with forces of 3.68 and 0.16 nt, or 3.84 nt total required.

This force is provided by the linear magnetic motor, which uses imbedded coils to allow minimal gap and maximum force. The motor is made with Alnico 5-7 (or equivalent) plates on the two sides, and pole plates at the top and bottom, making a square frame through which the square dihedral mirror support tube passes. This tube has high permeability, magnetically soft plates on four sides, similar to the pole plates, so that the magnetic flux is increased through the narrow gaps between the pole plates and the dihedral support tube. We believe that gaps of 0.01 cm can be achieved, given the stability of the roller bearing. The continuity of flux through one side of the symmetrical motor gives the relation, with MMF representing the magnet-motive force, R_i the reluctance, L_i the path length, A_i the area, and μ_i the premeability of the material.

$$\phi = \frac{\text{MMF}}{2R_{\text{pole}} + 2R_{\text{gap}} + R_{\text{armature}}} \; ; \quad R_i = \frac{L_i}{A_i \mu_i} \qquad (5.1.5\text{-}1)$$

$$= \frac{4590 \times 10^{-4} \times 4\pi \times 10^{-7}}{2\text{x}3.0/7.5\text{x}0.5\text{x}10000 + 2\text{x}0.01/7.5\text{x}3.0\text{x}1 + 15/77.5\text{x}0.5\text{x}10000}$$

$$= 4.0 \times 10^{-4} \text{ webers}$$

The parameters used are estimated from the physical configuration or obtained from vendor or reference literature. The MMF corresponds to a 9.0 cm magnet with a coercive force of 640 oersteds, and the resulting flux density in the magnet is approximately 11 kgauss. The factor of 10^{-4} converts cm^2 to m^2, and the permeability of free space is $4\pi \times 10^{-7}$ in MKS units. The pole and armature pieces can be made of many possible alloys including pure iron, and these represent small contributions to the total reluctance. The flux density in the gaps is about 0.15 webers/m^2, averaging over the entire area and including coil openings.

The desired force for turnaround is produced by a current-turns product of

$$NI = \frac{F}{BL} = \frac{3.84}{0.15\text{x}8.0\text{x}10^{-2}} = 320 \text{ ampere-turns} \qquad (5.1.5\text{-}2)$$

where F is the force, B the flux density, and L the effective length of a single turn. Since a multiphase drive is envisioned, each set of coils should have this drive capability. Using three phases, with 1.5 cm^2 of actual insulated wire area per phase, the number of turns of teflon insulated #34 AWG wire is estimated to be about 4300 in each phase, giving a turnaround current pulse of 75 milliamperes.

No resistive loss is present in the motor if superconducting wire is used, but even if copper magnet wire were incorporated, the power dissipated at 3°K would average 0.2 milliwatts, neglecting correctional effects during the linear motion. Since this power would be dissipated in the static pole plate, it would not enter the dihedral mirror assembly at all.

We can make an estimate of the hysteresis loss in the motor for the flux density-coercive force (B-H_C) curve of the material

$$P_h = \frac{dV}{dt} \S\, B\, H_c \cong \frac{dV}{dt} (4B_{max}H_c) \qquad (5.1.5\text{-}3)$$

where dV/dt is the volume of ferromagnetic material swept by the change in magnetic field. This change only occurs in a fraction (1/4 assumed) of the moving dihedral drive plates, and for the two plates,

$$\frac{dV}{dt} = 2\, v_{max}\, WT = 2x0.029x \left[\frac{0.1x0.005}{4}\right] = 7.2 \times 10^{-6} m^3/s \qquad (5.1.5\text{-}4)$$

with maximum velocity v_{max}, width W, and thickness T. The flux density in the plates is approximately 1.1 webers/m^2, and a typical coercive force for the material is 0.2 oersteds, or 16 amp-turns/m. The maximum power dissipated is then

$$P_h = 7.2 \times 10^{-6}\ x4x1.1x16 = 5.0 \times 10^{-4} \text{ watts} \qquad (5.1.5\text{-}5)$$

this assumes that the actual volume changed per second is one quarter of the volume of the drive plates facing the pole plates. The flux in the major part of the plates shifts slightly but does not diminish or reverse.

The losses due to eddy currents in the material are given by the relation (Handbook of Physics)

$$P_e = V(\pi f\ B_{max}T)^2/(6\ \rho\ 10^{16})\ \text{watts} \qquad (5.1.5\text{-}6)$$

in c.g.s. units. This is based on a.c. variations in the frequency f, but we may assume here that one change in flux per second at the scan end is equivalent to 1.0 Hz. The volume affected by each change in flux is estimated at 2 x 10 x 0.5/4 = 2.5 cm^3. The maximum flux density must be averaged over the area, since some concentration occurs at the edges, and a reasonable estimate is about 1500 gauss. The effective thickness is presumed to be 0.5 cm, including contributions in both the polse and drive plates. The cold resistivities of typical iron alloys will be on the order of 1×10^{-6} ohm-cm, giving a dissipation

$$\begin{aligned} P_e &= 2.5\ (\pi \times 1500 \times 0.5)^2/(6 \times 10^{-6} \times 10^{-6}) \\ &= 2.3 \times 10^{-4}\,\text{watts} \qquad (5.1.5\text{-}7) \end{aligned}$$

which is not a significant problem here. Lamination of the plates could be considered, but this is rather difficult in the configuration used here, and is not recommended.

Frictional losses in the bearings in normal operation will be entirely confined to the retainer. The loss in accelerating the dihedral mirror assembly results in a force F on the retainer amounting to 0.16 nt, and the use of a PTFE-loaded plastic should give a coefficient of friction of 0.05 at best. This dissipation occurs only in the 50 millisecond turnaround, and hence the duty cycle term enters. The surface velocity v_s of the retainer shafts averages to zero in this interval, but we should take twice mean for half the turnaround cycle, or 0.029 x 0.1 (1.15x2) = 1.3 × 10^{-3} m/s. With a duty cycle t_x/t_t of 0.05, we obtain

$$P_b = F\ v_s\ (t_x/t_t)\eta \qquad (5.1.5\text{-}8)$$

$$= 0.16 \times 1.3 \times 10^{-3} \times 0.05 \times 0.05 = 5.0 \times 10^{-7}\ \text{watts}$$

where the coefficient of friction η is 0.05 for PTFE. Tilting of the bearing due to a cocked retainer results in power loss through rubbing at the end and along the top and bottom contacts. If the tilting angle is ϕ the rubbing velocity is

$$v_r = v\ \text{Tan}\ \phi \qquad (5.1.5\text{-}9)$$

along the contacts. The surface velocity at the end is proportional to the radius of the contact edge there. This is given as $r_s/r_b = 0.2/1.15 = 0.17$. The power loss is the sum of the rubbing top/bottom and the end

$$P_{bt} = F_r v_r\ \eta + F_x v_x\ \eta \qquad (5.1.5\text{-}10)$$

The force F_r is the preload on the bearing, assumed to be 5 nt here, and the force on the end is $F_r\ \eta$ Tan ϕ. The result is

$$\begin{aligned} P_{bt} &= F_r\ v(1 + r_s/2\ r_b)\ \eta\ \text{Tan}\ \phi \\ &= 5 \times 0.029\ (1+0.087)\ 0.05\ \text{Tan}\ \phi \qquad (5.1.5\text{-}11) \\ &= 7.9 \times 10^{-3}\ \text{Tan}\ \phi \end{aligned}$$

Typically, we may expect that $\phi < 1°$ for worst case situations in real operation, and

$$P_{bt} < 1.4 \times 10^{-4}\ \text{watts per tilted bearing.} \qquad (5.1.5\text{-}12)$$

If the retainer frame is cocked, this would give

$$P_{bt} < 1.1 \times 10^{-3}\ \text{watts.} \qquad (5.1.5\text{-}13)$$

5.2 DYNAMIC ANALYSIS

Constraints are placed on the design of the FIRAS instrument by the spacecraft launch and insertion environment, in addition of the limitations in available volume and weight carrying capacity of the dewar. The 20 kg mass limit is a significant problem in terms of simply providing the basic instrumental components in a configuration that will survive and operate satisfactorily in orbit.

5.2.1 Weight vs. Stiffness

As is common for most zero-g equipment, many of the requirements for stiffness in the FIRAS sensor arise not from operational considerations, but from the launch environment of the spacecraft. Of course, there are also operational effects. The moving dihedral mirror assembly has significant mass, and the dynamic alignment tolerances are not trivial in terms of the quality of the spectrum. The angular alignment of the mirror optics should be maintained for both thermal and mechanical perturbations to a few milliradians in most cases.

The primary structural members in the FIRAS system are the vertical tubes and the bulkheads. These components are tied to the COBE support frame structure, and should derive some strength from that as well, but the instrument has been designed to be essentially self-supporting from the bottom mounting ring in the COBE dewar.

5.2.1.1 Sandwich Structure

The term "sandwich panel" is a generic meaning any laminate having high density face plate materials attached to a low density core material. Block has utilized such a sandwich panel for the optical baseplates of laboratory interferometer spectrometers, and thick faceplates are used with quite thin core layers to provide excellent high frequency acoustical damping. In the present application, much thinner faceplate materials would be used with relatively thick cores to minimize mass. A very large choice of materials can be considered, and three typical candidates are given in Table 5.2.1.1-I. We believe the strength and weight advantages of balsa wood are great, but the slow release of vapors may introduce spectral contamination which is totally unnecessary. Thus, we would tentatively advise a sealed aluminum honeycomb material, with face panels of aluminum alloy. Clearly, further consideration must be given to this point during the detail design portion of the program.

Another important advantage of the sandwich panel is simply that it is thick for a given weight. From the structural point of view, the rigidity of a structure is related to its moment of inertia, which for the sandwich goes as

$$I_s = T_f(T_f + T_c)^2/2 \qquad (5.2.1.1\text{-}1)$$

while for the single plate, it is

$$I_p = T_p^3/12. \qquad (5.2.1.1\text{-}2)$$

TABLE 5.2.1.1-I
PHYSICAL PROPERTIES OF COMMON CORE MATERIALS

Material	MIL Specs.	Density	Youngs Modulus kg 10^4	Crushing Strength kg	Shear Strength kg	Shear Modulus kg 10^3	Thermal Conductivity watts/cm^2/0°/cm
Aluminum Honeycomb	MIL-C-7438	0.47 gm/cm^3	5.45	111	59	5.45	1.29
Balsa Wood	MIL-S-7998 MIL-S-17917	0.13 gm/cm^3	9.55	318	73	9	.5
Polyurethane	MIL-P-26514	0.06 gm/cm^3	—	82	18	1	.22

Where T_f and T_c are the thickness of the face and core, and T_p is the thickness of the plate alone. Since the mass of the sandwich and plate (per unit area) are

$$M_s = 2T_f\rho f + T_c\rho_c \qquad M_p = T_o\rho_p \tag{5.2.1.1-3}$$

where ρ_f, ρ_c, and ρ_p are the densities of the face, core, and plate respectively, the ratio of the moment of inertia to mass is then

$$\frac{I_s}{M_s} = \frac{T_f^{\,2}}{2\rho_f} \frac{(1+T_c/T_f)^2}{(2+T_c\rho_c/T_f\rho_f)} \tag{5.2.1.1-4}$$

for the sandwich, and

$$\frac{I_p}{M_p} = \frac{T_p^{\,2}}{12\rho_p} \tag{5.2.1.1-5}$$

for the plate. If $T_c/T_f = 10$, and $\rho_f/\rho_c = 10$, the sandwich is about sixty times better, assuming $T_f - T_p/2$ and $\rho_f = \rho_p$. The sandwich and the plate become equivalent for $T_f = T_p/15.6$.

5.2.1.2 Vibration and Damping

It is necessary that the system be free of vibrational resonances that can couple into the signal through optical modulation (mirror vibration). It is true that the servo system will correct for errors in the velocity of the moving dihedrals, but any vibration of vignetting pupils or field stops will produce multiplicative noise in the system. The use of a composite sandwich plate for the mounting bulkheads will greatly reduce the possibility of resonances. The structure has many times the dynamic stiffness of a single plate structure, and very importantly, can be made to attenuate internally produced vibrations to the degree required to exclude resonances within the system bandwidth. This vibration damping quality is one of the most useful properties of sandwich plates in this application.

The dihedrals themselves are possible vibration sources, considered as restrained uniform beams, the mirror plates have a fundamental vibration frequency of

$$f = c_n \sqrt{\frac{gEI}{wl^4}} \text{ Hz} \qquad (5.2.1.2\text{-}1)$$

$$= 93 \text{ Hz}$$

In this expression,

E is the modulus of elasticity, $\times 10^7$ psi for aluminum

I is the moment of inertia, 1.7×10^{-4}, for each flat mirror,

G is 386 in/sec^2,

w is the weight per unit length, 3×10^{-2} ib/in,

L the length, 5.3 inches, and

c_n is a function of mode number, 0.56 for the first, most significant natural frequency for this application.

Since this is clearly within the higher frequency bands of interest, some care in the turn-around of the mirror drive assembly is indicated. The use of beryllium for the mirror assemblies would raise this frequency by 2.3 times through its higher modulus and lower density, but it is not clear that this would be necessary. Increasing the thickness of the mirrors from 0.08 inches would linearly increase the frequency of vibration. The use of ribs, as shown in the mechanical drawings, will act much more effectively to increase the moment of inertia while affecting the weight only slightly. The frequency with two ribs is estimated to be three times higher.

The remaining instrument is insensitive to normal vibrations during operation except in relation to the detectors. The analysis of the detector sensitivity to vibration is beyond the present analysis, since it is not clear how much of the detector sensitivity is due to electrostatic, electromagnetic, or other effects. The actual sensitivity must be determined by measurement in three axes, and the COBE and FIRAS vibration levels during operation must then be related to this sensitivity. The FIRAS instrument produces vibration during turn-around, and also in the course of calibrator motion, but in each case the detectors are not intended to obtain data at those times. The vibrations produced during normal scanning motion should be exceedingly small, provided that polished bearing surfaces are used, with minimal contour irregularities. It is also not clear how much vibration will be produced during normal operation by the other instruments and devices in the COBE satellite, but one would expect an essentially quiet vehicle in these circumstances.

The second aspect of vibration and damping in the FIRAS instrument is the level contributed by the scanning of the diagonal mirror assembly through the FIRAS mount to the COBE package. This is basically a force of

$$F = M_d \, dV/dt \qquad (5.2.1.2\text{-}2)$$

which can be controlled by adjusting the programmed turnaround in the motor drive.* The force is clearly proportional to the velocity of motion, and can be minimized by keeping this velocity as low as possible. We can consider the possibility of utilizing a compensated drive in which the dihedral mirror assembly motions are matched by an opposing mass motion in close juxtaposition to the drive. In general, this means that a duplicate assembly, without mirrors, would be moved simultaneously with the actual mirror assembly, but in opposition. The difficulty is that this introduces a second drive assembly, motion sensor system, and source of thermal power within the dewar, with generally undesirable results in terms of mission reliability and lifetime.

One answer to this is to make the anti-recoil device a part of the standard drive. In the design proposed, for example, the "fixed" motor poles can be mounted to provide an opposing mass motion, either exactly compensating for the dihedral mirror assembly or acting to integrate the recoil over a longer time. In the first case, the motor pole assembly is also mounted with roller bearings, allowing it to move freely in opposition to the mirror assembly and the two component assemblies move a correspondingly

---

* 3.84 nt at maximum velocity, see page 5-21.

greater distance (relative to each other) than the original drive motion requires. By making the motor pole assembly much more massive, its motion is reduced greatly, and the excess motion required is small. The second approach is the spring mounting of the pole assembly, allowing it to move enough at the turn-around to reduce the force conveyed to the main structure to an acceptable level, much as in the recoilless rifle or field gun. This is easier to implement, requires no rolling member, and dissipaits only a small additional amount of power. In either case, the motion is sensed from the FIRAS frame, and control is accurate for the desired optical path changes through feedback adjustment. Block does not recommend either of these approaches unless absolutely essential for the mission, since they involve additional complexity and power dissipaition in the dewar.

5.2.2 Structural Strength

The primary structure of the FIRAS instrument is the five 1.5 inch diameter tubular struts supporting the two open bulkheads, however, the two horn structures are important elements in themselves, especially the sky input horn which supports the calibrator mechanism. Detailed design and analysis has not been possible in the limited effort reported here, and a significant part of the detailed design is related to the structural strength of the individual components, Certainly the lightening of individual components to achieve the 20 kg design goal for the instrument must be approached with the clear necessity of maintaining structural integrity throughout.

The use of the interface support structure, into which the FIRAS instrument mounts, as part of the mechanical support of the instrument is not necessary in the vertical plane, but does give good lateral reinforcement. The five tubular struts are mounted with central rods or bolts to provide tensile reinforcement, but it is recommended that the tubes be welded to the bulkheads for thermal conductance as well as mechanical strength. The upper bulkhead is attached to the interface support structure, again to improve the thermal coupling to the dewar, but some mutual mechanical advantage is obtained as well.

The tubular struts can act in either tension or compression, depending on the forces acting. In tension, the five struts, excluding central rods, can withstand a force of

$$F_t = 5\ S_y A \qquad (5.2.2\text{-}1)$$

$$= 2.1 \times 10^4 \text{ lbs}$$

where S_y is the yield stress for aluminum 8×10^3 psi at 300K, and a is the area of each tube, 0.54 in^2. No plastic deformation occurs under this loading, which may be considerably higher for specific materials. The tensile strength is higher yet, and some moderate improvement generally occurs in going to low temperatures. The tension rods inside each tube, also made of aluminum, can withstand a tensile force of 1.9×10^3 lbs alone, on the assumption of 0.25 inch effective diameters. If the tubes are welded, these rods could be thinner to reduce weight with only modest initial tension introduced at installation, relying on the welded joints to bear the bulk of the strain.

In compression, the weakest links are the longest tube sections, which can be conservatibely treated as long columns, based on the Euler formula

$$F_C = 5 \frac{K \pi^2 EI}{L^2} \qquad (5.2.2\text{-}2)$$

$$= 2.5 \times 10^4 \text{ lbs}$$

where K is 0.25 for one end fixed and one end free, I is the moment of inertia, 0.13 in^4, and L is the column length, 25.4 inches, and we can see that in this design the failure will occur through simple strength failure before buckling occurs. It is perhaps too pessimistic to use the value of K indicated, since the "free" end is fairly constrainted due to the bulkhead, but it provides a worst case approach.

The application of this formula to the double walled sky input and reference blackbody horns results in an even greater columnar strength due to the higher values for the moment of inertia. The yield strength of nickel is generally considerably greater than 14 × 10^4 psi, so that the force capability in tension exceeds 11 × 10^4 lbs for the assumed area of 0.8 in^2 (0.02 inch inner wall and 0.04 inch outer wall.)

6.0 THERMAL CONTROL AND CRYOGENICS

The primary thermal control is implicit in the mechanical configuration, and consists of thermal conductance from each optical component and structure to the mounting frame and hence to the COBE dewar through the COBE instrument support frame. Secondary points of thermal control are the reference blackbody source and the calibrator source.

Two general conceptual approaches to the thermal design have been considered by the Science Team. In the first, the entire instrument is maintained at the 3K cosmic background temperature except for the calibrator source, which provides a range of precision test radiances. In the second, the entire instrument is held at as cold a temperature as possible, except for the reference blackbody source, held at the cosmic background temperature, and the calibrator as before.

From a theoretical standpoint the first approach is better, since instrumental radiation will be at the same temperature as the reference, making the reference emissivity accurately unity. From a practical standpoint, however, the second approach has merit because the introduction of a complex variety of thermal impedances and heaters to hold temperature at a set level will be very difficult, and for certain components virtually impossible (the dihedral mirror assembly controls thermal conductance discontinuously, and only heater control is continuously variable). Making the configuration flexible enough to deal with unanticipated problems and yet avoid introducing new problems in cooldown and stabilization also points toward the second, simpler approach. The use of super-conducting indium coatings on optical elements also suggests colder operation. We note that although the symmetry of the instrument design does not incline toward either approach, it is intended to eliminate the effects of instrumental radiance or the lack thereof through symmetrical cancellation.

Either approach can be implemented in the Block FIRAS design, by installing thermal barriers at appropriate connection points or by locking points tightly using high thermal conductivity connections. Block's recommendation is that the design be kept as cold as possible throughout, except for the two controlled blackbody sources. The main consideration is the preservation of instrumental simplicity, allowing any necessary compensation to be done in the processing of the data through accurate calibration techniques. The compensation will be a small factor, since we expect the symmetrical physical cancellation to be better than a part in one hundred if symmetry is rigorously maintained. (This means that the radiation emitted or scattered from the optics is reduced by this factor in terms of the detected interferograms.)

6.1 THERMAL ANALYSIS

The points of the thermal matrix which contribute directly to the instrumental measurement, and hence are absolutely critical in terms of thermal stability are the sky input and reference blackbody horns, the reference and calibrator blackbodies, and the mirror pairs in the input optical train. Other components that contribute indirectly to the instrumental measurement stability through scattering reflections are the dihedral mirror, the exit optical train, the detector assemblies, and the general instrumental structure. The beamsplitters are common to the two beams and hence contribute through scattering, but their thermal stability is of importance for dimensional reasons.

Analysis of the thermal performance of the FIRAS instrument was done by computer, using the thermal matrix shown in Figure 6.1-1. Each component or assembly noted was accurately modeled in terms of its thermal mass and surface area exposed to gaseous cooling. Thermal conductance members were modeled in terms of their effective area/length quotient, and their thermal masses were divided between the components on each end. The values used for all nodes are given in Table 6.1-I and the parameters for all links are given in Table 6.1-II.

Four sources of thermal power input are included in the analysis: the reference blackbody source (P3), the calibrator blackbody source (P4), the fixed scan drive motor poles, (P2), and the moving dihedral mirror/motor armature assembly (P1). The moving mirror/armature can operate in two nodes; a normal scanning mode in which the assembly does not contact at the end positions, and a locking node in which the assembly contacts the supporting frame alternately at each end of the support through copper mesh pads. The change in the flow of heat out of the moving assembly was approximated by switching the fraction of flow from node 10 to nodes 11 (A) and 12 (1-A) for each successive iteration. The moving mirror/armature assembly could also be kept at any position or locked in contact at either end. It is shown locked at the right side (Wo) in Figure 6.1-1.

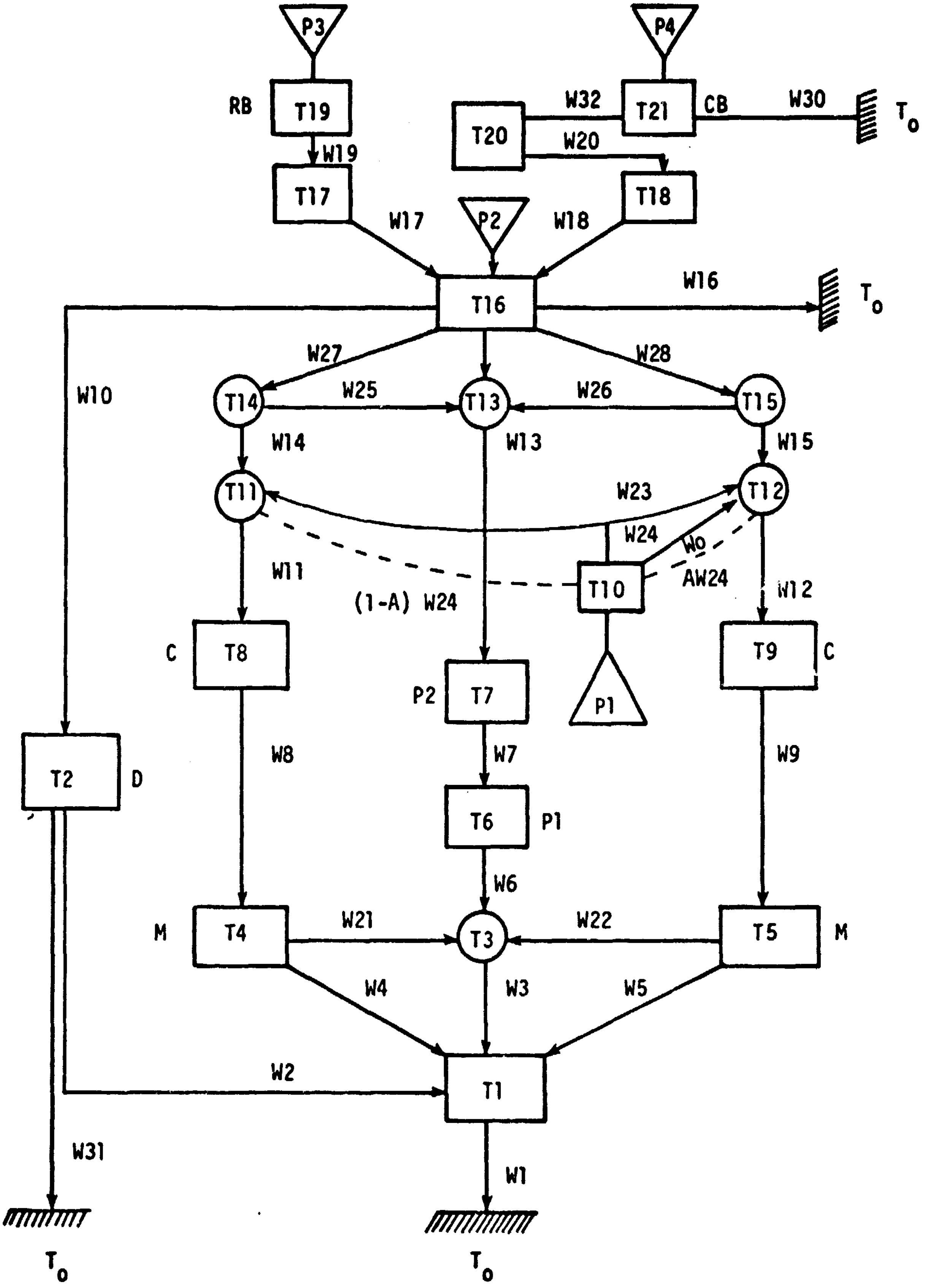

Figure 6.1-1. FIRAS THERMAL MATRIX

TABLE 6.1-I
THERMAL NODE PARAMETERS

Node	Designation	Material	Volume (cm^3)	Surface Area (cm^2)
1	Lower Bulkhead	Al	523	2100
2	Detector Assembly	Al	1975	3755
3	—	Al	135	466
4	Transfer Mirror (M1)	Al	583	631
5	Transfer Mirror (M2)	Al	583	631
6	I/Q Polarizer (P1)	Al	282	511
7	Beamsplitter (p2)	Al	273	484
8	Collimator (C1)	Al	643	1240
9	Collimator (C2)	Al	643	1240
10	Motor Armature	Al	886	2235
	Drive Plates	Ni	72	-
	Bearings	PTFE	76	-
11	—	Al	344	308
12	—	Al	344	308
13	—	Al	167	575
14	—	Al	83	287
15	—	Al	83	287
16	Upper Bulkhead	Al	677	3140
17	Reference Horn	Ni	329	3340
18	Sky Input Horn	Ni	655	8900*
19	Reference Source	Al	147	779
	Emissive Surface	PTFE	249	-
20	Calibrator Assembly	PTFE	3246	3479
21	Calibrator Source	Cu	38	0**
	Emissive Surface	PTFE	77	-

* Assumed gas flow through horn

** Assumed enclosed within cavity

TABLE 6.1-II

THERMAL LINK PARAMETERS

Link	Designation	Material	A/L (cm)
0	Motor Armature End Contact Pads	Cu	.05
1	Support Tubes (5)	Al	1.8
	Heat Strap	Cu	0.72
2	Support Tubes (2)	Al	0.34
3	Support Tube	Al	0.87
4	Support Tube	Al	0.87
5	Support Tube	Al	0.87
6	Support Tube	Al	0.25
7	Support Tube	Al	0.24
8	Cross Tube	Al	0.16
9	Cross Tube	Al	0.16
10	Support Tubes (2)	Al	0.21
11	Support Tubes	Al	0.26
12	Support Tube	Al	0.26
13	Support Tube	Al	0.22
14	Support Tube	Al	0.68
15	Support Tube	Al	0.68
16	Instrument Frame	Al	0.11
	Heat Strap	Cu	0.40
17	Reference Horn	Ni	0.84
18	Calibrator Horn	Ni	0.56
19	Reference Insulator	PTFE	2710
20	Calibrator Horn	Ni	0.56
21	Cross Tube	Al	0.12
22	Cross Tube	Al	0.12
23	Motor Support Shaft	Al	0.05
24	Motor Bearings	PTFE	1.25
25	Cross Tube	Al	0.094
26	Cross Tube	Al	0.094
27	Support Tube	Al	0.61
28	Support Tube	Al	0.61
29	Support Tube	Al	0.61
30	Calibrator Wires	Cu	0.025
31	Heat Strap	Cu	0.12
32	Calibrator Mount	PTFE	3.0

No external sources of input power were used. The instrument is contained within a cold cavity without penetrations. The open end of the system is shielded from external radiation with a helium cooled cover prior to and during injection into orbit. Once oriented properly in orbit, the cover is ejected and the open end is shielded from terrestrial and solar radiation by cold baffling in a bow-shaped radiation shield. Input wiring is assumed to be thermally locked to cold surfaces within the dewar cavity. It is important that these be symmetrically arranged if they are locked to structures within the FIRAS instrument.

Four materials are used in the primary structure, and these have been accurately modeled over the full temperature range. The primary structural material is aluminum, and the 6063-T5 alloy has been used in the thermal analysis. The horn structures are fabricated from the electroformed nickel, and the electrolytically pure material was used. Plastic structures and thermal isolators are modeled with teflon (PTFE). Thermal shunts and wires are fabricated from electrical tough pitch copper. All material functions are based on measured data, with integrated thermal conductances taken from Steward & Johnson (1961) and volumetric heat capacities from Stout (1959). Integrated thermal conductance functions used are shown in the Figures: 6063-T5 Al (Figure 6.1-2), E.P.Ni (Figure 6.1-3), teflon (Figure 6.1-4) and El.T.P. Cu (Figure 6.1-5).

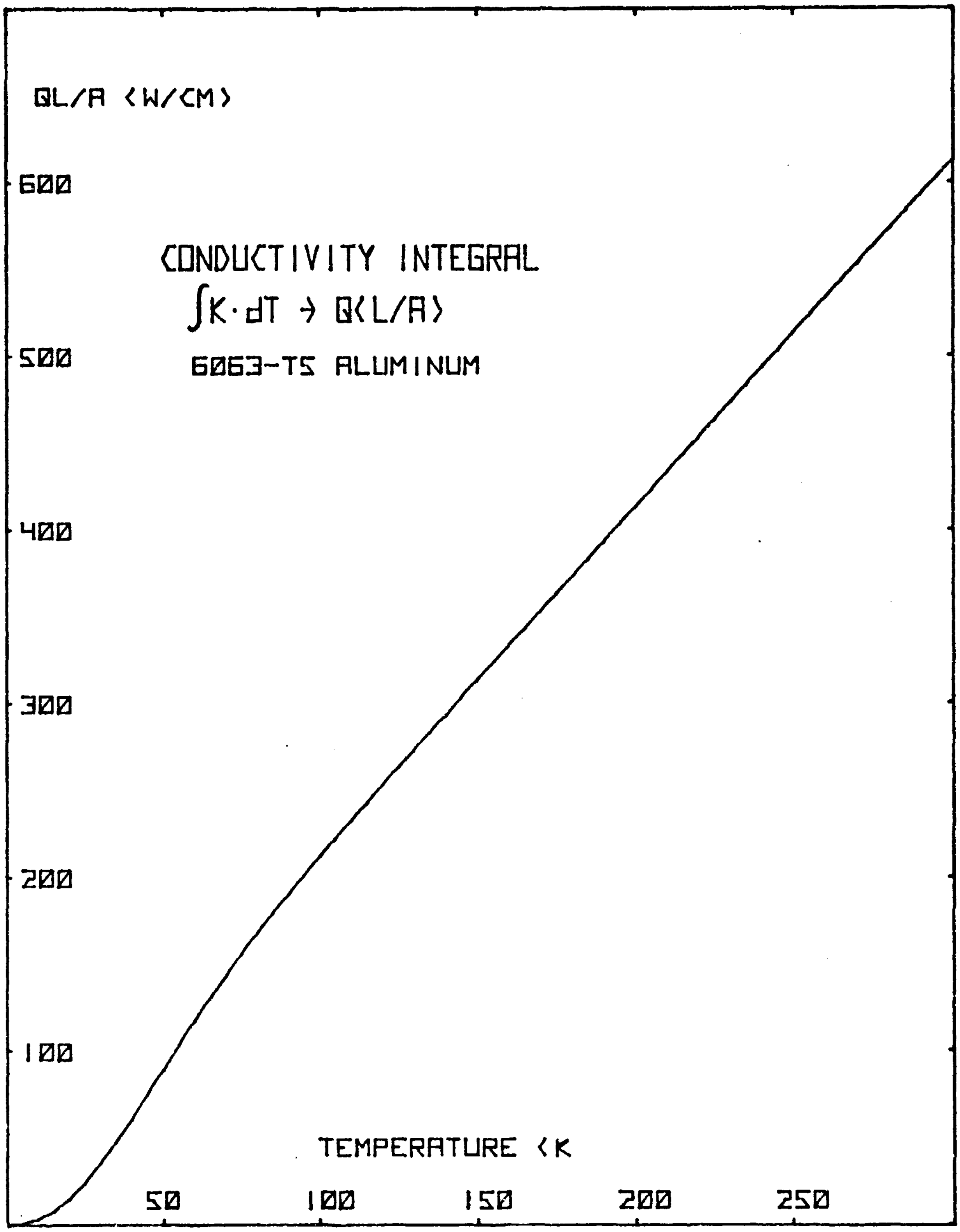

Figure 6.1-2. Conductance of 6063-T5 Aluminum

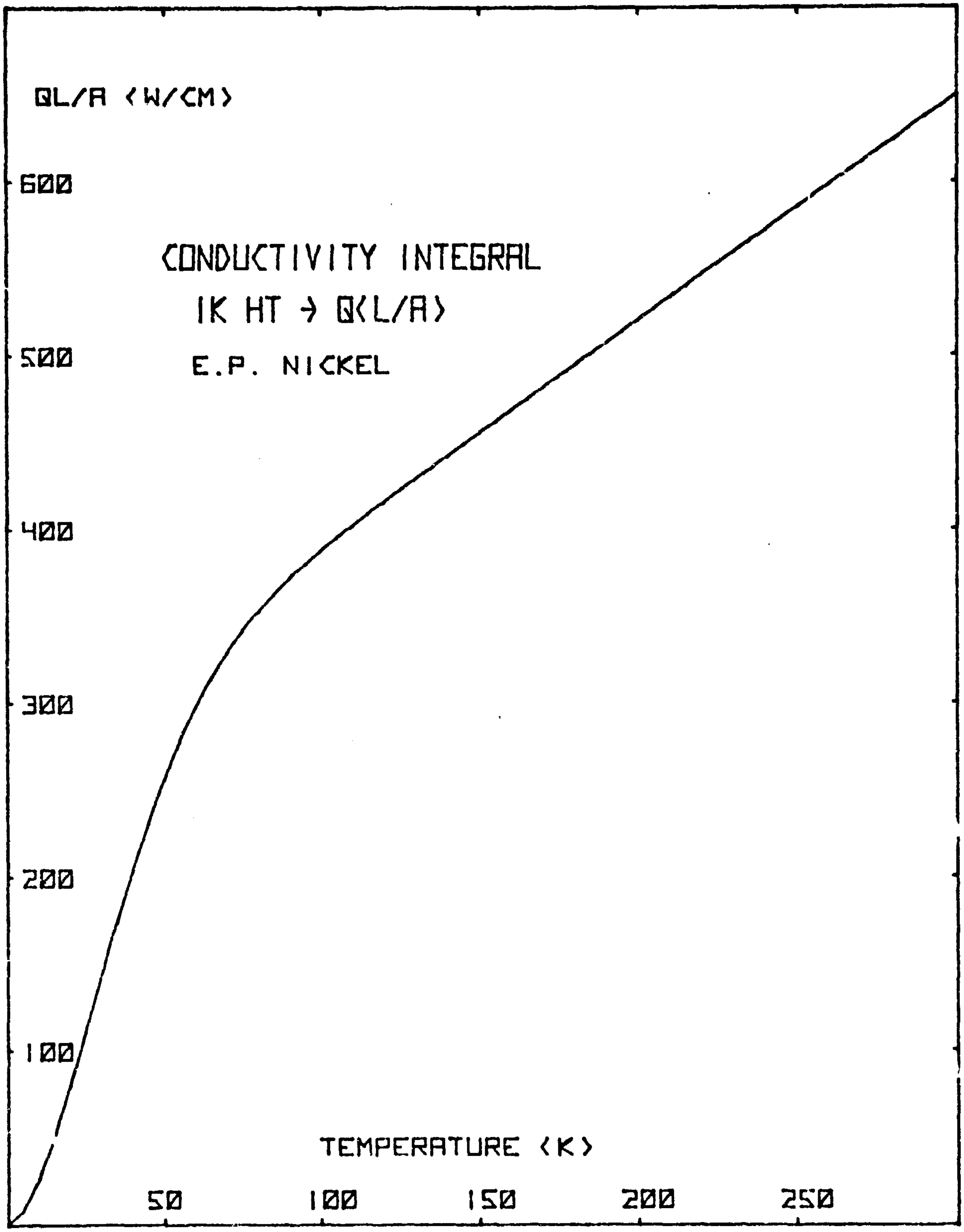

Figure 6.1-3. Conductance of E.P. Nickel

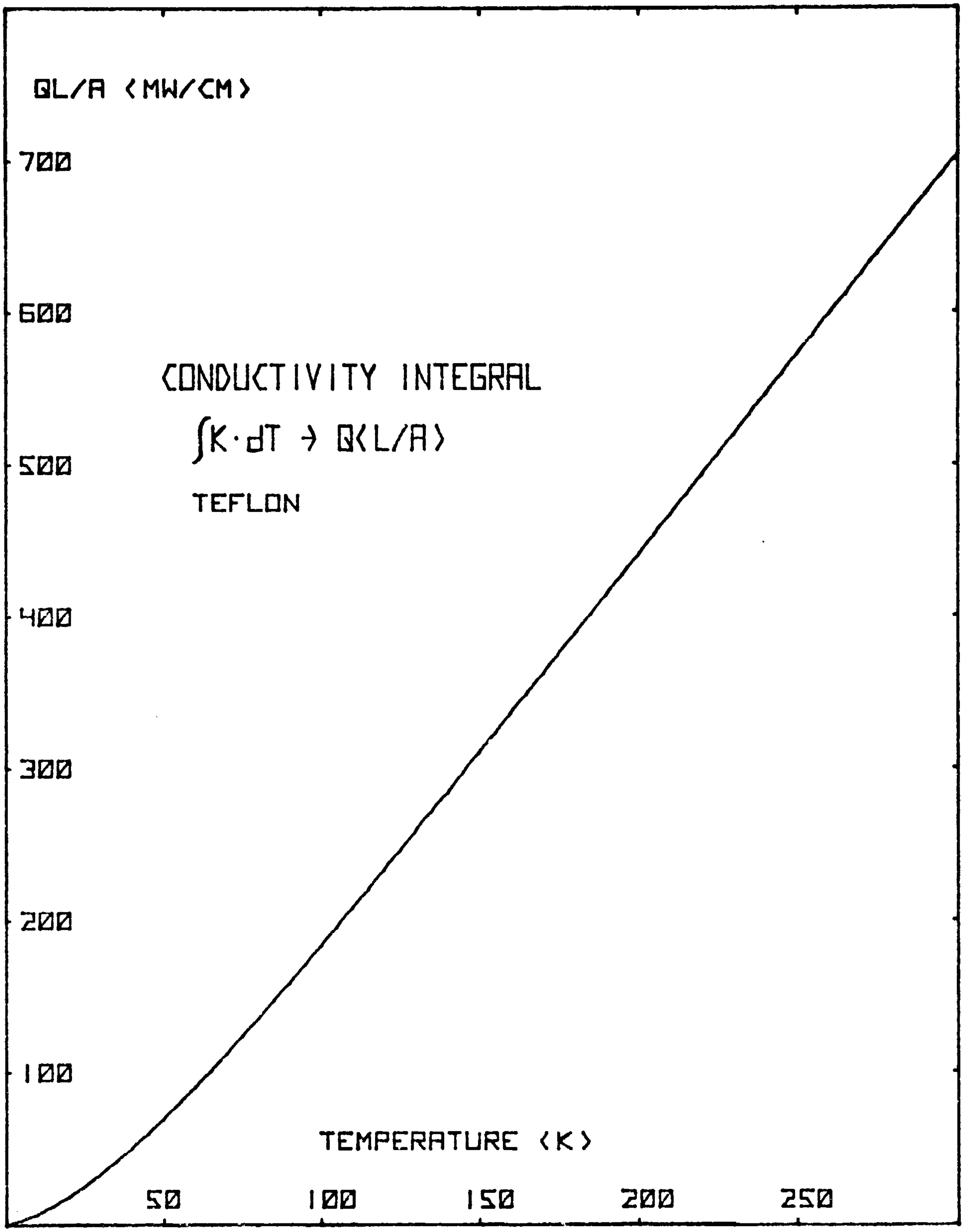

Figure 6.1-4. Conductance of Teflon

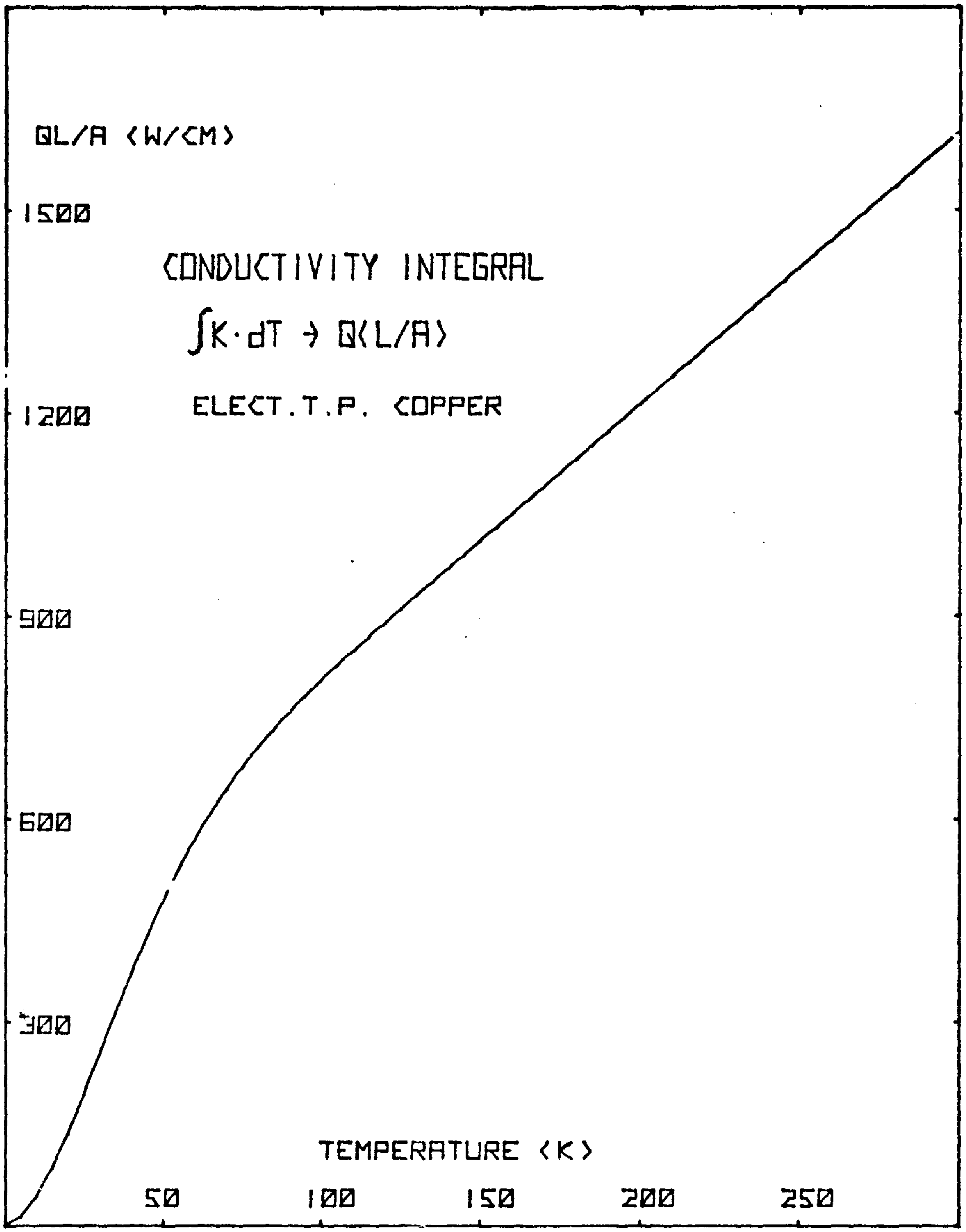

Figure 6.1-5. Conductance of Elect. T.P. Copper

The actual conducted power between two points is obtained by subtracting the integrated conductance at the higher end temperature from that for the lower end temperature, and multiplying the result by the area/ length quotient. The volumetric specific heats for all four materials are given in Figure 6.1-6, and these are multiplied by the volume of material to obtain the temperature derivative of heat energy.

The analysis was carried out by computing all power flows at a given moment, and then computing the temperatures changes at each mode over the time increment selected. Since the thermal conductances vary widely with temperature and differences are computed, the time derivative of conductance is calculated and used to correct the computed temperature change. This follows from the expression for the change in energy at a given mode n,

$$\Delta Q_n \approx \sum_j V_{nj} C_{vj} \Delta T_n = \Delta t \sum_i \left(\frac{A_i}{L_i}\right) \left(w_i + \frac{dw_i}{dT} \Delta T_{in}\right) \qquad (6.1\text{-}1)$$

$$= \Delta t \sum_i \left(\frac{A_i}{L_i}\right) \left\{ \int_0^{T_i} K_i dT - \int_0^{T_n} K_i dT + \left[\frac{d}{dT} \int_0^{T_i} K_i dT\right] \Delta T_i - \left[\frac{d}{dT} \int_0^{T_n} K_i dT\right] \right\} \Delta T_n \, . \qquad (6.1\text{-}2)$$

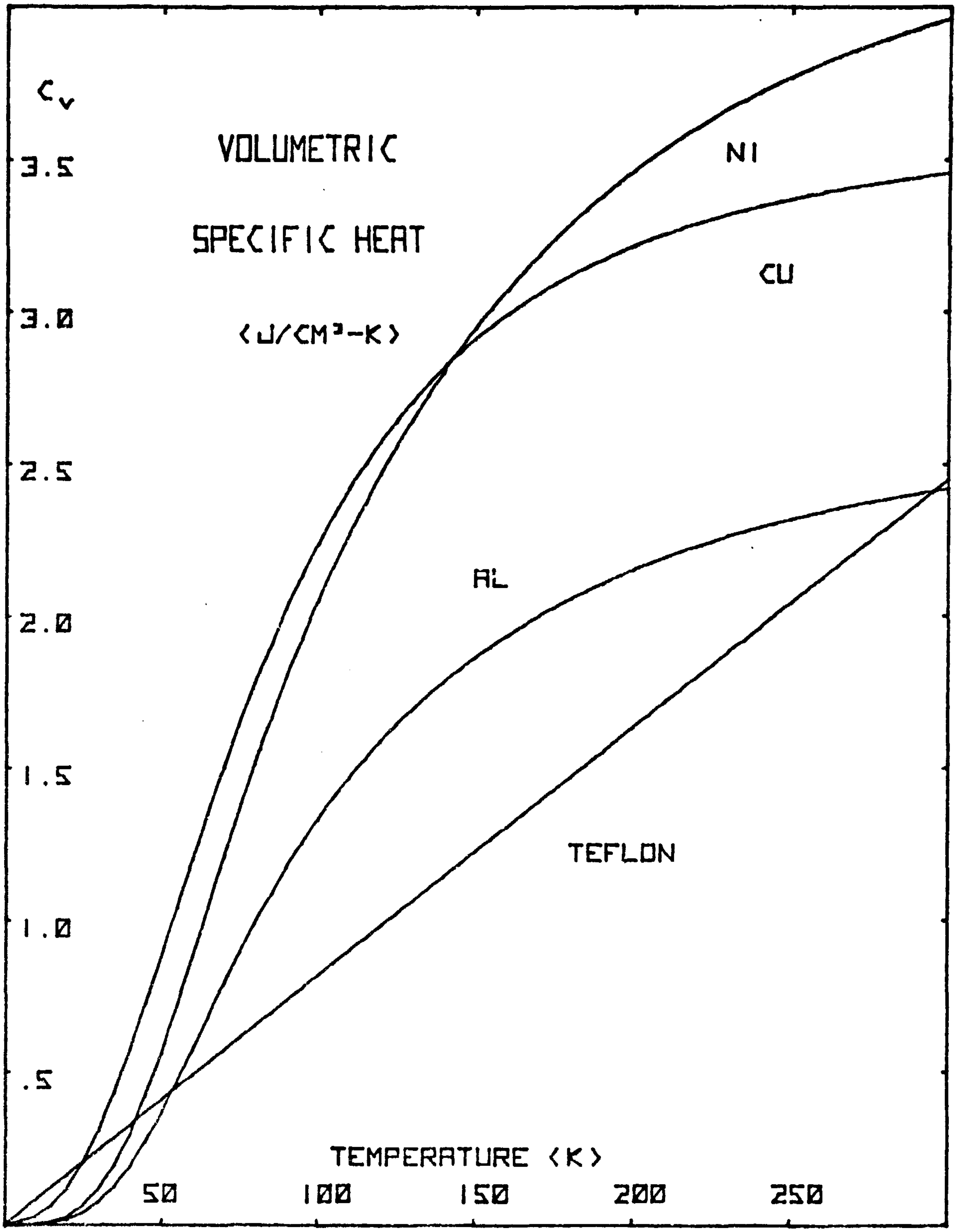

Figure 6.1-6. Volumetric Specific Heat

In which V_{nj} is the volume of component j of node n

C_{vj}	the volumetric specific heat of compnent j
T_n	the temperature of all j components of node n
ΔT_n	the change in T_n
Δt	the selected time increment
(A_i/L_i)	the area/length quotient for link i to node n
W_i	the power input along link i
$\frac{dw_i}{dT}$	the temperature derivative of the power on link i
$\int_0^T K_i dT$	the integrated thermal conductance of link i taken to temperature T.

Since we only permit T_n to vary for each node n computation, we null any variation at the far end of each link i, $\Delta T_i = 0$. We obtain:

$$\Delta T_n = \frac{\Delta t \sum \left(\frac{A_i}{L_i}\right) w_i}{\sum_j V_{nj} C_{vj} + \alpha \Delta t \sum_i \left(\frac{A_i}{L_i}\right)\left[\frac{d}{dT} \int_0^{T_n} K_i \, dT\right]} \qquad (6.1\text{-}3)$$

where $\alpha \geq 1$ is a damping factor introduced to permit increase in the time increment and consequent reduction in computation time.

6.2 INITIAL COOLDOWN

The cooling of the instrument from a uniform temperature of 300°K to a dewar temperature of 1.8°K is shown in vacuum in Figure 6.2-1, with log temperature (°K) plotted against log time (seconds). Various model points are shown, and in several instances two symmetrical points are indicated by a single curve, where the actual differences are too small to distinguish. We note the delay in cooldown of the reference blackbody source (19) which arises mainly from its high degree of thermal isolation from the rest of the system. The cooling of most other components is somewhat better, but generally over 100 hours of cooling appears to be necessary in vacuum.

The use of gaseous conduction during cooldown was considered, with the marked improvement shown in Figure 6.2-2. Helium gas at low pressure (conduction is essentially independent of pressure over a broad range) is kept in the dewar cavity until 10,000 seconds, at which time it is pumped out. Static conductance of the gas is assumed, with a path 10 cm from each component to a 4.2°K temperature. The cooldown of the calibration blackbody (21) is poorest, since it is shielded from gaseous conduction to the cold surfaces by its own cavity. Cooldown is now on the order of ten hours, which would seem to be quite satisfactory.

The flow of cold helium gas venting from a dewar is shown in Figure 6.2-3, with the venting continued until 4000 seconds, at which time the system must be evacuated. Flow of cold gas is approximated by assuming static conductance with a 1 cm path to the 4.2°K temperature. Again, no gas cooling was applied to the calibration blackbody. Although these approximations are considered pessimistic, the conclusions that either method of gaseous cooling is highly effective is valid.

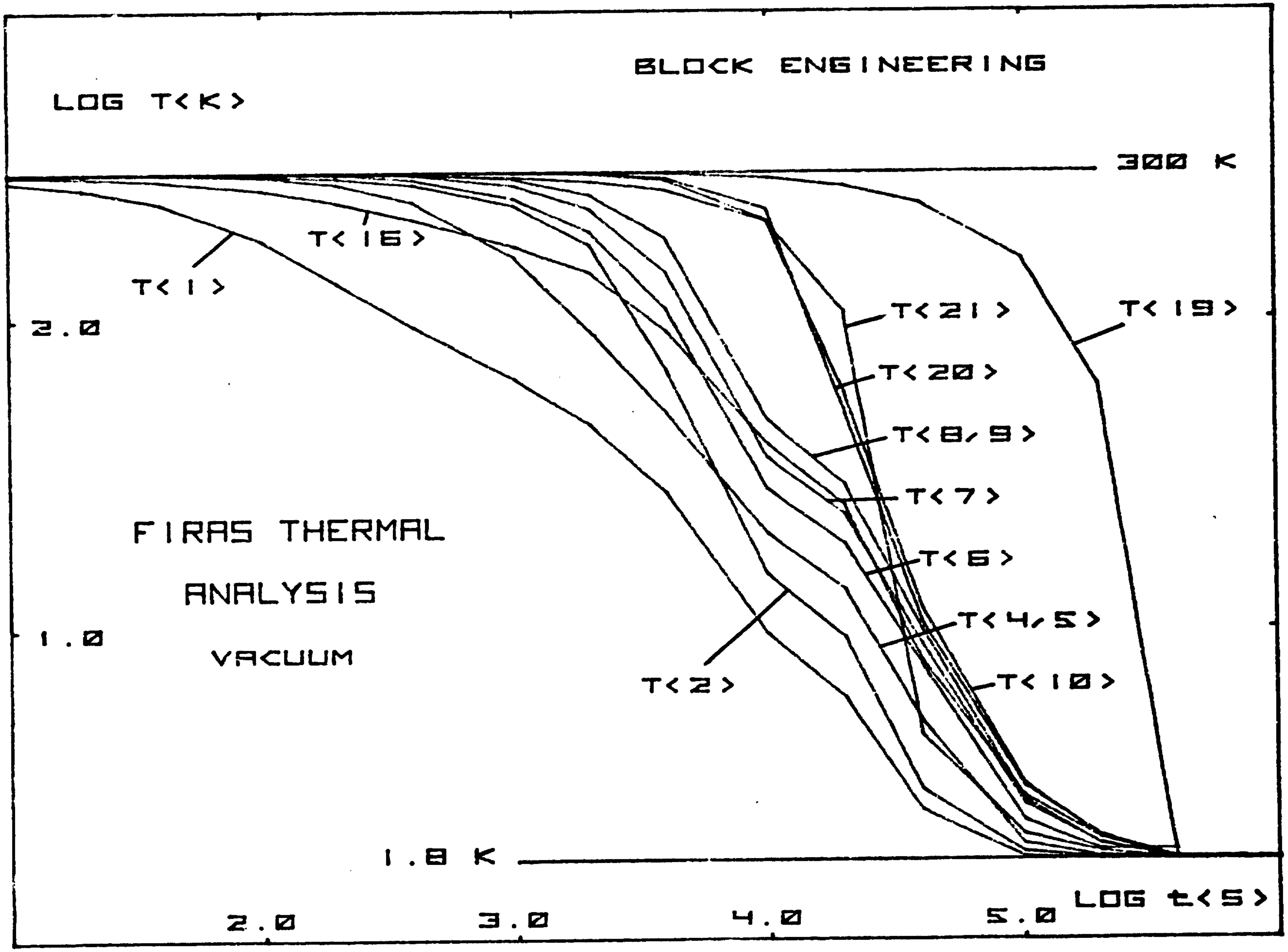

Figure 6.2-1. Initial Cooldown (Vacuum)

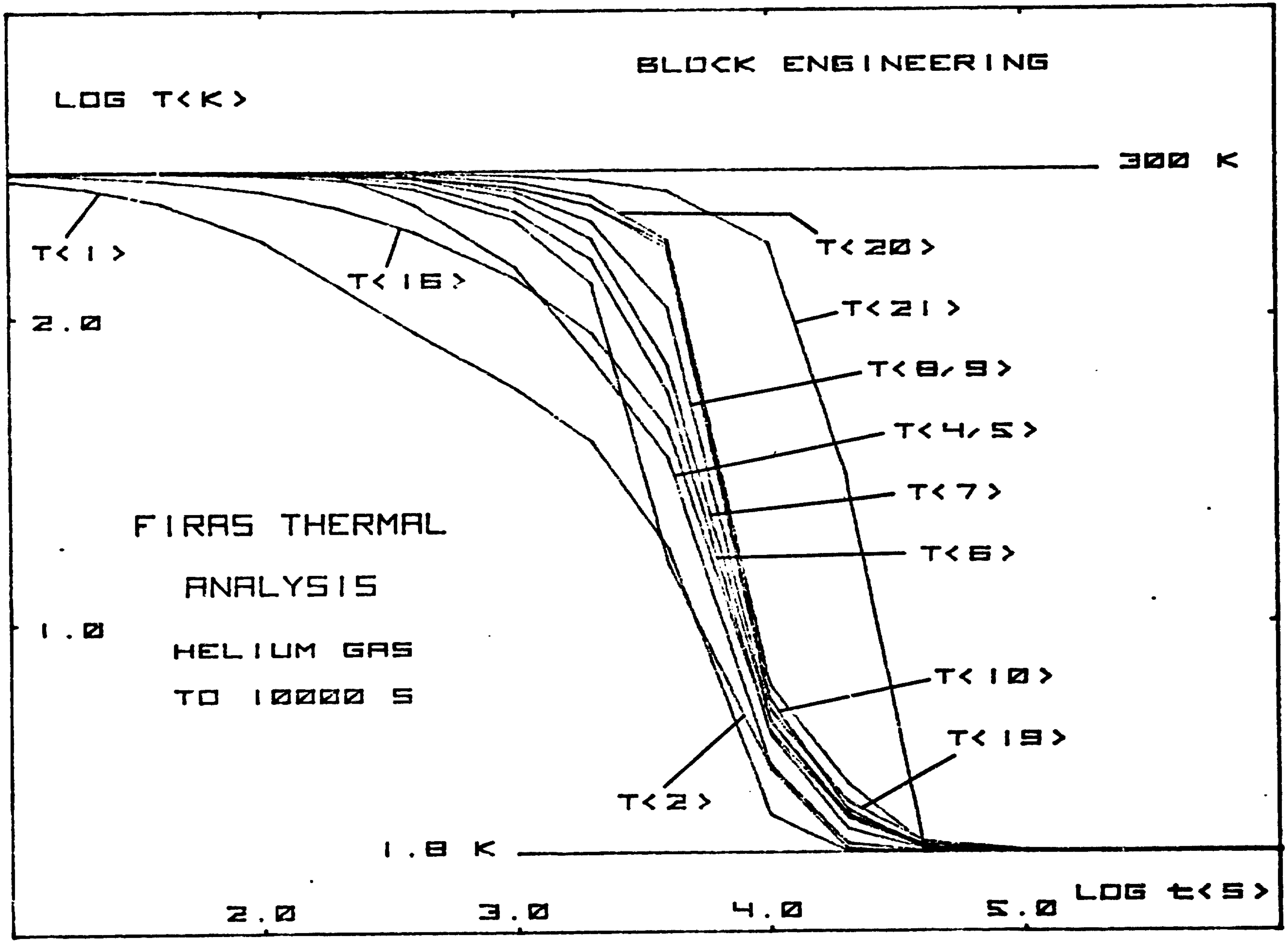

Figure 6.2-2. Initial Cooldown (Helium Gas to 10,000 Seconds)

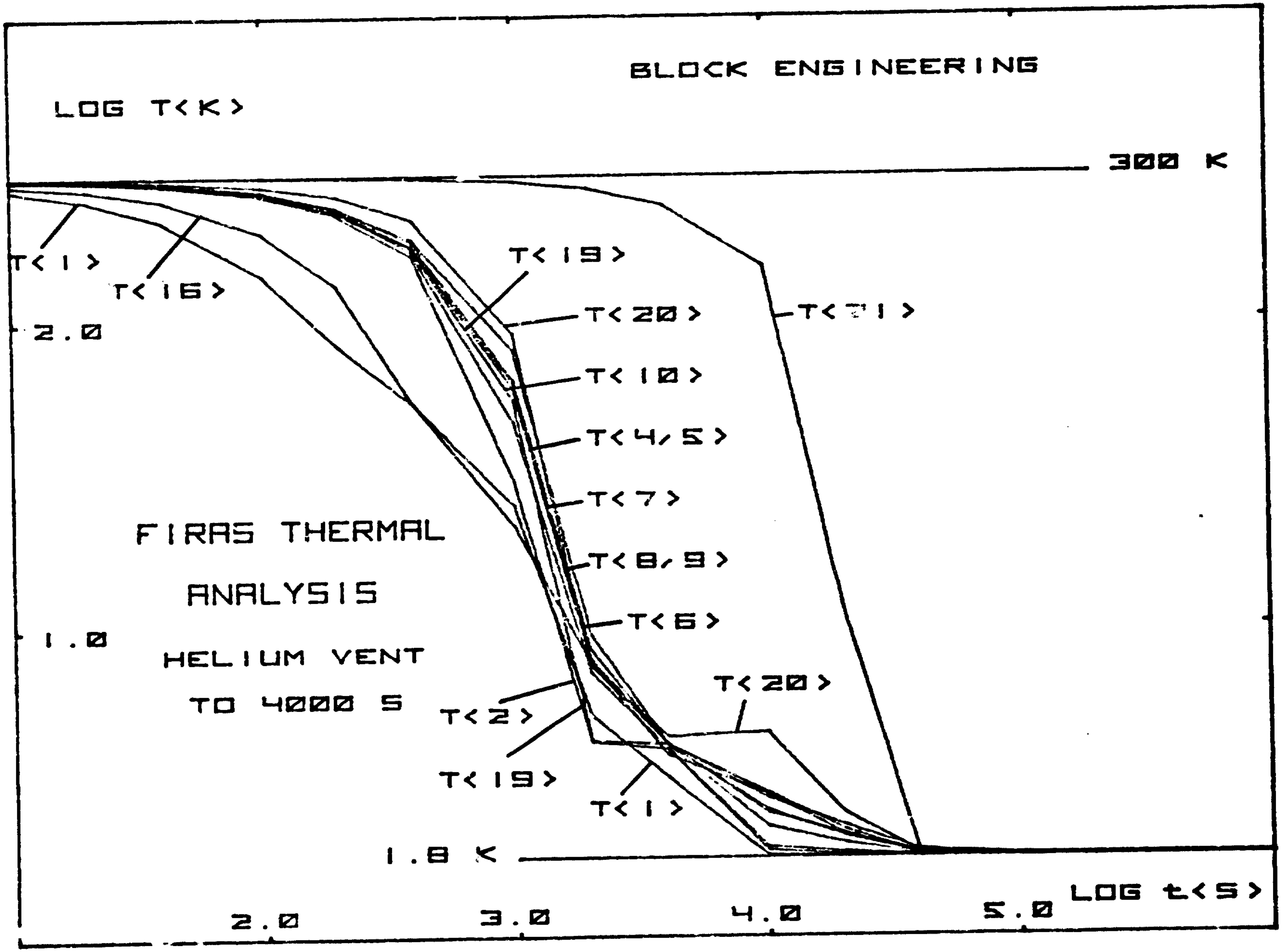

Figure 6.2-3. Initial Cooldown (Helium Vent to 4000 Seconds)

The entire structure will cool to 1.8°K very accurately if no power is dissipated within the instrument. In the above computations, the motor was assumed to be scanning slowly making thermal contact at the ends of the scans. Other computer runs show that this thermal "locking" is unnecessary when gaseous conduction is present, although desirable in vacuum.

6.3 CRYOGENIC THERMAL CONTROL

The effect of introducing power inputs to the FIRAS system was evaluated by setting all temperatures at 1.8°K at the start of the computation. Figures 6.3-1 and 6.3-2 show the introduction of 1.0 mw in the motor poles, armature, and reference blackbody source, and 10 mw in the calibrator blackbody source. Temperatures are shown linearly (°K) vs. log time (seconds), but note that the time scale is one-tenth that of the figures in Section 6.2. The time constant of the calibrator (21) is about five minutes as configured here, in order that the power dissipation does not become excessive, even short term. The thermal conductance to the calibrator source is fixed, and the time constant is larger in consequence, with stabilization accomplished in the enclosing cavity. Increase in temperature can be quite rapid if the calibrator heater is overdriven, and the slow cooldown relegated to the enclosing cavity. An alternative method could utilize higher thermal conductance in the cavity through mesh contact with a cold surface, allowing more rapid resetting after a high calibration temperature has been attained.

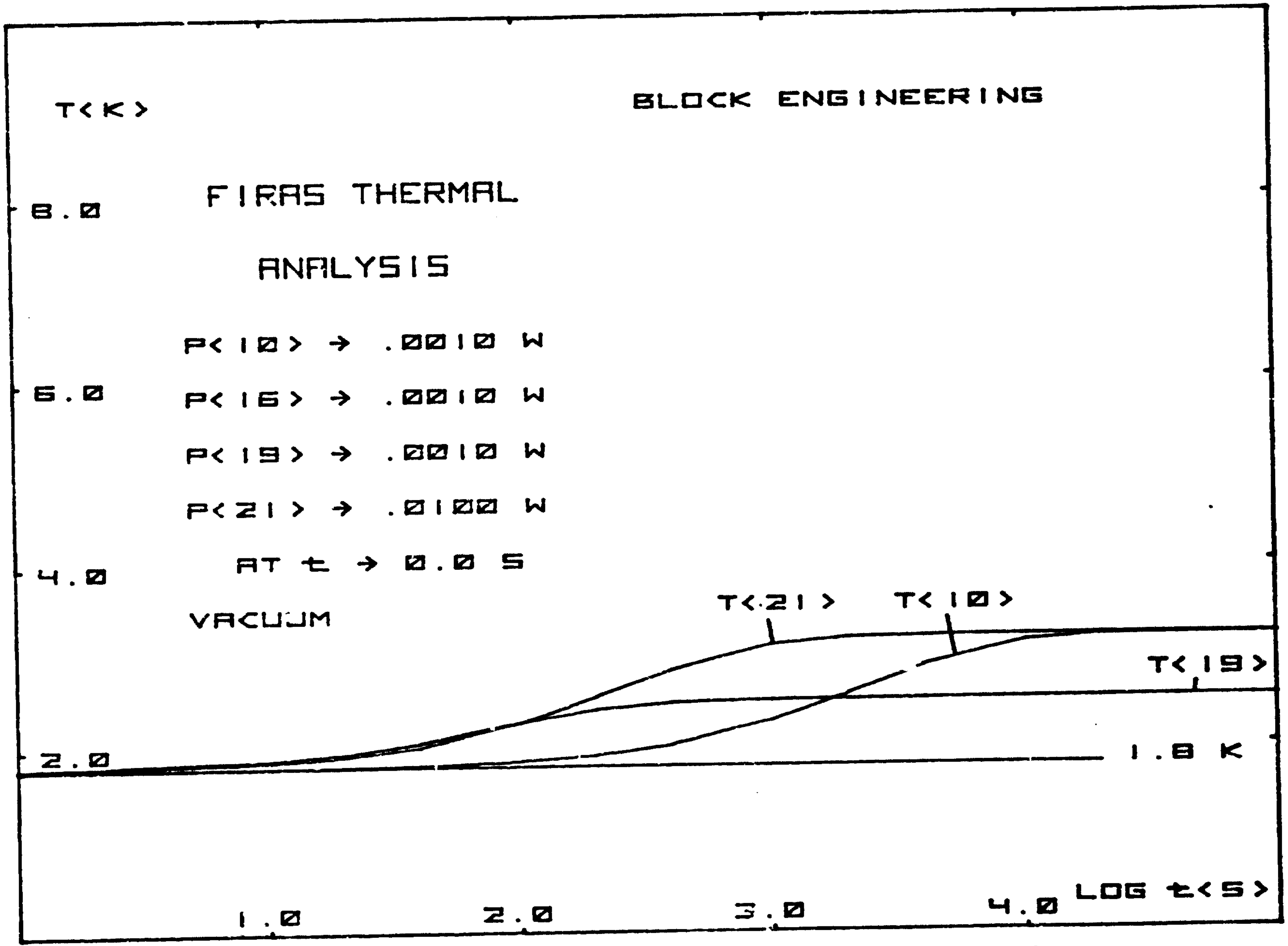

Figure 6.3-1. Cryogenic Control, Low Power (Sources)

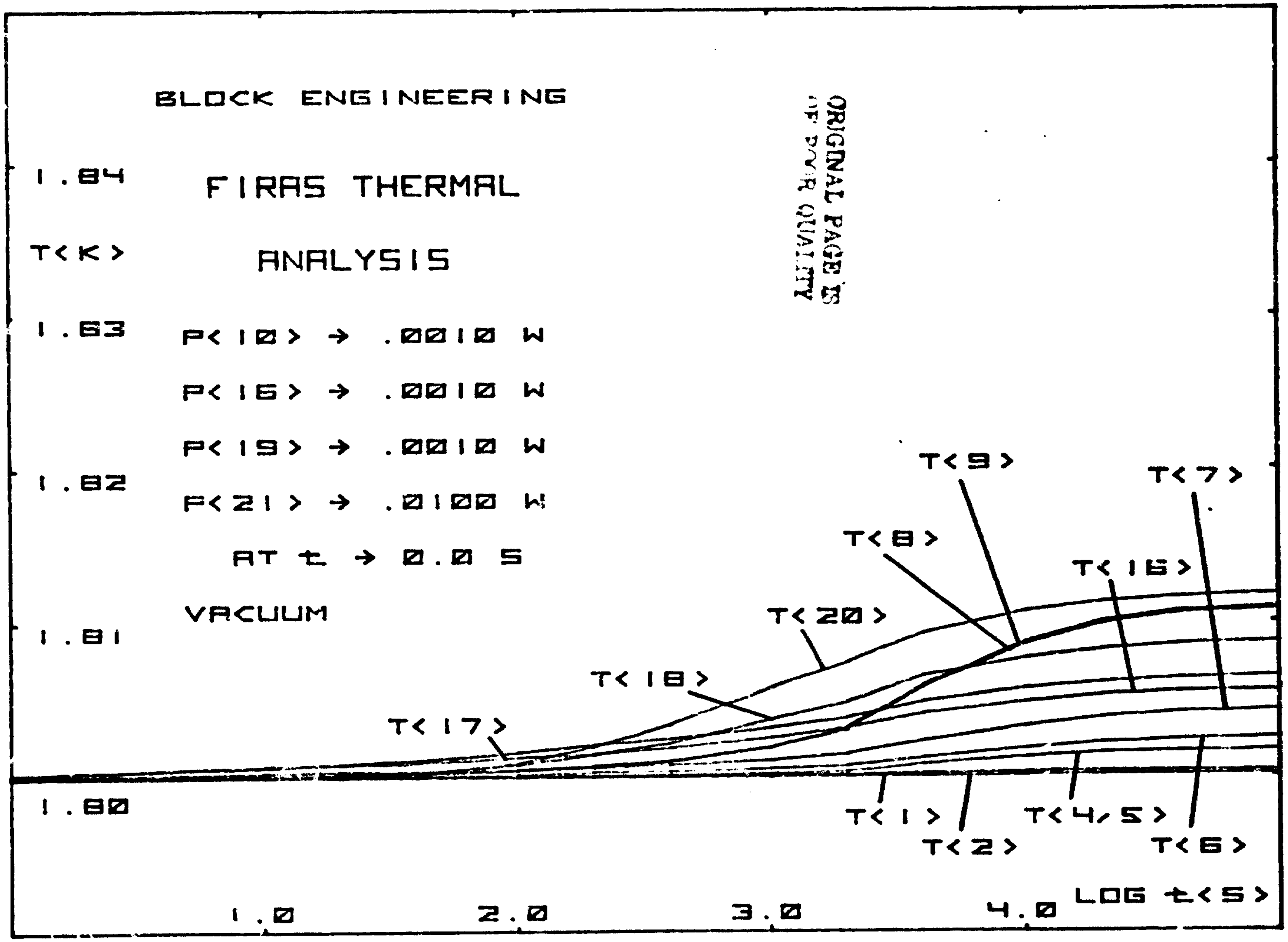

ORIGINAL PAGE IS
OF POOR QUALITY

Figure 6.3-2 Cryogenic Control, Low Power (System)

We note that the reference blackbody (19) time constant is faster than that of the calibrator blackbody, or about one minute. This primarily results from the much lower heat capacity of the aluminum used in the reference blackbody, despite the higher thermal conductance of the copper wires used to cool the calibrator source. The motor armature time constant is about one hour, not contacting at the end positions. The motor alternated position with each iteration, resulting in a minor assymetry of power conducted from each end, giving the slight difference between the collimator mirror (8 and 9) temperatures (<0.001 °K). Locking the motor at one end with power applied results in a differential of about 0.1°K in the collimator mirror temperatures, and is certainly not desirable in normal operation, although it could be tolerated during launch.

Figures 6.3-3 and 6.3-4 show the effects of higher power dissipation in the calibrator (21) and reference (19) sources. Motor (10) power was reduced to show the effects of the sources more clearly, while maintaining non-contacting alternation of position. The system responds to the higher power levels through conduction, with a greater increase in temperatures near the sources. We observe that the calibration cavity (20), the calibrator and reference cone (18 and 17), and the top plate (16) are most affected. These differences are strong indicators that superconducting coatings are most desirable, especially in the blackbody cones. In the other optical elements, the strict symmetry of the system and the shielding of the interferometer from the upper cones and the calibrator element (except as seen through its cone) prevents any significant thermal imbalance in the radiation fields.

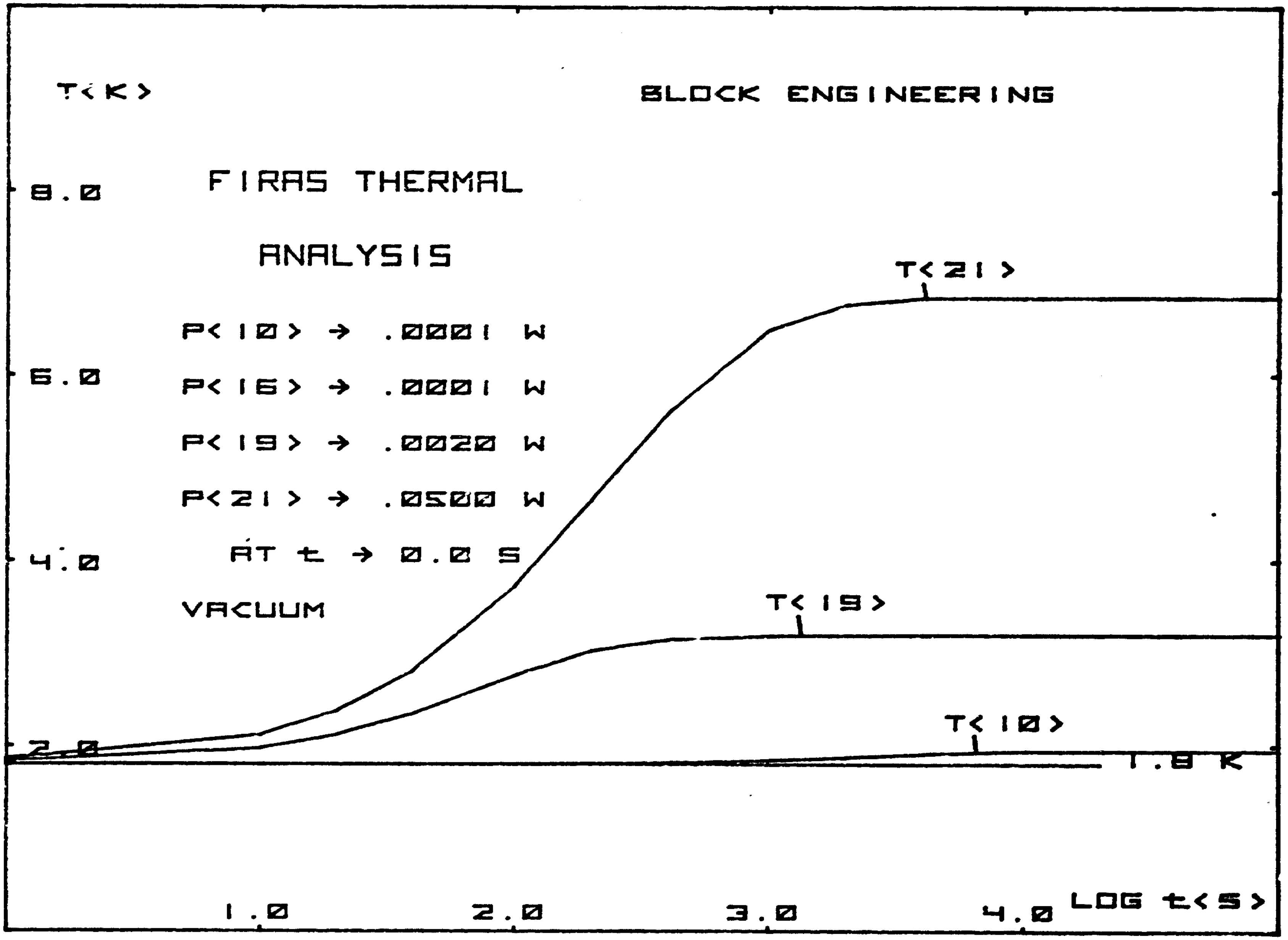

Figure 6.3-3. Cryogenic Control, High Power (Sources)

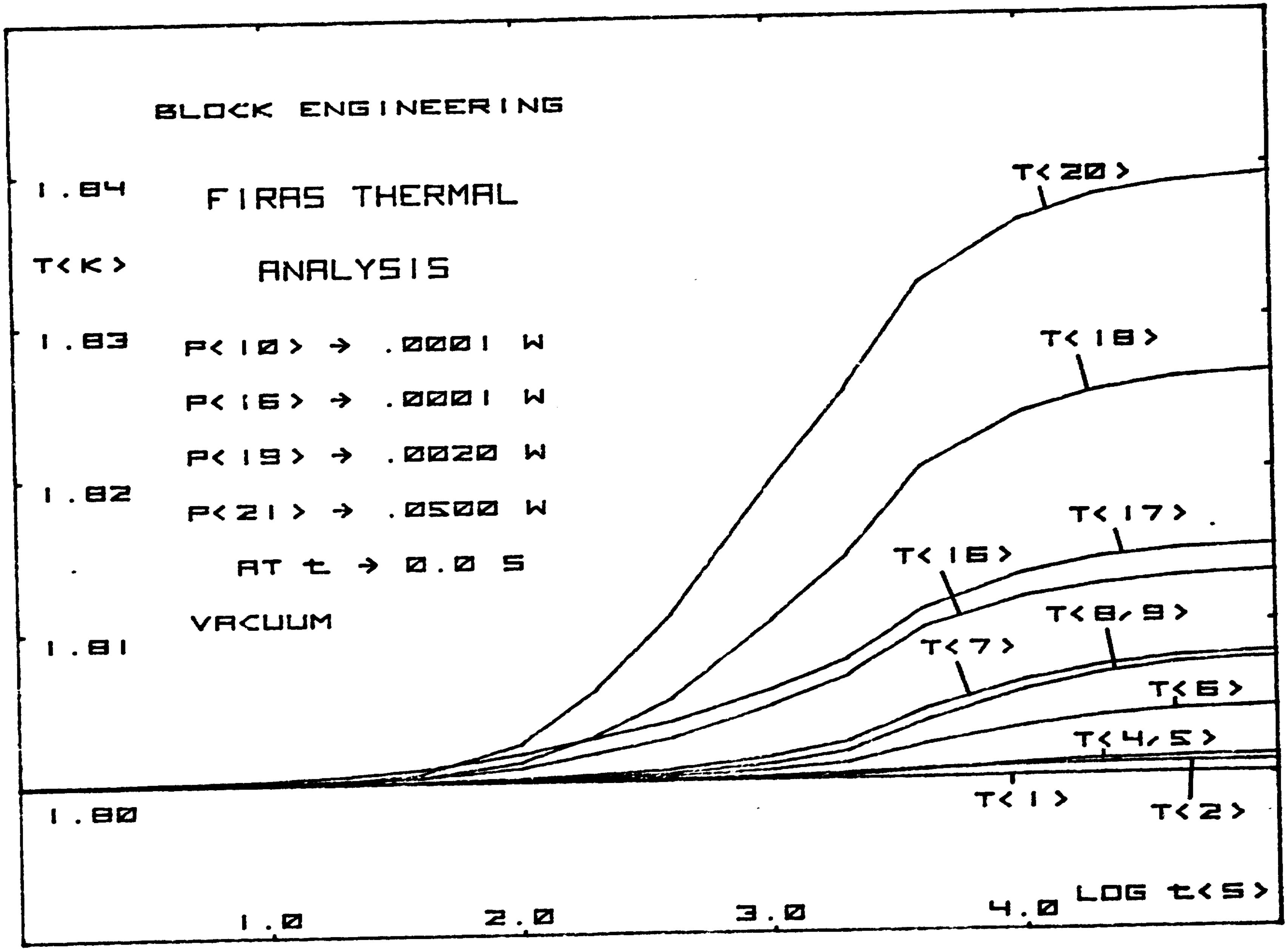

Figure 6.3-4. Cryogenic Control, High Power (System)

7.0 ELECTRONICS AND POWER SYSTEMS

The electronic and power systems for the FIRAS system are indicated in block form in Figure 7.0-1. Signal electronics consist of four detector channels with band-limited amplification, multiplexer and analog-to-digital converter. Motor drive electronics consist of three position sensors, amplification and digital processing, and drive power circuitry. Temperature control electronics utilize temperature sensors, summing amplifiers, and heater drive circuitry. Temperature indicator electronics require sensors and amplifiers, and with other housekeeping functions are multiplexed for telemetry.

Detector bias and preamplifier circuitry are discussed briefly in Section 3. Digitized outputs are stored in memory for editing on the basis

$$I_j = AM_j + (1-A)\ I_j \qquad (7.0\text{-}1)$$

where A is a storage weighting factor,

$A = 1$ on first scan

$A = k < 1$ on subsequent scans

I_j is the accumulated $j^{\underline{th}}$ interferogram point

M_j is the measured $j^{\underline{th}}$ interferogram point

Prior to storage, the M_j point is compared to the I_j point to determine if it lies within acceptable limits. If it is not, the point can be replaced with I_j point for telemetry, or the point can be identified for later processing and an error signal communicated.

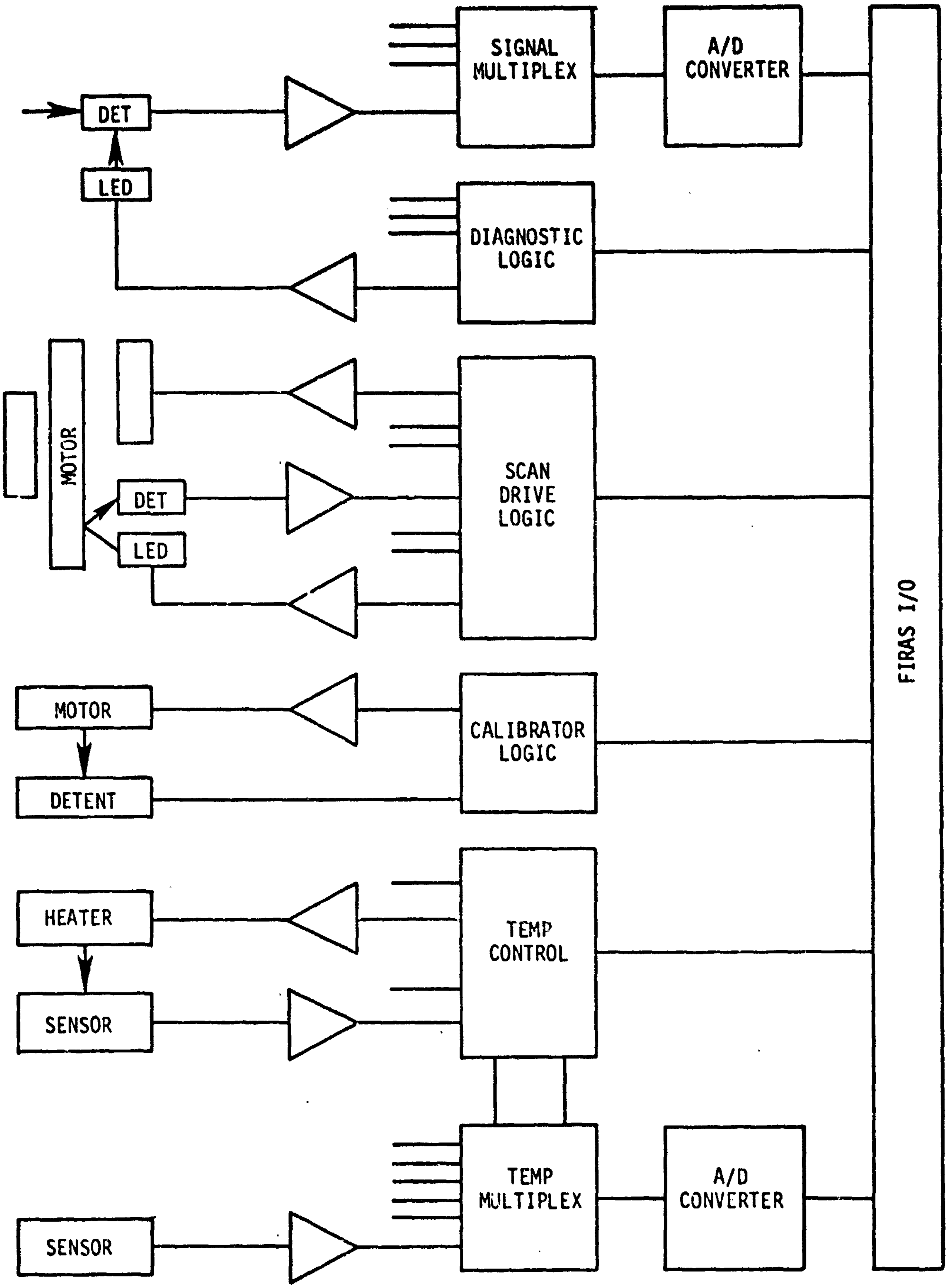

Figure 7.0-1. FIRAS Electronic Block Diagram

Needless to say, a bad point need not be stored in the I_j matrix, but a better technique would be the suppression of the questionable point by reducing A in proportion to the error for the point in question. This permits the matrix to follow gradual changes in the interferogram without affecting its "deglitching" capability.

The motor drive servo control scheme is described in the block diagram in Figure 7.0-2. Three sensors are used, although one of these simply provides a non-contacing absolute fiducial mark necessary only in initializing the scanning sequence. The sensors are excited from micropower light emitting diodes, which illuminate strips of dark-banded reflecting material. The LED illuminators are excited at a "carrier" frequency, w, producing a modulated sinusoidal detector output. The two banded strips are coded in quadrature to provide a frequency

$$N\dot{B} << w \tag{7.0-2}$$

where N is the number of bands/cm and $\dot{B}$ is the velocity of the armature, cm/second. The resulting detector output are summed to give a signal

$$E_s = \text{Sin } (w + gn\dot{B})t \tag{7.0-3}$$

where $g = 2\pi$ and t is the time in seconds. The quantity $\dot{B}$ can be positive or negative, and could be considered as the retardation rate with an appropriate adjustment in g.

The desired velocity is input to the system as a constant K, used to divide the oscillator frequency w in order to produce a reference input.

$$E_r = \text{Sin } (W \pm w/K)t. \tag{7.0-4}$$

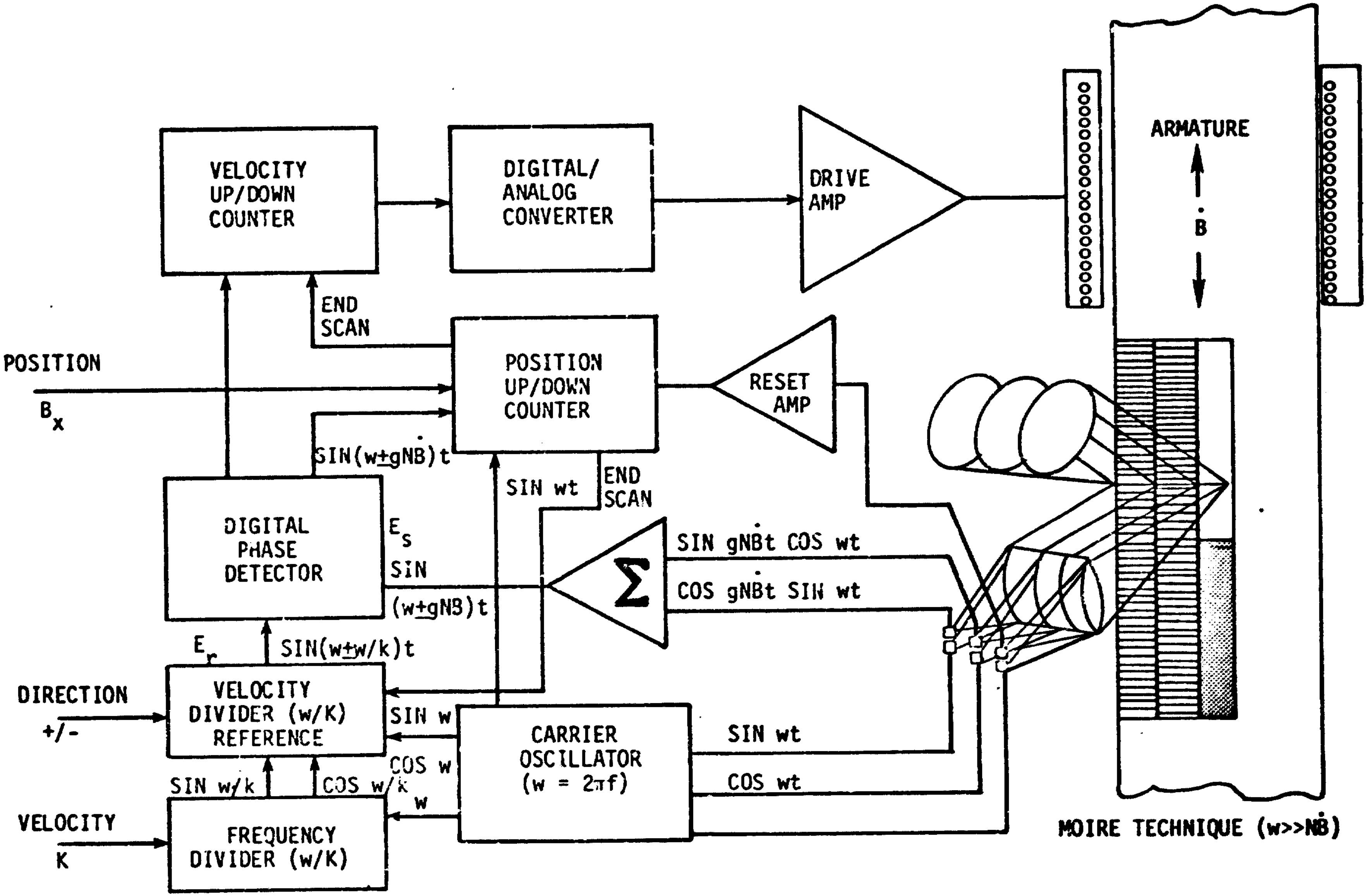

Figure 7.0-2. FIRAS DRIVE SERVO CONTROL

The signal and reference inputs are compared in a digital phase detector, which produces positive or negative output pulses at a rate proportional to the phase error between E_r and E_s for phase errors between ±90°, and at a constant rate for larger phase errors. The velocity is held in a bipolar up-down counter, and the motor drive amplifiers respond to this accumulated count through a digital-to-analog converter.

Position is monitored by another up-down counter buffered to permit simultaneous inputs of E_s and the carrier frequency, which act in opposition. The desired position extremes are input, and an end-of-scan signal is generated when the positions are attained. This signal simultaneously reverses the direction input to the reference generator and resets the velocity counter to stop the scan. This reset can introduce a fast, high energy reversing pulse to the drive amplifier, resulting in more rapid turn around. An external direction command can be used to override the end-of-scan signal and force the drive to the end position for higher thermal conductance (the adjustment of the velocity parameter K permits adjustment of the effective force maintained at this contact. The position counter is reset each time the reset detector senses the band termination at the central "zero path difference" position in the scan. Alternatively, this reset can be done by command, but the counter position checked each scan and an error signal is provided if the position count is incorrect.

Temperature control of the reference and calibrator sources requires accurate temperature measurement, comparison with input desired temperature values, and generation of suitable heater drive signals. Power is minimized if low thermal conductance is used, but this leads to slow thermal response. Rapid increase in calibrator temperature is possible by using high power pulsing to change the temperature, and low continuing power to maintain temperature. Cooldown to instrument ambient occurs after calibration by shifting the "hot" calibrator into its cavity, where it could shift to contact a higher conductance pad at the end of the shift motion. Four temperature sensors are mounted on each source, and then outputs are combined to provide the control signal. All temperature sensor outputs can be sampled by the temperature multiplexer to facilitate system error analysis. If it is elected to provide a small, higher temperature source in the calibration for the short wavelength detectors, only one temperature sensor would be used for that part of the calibrator.

Insertion of the calibrator is accomplished by a geneva drive activated by a servo motor. Simple electrical switching at the stop positions is adequate, since the geneva permits a broad tolerance in drive motor positioning at the mechanically precise lock points. Switch outputs also provide indications of calibrator detent position lock.

8.0 COMMAND AND CONTROL

A micro-processor-based sequencer is suggested to control system operation. Figure 8.0-1 shows a recommended command/control system block diagram using such a sequencer. Functions under control of the micro-processor would be:

Data Collection, Storage and Dump

Prestored data collection routine would determine the number of scans collected for each scan direction, add housekeeping data, and indicate diagnostic routines in effect.

Overall Instrument Operation

Prestored scan routines would include independent control of forward and reverse scan velocity, retardation distance, and acceleration and deacceleration profiles, as well as radiometric calibration routines.

Diagnostic Routines

This would include programmed changes in scan parameters, detector bias control, control of the test LED inputs (simulating single pulses, pulse trains, interferograms, control of detector photon background level). It also would include reference and calibrator diagnostics, e.g. individual temperature sensor and heater circuit verification.

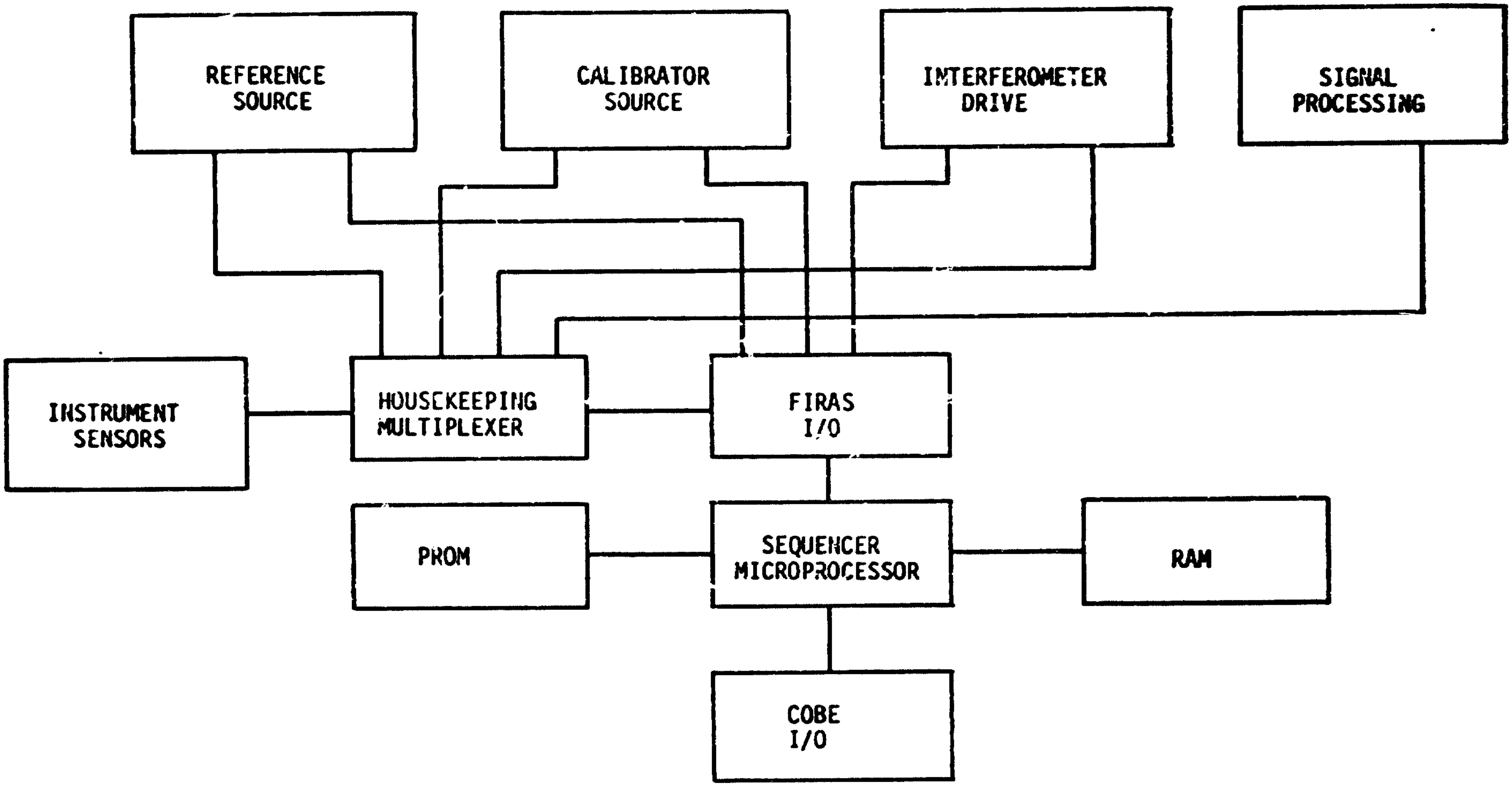

Figure 8.0-1. FIRAS COMMAND AND CONTROL

All these sequences would be stored in programmable read-only memory (PROM) with an alterable memory (RAM) to accept new commands via the command and control interface link. Some aspects of the data processing system requirements are given in Appendix C.

9.0 CALIBRATION

The calibration of the FIRAS instrument involves the radiometric calibration of the optical system through to each detector and the spectral calibration of all detectors under each anticipated scanning mode. Calibration of radiometric and spectral response is made on the ground, and the calibrator source radiometry is determined relative to an accurately known ground-based standard. In space, the calibrator permits in-flight radiometric calibration of the instrument, but no further spectral calibration is provided due to the fundamentally mechanical character of the instruments spectral response.

9.1 RADIOMETRIC CALIBRATIONS

Proper radiometric calibration of the FIRAS instrument requires that the input horn be filled with radiation from a precisely known blackbody source. Although many approaches can be used that are more compact, it is suggested that the largest possible cavity source be fabricated, within a dewar housing permitting accurate control of temperature using helium vapor or liquid. Indeed, if two COBE dewars were available it might be convenient to place a large cavity emitting surface inside one and make a vacuum-tight connection to the FIRAS dewar in the other. Eccosorb surfaces within the large source would give improved emissivity.

Calibration of the instrument response within the field-of-view requires the placement of the entire instrument into a large vacuum chamber. If accurately controlled chamber walls are not present, cold shrouds may be used to shield the system input from uncontrolled background. A small aperture source can be moved into the field to determine the differential signal, or a cold shutter opened and closed to block its aperture. The instrument field of view can be mapped using a movable, shuttered source, and this field responsivity is an important instrumental parameter.

The internal FIRAS calibrator must be compared with an external source which entirely covers the horn entrance, such as the large cavity source indicated above. Several test temperatures need to be measured to establish the linearity of the calibrator response.

The programming of the diagnostic interferogram input provided to each detector from a light emitting diode is another calibration of value, since these diodes are highly repeatable, with very stable photon/electron gains. This diagnostic interferogram can be a duplication of a blackbody or laser source interferogram calibrated by independent means, stored in memory and adjusted in LED drive amplitude to match the calibrated signal. Other functions can be programmed based on the measured photon/electron gains.

The use of astronomical objects, such as planets, as calibration sources is not recommended. These sources will serve as valuable test inputs to check the calibration, but are not know well enough to provide accurate calibration to the levels required here.

9.2 SPECTRAL CALIBRATION

Measurement of the signal interferogram obtained when illumination from a far-infrared laser input of constant amplitude allows the examination of the spectral response. Observed apodization as a function of scan length and speed can be examined directly, or the output can be transformed to provide the spectral line(s) for verification. The laser input can be shifted in angle to obtain an effective indication of spectral response variations, which may be of interest if point sources of line emission are anticipated. (We note that the mixing effects of the Winston cones complicate the input angle relationship to the interferometer obliquity angle, producing slight spectral effects in the field of view.)

The use of a radio frequency generator to provide a spectral signal for calibration is subject to the uniformity of field of that source with angle. Since this field response must be convolved with the FIRAS field, including apodization effects, this calibration may be less reliable.

9.3 SYSTEM LINEARITY CALIBRATION

The possibility of non-linearity in the detector responsivity function requires that an accurate calibration of system linearity be made. The detector responsivity is specifically related to the photon flux and the detector temperature, and the electrical gain is highly stable, so the measurement of signal output can be accurately and reproducibly corrected.

The detector itself is used as the calibration standard, operated in the low flux linear portion of its response. In order to provide a calibration extending over the range of signals expected, a far infrared laser reference source is used with multiple attenuators, all of equal attenuation. The source is chopped at a frequency within the amplifier band by scanning the interferometer over a limited retardation interval about the centerburst position. All attenuators are placed in the optical path and the measurement made to obtain low flux response. This sequence is repeated for a range of input radiation levels, allowing the full system linearity to be determined. The advantages of this approach are that the laser radiation levels do not have to be known, nor does the system efficiency. It is necessary to determine precise peak-to-peak amplitudes of the signals, since the waveforms may be deformed sinusoids, or to transform the output to obtain spectra.

The same laser can be used to verify the envelope modulation efficiency in the interferogram. A different laser could be used to demonstrate spectral effect in the system linearity, but there are no inherent reasons to expect such spectral variation.

9.4 SYSTEM NOISE CALIBRATION

The measurement of a cold source with the scan locked at either extreme provides an indication of system noise exclusive of any sampling noise, as well as digitizing noise in the data chain. Since the scan is inoperative, an artificial sampling signal of great precision can be provided by dividing down the reference oscillator signal. Other than this, the measurement is treated like any other measurement.

10. SYSTEM TEST REQUIREMENTS

A variety of subsystem and system testing is recommended for the FIRAS instrument. Most important subsystem tests are detector, scan motor, and calibrator mechanism tests. System tests include cooldown, cryogenic operation of mechanisms and thermal controls, and electronic processing evaluation. Environmental testing is an important requirement for instrucment evaluation. Finally, careful accpetance testing is essential to determine system readiness prior to launch.

10.1 SUBSYSTEM TESTING

Testing and evaluation of detectors and preamplifier stages is necessary prior to their installation in the detector subassembly. Great care is needed in this testing to reduce background radiation to 1.8°K and provide low level signal radiation of known power. It is useful to use a metal reflecting integrating sphere connected to a blackbody cavity and/or other sources of radiation (laser, oscillator), with the detector mounted at a port 90° from the source port, backed by a metal reflective cavity which could be a second integrated sphere. A second useful approach is the use of a collimated narrow band far infrared beam to illuminate the detector mounted over an aperture in a flate reflective plane, with absorbing material in front and behind the plane to prevent multiple reflections. In this approach, the detector response at selected incident angles is determined, allowing definition of the angular field responsivity. This is useful if anomalies appear in the straight radiometric measurement indicated above, which integrates the response to a Lambertian field over 4π sterradians.

Detector testing should also be evaluated after mounting in the Winston cone condensor optics. This optic can be illuminated from the integrating sphere above to obtain total response over 2π sterradians. The optic can then be illuminated by a "point" source of small angular extent which can be moved relative to the detector-cone field to map the combined angular response function. Vibration testing of the mounted detector is, of course, desirable.

A prototype scan motor assembly should be tested and evaluated at cryogenic temperature in vacuum after repeatedly cycling to ambient in the first phase of life testing. Motor components should be examined after each cryogenic test for wear and damage, preferably without dissassembly. Life testing should extend at cryogenic temperature in vacuum for as long a period as possible, up to the desired one year mission period. During testing, motor power should be monitored and alignment verified optically using flat mirrors mounted orthogonally to the drive direction. (Remote measurement using aligned collimators or HeNe lasers outside of the cryogenic tank are satisfactory.) A duplicate scan motor assembly should be tested in vibration and shock to determine its capability to survive launch and injection into orbit. This assembly should include reference sensors and LED components, and the motor should be powered during testing, either scanning or locked at some selected position. Dissassembly and examination after testing are an important part of the evaluation of the motor assembly.

The calibrator insertion mechanism requires cryogenic testing with cycling to ambient, and repeated operational cycles with long cold soak times between operations. A duplicate calibration mechanism should be tested in vibration and shock if it is not intended that the entire FIRAS system be so evaluated.

10.2 SYSTEM TESTING

Tests of the entire FIRAS system, mounted in the COBE dewar, are recommended. Cooldown of the entire assembly should be performed with temperature monitors added for the test to evaluate the entire system's thermal performance. Of special interest are the sky and reference blackbody houns, the calibrator mechanism, the motor assembly, and the optical components.

11.0 INSTRUMENT INTERFACE

The interface of the FIRAS instrument with the remainder of the COBE satellite is mechanical, thermal, and electrical in nature. The details of the interface are, of course, dependent on the detailed system design, particularly in terms of the electrical and data system interface.

Block requested and was provided with drawings of the COBE dewar (Ball Brothers Dwg. SK57740) and the instrument support framework (NASA/GSFC FIRAS Interface Concept*) which provided the basis of the mechanical and thermal interface. The instrument is mounted at its base, attaching to the instrument support near the points of that attachment to the COBE dewar mounting ring. Secondary attachment points are made roughly half way up the instrument support framework. The sky input and reference blackbody hours are essentially free-standing structures, either unattached or flexibly connected to the top instrument cover. Block recommends mechanical isolation from this cover to avoid distortion of the houn structures, thermal isolation from the cover if the DIRBE instrument contributes notable heating there, but full peripheral electrical connection to improve sidelobe rejection in the antenna pattern.

Thermal analysis has led to heat strap requirements, particularly in the event that gaseous cooling is not permitted. The upper bulkhead, the detector assembly, and the calibrator assembly require minimum length flexible copper straps to the dewar surface. The first two utilize conventional strapping, but the calibrator plate itself is cooled

---

* Incomplete

by conduction through the copper heater wires. These wires must be thermally locked to the dewar or to a free surface connected by heat strapping to the dewar (not the upper bulkhead or the support structure). Actually, most wiring entering the dewar should be thermally connected to the upper bulkhead within the FIRAS instrument, but this is insufficiently stable for the calibrator and the detectors. (In the reference blackbody source, it may be possible to simply use the wire thermal input as a part of the two milliwatt heating power, since electrical control is provided.)

The electrical interface is less certain, and depends on the extent of temperature sensing desired. The electrical interface has two entirely separate aspects: the interface at the COBE dewar and the system interface at the electronics bay. Table 11.0-I shows a tentative wire distribution for the dewar. We have assumed temperature sensors at each side of the detector assembly, on the two preamplifier mounting plates, at each collimator mirror, on each polarizer frame, on the motor armature (dihedral mirrors) and pole assemblies, on the upper and lower portions of the sky input and reference blackbody cones, on the calibrator and reference blackbody plates (4 each), on the calibration cavity, and on the upper FIRAS bulkhead. Two wires are assumed for each, but in some cases (calibration and reference sources) a four wire scheme may be preferable. An additional sensor may be used for a hot spot section of the calibrator source. Three wires are assumed for each detector on the assumption that an input stage of preamplification is used, and shielding of the signal wires is recommended.

TABLE 11.0-I
COBE/FIRAS DEWAR INTERFACE

Item	Qty	Wires
Detectors	4	4 + 8 shielded
Light Emitting Diodes	4	5
Motor Reference Detectors	3	4
Motor Light Emitting Diodes	3	3
Motor Drive	1	6
Temperature Sensors		1 common
Detector	2	2
Preamplifier Mounts (60°K)	2	2
Collimator Mirror	2	2
Polarizer Frame	2	2
Motor Armature	1	2 flexible coils
Motor Pole	1	1
Sky & Reference Horns	4	4
Calibrator Blackbody Source	4	8(16b)
Reference Blackbody Source (a)	4 or 5	8(16b) or 10(20b)
Calibrator Cavity	1	1
Upper FIRAS Bulkhead	1	1
Heaters		
Preamplifier Mounts (60°K)	2	4
Calibrator Blackbody Source (a)	1 or 2	2 or 4
Reference Blackbody Source	1	2
Total Wire Count		72(886) a: 76(926)

a: Hot spot option additional

b: Four wire connection option additional

Heater wires are provided for the calibrator and reference sources and the two first stage preamplifier mounts. The wire count is high, but a considerable reduction has been obtained consolidating ground returns wherever possible. Detector and motor drive wiring should be isolated, as well as temperature sensor and heater wires from the calibration and reference blackbody sources.

12.0 RECOMMENDATIONS FOR CONTINUED WORK

The activities believed most essential to the successful completion of the FIRAS instrument are the detailed mechanical design effort, the test and evaluation of the motor, and bearing, and the development and implementation of superconducting reflective horns.

12.1 SUPERCONDUCTING REFLECTIVE HORNS

The most pressing requirement for the FIRAS program is the development and testing of superconducting coatings for the sky input and reference blackbody horns, using a technique consistent with the fabrication of the horn structures. The integrity of these blackbody sources is significantly compromised if ordinary metal reflection must be used for these surfaces, since the measured data then require computer correction for the erroneous component and accurate thermal stabilization of the massive horn structures is essential. Block has suggested electroforming the horn in sequence beginning with a superconducting indium coating, and proceeding to the structural support metal. The application of superconducting coatings to the other metal optics is of interest, but easier and less important to attain.

12.2 MOTOR BEARING AND DRIVE

The test and evaluation of a motor bearing and drive is considered of major importance to the design. Block has designed and fabricated a linear roller bearing assembly under an independent R&D house program, and hopes to conduct further evaluation of this device. Preliminary tests showed that the bearing has been fabricated with a warped drive shaft, leading to a tilt variation of several arc minutes. The drive shaft has been remade, and all bearing surfaces have been polished to eliminate roughness. Block would prefer to perform preliminary testing of the bearing, both at ambient and at cryogenic temperatures before providing a life test assembly to NASA/GSFC for extensive testing. A modest support program would greatly accelerate this process, which otherwise must wait upon higher priority contracted efforts. We believe that the immediate initiation of an extended life program without a preliminary evaluation would almost certainly predispose the assembly to failure, probably for trivial design reasons.

The program recommended by Block for the preliminary evaluation of the bearing and drive is given in Table 12.2-I. In view of the difficulty of maintaining responsive liaison with NASA/GSFC through intermittent support, Block urges a very low level continuing program rather than a compressed effort.

12.3 DETAILED DESIGN

The completion of the detailed instrument design is, of course, essential to the continuation of the COBE effort. Block is most interested in participation in this detail design effort under contract, in terms of limited specific assignments, overall design, or as a supportive consultant.

TABLE 12.2-I

FIRAS Bearing/Drive Evaluation Program

I. Bearing Evaluation	
Ambient Testing:	Tilt, force, uniformity, microphotographic record
Cryogenic LN_2 Testing:	Tilt, force, uniformity
Cyclic Testing:	Five additional cycles between ambient and LN_2, at least 24 hours at each temperature
Final Ambient Evaluation:	Tilt, force, uniformity microphotographic record, comparison
II. Drive Fabrication	
Detail Design:	Pole, armature, position sensors, control servo, electronic
Procurement:	
Assembly:	Build on FIRAS bearing assembly
Debugging:	Ambient
III. Drive Evaluation	
Ambient Testing:	Power, force, inductance, uniformity, velocities from zero to ±3.0 cm/s (±10 cm/s retardation rate)
Cryogenic LN_2 Testing:	Power, force, uniformity, velocity range

APPENDIX A

A. HORN EMISSIVITY

The approach to the analysis of the emissivity of the two blackbody sources in the FIRAS system was developed from the work of Hochheimer (1977). The sources consist of an emissive plate at an angle θ to the optical axis of a reflective Winston cone, measured from the plate normal. The emissive plate is cut with V-grooves running parallel to the long dimension of the plate, where the V-angle is 2α and the local surface emissivity is $\underline{e}$. The area of the emissive surface is A, which is larger than the projected area by the factor of the V-grooves. The area of the reflective surface is B, with mean reflectivity of $\underline{r}$ and mean emissivity assumed to be given by $\underline{1-r}$. Rays exit at the reflective end through the opening $\underline{s}$.

In this analysis, we will not integrate the contributions from each point over the interior surface, but will obtain these factors through various techniques for each area, A and B. The radiation emitted from the area A is

$$P_a = N_a e A \pi \tag{A-1}$$

where N_a is the blackbody radiance at temperature T_a. The energy which leaves the cavity through the aperture $\underline{s}$ is

$$P_{ao} = P_a K_a \tag{A-2}$$

where

$$K_a = \Omega_a (\mathrm{Cos}\ \theta_a)/\pi \tag{A-3}$$

The angle between the local surface normal and the centerline of the effective solid angle Ω_a is θ_a, which is essentially invarient over the entire area A for the afocal Winston cone. This angle is given by

$$\text{Cos}\ \theta_a = \text{Cos}\ \theta\ \text{Sin}\ \alpha \qquad (A-4)$$

The nature of the Winston cone is such that radiation exits either directly or after one reflection. Direct radiation exits within the solid angle defined by

$$\Omega_s = 2\pi\ (1 - \text{Cos}\ \phi_s) \qquad (A-5)$$

while singly reflected radiation exits within the solid angle extending from Ω_s out to

$$\Omega_w = 2\pi\ (1 - \text{Cos}\ \phi_w) \qquad (A-6)$$

where ϕ_s is the half-angle of the aperture viewed from the source and ϕ_w is the half-angle of the Winston cone (3.5° in the present case). The weighted value for the solid angle is

$$\Omega_a = r\ \Omega_w + (1-r)\ \Omega_s \qquad (A-7)$$

The remaining power emitted from the A surface, $P_a(1-K_a)$ can never exit without first reflecting from the A surface again, assuming that reflective surface scattering is neglible. The paths of all rays returning to the source experience complex reflections too involved to treat analytically here, and an approximation technique is used. The attenuation of reflected radiation returning to A is characterized by a function

$F(r)$, which will vary depending on the exact configuration. Of this returned radiation, only a fraction $P_a(1-K_a)\,F(r)\,(1-e)\,K_a$ will exit from the cavity, on the assumption of Lambertian scattering from the A surface. Again, $(1-K_a)$ of this remains, and $P_a(1-K_a)^2F(r)^2(1-e)$ returns for a second scattering. This results in the following series for the exiting A radiation:

$$\begin{aligned} P_{at} &= P_aK_a + P_aK_a(1-K_a)F(r)(1-e) + P_aK_a(1-K_a)^2F(r)^2(1-e)^2 \\ &\quad + P_aK_a(1-K_a)^3F(r)^3(1-e)^3 + \cdots \qquad \text{(A-8)} \\ &= P_aK_a\,[1 - (1-K_a)F(r)(1-e)]^{-1} \\ &= P_aK_aM \end{aligned}$$

In determining an approximation to the reflection distribution function $F(r)$, we note that the A surface end of the Winston cone can only reflect back to itself in one or two reflections if there is some tilt, and that the relative magnitude of these first few reflections is proportional to the amount of the tilt in a complicated way. A series of arbitrary constants can be used to weight the r^N terms to correspond to any complex reflective configuration, but a functional, convergent series permits greater operational flexibility. No single series form provides such suppression of the first and second terms, but the difference between the series

$$r(1 + kr + k^2r^2 + k^3r^3 + \ldots) = r/(1-kr) \qquad \text{(A-9)}$$

and

$$r(1 + kr + k^2r^2/2! + k^3r^3/3! + \cdots) = re^{kr} \qquad \text{(A-10)}$$

will provide this suppression. The effect of the choice of k on the weighting is shown in Figure A-1, for the first thirty terms. A more general form of this function provides for a direct coupling term m which designates the fraction of the unexiting energy that is transmitted directly to the other side of the V-grooves. This expression is

$$F(r) = \frac{m + r^m \, (1/(1-kr) - me^{kr})}{m + 1/(1-k) - me^{k}} \qquad \text{(A-11)}$$

in its fully normalized form.

Maximization of the first and second terms is obtained when m=0 in the normalized expression

$$F(r) = \frac{1 + kr + k^2r^2 + k^3r^3 + \cdots}{1 + k + k^2 + k^3 + \cdots} = \frac{1 - k}{1 - kr} \qquad \text{(A-12)}$$

which is represented in Figure A-2 for different values of k.

In treating the emission from the reflecting walls, we note that the direct emission is similarly given as

$$P_{bo} = P_b K_b \qquad \text{(A-11)}$$

where

$$P_b = N_b(1-r)B\pi \qquad \text{(A-13)}$$

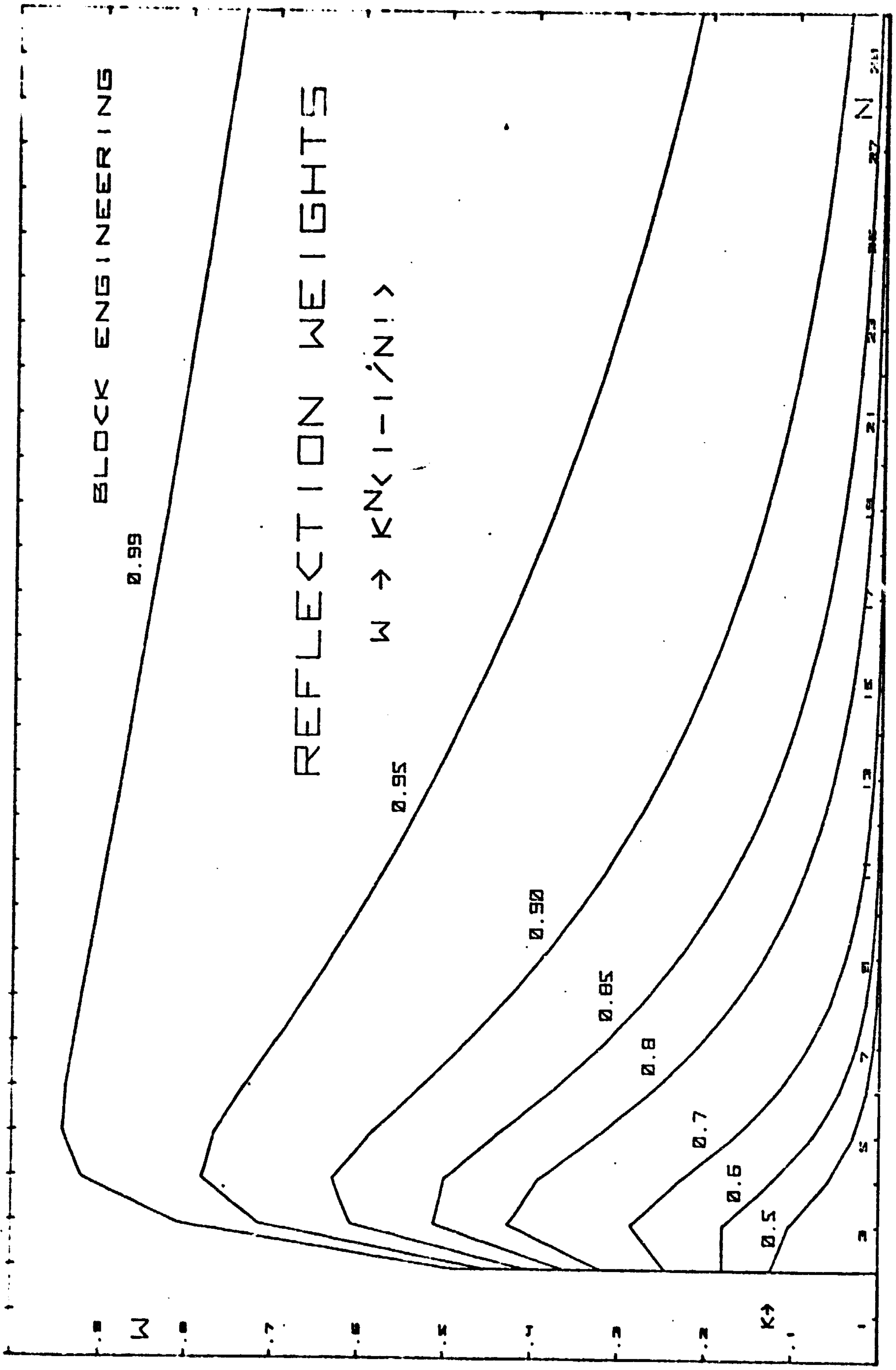

Figure A-1. F(r) Reflection Weights (m=1)

ORIGINAL PAGE IS
OF POOR QUALITY

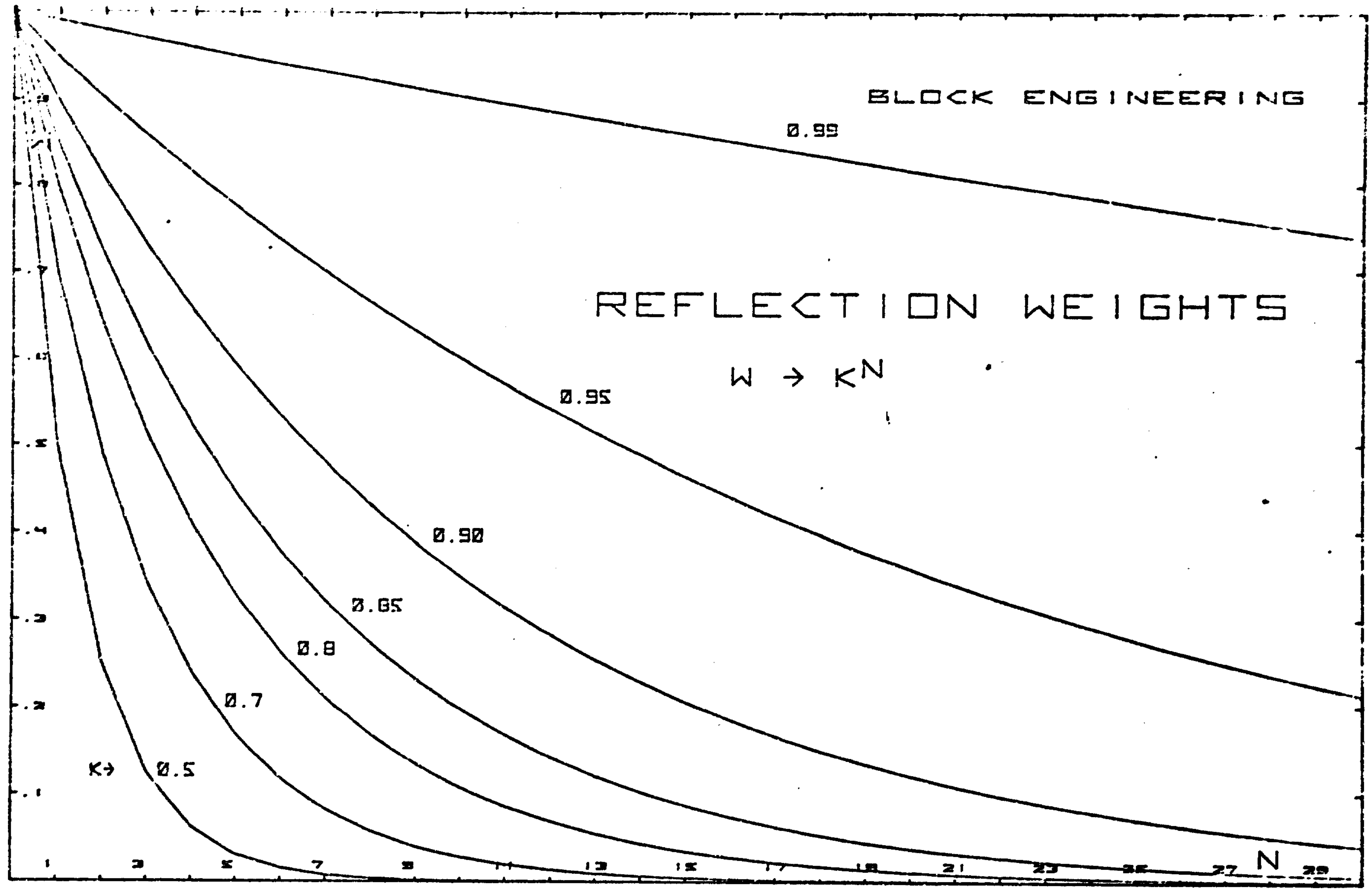

Figure A-2. F(r) Reflection Weights (m=0) and N_b is the blackbody radiance at temperature T_b, perhaps $\neq T_a$ and

$$K_b = \overline{\Omega_b(\cos\theta_b)/\pi} \qquad \text{(A-14)}$$

Here θ_b is the angle between the local surface normal and the center line of the solid angle cone subtended by the aperture <u>s</u>, as viewed from a point on the reflective surface. We will see that simplification is possible in obtaining K_b through application of boundary conditions, even though the surface is not Lambertian.

Of the radiation remaining within the cavity, $P_b(1-K_b)$, only A/B of this can experience diffuse reflection from the A surface before exiting, limited by throughput for each reflection. The attenuation of this in reaching the A surface is given by the reflection function G(r), which includes suitable weighting for each r^N factor. Once reaching the A surface, however, the subsequent surface interactions are exactly the same as for the normal emission from that surface itself, and we obtain

$$\begin{aligned} P_{bt} &= P_bK_b + P_bK_a(1-K_b)G(r)(1-e)A/B && \text{(A-15)} \\ &\quad + P_bK_a(1-K_b)G(r)(1-K_a)F(r)(1-e)^2A/B \\ &\quad + P_bK_a(1-K_b)G(r)(1-K_a)^2F(r)^2(1-e)^3A/B + \cdots \\ &= P_bK_b + P_bK_a(1-K_b)G(r)(1-e)M\ A/B && \text{(A-16)} \end{aligned}$$

The reflection distribution function G(r) views the A surface end through the Winston cone as roughly a series of concentric rings due to the almost tubular nature of the reflecting surface. A series which produces this distribution of r^N factors is easily obtained

$$G(r) = C\ (1 + 8r + 16r^2 + 24r^3 + \cdots) \qquad \text{(A-17)}$$

$$= C\ (1 + 8r/(1-r)^2)$$

which would be suitable except that it blows up at r = 1 and cannot be normalized. A more useful series is obtained by using a factor P to suppress the higher order terms and thereby truncate the series as actually occurs in the real, Winston cone. The normalized series is

$$G(r) = \frac{1 + 8Pr + 16P^2r^2 + 24\ P^3r^3 + \cdots}{1 + 8P + 16P^2 + 24P^3 +} \qquad \text{(A-18)}$$

$$G(r) = \frac{1 + 8rP/(1-Pr)^2}{1 + 8P/(1-P)^2} \qquad \text{(A-19)}$$

which is represented as normalized in Figure A-3 for different values of P. With larger tilt angle, the lower order terms become more heavily weighted, and lower value of P is indicated. Replacement of the factor (8) by an arbitrary factor could give moderate control over the weighting, especially for the first direct term relative to the other reflected terms.

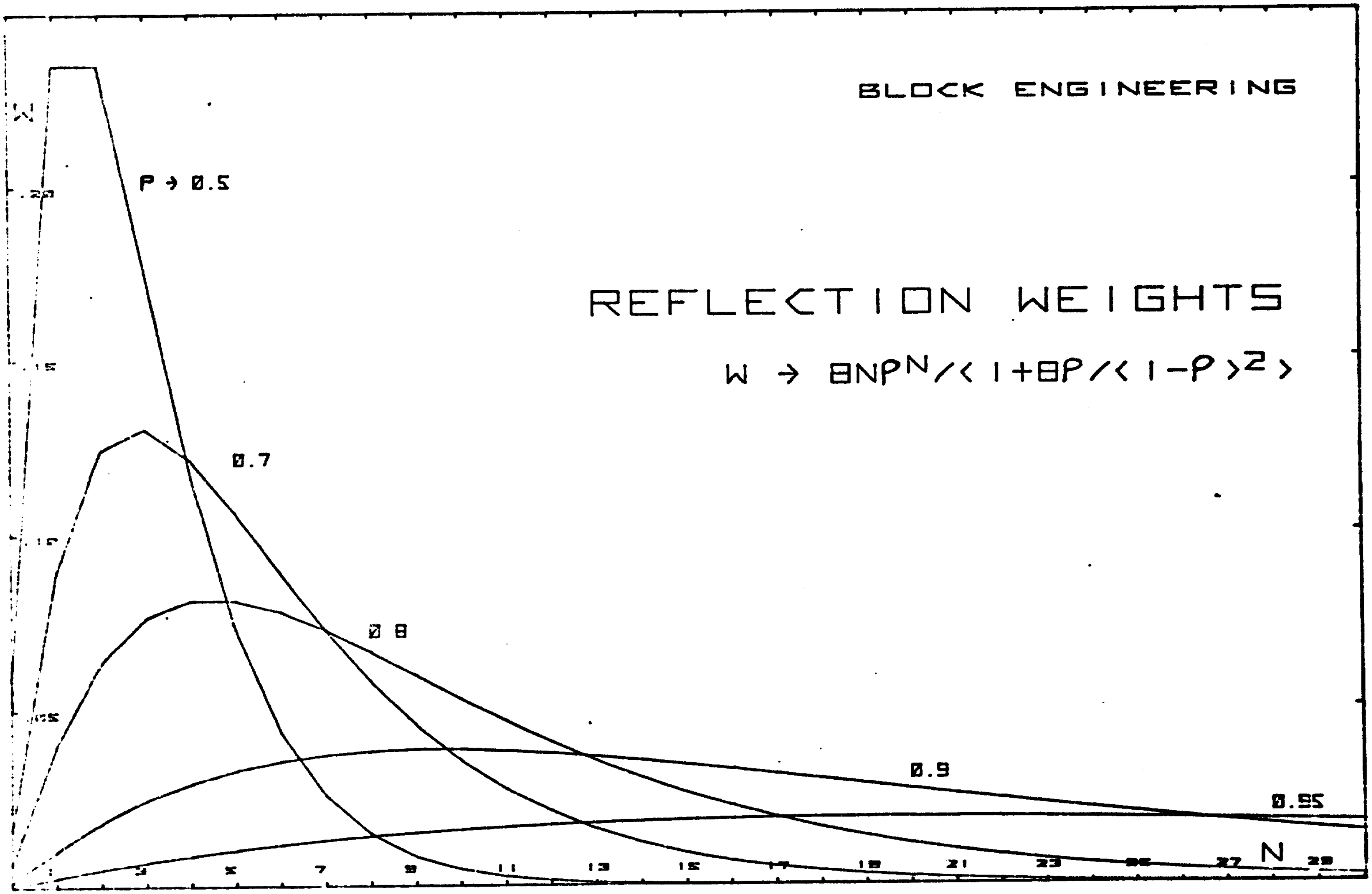

Figure A-3. G(r) Reflection Weights

The total power exiting from the aperture is then

$$P_t = P_{at} + P_{bt} \tag{A-20}$$

and an effective emissivity can be derived if $N_a = N_b$, or if we can relate these radiances at the specific wavelength region of concern.

Since an ideal greybody emission from the aperture <u>s</u> at the temperature T_a is

$$P_t = \varepsilon N_a \ (A_s \ \Omega_s) \tag{A-21}$$

which for the Winston cone we can equate to

$$P_t = \varepsilon N_a \ A \ \text{Cos} \ \theta_a \ \Omega_w \tag{A-22}$$

Introducing these terms into the total power expression

$$\varepsilon_t = eM(\Omega_a/\Omega_w) + (N_b/N_a)(1-r)\Big[\overline{3\Omega_b \ \text{Cos} \ \theta_b}/A\Omega_w(\text{Cos} \ \theta_a + (1-K_b)G(r)(1-e)M\Omega_a/\Omega_w\Big] \tag{A-23}$$

$$= \varepsilon_a + (N_b/N_a) \ \varepsilon_b \tag{A-24}$$

The selection of reflection weights and the determination of the B surface mean solid angle factor is essential if high accuracy is desired. If the emissivity of the A surface is set equal to 1.00 and the surfaces are isothermal, the total emissivity must be exactly 1.00 in the absense of surface scattering. This permits the solution

$$\begin{aligned} \Omega_b(\mathrm{Cos}\ \theta_b) &= (\Omega_w - \Omega_a)\ A\mathrm{Cos}\ \theta_a/B(1-r) \\ &= (\Omega_w - \Omega_s)\ A\mathrm{Cos}\ \theta_a/B \end{aligned} \qquad \text{(A-25)}$$

The determination of a second point to fix the value of k in the F(r) term is possible through the use of Gouffe's method. The emissivity e and the effective emissivity 1-r are equated, and the overall cavity emissivity is calculated from the expression

$$\varepsilon_g = \frac{e\ [1 + (1-e)(s/(A+B) - s/S_o)]}{e\ [1 - s/(A+B)] + s/(A+B)} \qquad \text{(A-26)}$$

This value can be used in an iterative solution, compared with the computed total emissivity ε_t using a large value of r to accentuate the contribution of the dominant F(r) factor. The area S_o in the above expression is the area of a sphere which has a diameter equal to the depth of the cavity along the normal to the entrance aperture s.

A third point is used to determine the value of P in the G(r) expression, again by Grouffe's method. In this case, a small value of r is used to accentuate the contribution of the G(r) term. The iterations for k and P are done together, with emissivities computed for each parameter compared with Grouffe emissivities, and the error use directly to correct the parameter.

APPENDIX B

Boost Surface Parameters

B. BOOST SURFACE PARAMETERS

In the representation of optical surfaces in this optimization program,

$$x = \frac{C(y^2 + z^2)}{1 + [1-KC^2(y^2+z^2)]^{1/2}} = A_1(y^2 + z^2)^2 + A_2(y^2 + z^2)^3 + \ldots \qquad \text{(B-1)}$$

is the equation of a general surface of revolution expressed as the sum of a conic term and a perturbation term. The vertex is at the origin and the x axis is the axis of rotation.

If $C \neq 0$, then the parameter K determines the conic term as follows:

$K > 1$	Ellipsoid rotated abour the minor axis
$K = 1$	Spheroid
$0 < K < 1$	Ellipsoid rotated about the major axis
$K = 0$	Paraboloid
$K < 0$	Hyperboloid

If $C = 0$, the conic term reduces to the yz plane.

Note that as C is positive or negative, the equation above determines a concave or convex surface.

An equivalent form to the conic term is the equation:

$$C[Kx^2 + y^2 + z^2] - 2x = 0 \qquad \text{(B-2)}$$

and the 'centered' version is:

$$K \neq 0 \quad C \neq 0 \qquad \frac{x^2}{(1/K^2C^2)} + \frac{y^2 + x^2}{(1/KC^2)} = 1 \tag{B-3}$$

$$K = 0 \qquad x = \frac{C}{2}\,(y^2 + z^2) \tag{B-4}$$

$$C = 0 \qquad y - z \text{ plane} \tag{B-5}$$

C is the vertex curvature and K is equal to 1 - (eccentricity)^2.

$C \neq 0$

$K > 1$ Ellipsoid Rotated about minor axis

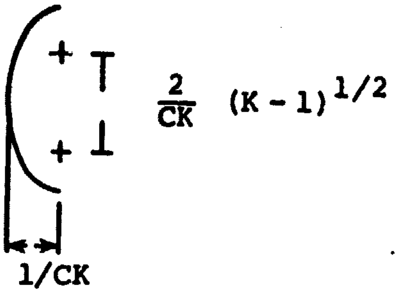

$K = 1$ Spheriod

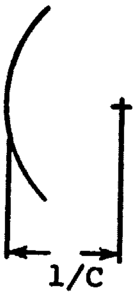

$0 < K < 1$ Ellipsoid Rotated about major axis

$\frac{1}{CK}(1 - (1 - K)^{1/2})$

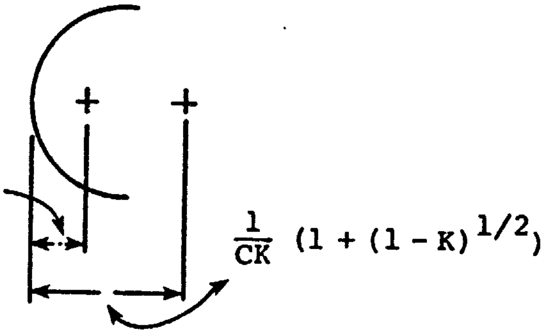

$K = 0$ Paraboloid

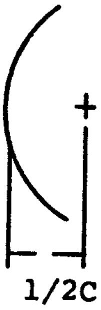

$K < 0$ Hyperboloid

$\frac{1}{CK} ((1-K)^{1/2} + 1)$

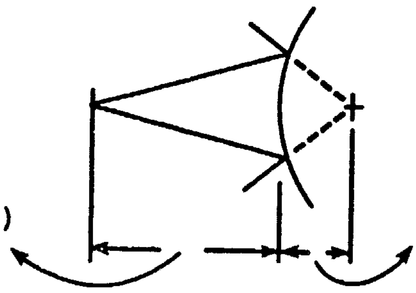

$\frac{1}{CK} ((1-K)^{1/2} - 1)$

APPENDIX C

The following sections, taken from a proposed ATMOS system design, are included as being of special interest here.

2.3.4.1 Signal Handling Subsystem

In order to insure maximum instrument sensitivity, the intrinsic detector noise must be the dominant noise source in the system. This requires a detector preamplifier with a lower input noise voltage than the detector. A very common type of HgCdTe preamplifier employs a transformer to couple the detector to an operational amplifier used in the inverting amplifier mode. This effectively multiplies the detector noise before it is applied to the input stage of the op amp, thus swamping the amplifier input noise. These detector/preamplifier combinations are easily detector noise limited, but are subject to certain disadvantages. One disadvantage is that the transformers are susceptable to magnetic interference. The other disadvantage is that the frequency response of the preamplifier is limited by the transformer and is difficult to achieve more than a 40 kHz upper frequency cut-off.

Another type of preamp that has been successfully used at Block employs an extremely low noise dual FET for the input stage in place of the transformer. A typical high transconductance dual J-FET has an input noise of about 2×10^{-9} $V\sqrt{Hz}$ above 20 kHz. This is less than the typical noise of a HgCdTe detector which is about 3.5 to 4.0×10^{-9} $V\sqrt{Hz}$. These FET input stages, when combined with a high gain bandwidth product amplifier, can easily achieve frequency response up to 1 MHz.

Since the output of the preamp is a wideband signal, and noise is proportional to the $\sqrt{\text{Bandwidth}}$, a filtering system is required after the preamp to limit the bandwidth to the minimum required by the signal frequencies. This is generally done using Bessel response filters which have a maximally flat time delay. The filters can have either a fixed or variable bandwidth. Filters with an externally selectable bandpass would provide the most flexibility.

Several techniques used in the past by Block to minimize noise pickup on the signal channel are available to use in this system. One method is to isolate the detector/preamplifier ground from A/D converter ground. This prevents ground loop currents from entering the sensitive detector ground circuit and producing unwanted noise. Another method is to keep the A/D converters as close to the analog amplifiers as possible. This would suggest keeping the A/D's up in the optical sensor and sending only the digital outputs to the electronics rack.

Since a high gain amplifier will be used to amplify the preamp output for one of the A/D's, a unity gain amplifier with a phase matching capability should be used to buffer the signal to the other A/D. By the use of a voltage divider on the output of the high gain amplifier, the two outputs can be compared and balanced with respect to phase.

2.3.4.2 Command and Control - Interface Subsystem

The command and control electronics performs a preprogrammed sequence of actions upon command. The preprogramming information could be stored in a variety of ways from a built-in patch panel to a bit pattern in the Spacelab's on board computer system. Our method of choice is to include a programmable read-only memory in the control electronics. This provides relatively compact, low cost and low power way of storing experiment sequence information. This approach requires no interaction with the Spacelab's computer systems and avoids developing software for the Spacelab's Experiments Computer.

The actual sequencing of the preprogrammed experiment could be done by a hardwired sequencer, a software controlled sequencer, or the Spacelab's Experiments Computer. Our method of choice is to build a software controlled sequencer based on a readily available microprocessor family such as INTEL 8080/AMD 9080 series. A microprocessor based sequencer is more compact and considerably more flexible than a hardwired sequencer. Use of the Spacelab's Experiments Computer was considered and ruled out due to the larger software development expense. In addition we feel the microprocessor based sequencer approach will be more reliable than a program running on the Spacelab's computer due to simpler design and more thorough testing.

The microprocessor based sequencer with experiment sequences stored in programmable read-only memory (PROM) will allow several different experiments to be predefined as well as providing the possibility of loading new sequence definitions into read-write memory during the flight.

2.3.4.2.1 PCM Formatter

The Command and Control subsystem has been partitioned so that all high rate interferometer data from the sensor is handled by a pulse code modulation (PCM) Formatter and then transmitted directly to the Spacelab High Rate Multiplexer (HRM), requiring a minimum of attention from the microprocessor. This allows the microprocessor to operate at rates independent of the interferometer data rate and represents an efficient hardware/software tradeoff, as the formatting is a repetitive, high rate task.

As Figure 3.2-28 indicates, the sensor will present the high rate data to the Formatter via a FIFO. The clock source for loading this FIFO will be the A/D trigger, whereas the Formatter will operate on its own clock. Rate buffering will be achieved by zero stuffing the data link when the FIFO is not ready to supply data.

In addition to handling high rate data, the Formatter will interleave low rate data into the serial output bit stream. This data will be available via FIFO, loaded by the microprocessor, as described in Section 3.2.4.

The Formatter will be designed and fabricated under a subcontract by Spacetac, Inc. of Bedford MA. Block feels that their contribution provides a valuable program advantage. As described elsewhere in this proposal, they have extensive experience in spaceborne data handling, including a man-rated package built for MSFC and used within Skylab's Multiple Docking Assembly. They will provide the Formatter as a single Printed Circuit card that we will integrate into the Data Handling Subsystem.

As an alternate proposal, correction for bit errors in the PCM telemetry data can be provided by using a convolution encoder.

This will enable ground correction of virtually all bit errors including burst errors occurring anywhere within the data. The price that must be paid for this virtually error free data is that extra non data bits must be added to the PCM and a deconvolution decoder must be used in the ground station. In order to accommodate the extra non data bits (from 33% to 100% more bits are required depending on the code used) either the telemetry bandwidth (maximum bit rate) must be increased, or the mirror position data (which we believe to be unnecessary) must be eliminated, or both if higher interferogram sampling rates are used. See Section 2.3.5.1.2 (PCM Decoding) for additional discussion.

In either the basic proposal or in the option proposal, the approach to implementing the Formatter is the same except for the addition of the convolution encoder. The basic telemetry format is the same in either case.

2.3.5 Ground Support Equipment

The Ground Support Equipment (GSE) for ATMOS is required to perform the following tasks:

1) Decode and reformat PCM telemetry
2) Subsystem checkout
3) Acceptance testing
4) Spacelab integration
5) Storage, handling, servicing, and transport

To perform the tasks of PCM telemetry decoding and reformatting, a ground station is required. This ground station must be capable of reading previously recorded PCM telemetry tapes, docommutating the data and reformatting it on digital magnetic tape in a form suitable for inputting to the JPL Data Processing System (DPS). In addition, the ground station must be capable of generating hard copy, both graphic and tabular, of ATMOS engineering and housekeeping data.

An assembly of Bench Checkout Equipment (BCE) is required. The BCE will be used in conjunction with the ground station to perform the functions of subsystem checkout, and acceptance testing. These equipments will be used in the process of integrating ATMOS with Spacelab and will also serve as servicing aids.

Additional mechanical GSE for the storage, handling, servicing and transport of ATMOS hardware will be required.

2.3.5.1 Ground Station

The function of the ground station is to accept data from the ATMOS sensor and reformat it into a more useable form. Figure 2.3-24

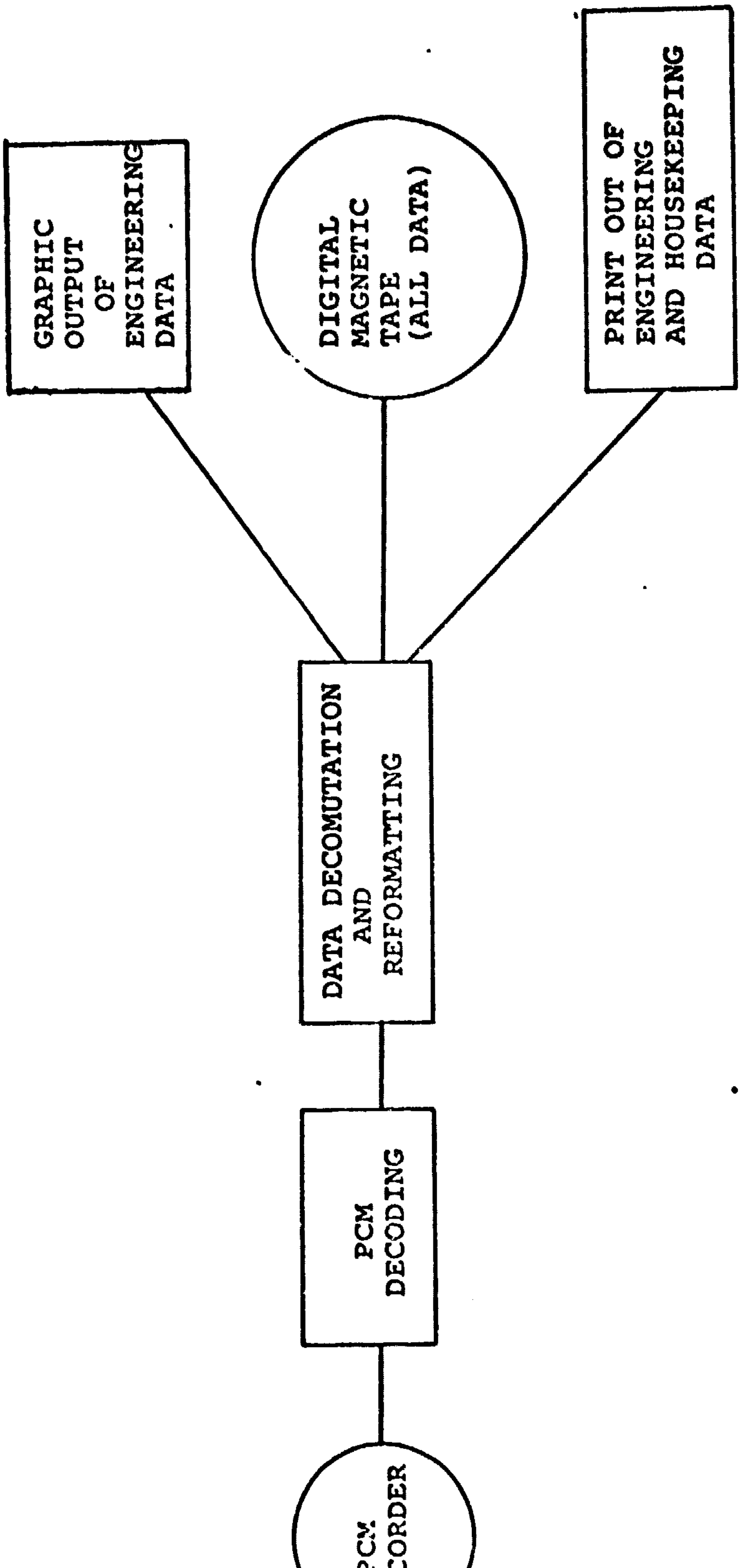

Figure 2.3-24 Functional Block Diagram of ATMOS Ground Station

shows a functional block diagram of the ground station. It must be capable of accepting the high rate down link telemetry and after suitable decommutation, decoding and reformatting, write the transmitted data on digital magnetic tape for subsequent processing by the DPS. The ground station will also be used in conjunction with the BCE for conducting ground tests.

2.3.5.1.1 PCM Recorder

As will be shown below, the high rate telemetry is too fast to record on industry standard digital tape and also too fast for most commercially available PCM decoding products. Thus, as suggested in the RFP, the ground station must include a PCM magnetic tape recorder capable of playing recorded PCM tapes at a reduced rate. The PCM tape subsystem must have a record as well as a playback capability so that the high rate PCM which would normally go to the Spacelab HRM can be recorded during ground tests.

Since this recorder must be capable of recording 10 million bits per second (10 Mb/S), a multitrack parallel recorder is required. Most suppliers offer a maximum recording rate between 2 and 4 Mb/S per track, with a tape speed of 120 inches per second. Thus a minimum of 3 to 5 tracks is required. By using more than the minimum number of tracks, the data rate requirements on a given track are reduced, allowing slower recording tape speeds and longer record times. (At 120 ips, a standard 14 inch reel of tape will run for about 7.5 minutes.)

It is important to match the tape format of the ground station recorder to that of the machine which will be used to record the ATMOS high rate down link telemetry (if a different machine is used). It has also been tacitly assumed that one PCM recorder will be common to both the BCE and the ground station. If this is not desirable, then the ground station and BCE recorders must also have the same format.

The tape format consists not only of the number of tracks, but also how the data is encoded. Different manufacturers use different encoding techniques, even for single track systems. This suggests the advisability of procuring all recorders from a common vendor to insure compatability.

Since the ground station must handle engineering and housekeeping data from a second data path, i.e. through the RAU, telemetry from this source must be recorded on a similar system. Alternately, since the data rates are so much lower, a less costly, lower performance recorder could be used. This would necessitate a second matching reproduce system for the ground station.

An important parameter to consider in PCM record/reproduce systems is the error rate. Most systems, including the High Rate Digital Recorder (HRDR) in Spacelab's High Rate Data Acquisition assembly, do not specify error rates better than 1 in 10^6 bits. In a well designed system, the limiting factor is the medium, i.e. the magnetic tape. By using selected certified tape and careful handling procedures, error rates of 1 in 10^7 are sometimes quoted. Even using the more optimistic rate, in a single 2 second ATMOS scan at 10 Mb/S, 2 errors per scan can be expected assuming a random distribution of errors. This becomes 20 errors per scan using the nominal error rate! And this is in addition to any errors which may occur in the down link process. Note that we suffer the tape error rate twice if the HRDR must be used. Since even one error in interferogram amplitude will cause errors throughout the spectrum, no errors can be tolerated. The next section on decoding will discuss this problem and its possible solutions.

2.3.5.1.2 PCM Decoding

PCM decoding equipment is required to reconstruct the data supplied by ATMOS. This would nominally consist of a bit synchronizer and a decomutator. The bit synchronizer filters and reconstructs the PCM signal and regenerates a coherent (perhaps multiphase) clock. The decomutator operates on the reconstructed PCM signal and clock, locates frame and subframe sync codes and converts the serial input data to parallel output.

This type of decoding system will transmit parallel data to the reformatting hardware with a bit error rate of 1 in 10^6 introduced by the PCM recorder - see previous section. There are several ways to deal with this problem. It could be ignored (unacceptable); provision for error detection (e.g. parity) could be incorporated in the data; or error correction codes could be employed.

If isolated errors are detected, it may be possible to correct them by taking advantage of the fact the interferogram data values are not all independent but form a continuous function with their surrounding data points. By utilizing parity checking, isolated errors can be localized. During data processing "corrected" values could be inferred or interpolated from surrounding data. Even in the absence of parity information it would be possible in principal to locate as well as "correct" errors using this type of approach. This is risky in that not all errors may be found or that valid data may be corrupted by incorrectly identifying it as erroneous. Even after "correction" of the offending erroneous data, the resulting value is only a best guess since the original correct value cannot be known with certainty. A strategy which may improve the chances that the best guess is in fact correct is to choose a corrected value which differs from the erroneous value in only one bit.

It is possible to encode data with an error correcting code prior to transmitting (recording) the PCM. The class of errors which are recoverable depends on the type of code employed. One thing that all such codes have in common is that they add extra non data bits to the PCM stream and to that extent are inefficient. For instance, it is possible to add a 5 bit Hamming code to each 16 bit data word which allows the correction of any single bit error and the recognition of most 2 bit errors.

When considering error correction, the nature of the errors is important. The above discussion assumes that bit errors are random and independent. For media limited PCM record/reproduce errors this may not be the case. A bad spot on the tape is likely to cover more than a single bit since data may be recorded at up to 33,000 bits per inch on each track. It is quite conceivable that multibit errors could corrupt several successive words making correction by any of the above methods at worst impossible or at best subjective. Fortunately, there exist coding techniques which enable recovery from so called burst errors.

This section is not intended as a general dissertation on error correction. Suffice it to say that there exists commercially available equipment for the implementation of convolutional type coding and decoding. Linkabit Corporation of San Diego, California markets a line of convolutional decoders capable of recovering from and correcting burst errors of up to 256 or more bits, assuming properly encoded data. Such a device could be incorporated in the PCM decoding hardware between the bit synchronizer and the decomutator to provide virtually error free data decoding. This would also necessitate the inclusion of an appropriate convolutional encoder stage in the ATMOS PCM formatter.

2.3.5.1.3 Data Reformatting Processor

Data from the PCM decoding system is passed to the reformatting system as a series of parallel words. The RFP suggests that a hardware demultiplexer be employed to output engineering and housekeeping data to chart recorders and that a minicomputer be used to format data onto industry compatible digital magnetic tape.

The minicomputer approach is a very powerful one. It avoids the necessity of building a complex one-of-a-kind digital tape formatter. Such a system would be readily programmable to sort out "stuff" words, perhaps perform some simple error corrections, demultiplex data from any format (including free format tagged data) and write the data on digital tape in any desired format. Given the appropriate output peripheral(s) the computer could also generate graphic outputs of engineering/housekeeping data, eliminating the requirement the hardware demultiplexer.

The choice of minicomputer is to some extent subjective. Digital Equipment Corp. (DEC), Hewlett Packard (HP), Data General Corp. (DGC) or any of several other reputable minicomputer manufacturers could supply a computer which is well supported with software and peripheral hardware and which could be programmed to perform the required tasks. JPL has indicated a preference for a DEC PDP-11 by including one in the sample ground station configuration in the RFP. DEC also has the advantage of being the largest minicomputer manufacturer, and telemetry decoding equipment (EMR) exists which has already been interfaced to the PDP-11 Unibus. In the absence of overriding reasons to the contrary, a PDP-11 computer would seem to be an obvious choice.

The range of PDP-11 models suggested in the RFP is obsolescent. The current models in the PDP-11 line range from the LSI-11 (PDP-11/03) and PDP-11/04 to the top of the line PDP-11/70 with the intermediate PDP-11/34 and PDP-11/60 models. The 11/70 is clearly overkill for this job and the LSI-11 is not fast enough, particularly if the computer must handle graphic as well as tape output. The PDP-11/34 should have sufficient throughput to handle both graphic and tape output simultaneously if the hardware floating point option is included. The PDP-11/60 could also be considered to considerably increase the safety margins for a modest cost increase.

2.3.5.1.4 Digital Tape

In the illustrative example given in the RFP, the digital magnetic tape unit is a DEC TU10. This is a 45 ips machine which can be either 7 or 9 tracks. We shall assume the more efficient 9 track, 800 bits per inch version. Assuming that records are written in blocks of 8K bytes and that it takes 25 msec to write a record gap, each record will take 0.08 sec to write. We shall further assume that any moving mirror position checking required is performed during reformatting and that only interferogram amplitudes need be written on the digital tape (to be followed of course by a housekeeping/engineering data record at the end of each scan). It is also assumed that reformatting includes expansion of the compressed interferogram data from 16 to 32 bits (4 bytes). This means that the TU10 can output data at an average maximum rate of 6,400 data points per second. If the data were digitized at the nominal maximum rate of 200 kHz, it would have to be played back with a time expansion of at least 31.2 so that it would not get ahead of the digital tape. This appears to fit nicely with a PCM playback speed reduction of 32:1. There is virtually no room for error however, and to allow for a safety margin, the PCM tape could be played back with a speed reduction of 64:1. In other words, it would take more than 2 hours to transcribe the data from a single 2 minute measurement cycle.

There are several possible ways to improve on this performance. The most obvious way is to use a higher performance tape drive. It is desirable to use DEC hardware to avoid software support and licensing problems with DEC. These are not insurmountable problems and high performance 200 ips, 1600 bpi machines are available with compatible interfaces from other vendors. However, in this proposal, we will consider only DEC alternatives. The only higher performance tape system available for the PDP-11 is the TU16 which is a 45 ips machine capable of 1600 bpi. This machine would provide a more than adequate safety margin to operate with a time expansion of only 32.

Another possibility would be to record the compressed form 16 bit interferogram data words on tape. This data would then have to be expanded in the DPS as the initial processing step. Implementation of this convention would result in a factor of two increase in speed. If used with the TU10, a 32:1 playback speed could be used; 16:1 with the TU16.

As discussed elsewhere in this proposal, it would be desirable to digitize data at a higher rate than the nominal maximum of 200 kHz; perhaps as fast as 500 KHz. If this higher digitization rate were implemented, the PCM playback time expansion would have to increase proportionately, other things being equal. With the 32 bit output format, the TU10 would require a 128:1 playback ratio or 64:1 for the TU16. Using the 16 bit output format, the TU10 would require a 64:1 playback ratio or 32:1 for the TU16.

With standard 2400 ft. reels, 800 bpi, 32 bit words, 400,000 words per scan, only about 13 scans (less than 30 seconds) will fit on a tape. With 16 bit words and 1600 bpi, a tape will hold about 51 scans or slightly less than 2 minutes of data. Thus, several tapes will be required to hold the data from a single PCM tape. By having two digital tape drives, PCM tape processing could be continuous, using one drive while the other is being rewound, unloaded and reloaded and then switching drives at the end of each digital tape.

2.3.5.1.5 Hard Copy/Operator's Terminal

The hard copy requirements are for graphic and tabular outputs of engineering/housekeeping data. As the RFP suggests, a hardware demultiplexer driving chart recorders and a Teletype ASR33 could be adequate for those purposes. In this case, the ASR33 is also the operator's terminal. However, there are some interesting alternatives. The LA36 DECWRITER II is a very popular terminal built by DEC. It has the advantage of being 3 times faster and much quieter than the Teletype. It does not have the Teletype's paper tape reader and punch but this capability is of negligible importance in a system such as this with alternate digital I/O (mag tape) devices. An even more preferable operator's terminal is the DEC VT52 DECscope, a CRT terminal which is almost 90 times faster than a teletype and is virtually silent. The fact that it has no hard copy output means that the operator is not cluttered with unwanted paper but an alternate printer is necessary for the required tabular outputs.

The proposed PCM format makes it difficult - impossible with standard hardware - to demultiplex the engineering/housekeeping data for chart recorder display. This demultiplexing is easily done in the computer. Thus, the computer could drive the D/A's for the chart recorder, or a digital plotter could be used. By using an electrostatic printer/plotter, a single device could be used for both graphics and tabular hard copy. This would enable the use of DECscope CRT terminal and eliminate the requirement for the hardware demultiplexer with A/D's and chart recorder(s). Aside from the increased performance aspect, the DECscope, printer/plotter combination is nearly identical in cost to the Teletype, hardware demultiplexer combination.

2.3.5.1.6 Moving Head Disk

The inclusion of a moving head disk memory would be an invaluable addition to the computer system because it would enable the use of one of DEC's disk operating systems. Such an operating system provides a foundation for operational software and facilitates the process of software generation.

A disk is non volitile storage; programs can be stored ready for instant loading into the computer and execution by the operating system. Since programs are so easily and rapidly loaded, there is no requirement for non volitile (core) main memory in the computer and the more reliable and faster MOS memory may be used instead.

Since the computer will be used also for the BCE, BCE software can also be stored on the disk ready for immediate execution. The use of a disk operating system (RSXM-11) is a prerequisite for FORTRAN 4 PLUS. FORTRAN 4 PLUS code is nearly as efficient as programs written in assembly language, but by using this high level language to the maximum extent possible, software generation labor costs will be minimized.

A very moderate amount of disk storage is required since its primary function is program storage. A single RK11 DEC pack cartridge disk drive gives 1.2 million words of storage which should be adequate.

2.3.5.1.7 Software

In addition to RSX-11M and FORTRAN IV PLUS from DEC, there are two additional software packages which will substantially simplify the new software required for this system: TELEVENT-11 and associated software from EMR and VERSAPLOT from Versatec.

TELEVENT-11 is a special operating system, compatible RSX-11M and other DEC operating systems, that includes front-end device setup drivers for EMR devices, digital tape formatting for data acquisition and a convenient means of integrating user written programs. EMR offers optional extensions to TELEVENT-11 for data decomutation and strip chart emulation on a Versatec 1100A Printer/ Plotter.

VERSAPLOT is a set of FORTRAN capable subroutines similar to the familiar CALCOMP pen plotter routines. Given the EMR strip chart emulator software, VERSAPLOT would not be required for the Ground Station. However, for BCE use, it will be useful in plotting interferograms and low resolution spectra for ATMOS checkout and calibration.

2.3.5.2 Bench Checkout Equipment

The Bench Checkout Equipment (BCE) is required for the ground testing of ATMOS: subsystem checkout, acceptance testing and Spacelab integration. The BCE must simulate all pertinent Spacelab functions and contain all of the necessary test and calibration equipment to fully excercise ATMOS. A functional block diagram of the BCE is given in Figure 2.3-25.

2.3.5.2.1 Spacelab Subsystems Simulation

In order to operate and fully test ATMOS on the ground, including its interaction with Spacelab, all pertinent Spacelab subsystems must be simulated to the degree that they interface with ATMOS. Specifically, the Electrical Power Distribution Subsystem (EPDS), the Remote Acquisition Unit (RAU), and the High Rate Multiplexer (HRM) input must be simulated.

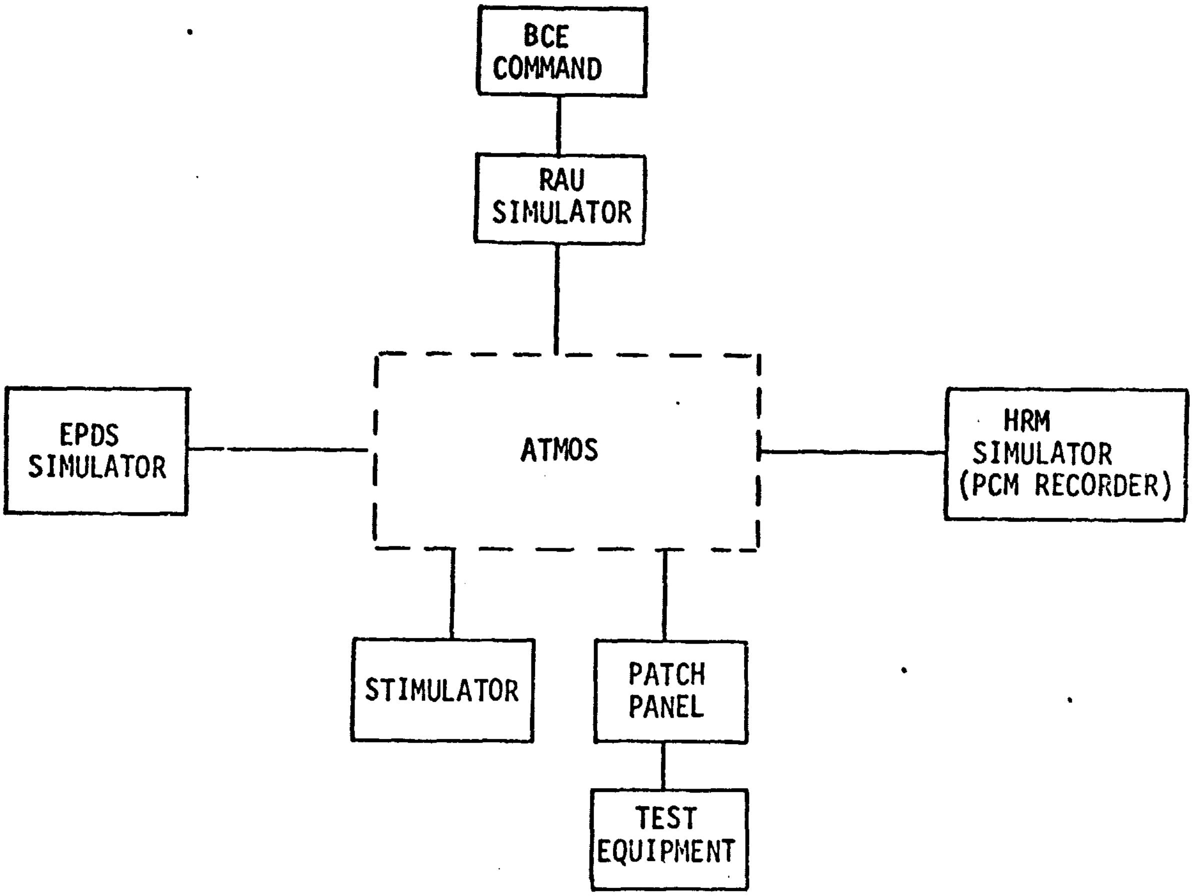

Figure 2.3-25 Functional Block Diagram of ATMOS BCE

2.3.5.2.1.1 Power Supply and EPDB Simulator

The BCE power supply is required to supply 28 ± 4 VDC to simulate spacecraft power. The output of the supply is to be routed through the EPDB simulator, which will simulate the functions of an Experiment Power Distribution Box used on the spacecraft.

The power supply will be either designed and built by Block Engineering or purchased from a commercial manufacturer, depending upon cost effectiveness and specifications. If the supply is built by Block, it will be designed to restrict the output voltage to the 24 to 32 VDC range. As most commercial variable output power supplies are capable of a much greater output voltage range, if a commercial supply is used, it will be modified by Block to restrict the output to 28 ± 4 VDC. This will avoid damage to the instrument by accidental extreme over or under voltage conditions outside of the normal operating range.

The Spacecraft Experiment Power Distribution Boxes have two DC outputs with 75A protection per output, two DC outputs that together are protected for 75A, and four AC outputs that are not protected. There are three circuit breakers for DC and three latching relays for AC that can be switched selectively by RAU on/off commands. The EDPB simulator will provide control over the 28 VDC power from the power supply via the RAU simulator. As only one EPDB DC output is routed to the Experiment Power Switching Panel located on the instrument rack, the EPDB simulator will not require the additional three DC and four AC outputs normally supplied by the spacecraft EPDB.

APPENDIX D

D.1 ERRORS IN THE COMPUTED SPECTRUM CAUSED BY AMPLITUDE FLUCTUATIONS

In the operation of a two-beam Fourier spectrometer, samples of the interferogram are collected during one scan of the movable mirror, during which time it is assumed that the energy received at the instrument input remains stationary. If this is not the case, the resulting interferogram contains a component of amplitude error which gives rise to errors in the computed spectrum.

Amplitude fluctuations of the received input signal may be caused not only by actual variation of the source intensity, but may also arise from variations in the attitude of the instrument with respect to the source during a scan. These variations may be deterministic (such as the transit of the source through the field of view) or may be describable only statistically (as when random 'pointing' errors are caused by atmospheric diffraction, or when the source is 'tracked' and random pointing errors are modified by the error-corrections induced by the tracking servo loop). Also, amplitude variations may be caused by electronic filtering of the received interferogram signal (depending upon the amplitude and phase characteristics of the filter used), a step which is normally used to reduce high-frequency detector noise.

When actual source fluctuations exist, the noise induced in the computed spectrum can be seen to be related to the spectrum of the source fluctuations. When the source is stationary, but fluctuations arise due to random or pointing errors, the noise spectrum is related to the spectral structure of the turbulence, or the spectrum of the pointing error and also to the spatial distribution of the source intensity as a function of pointing angle.

The effects of systematic components of radiation source fluctuations on obtained spectra have been discussed by Kiselev and Pivovar (1973). This study concluded that such amplitude errors introduce the largest contribution to the peak of the resolution spread function, but that the broadening of the central peak of the spread function is insignificant for small amplitude fluctuations. The spectral error caused by errors in pointing is analyzed by Schroeder and Lee (1976) who demonstrate that for small pointing errors, the spectrum of the noise is proportional to the spectrum of the pointing error.

It would seem reasonable to assume that the spectral error due to fluctuations (either of the source or of the intervening medium or instrument) could be filtered out from the interferogram information if the two were well separated in spectral terms. This is in fact the case, and also, since in practice the interferogram temporal frequency may be made quite high by using a rapid scan rate, we do in fact have some control over the degree of separation of the received signal and the fluctuation noise. For a given scan rate, both the characteristic source fluctuation time and the servo loop bandwidth of the tracking or pointing characteristic will determine whether simple low pass filtering is adequate to separate the low-frequency noise.

Even if there is a frequency overlap, more sophisticated methods can be used to obtain a separation, as discussed by Schroeder and Lee.

The second effect of the fluctuation in received signal is an envelope modulation of the recorded interferogram which, if the fluctuations are small, amounts to a weak amplitude modulation. The effect on the spectrum is to create 'ghost' sidebands for each real spectral feature, which are separated by the modulating frequency from the parent line; however, there are no intermodulation products on sum and difference frequencies. Also, the amplitude of original spectral features is unchanged except by contribution from other features separated by the modulating frequency. These results may be seen in the following analysis.

The resulting signal component at ν_s in the interferogram may be represented by the equation

$$\varepsilon(t) = \varepsilon_o f(t) \cos 2\pi(\nu_s t + \phi_s) \qquad \text{(D-1)}$$

where $\varepsilon(t)$ is the time signal corresponding to the interferogram frequency ν_s; $f(t)$ is the modulating waveform.

Let $f(t) = 1 + \sum_n \varepsilon_n \cos 2\pi(\nu_n t + \phi_n)$ (D-2)

where each of ε_n is << 1 (i.e., small amplitude modulations are assumed.

Then,

$$\varepsilon(t) = \varepsilon_o \{1 + \sum_n \varepsilon_n \cos 2\pi(\nu_n t + \phi_n)\}\{\cos 2\pi(\nu_s t + \phi_s) \quad \text{(D-3)}$$

$$= \varepsilon_o \cos 2\pi(\nu_s t + \phi_s) + \frac{\varepsilon_o}{2} \sum_n \varepsilon_n \cos 2\pi$$

$$\times \{(\nu_s + \nu_n)\ t + \phi_s + \phi_n\}$$

$$+ \frac{\varepsilon_o}{2} \sum_n \varepsilon_n \cos 2\pi\{(\nu_s - \nu_n)\ t + \phi_s - \phi_n\}. \quad \text{(D-4)}$$

Then the amplitude of each sideband is $\frac{\varepsilon_o \varepsilon_n}{2}$, i.e. for a 1% modulation ($\varepsilon_n = 0.01$), the sideband amplitude is ½% of the parent amplitude, at each of the frequencies $(\nu_s \pm \nu_n)$.

When the amplitude fluctuations are random in nature rather than deterministic, we can still relate the amplitude flucutations to errors caused in the spectrum. In this case the error spectrum is replicated around each spectral feature. In this case f(t) is

$$f(t) = 1 + \sum_n \varepsilon_n \cos 2\pi(\nu_n t + \phi_n) \quad \text{(D-5)}$$

where ε_n are now samples of a random function instead of being constant. In this case the noise power is given by

$$\frac{\varepsilon_o^2}{4} \sum \left[\varepsilon_n \cos 2\pi\{(\nu_s - \nu_n)t + \phi_s - \phi_n\}\right]^2 \quad \text{(D-6)}$$

for each sideband. Thus, the amplitude of each sideband is

$$\frac{\varepsilon_o}{2} \cdot (\sum \overline{\varepsilon_n^2})^{\frac{1}{2}} \quad \text{(D-7)}$$

Thus again, the "signal/noise" ratio in the output spectrum is $(\overline{\varepsilon_n^2}/2)$ as a result of amplitude fluctuations.

D.2 SPECTRAL ERRORS CAUSED BY ERRORS IN THE SAMPLING INTERVAL

In this appendix we assess the magnitude of error in the computed spectrum which may occur as a result of non-uniform sampling. Although more involved analysis are possible, we can obtain simple estimates of these spectral errors provided certain simplifying assumptions are made. These assumptions amount to the restriction that the time jitter causing the sampling error is small compared to the inter-sample interval.

Under these conditions, an analysis of spectral errors due to sampling errors has been made by N. Connes (1961). She computed the spectral error caused by a sinusoidal variation in the sampling interval, a situation which is equivalent to narrowband phase modulation of an otherwise fixed electrical carrier frequency. For this case, the amplitude of the spectral error is

$$\beta(\nu_s \pm m\nu_\varepsilon) = (-1)^m J_m(2\pi\varepsilon\ \nu_s(E(s), \qquad m = \pm 1, \pm 2, \ldots\ldots \tag{D.2-1}$$

where

$\beta(\nu_s \quad m\nu_\varepsilon)$ are the amplitudes of the spectral sidebands at the frequencies $\nu_s \pm m\nu_\varepsilon$, and

ε is the sinusoidal error maximum (cm)

ν_ε is the frequency of the error ε, cm^{-1}

$E(s)$ is the signal amplitude, and

J_m is the Bessel function of first order.

For the narrowband assumption made here, ie, for

$$\varepsilon \nu_s << 1. \tag{D.2-2}$$

$J_1(2\pi\varepsilon\nu_s)$ may be replaced by the approximation $\pi\varepsilon\nu_s$. Moreover, with the narrowband approximation only the first term in the series expansion for β is significant. Therefore we write

$$\beta(\nu_s \pm \nu_\varepsilon) = \pi\varepsilon\, \nu_s\, E(s). \tag{D.2-3}$$

In order that errors due to sampling remain small compared to those based upon radiometric considerations, we then have the restriction that the above noise amplitude be less than the spectral signal/noise ratio $(\mathrm{SNR})_s$. Therefore,

$$\frac{E(s)}{\beta(\nu_s \pm \nu_\varepsilon)} > (\mathrm{SNR})_s \tag{D.2-4}$$

or

$$\varepsilon \leq \frac{1}{\pi\nu_s} \frac{1}{(\mathrm{SNR})_s}. \tag{D.2-5}$$

If β the noise amplitude is expressed in RMS terms, we get the modified expression

$$\varepsilon \leq \frac{\sqrt{2}}{\pi\nu_s} \frac{1}{(\mathrm{SNR})_s}. \tag{D.2-6}$$

When the sampling error is random or quasi-random in nature (due for example to mechanical resonances or to impulse noise, etc.), ε should be replaced by its amplitude density function $\varepsilon(\nu)$. In this case, the noise, being proportional to the square-root of the bandwidth element, is given by

$$\beta(\nu) = \pi\nu_s \, \varepsilon(\nu)(\Delta\nu)^{1/2} \, E(s). \tag{D.2-7}$$

For a bandwidth of $\varepsilon(\nu)$ which is S_ν, where $S_\nu < (\nu_{max} - \nu_{min})$, the spectral coverage, because the number of spectral elements that contribute to spectral errors is

$$S_\nu/(\Delta\nu), \tag{D.2-8}$$

the total error due to sampling interval errors (assuming each element to be uncorrelated) is

$$\beta = \pi\nu_s \, \varepsilon(\nu) \, (\Delta\nu)^{1/2} \, [S(\nu)/(\Delta\nu)]^{1/2} \quad E(s) \tag{D.2-9}$$

or, since

$$\varepsilon(\nu) \quad [S(\nu)]^{1/2} = \varepsilon, \tag{D.2-10}$$

$$\beta = \pi\nu_s \, \varepsilon \, E(s).$$

Therefore, as before, the RMS error ε is limited to

$$\varepsilon \leq \frac{1}{\pi\nu_s} \quad \frac{1}{(SNR)_\varepsilon} \tag{D.2-11}$$

if it is to be small compared to the radiometric signal/noise ratio.

In the above discussion, all errors and bandwidths were expressed in wavenumbers (cm^{-1}). Since many disturbances are electrical in nature, they need conversion in order to be expressed in wavenumber space.

Since $S(f) = (B/t) \quad E(\nu),$ (D.2-12)

where B is the optical retardation, one can be converted to the other readily by multiplying or dividing by the scan velocity, v, given by

$$v = (B/t). \qquad \text{(D.2-13)}$$

Ade, P.A.R., Costley, A.E., Cunningham, C.T., Mok, C.I., Neill, G.E., and Parker, T.L., Infrared Physics 19, 599, 1979.

Bor, J. and Bartholomew, C., Proc. Phys. Soc (London) 90, 1153, 1966.

Brixner, B., Appl. Opt. 2, 1281, 1963; see also 12, 2703, 1973.

Chambers, W.G., Mok, C.L., and Parker, T.J., to be published in Jnl. Phys. D: Appl. Phys., 1979.

Connes, J., Rev. Opt. 40, 45, 1961.

Connors, R., private communication, 1978.

Garg, R.K. and Pradhan, M.M., Infrared Physics 18, 293, 1978.

Grammer, J.R., Aff, C.H., Plue, H.H., and Perkowitz, S. 1978.

Harper, D.A., Hilderbrand, R.H., Stienging, R. and Winston, R., Appl. Opt. 15, 53, 1976.

Hochheimer, B.F., Appl. Opt. 16, 2039, 1977.

Holah, G.D. and Auton, J.P., Infrared Physics 14, 217, 1974.

Holah, G.D., Davis, B., and Morrison, N.D., Infrared Physics 18, 621, 1978.

Johnson, N.J.E., See Interim Study Report for Cosmic Background Explorer, NASA/GSFC, pgs. D-24 and D-25, Feb. 1, 1977.

Kiselev, B.A. and Pivovar, N.I., Optical Technology 40, 663, 1973.

Lambert, D.K. and Richards, P.L., Appl. Opt. 17, 1595, 1978.

Martin, D.H. and Puplett, E., Infrared Physics 10, 105, 1969.

Mather, J.C., Far Infrared Spectrometry of the Cosmic Background Radiation, Thesis, Lawrence Berkeley Laboratory, University of California, LBL-2258, January 1974.

Mather, J.C. Richards, P.L., and Woody, D.P., IEEE Trans. Microwave Theory Tech. 22, 1046, 1974.

Mather, J.C., private communication, 1979.

Mok, C.L., Chambers, W.G., Parker, T.J., and Costley, A.E., Infrared Physics 19, 437, 1979.

Motulevich, G.P. and Shubin, A.A., Soviet Phys.-JETP 17, 33, 1963.

Pradhan, M.M., Infrared Physics 10, 199, 1970.

Prettl, W. and Frank, W.F.X., Infrared Physics 19, 491, 1979.

Schroeder, G. and Lee, A., Appl. Opt. 15, 604, 1976.

Scott, R.B., *Cryogenic Engineering*, Van Nostrand Company, Princeton, NJ, 1959.

Soglasnova, V.A., Sov. Jnl. Opt. Tech. 45, 66, 1978.

Stewart, R.B. and Johnson, V.J., Ed., *A Compendium of the Properties of Materials at Low Temperatures (Phase II)*, Nat. Bur. Standards, WAAD Technical Report 50-56, Part IV, Dec. 1961.

Ulrich, R., Infrared Physcis 7, 37, 1967a.

Ulrich, R., Infrared Physics 7, 65, 1967b.

Weiss, R., M.I.T. Report to the COBE Science Team, 1979.

Welford, W.T. and Winston, R., J. Opt. Soc. Am. 68, 531, 1978.

Winston, R., J. Opt. Soc. Am. 60, 245, 1970.

Winston, R., and Welford, W.T., J. Opt. Soc. Am. 69, 532, 1979.